13

Modeling

E. Loth
University of Illinois

G. Tryggvason
Worchester Polytechnic Institute

Y. Tsuji
Osaka University

S.E. Elghobashi
University of California

Clayton T. Crowe
Washington State University

A. Berlemont
National Centre for Scientific Research

M. Reeks
University of Newcastle upon Tyne

O. Simonin
Institute of Mechanics of Fluids of Toulouse

Th. Frank
ANSYS Germany GmbH

Y. Onishi
Pacific Northwest National Laboratory

B. van Wachem
Chalmers University of Technology

13.1 Overview of Multiphase Modeling

E. Loth

13.1.1 Classification of Multiphase Flows

To numerically model a multiphase flow, it is often important to use separate formulations for the different phases. Let us define the *particle phase* as the phase that consists of bubbles, particles, or drops, and the *continuous phase* as the fluid in which these particles are generally immersed. The particles can be composed of solid, liquid, or gas, whereas the continuous fluid can be a liquid or a gas.

The coupling between the particle motion and its surroundings can be used to classify the character of the multiphase flow, and thus help determine appropriate numerical techniques. The broadest division is between dispersed and dense flows, and refers to which coupling mechanism primarily determines the particle motion. As shown in Figure 13.1, a multiphase flow can be considered dispersed if the effect of particle–fluid interactions dominates the overall transport of the particles. Particle–fluid interaction generally

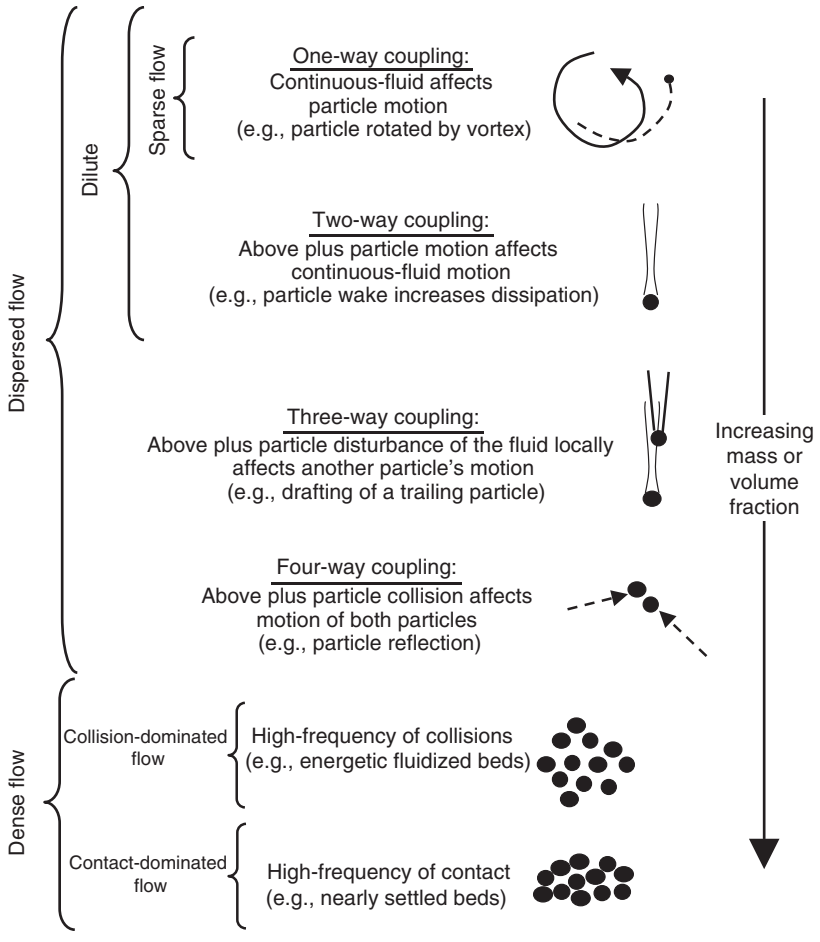

FIGURE 13.1 Dilute, dispersed, and dense flow conditions based on various interphase and intraphase coupling.

includes a drag force, which hinders the relative velocity of the particle, and thus causes particle trajectories to tend toward continuous-fluid trajectories. If the particle–particle motion dominates, the flow can be considered to be dense. Particle–particle interactions can refer to two separate mechanisms: particle–particle collisions (where the particles can rebound, shatter, or coalesce by impinging on each other) and particle–particle fluid dynamic interactions (where the proximity of the particle affects their fluid dynamic forces). Dispersed flow will generally include one-way coupling (where the dispersed-phase motion is affected by the continuous phase, but not vice versa), two-way coupling (where the dispersed phase also affects the continuous phase through the interphase coupling, e.g., drag force), three-way coupling (where particle wakes and other continuous-phase disturbances affect the motion of other particle interactions), and four-way coupling (where collisions and other particle–particle interactions influence, but do not dominate, the overall particle motion). Dense flows will be generally defined as having four-way coupling, although is some cases (e.g., granular flows), the effects of the particles on the continuous fluid are weak and often neglected.

13.1.2 Classification of Methodologies

In addition to the above classification for multiphase flow phenomenon, we can also classify the various numerical formulations. For one-way coupling conditions, the continuous phase can be computed independent of the particle phase. The optimum numerical formulation of the continuous flow is often strongly dependent on the flow Reynolds number, and is discussed in the following section, but is typically described with an Eulerian reference-frame methodology. Typically, a spatial grid resolution (Δx) is specified for which

the continuous-flow equations are discretized in the Eulerian domain and solved. For two-way coupling, these equations need to be modified to include the interphase mass, force, and heat transfer.

Several variations and combinations of these numerical treatments have been put forth, but relevant fluid-particle physics and the available computational resources are the primary determinants for which a set of treatments is more appropriate for a particular flow field. The following two sections separately overview various techniques for simulating the continuous-phase flow and that of the particles, respectively.

13.1.3 Overview of Continuous-Phase Flow Methodologies

In the numerical treatment of the continuous-phase flow, the solution domain and reference frame must be considered. Continuous-flow simulations are typically carried out in an Eulerian reference frame, since it is usually the most computationally efficient description for solution, particularly for steady flows. In the Eulerian reference frame, a domain of fluid is typically considered where the domain motion and boundaries are selected based on convenience, e.g., moving at the speed of a reference frame and with boundaries parallel to solid surfaces. Different spatial discretizations for the fluid characteristics (velocity, temperature, and pressure) are possible, e.g., constant, linear, quadratic, etc. These discretizations can be used with finite-difference, finite-volume, and finite-element treatments. In addition, discretization can be by wavelength, such that spectral and pseudo-spectral representations can be used to describe the flow quantities throughout the domain. Although less common than the Eulerian treatment, the continuous fluid is sometimes treated in a Lagrangian manner, e.g., the discrete eddy tracking techniques termed vortex dynamical models. In addition, there are some hybrid methods such as the Arbitrary-Lagrangian–Eulerian (ALE) technique. In general, the treatments of the continuous-phase flow are subject to standard resolution convergence issues (spatial and temporal) to satisfy the governing differential equations.

In determining the proper equations of motion, it should be noted that various mathematical representations of the continuous-phase fields are possible, depending on the controlling physics. A key issue regarding formulation of the flow surrounding the particles is whether the flow can be considered as a continuum, or whether the effects of random molecular collisions must be considered. In particular, two classes of noncontinuum effects can arise in multiphase flow: first, the entire domain can have features that depend on the discrete molecular interactions (regardless of the particle interactions), in which the assumption of a continuous phase is no longer appropriate. In this case, some critical length scale of the domain is on the order of the molecular mean free-path for the surrounding fluid. In the second case, we can assume that all the fluid domain length scales (including particle diameter) are much greater than the molecular mean free-path (as is generally assumed here), and the flow that a particle ″sees″ can be considered a continuum.

Assuming a continuum, generally, the most important characterization of the continuous-phase flow is whether it is assumed to be inviscid or viscous, since this determines the relevant partial differential equations (PDEs) to be numerically solved. For inviscid flow formulations, the quantitative effects of friction over surfaces and dissipation of vorticity are not of primary relevance to the desired flow properties and are thereby neglected. Note that an inviscid continuous-phase solution does not preclude the effects of viscosity with respect to particle motion, e.g., simulations of a dusty-shock flow can neglect viscosity with respect to interactions with solid surfaces, but can still consider the viscous drag effects on the particles. Inviscid flow formulations primarily fall into three categories with an increase in physical complexity:(1) potential flow (incompressible and irrotational), (2) incompressible rotational flow, and (3) compressible rotational flow (Euler equations); which require a transport equation for energy.

Viscous flows require inclusion of shear stresses in the PDE formulation and thus in the numerical solution. These flows can be subdivided by effects of compressibility, unsteadiness, etc., but they are primarily classified as laminar, transitional, or turbulent. In general, the Reynolds number largely determines the type of numerical treatment. In the following sections the formulations and numerical approaches are considered for various flow Reynolds number regimes.

13.1.3.1 Reynolds Number Effects on Continuous-Phase Flow

The Reynolds number of the flow is often the most important characteristic that determines the flow physics. The flow Reynolds number represents the ratio of convective forces to viscous forces. On a macroscopic scale,

it can be generally defined as $Re_L = \rho_f L u_L / \mu_f$, where L and u_L are a length and a velocity scale associated with the continuous-phase flow domain (e.g., pipe diameter and the mean streamwise flow speed) and ρ_f and ν_f are the density and kinematic viscosity of the continuous phase. Another important characteristic is the flow Mach number, which represents the ratio of convection speed to the speed of isentropic pressure fluctuations (the speed of sound). The macroscopic Mach number can be defined as $M_L = u/a_f$, where a_f is the speed of sound of the continuous phase. It is helpful to consider the limit of $M_L \ll 1$ and negligible thermal variations or stratification, so that one may generally assume constant density of the continuous fluid. In addition, let us ignore the effects of two-way coupling at this point (for simplicity), so that there is no influence of the particle phase on the continuous-phase motion. Written in tensor notation, the continuity and momentum equations in the i direction for the single-phase fluid momentum (White, 1991) become

$$\partial u_{fj}/\partial x_j = 0$$

$$\rho_f u_i/t + \rho_f u_j\, \partial u_i/\partial x_j = \rho_f g_i - \partial p/\partial x_i + \partial \tau_{ij}/\partial x_j$$

where p is pressure, u_i the velocity in the i direction, g_i the magnitude of the gravity vector in the i direction, and $\tau_{ij} = \mu_f(\partial u_i/\partial x_j + \partial u_j/\partial x_i)$ which the viscous stress tensor. In the limit of no flow (quiescent conditions), this equation yields $\rho_f g_i = \partial p/\partial x_i$, which is the hydrostatic pressure gradient equation.

If we further assume constant viscosity, the Navier–Stokes PDE becomes (in either tensor or vector form)

$$u_i/t + u_j\, \partial u_i/\partial x_j = g_i - (1/\rho_f)\partial p/\partial x_i + \nu_f\, \partial^2 u_i/\partial x_j^2$$

$$\partial \boldsymbol{u}/\partial t + \boldsymbol{u}\cdot\nabla \boldsymbol{u} = \boldsymbol{g} - \nabla p/\rho_f + \nu_f \nabla^2 \boldsymbol{u}$$

where $\nu_f = \mu_f/\rho_f$, $\boldsymbol{u}$ the continuous fluid velocity, $\boldsymbol{g}$ the gravity vector, and the divergence of the fluid velocity is zero ($\nabla\cdot\boldsymbol{u} = 0$). As the convective terms become stronger than the viscous terms (corresponding to an increase in the flow Reynolds number), the flow will proceed from laminar conditions to transitional and then to turbulent flow conditions. In the following section (and in Table 13.1), various Reynolds number flow regimes are considered under the assumption that the presence of the dispersed phase does not alter the numerical approach significantly (e.g., as in one-way coupled systems).

13.1.3.1.1 Laminar Flow

For $Re_L \ll 1$, the flow is highly laminar and is typically termed creeping flow. This condition arises in many low-speed flows and microfluidic systems. In this case, the viscous effects dominate and convection

TABLE 13.1 Forms of the Continuous-Flow Incompressible Navier–Stokes Momentum Equations, Assuming No Coupling from the Particles (i.e., Assuming One-Way Coupling)

Flow Condition	Flow Reynolds No.	Tensor Form of Fluid Momentum Equation
Steady creeping flow	$Re_L \ll 1$	$0 = \rho_f g_i - \partial p/\partial x_i + \mu_f \partial^2 u_i/\partial x_j \partial x_j$
Steady laminar flow	$Re_L < Re_{crit}$	$\rho_f u_j \partial u_i/\partial x_j = \rho_f g_i - \partial p/\partial x_i + \mu_f \partial^2 u_i/\partial x_j \partial x_j$
Transitional flow	$Re_{crit} < Re_L < Re_{turb}$	$\rho_f\, \partial u_i/\partial t + \rho_f u_i \partial u_i/\partial x_j =$ $\rho_f g_i - \partial p/\partial x_i + \mu_f \partial^2 u_i/\partial x_j \partial x_j$
Turbulent flow (DNS)	$Re_L > Re_{turb}$	Same as for transitional flow
Turbulent flow (LES)	$Re_L > Re_{turb}$	$\rho_f \partial \bar{u}_i/\partial t + \rho_f \bar{u}_j\, \partial \bar{u}_i/\partial x_j + \rho_f\, \partial(\overline{u_i' u_j'})/\partial x_j =$ $\rho_f g_i - \partial \bar{p}/\partial x_i + \mu_f \partial^2 \bar{u}_i/\partial x_j \partial x_j$ where $(\bar{\ })$ is a spatially filtered quantity
Turbulent flow (RANS)	$Re_L > Re_{turb}$	$\rho_f \bar{u}_j \partial \bar{u}_i/\partial x_j + \rho_f \partial\, (\overline{u_i' u_j'})/\partial x_j =$ $\rho_f g_i - \partial \bar{p}/\partial x_i + \mu_f\, \partial^2 \bar{u}_i/\partial x_j \partial x_j$ where $(\bar{\ })$ is a time-averaged quantity

Note: Re_{crit} corresponds to the Reynolds number at which the flow begins to become transitional and Re_{turb} corresponds to the Reynolds number at which the flow becomes fully turbulent.

(second terms on the LHS) is of secondary importance or can be neglected all together. Owing to the Laplacian nature of the viscous term (third term on the RHS), the effects of viscosity are felt throughout the flow and yield a strong elliptic character to the PDE, i.e., the flow features are highly coupled throughout the domain in all directions. To ensure this, elliptic coupling is properly treated; numerical methods typically employ an implicit solution technique, which is converged for a steady-state condition or given as a physically consistent time increment for an unsteady condition. As Re_L becomes an order of unity, the convective terms become important and nonlinear, but the elliptic character of the PDE remains strong, hence direct or iterative numerical approaches are required. As always, the domain discretization in space and time is carefully considered, such that it does not play a significant role in the flow solution.

For $1 \ll Re_L < Re_{crit}$, the flow may retain its laminar character and stability, but typically a boundary layer approximation may be applied to certain regions of the flow. The boundary layer approximation allows certain components of the viscous stress tensor to be ignored, since velocity gradients tend to much larger, normal and perpendicular to the convection direction (e.g., for attached wall-bounded flows the streamwise viscous gradients can be ignored). In this case, a parabolic approach may be employed in the direction for which the viscous diffusion may be neglected. Such an approach allows a space-marching scheme that needs to be coupled (i.e., solved directly or iteratively) along perpendicular planes. However, complex features and flow separation can cause the gradients to be significant in all directions, in which case the full Navier–Stokes equations of momentum are needed. The numerical approaches often include implicit schemes to properly capture the elliptic character of the viscous terms and the pressure coupling (since pressure fluctuations may travel in all directions for $M_L \ll 1$). However, since the convective terms begin to dominate at higher Reynolds numbers and are essentially parabolic locally, explicit schemes are sometimes used to treat these particular terms more efficiently. Often, the overall numerical approach becomes a hybrid of implicit and explicit schemes for incompressible laminar flow. At larger Mach numbers, PDE may become parabolic or hyperbolic such that purely explicit schemes are often appropriate.

13.1.3.1.2 Transitional Flow

For $Re_L > Re_{crit}$ (the critical Reynolds number where transition begins), the flow instabilities become profound and unsteadiness and multidimensionality become important. This can occur in wall-bounded flows where Tollmien–Schlichting instabilities arise, pipe flows where the Taylor–Gortler mechanism arises, free-shear flows where Kelvin–Helmhotz instabilities arise, etc. While transitional flow may be initially two dimensional, the instabilities typically lead to significant three-dimensional characteristics. Transitional is a difficult flow field to simulate, since the higher Reynolds numbers coupled with the small-scale features arising from the flow instabilities place severe restrictions on the space and time discretization employed in these simulations for full Navier–Stokes resolutions. Moreover, unlike fully developed turbulent flow, it is difficult to robustly recast the flow in a time-averaged description.

While most of the numerical approaches for these continuous-phase flows are Eulerian-based, noticeable exceptions are the Lagrangian treatments of vortex points or blobs or filaments (where the latter is used in three dimensions). These techniques can be very useful in predicting the initial instability features for free-shear flows and the Reynolds number effects can be included through viscous diffusion of the vortices. These techniques have the significant advantage of avoiding discretization of the entire computational domain and thus can be efficient in terms of reduced degrees of freedom for similar accuracy as compared with Eulerian methods. However, in highly three-dimensional flows (as the instabilities become highly nonlinear), the technique is highly complicated by the Lagrangian tangling, merging, and rupture of the vortex filaments and blobs. Thus, they can become impractical for complex vortex dynamics.

13.1.3.1.3 Turbulent Flow

For $Re_L > Re_{turb}$ (the minimum Reynolds number for fully developed turbulence), the flow instabilities have become sufficiently profound to have caused a flow field, with vortices and flow structures that occur over a large range of length and time scales. These features are three dimensional, unsteady, and effectively

stochastic at the smallest scales. The flow is sufficiently nonlinear to prevent a unique solution for a given set of initial flow conditions, such that comparisons often requires comparison of statistical quantities rather than instantaneous realizations. The range of wavelengths, which must be described to fully resolve such flows, is considerable. To illustrate this aspect, consider a turbulent flow with a relatively low Re_L of the order of 10^5, for example, a water flow moving at 1 m/sec within a 10 cm pipe. The range of spatial resolution required is based on the domain length scale and the Kolmogorov length scale, the ratio of which increases with Reynolds number, e.g., $L/\lambda_K \sim Re_L^{3/4}$. Thus, the range of length scales can be of the order of 10,000 in each direction in this simple flow example.

13.1.3.2 Numerical Methods for Continuous-Phase Turbulent Flows

Based on the above wavelength range, the total number of points required for the fluid resolution in all the three directions of turbulence approximately scales with $8Re_L^{9/4}$ (assuming two grid points to describe the smallest wavelength). Thus a Reynolds number of 10^5; this simulation would requires an excess of 10^{12} computational nodes. Thus, turbulent flow predictions at large Reynolds numbers require some time averaging of the PDEs to be simulated (of at least the small-scale structures) in order to allow practical computational resources. Such averaging formulations unfortunately involve some empiricism, and thus it is best to avoid (or minimize) this averaging whenever possible. The degree of averaging can vary, depending on the physics of interest. An important distinction is whether none, some, or all of the eddy structures can be resolved. However, the turbulent flow techniques can be broken up into two categories: (1) time-averaged simulations (no structures resolved) and (2) eddy-resolved simulations (some or all of the structures resolved).

Time-averaged simulations employ a time average with respect to the turbulence, such that only mean statistics are predicted. Moreover, only an average turbulence length scale and time scale can be identified, but no eddy structures or dynamics are produced. The most common example is the Reynolds-averaged technique, where all flow variables are individually time-averaged and the resulting equations are generally called the Reynolds-averaged Navier–Stokes (RANS) equations. Another time-averaged example is the Favre-averaged equations, where the fluid properties are weighted with the instantaneous density before being time-averaged.

Eddy-resolved simulations predict at least some of the individual spatiotemporal features of the turbulent eddy structures (e.g., at least some of the turbulent eddies are resolved within the computational grid). This category includes direct numerical simulations (DNS) where the turbulence is described for all eddy-containing wave numbers (spatial frequency), i.e., up to the wave number constrained by viscosity $1/\lambda_k$. The eddy-resolved category also includes large-eddy simulations (LES) where the turbulence is only resolved upto some cutoff wave number $(1/\Delta)$, beyond which a subgrid scale is employed. In addition, hybrid RANS–LES techniques have been used, wherein only the separated flow regions are treated with an LES approach while attached flow regions are treated with a RANS approach. Other eddy-resolved techniques, that predict only some of the spatiotemporal features include detached eddy simulations (DES) and proper orthogonal decomposition (POD), which will be discussed.

The difference between the flow predicted by a time-averaged and an eddy-resolved technique is substantial. Figure 13.2 shows the difference for a turbulent boundary layer, where the RANS discription is two-dimentional and steady while the DNS discription is three-dimentional and unsteady. Because eddy-resolved techniques can capture the energy-containing eddy structures associated with the turbulence, they have been shown to provide much higher accuracy than the time-averaged techniques in terms of turbulent diffusion and other statistical flow features.

The choice of the continuous-phase eddy-resolving description has a considerable impact on the dispersed-phase predictions. The time-averaged descriptions of the continuous flow allow only approximate prediction of particle mean diffusion, whereas the eddy-resolved techniques can more accurately predict such diffusion, while additionally providing aspects of particle preferential concentration (see Figure 13.3). In the above, *diffusion* refers to mean-spread of the particle cloud and thus indicates a time-averaged description of the particle concentration, whereas preferential concentration refers to particle motion associated with an individual turbulent flow features (spatio-temporal turbulent structure).

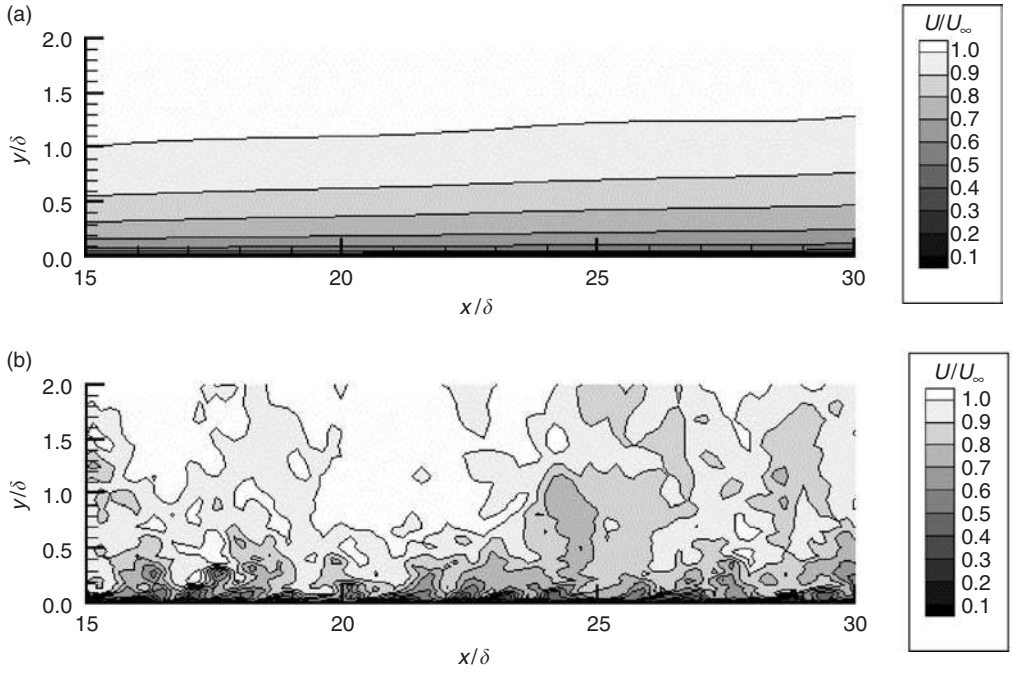

FIGURE 13.2 Different representations for a turbulent boundary layer, where δ is the mean boundary layer thickness, x the streamwise direction, and y normal to the wall showing: (a) a time-averaged (RANS) description and (b) an eddy-resolved (DNS) description for one span wise plane at a single instant in time.

In the latter case, this can include phenomenon such as the collection of light particles (with density less than the continuous-fluid density) in low-pressure vortex cores or the centrifugal expulsion of heavy particles (with density greater than the continuous-fluid density). Capturing such structural dispersion physics can be extremely important in predicting instantaneous local regions, which are either depleted or excessive in particle concentration levels as compared to the time-averaged values (Crowe et al., 1998). This "preferential concentration" can result in substantial changes in the relative velocity of the particle measured in an Eulerian framework (Maxey et al., 1997). In addition, structural dispersion can have great importance, when two-, three-, or four-way coupling effects are to be included, since interphase force transfer, particle collision, and particle wake interaction can be locally and nonlinearly enhanced in regions of high local concentration.

The variety of wavenumbers directly simulated by these different techniques ranging from RANS (no dynamics i.e., just an integral length-scale), LES (dynamics of the most energetic eddies) to DNS (the dynamics of all the eddies) is schematically represented in Figure 13.4. However, eddy-resolved formulations come at a price of higher computational resources (in terms of both CPU memory and time). Figure 13.5 shows the approximate computational resources required for attached boundary layers over a distance of L (free shear flows are even more demanding in terms of computational resources). It can be seen that even modest boundary Reynolds numbers of 10^6 require a substantial number of grid points for DNS and LES approaches, as compared with RANS approaches (especially if the time-averaged flow can be considered two-dimensional). In the following section, additional description is given with regard to both time-averaged and eddy-resolved formulations.

13.1.3.2.1 Time-Averaged Formulations

For the category of RANS simulations, all the velocity components are separated into their steady and fluctuating components, $u_i = \overline{u_i} + u_i'$, where $\overline{u_i}$ represents a time-averaged quantity over a time period much greater than τ_Λ. Application of this averaging quantity to the incompressible constant viscosity

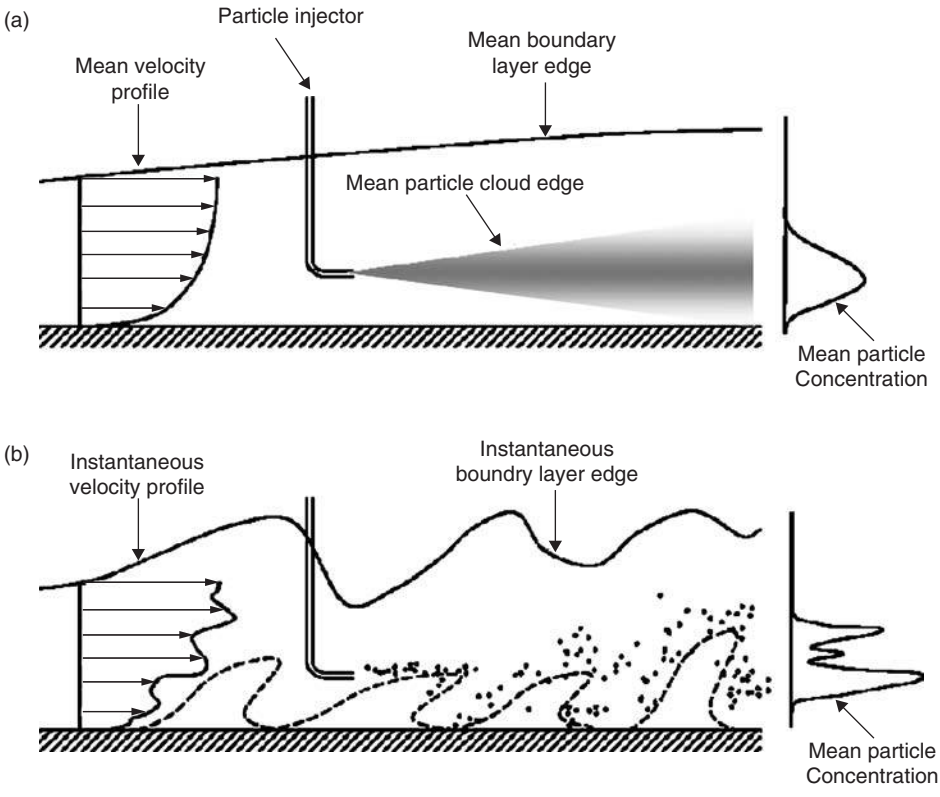

FIGURE 13.3 Schematic of particles injected near the wall of the turbulent boundary layer comparing (a) particle mean (time-averaged) diffusion where a steady particle concentration distribution is obtained and (b) preferential concentration where an unsteady particle distribution is obtained.

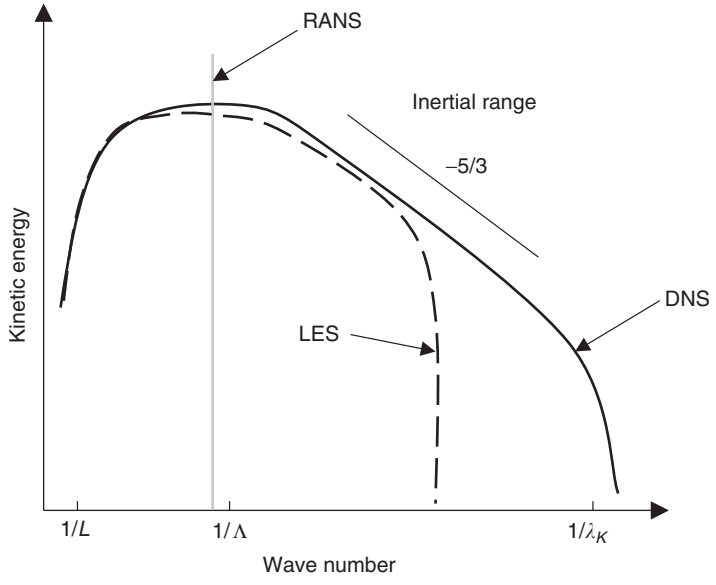

FIGURE 13.4 Schematic of turbulence spectrum described by RANS, LES, and DNS approaches.

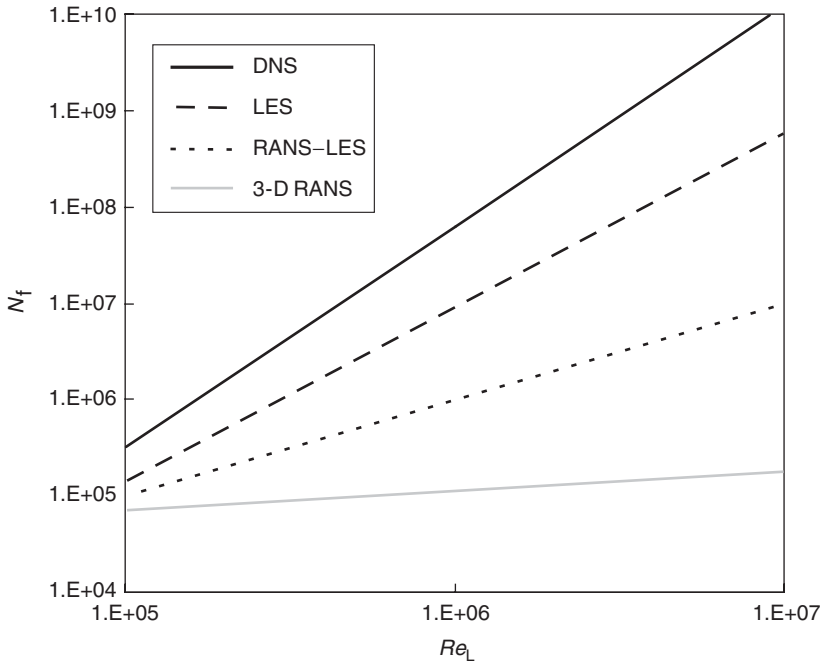

FIGURE 13.5 Approximation of computational node requirements for RANS, LES, and DNS and hybrid RANS–DNS approaches.

Navier–Stokes equation is shown in Table 13.1, where the $\overline{u_i' u_j'}$ term represents the transport of momentum due to turbulent mixing. The primary aim of RANS models is to represent empirically the Reynolds-stress terms (appearing in the source term of the momentum transport equations) using some of the mean flow velocity features. Several of the recent developments in this field for both incompressible and compressible flow are discussed by Vandromme (1997) and briefly overviewed below. The turbulence models are generally classified into the traditional eddy viscosity models and the more advanced Reynolds-stress closure models.

For the eddy viscosity models, $\overline{u_i' u_j'}$ is related to the mean velocity gradients and a mean turbulent viscosity, the latter of which requires modeling and is typically several orders of magnitude higher than the fluid viscosity. The eddy-viscosity models are generally classified according to the number of partial differential transport equations, which must be solved (in addition to those for mean mass, momentum, and energy conservation) to compute $\nu_{f,t}$. These generally range from zero-equation (algebraic) models where the turbulence is essentially assumed to be in a state of local equilibrium, to two-equation models, to three-equation models where finite-rate production, diffusion, and dissipation processes are individually modeled. In all the cases, empirical coefficients (often several) are used to close the equations, and these are obtained by "tuning" the model to some basic turbulent flow results. Therefore, the robustness of turbulence models will always be limited to conditions for which it has been validated and empirically calibrated, and there is no single "ideal" turbulence model.

For turbulent multiphase simulations, two-equation models (including k–ε, k–ω, and q–ω) have a distinct advantage, since they describe two independently varying properties of the turbulence; for example, the turbulent kinetic energy (TKE) k and the turbulent dissipation ε. Modeling two independent turbulence properties allows specification of a mean eddy integral length λ and eddy time-scale τ_Λ throughout the flow. These two scales can be used to characterize particle diffusion using random walk approaches.

The Reynolds-stress closure models are inherently anisotropic and seek to avoid a gradient transport approach to the turbulent stress tensor terms by employing individual equations for the individual

turbulent stresses (and potentially the turbulent fluxes as well). The zeroth-order version of this model is Rodi's algebraic stress model, which supplements the k–ε transport equations with an anisotropic algebraic relationship (White, 1991). As such, it does not allow significant advantages over two-equation eddy viscosity models in terms of sophistication. However, modern Reynolds-stress closure models employ separate transport equations for each tensor component (six equations due to symmetry). This has the obvious advantage of more directly obtaining the anisotropy of the Reynolds-stress tensor by allowing varying states of nonequilibrium for each term. Since Reynolds-stress closure models are well suited to the framework of particle diffusion computation in anisotropic turbulence, they may become increasingly important as they mature in fidelity and convenience. Unfortunately, the large number of transport equations results in a much more computationally intensive and complex CFD (Computational Fluid Dynamics) solution with additional terms to be modeled. Of particular concern are the several third-order (and fourth-order) stress terms, which require modeling not easily gleaned from experiments. While some closure models have shown success for simple flows using heuristic arguments for these terms, e.g., Speziale et al. (1991), a robust set of closure terms tested for several engineering flows has yet to be developed (although the DNS techniques described below are expected to provide improved closure models for such terms at lower Reynolds numbers). Because of these issues and the inability to incorporate preferential concentration, eddy-resolved formulations are becoming much more common for multiphase flow.

13.1.3.2.2 Eddy-Resolved Formulations

For the eddy-resolved simulations, there are quite a number of descriptions of the eddy structures. These can be roughly arranged in order of increasing complexity, physical representation, and required computational resources as follows (see also Figure 13.5).

Proper Orthogonal Decomposition (POD) models. These simulations employ a low-order construction of the turbulent flow field, typically using spectral or pseudo-spectral functions (Joia et al., 1997), which are tracked in time as 3D dynamical features. As such, they employ only a modest number of degrees of freedom (as compared to full Navier–Stokes resolution) while simulating the large-scale nonlinear flow physics. Unfortunately, POD models typically require a detailed realization (experiment or simulation) in order to solve for the "best fit" of their lower-order dynamical system. Thus, they are sometimes empirical, i.e., they cannot quantitatively self-determine the continuous-flow vortex structures for a general set of boundary and initial conditions. However, once a POD is constructed for a particular flow, it can be reasonably rendered many times to test the transport of a variety of particle conditions.

Hybrid RANS–LES models. Several numerical treatments have emerged which attempt to treat a part of the computational domain using a RANS formulation and on the other part with a LES formulation. Among the first of such models was the DES methodology developed by Spalart (2000). The basic concept was to allow for a one-equation RANS treatment in the attached boundary layer regions (where the approach is known to be robust) and LES treatment in the separated and free-shear flow regions (where the approach is known to be robust). This is achieved by using a wall distance to spatially separate the RANS and LES regions. Several other models have been developed recently based on similar formulations.

Large Eddy Simulations (LES). The governing equations are obtained by a low-pass spatial filtering of the Navier–Stokes equations such that all the velocity components are separated into their resolved (unfiltered) and unresolved (filtered) components. Using a notation similar to that used for the RANS approach, the velocity components for the spatial filtering process are given as $u_i = \overline{u_i} + u_i'$, where some modeling is required for the fluctuations that are at the subgrid level; for example, $\overline{u_i' u_j'}$, which is the velocity tensor of the unresolved fluctuations. Ideally, this spatial filtering is applied at sufficiently small scales so that the filtered turbulence is at or below the inertial range and thus nearly homogeneous and isotropic, such that Smagorinsky-type models can be reasonably employed. However, the inertial range develops for only very high Reynolds number conditions (Tennekes and Lumley, 1972), such that spatial filtering can be a complex phenomenon sometimes making it difficult to provide accurate and robust predictions of the subgrid turbulence. This problem can be effectively overcome in some flows by allowing

high enough grid resolution, such that the subgrid component is not substantial, but this is not straightforward in wall-bounded flows where small-scale stresses are critical. The LES technique is perhaps the most promising for low to moderate Reynolds number engineering flows, since, with proper care, it can simulate complex separated flow in both the mean and rms statistics. For particle dispersion, the key advantage of LES is the detailed spatio-temporal evolution of the unfiltered large-scale turbulent motions. It should be noted that other variations of LES include very large eddy simulations (VLES), for which the subgrid model is determined by the numerical grid diffusion and RANS-type turbulent viscosity. While the representation of the subgrid scale turbulent stresses of VLES is not formulated based on a rigorous evaluation from the filtered fluid equations of motion, these models can reproduce many features of turbulent flow, since the subgrid turbulence is often not critical to the overall flow development (especially for free-shear flows).

Direct Numerical Simulations (DNS). The governing equations in this case are the full time-dependent Navier–Stokes equations. Typically, the high resolution required for grid-independent solutions results in low Reynolds numbers, simple geometries, and use of spectral methods if flow discontinuities (shock waves, concentration fronts, etc.) are not critical to the flow physics. The primary advantage of DNS is that all the eddy structures are duly resolved and no (empirical) turbulence modeling is necessary. However, for most engineering flows, DNS computations are simply too computationally intensive.

13.1.4 Overview of Particle-Phase Flow Methodologies

Various treatments of the particle field (composed of solid particles, droplets, or bubbles) can be employed. As mentioned earlier, these can include an Eulerian or a Lagrangian reference frame. The Eulerian approach can be further classified into mixed or point-force approaches, while the Lagrangian approach can be further classified into point-force or resolved-surface approaches. Table 13.2 shows the various treatments of the particle and continuous-phase velocity fields without any averaging or mass transfer. In this table, the Eulerian treatments describe the particle concentration through a volume fraction α_p, which is the fraction of the computational volume composed of particles, and where the volume fraction taken up by the continuous phase is α_f, such that $\alpha_p + \alpha_f = 1$. When a Lagrangian treatment is used for the particles, the two-way coupling effect on the continuous phase is usually related to the particle number density n_p, which is the number of particles per unit volume.These particle concentration variables can be related to the average particle volume V_p, such that $\alpha_p = n_p V_p$.

The particle phase has two sets of key classifications. The first is based on the reference frame for the particle properties and is classified as either a Lagrangian or an Eulerian treatment. The second is based

TABLE 13.2 Forms of the Incompressible Unsteady Navier–Stokes Momentum Equations

Dispersed-Phase Approach	Dispersed-Phase Momentum	Continuous-Phase Momentum
Eulerian with mixed-fluid treatment	$\partial(\rho_m u_{mi})/\partial t + \partial(\rho_m u_{mi} u_{mj})/\partial x_j = \rho_m g_i - \partial p/\partial x_i + \mu_m \partial^2 u_{mi}/\partial x_j \partial x_j$ where $\rho_m = \alpha_p \rho_p + \alpha_f \rho_f$ applied throughout the domain	
Eulerian with point-force treatment	$\rho_p \partial(\alpha_p v_i)/\partial t + \rho_p \partial(\alpha_p v_i v_j)/\partial x_j = \alpha_p \rho_p g_i - \alpha_p \partial(p + p_{coll})/\partial x_i + \alpha_p \mu_f \partial^2 v_i/\partial x_j \partial x_j + \alpha_p F_{int,i}/V_p$ applied throughout the domain	$\rho_f \partial(\alpha_f u_i)/\partial t + \rho_f \partial(\alpha_f u_i u_j)/\partial x_j = \alpha_f \rho_f g_i - \alpha_f \partial p/\partial x_i + \alpha_f \mu_f \partial^2 u_i/\partial x_j^2 - \alpha_p F_{int,i}/V_p$ applied throughout the domain
Lagrangian with point-force treatment	$m_p \partial v_i/\partial t = F_{body,i} + F_{surf,i} + F_{coll,i}$ where $F_{surf,i} = F_{Di} + L_i + A_i + S_i + H_i$ applied along particle trajectories	$\rho_f \partial(\alpha_f u_i)/\partial t + \rho_f \partial(\alpha_f u_i u_j)/\partial x_j = \alpha_f \rho_f g_i - \alpha_f \partial p/\partial x_i + \alpha_f \mu_f \partial^2 u_i/\partial x_j^2 - n_p F_{int,i}$ applied throughout the domain
Lagrangian with resolved-surface treatment	$m_p \partial v_i/\partial t = F_{body,i} + F_{surf,i} + F_{coll,i}$ where $F_{surf,i} = \int[-p\, n_j + \tau_{ij})]\, n_j dA_p$ applied along particle trajectories	$\rho_f \partial u_i/\partial t + \rho_f u_j \partial u_j/\partial x_j = \rho_f g_i - \partial p/\partial x_i + \mu_f \partial^2 u_i/\partial x_j^2$ applied outside of particle volume

Note: In the above, n_p is the number density of particles per unit volume of mixed fluid, $F_{int,i}$ is the interphase hydrodynamic force acting on the particles, and p_{coll} is the particle collisional pressure.

on the treatment of the surface forces on the particle and is classified as either a point-force or a resolved-surface treatment. These two sets of classifications will be discussed in more detail.

For the reference frame, the Lagrangian method is sometimes referred to as the discrete method, since it assumes that each particle (or a group of particles) is represented as an individual identity (as opposed to the continuum description for the Eulerian method). For Lagrangian particles, the properties (such as velocity and temperature) are updated along the path of an individual (or cloud of) particles, while in the Eulerian method, the particle properties are averaged in a computational volume, which is generally on a convenient stationary (Eulerian) grid, as demonstrated in Figure 13.6.

For the treatment of the surface forces, the point-force treatment represents the flow over the particle with empirical and theoretical treatments (e.g., specifying a drag coefficient) to obtain the force on the particle. For the resolved-surface treatment, the fluid dynamics (e.g., pressure and shear stress distributions) are fully resolved over the entire particle's surface and then integrated to obtain the overall hydrodynamic forces. Hence, for the resolved-surface treatment, high spatial resolution of the continuous phase is thus required over the particle surface. Therefore, this method is sometimes called "direct simulation." On the other hand, the continuous-flow grid scale can be course with respect to particle size for the point-force approach (see Figure 13.7), such that it is much less demanding in terms of computational resources.

13.1.4.1 Lagrangian Approaches: Point-Force Versus Resolved-Surface Treatment

The classification of point-force vs. resolved surface is considered in terms of the Lagrangian equation of motion for the particle momentum (although the same differences are found for an Eulerian approach to the particle equations of motion).

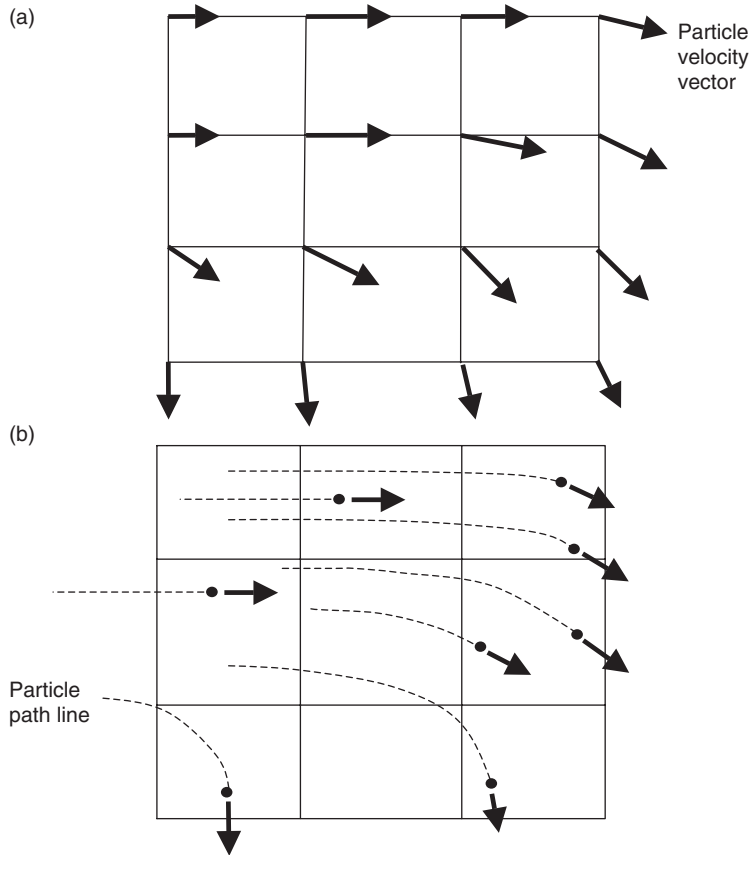

FIGURE 13.6 Comparison of Eulerian and Lagrangian particle velocity fields.

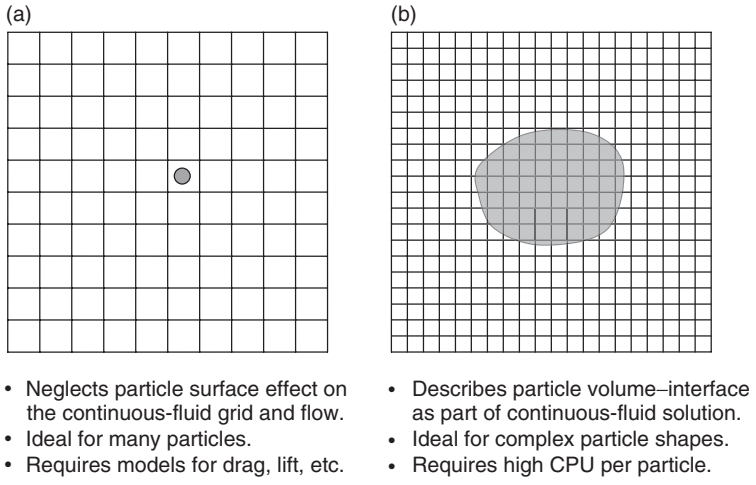

FIGURE 13.7 Different representations for particle treatment where shaded area represents the particle (where d is the effective diameter) and the grid represents the computational resolution for the continuous phase solution (where Δx is the effective cell resolution): (a) point-force representation ($d < \Delta x$) and (b) resolved-surface representation ($\Delta x \ll d$).

For the point-force approach coupled with the Lagrangian reference frame, the fluid or particle is commonly described at a single point that moves at its own (independent) velocity; hence, this approach is often called a discrete element approach, i.e., each particle is treated individually, but with a pointwise representation. If a point-force approximation is used, individual particle trajectories are computed in a Lagrangian-sense (i.e., with ordinary differential equations [ODEs] based on the moving particle location), while the continuous-phase flow is typically treated throughout in an Eulerian sense (i.e., with PDEs based on a fixed computational grid). For a large number of particles, computational "parcels" can be used where each parcel represents a cloud of many particles with the same characteristics. The size of the parcel cloud should be less than the continuous-phase local grid resolution (Δx).

For dense flows with the Lagrangian point-force technique, every particle is ideally considered and the possible particle–particle reflections are numerically monitored and then modeled using various collision models. A collision model for smooth solid elastic spheres is reasonably straightforward using conservation of momentum and energy, but finite energy losses are usually important to be considered, using coefficients of restitution and friction. Incorporation of a large number of particles or particles with nonspherical shapes substantially complicates particle collision detection and momentum interaction, hence empirical probabilistic models are needed (Crowe et al., 1998).

If a resolved-surface approach is used, the detailed flow around each particle must be solved to a high resolution. Then, the flow solution can be numerically integrated over the surface to obtain the net momentum interaction of the fluid on the particle. Thus the Lagrangian method updates the particle position based on this integrated interaction. If the particle rotation is allowed, a torque equation can be used to determine the particle angular velocity. The primary drawback of the resolved-surface technique is that the computational requirements of many continuous-fluid grid points around each particle, such that simulation of many (e.g., hundreds or thousands of) particles will generally be impractical on even the most advanced computers.

To highlight the differences between the point-force and the resolved volume approaches, consider the following dynamic equation for a particle, for which v is the velocity at the particle centroid ($\mathbf{x}_p$) and m_p the particle mass:

$$m_p \mathrm{d}\mathbf{v}/\mathrm{d}t = \mathbf{F}_{body} + \mathbf{F}_{surf} + \mathbf{F}_{coll}$$

In this formulation, the description of the particle equation of motion can be given as an ODE along the particle path. The LHS represents the particle mass times the acceleration of the particle along the particle path. The first term on the RHS ($\mathbf{F}_{body}$) represents the forces directly proportional to the particle mass, for example, gravitational forces, while the second term ($\mathbf{F}_{surf}$) represents the fluid dynamic surface forces on the particle, which are proportional to the surface area, and the third term ($\mathbf{F}_{coll}$) represents the forces due to particle–particle or particle–wall collisions.

The body force expression is typically the simplest (if electromagnetic and other body forces are neglected) as it is based on gravitational forces. The resulting expression for the body force of a particle sphere is

$$\mathbf{F}_{body} = \mathbf{g}m_p = \mathbf{g}\rho_p V_p$$

where V_p is the particle volume and ρ_p the volume-averaged density of the particle. The particle volume for spherical shapes can be written as $V_p = \pi d^3/6$, but this equation still remains valid for nonspherical objects as long as d is interpreted as the equivalent diameter based on the particle volume.

As mentioned above, the surface force ($\mathbf{F}_{surf}$) can be treated with two fundamentally different approaches: the resolved-surface approach and the point-force approach. The choice is often based on computational convenience for a given multiphase flow system.

In the resolved-surface (direct simulation) approach, the surface force is determined by integrating the pressure and fluid dynamic shear stress and is shown below in tensor notation as

$$F_{surf,i} = \int [-p + \mu_f(\partial u_i/\partial x_j + \partial u_j/\partial x_i)]\, n_j \, dA_p$$

where A_p is the particle surface area and n_j the j projection of the normal unit vector outward from the surface. No specific decomposition of lift, drag, or other surface force effects are needed in this formulation, since all these effects are directly incorporated by the above integration, and thus no limiting assumptions of particle shape, particle Reynolds number, particle or flow acceleration, flow gradients, etc., are required for this formulation. Note that buoyancy effects, which are based on the hydrostatic pressure gradients, are naturally included in this formulation if the gravity force is part of the continuous-phase solution for u_i and p (as discussed in the previous section). The resolved-surface approach allows for the details of the fluid pressure and shear stress to be integrated over the particle surface and avoids empiricism associated with the prescription of fluid dynamic forces.

In the case of a fluid particle, such as a droplet, the interior fluid dynamics may also be resolved. This may be done with a Lagrangian approach (e.g., internal particle domain is given body-fitted coordinates that translate with the particle movement) or an Eulerian approach (e.g., volume-of-fluid method or level set method). The former is better for nondeforming particles where high accuracy of the interface discontinuity is desired, which the latter is more efficient in terms of particle breakup or coalescence. In either of resolved-surface methods, the spatial grid resolution for u_i in the region of the particles must be fine enough to allow description of the detailed stresses around the particle, e.g., the grid scale must be small compared with the particle diameter ($\Delta x \ll d$) as shown in Figure 13.3a. The resolved-surface approach is the most desirable in terms of accuracy as it allows the most physically realistic surface force methodology; however, it is also the most computationally intensive per unit particle. Hence, the resolved-surface technique is only reasonable when there is a single or modest number of particles in the computational domain.

If the number of particles in the simulation is too high for the given computational resources, then the point-force technique can be used as a single equation can be used to describe the force on the particle without actually resolving the flow around the particle surface (such that one may employ $\Delta x > d$, see Figure 13.3b).

For a point-force treatment, the force interaction between the fluid and particles is not computationally integrated over the particle directly, and instead, a surface-averaged force is employed, which is based on

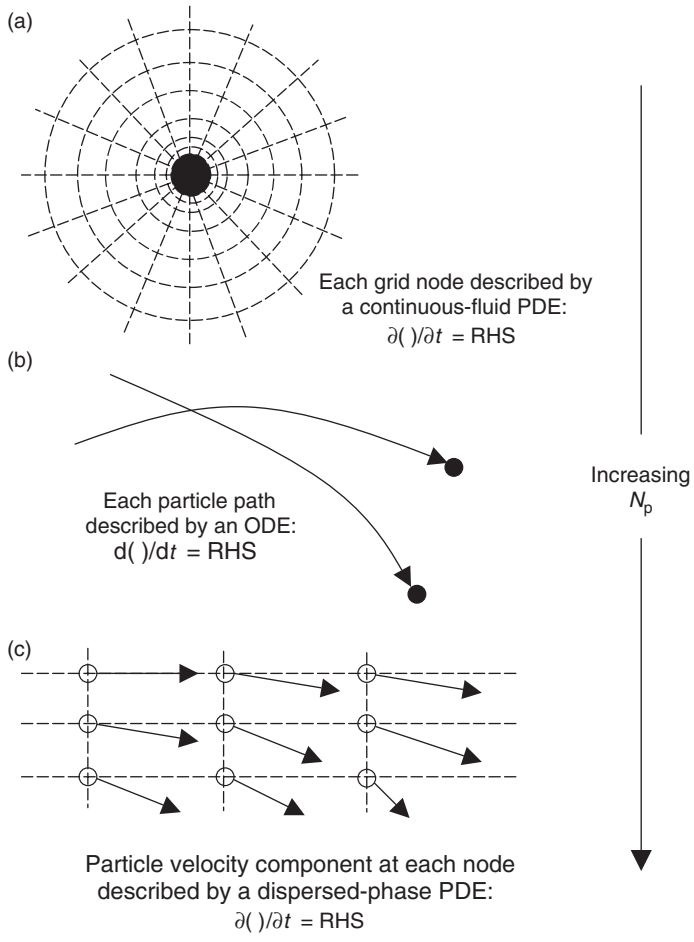

FIGURE 13.8 Comparison of particle treatments for: (a) the resolved surface approach employing body-fitted computational nodes (with a Lagrangian description of particle motion if moving); (b) the Lagrangian approach defined on particle centroids (paths can cross); and (c) the Eulerian approach defined on Eulerian computational nodes.

analytical or empirical force expressions. In general, a surface-averaged force is a linear combination of specific forces, such as drag $\mathbf{F}_D$, lift **L**,added mass **A**, stress gradient **S**, history **H**, etc.

$$\mathbf{F}_{surf} = \sum_{k=1}^{K} \mathbf{F}_{surf,k} = \mathbf{F}_D + \mathbf{L} + \mathbf{A} + \mathbf{S} + \mathbf{H} + \cdots.$$

where coupling between these K number of components is generally neglected. The particle hydrodynamic surface forces are generally related to the continuous-fluid properties extrapolated to the particle centroid, (X_p) while neglecting the local influence of the particle . The continuous-fluid velocity and vorticity at the particle centroid defined in this way can be denoted as $\mathbf{u}_{@p}$ and $\boldsymbol{\omega}_{@p}$.

The definition of hypothetical continuous-fluid properties at the particle centroid is a key assumption for the point-force treatment and allows significant computational convenience. Thus, this condition assumes that the continuous-fluid velocity is defined everywhere, i.e., $\mathbf{u}_{@p}$ corresponds to $\mathbf{u}(\mathbf{x}_p)$. If the continuous-flow characteristics are spatially uniform in instances where the particle presence is not considered (i.e., **u** without particles would be everywhere $\mathbf{u}_\infty$), then $\mathbf{u}_{@p} = \mathbf{u}_\infty$ is consistent with the proper limiting value. It should be noted that if there is a nonlinear flow in the region of the particle,

then employing a velocity from a single point may not be sufficient to characterize the surrounding conditions and that some averaging in the vicinity of the particle may be more appropriate. Thus the variations of $\mathbf{u}_{@p}$ in the local vicinity of the particle (neglecting the velocity variations caused by the presence of the particle) are assumed to be weak. Based on the above, a relative particle velocity can be then defined as

$$\mathbf{w} = \mathbf{v} - \mathbf{u}_{@p}$$

This relative velocity can be used to define the direction of the hydrodynamic surface forces, for example, the drag force is defined as a value opposing **w**. Similarly, the lift force **L** is defined perpendicular to **w** and $\boldsymbol{\Omega}_{rel}$ (the relative rotation of the particle with respect to the fluid):

$$\boldsymbol{\Omega}_{rel} = \boldsymbol{\Omega}_p - \frac{1}{2}\boldsymbol{\omega}_{@p}$$

where $\boldsymbol{\omega}_{@p}$ is the continuous-fluid vorticity extrapolated to the particle centroid, while neglecting the influence of the particle. This rotation can also be used to track the angular momentum of the particles (Crowe et al., 1998).

A well-known example of the point-force description for linear momentum particle dynamics is the Maxey–Riley (1983) equation, which is derived analytically for the case of incompressible creeping flow (i.e., viscous terms, dominate convective terms, such that the latter can be linearized) around a single solid spherical particle far from any boundaries or other particles. The creeping flow assumption is defined as $Re_p \ll 1$, where $Re_p = \rho_f d|\mathbf{w}|/\mu_f$. If the free-stream velocity gradients are assumed to be weak when considered on the scale of the particle diameter (e.g., particle diameter smaller than the Kolmogorov length scale), the Faxen forces (which are proportional to $\nabla^2\mathbf{u}_{@p}$) and the lift forces (which can arise from fluid shear and particle rotation) can be neglected. If one also neglects mass and heat transfer as well as any temporal discontinuities in **u**, the resulting creeping-flow point-force terms are as follows (see Section 13.1.4):

$$\mathbf{F}_D = -3\pi d\mu_f \mathbf{w}$$

$$\mathbf{A} = -\frac{1}{2}\rho_f V_p(\mathrm{d}v/\mathrm{d}t - \mathrm{D}\mathbf{u}_{@p}/\mathrm{D}t)$$

$$\mathbf{S} = \rho_f V_p \mathrm{D}\mathbf{u}_{@p}/\mathrm{D}t - \mathbf{g}\rho_f V_p$$

and

$$\mathbf{H} = -\frac{3}{2}d^2(\pi\rho_f\mu_f)^{1/2}\int_0^t \left[\frac{\mathrm{d}w/\mathrm{d}\tau}{\sqrt{t-\tau}}\right]\mathrm{d}\tau$$

The drag force ($\mathbf{F}_D$) assumes a no-slip condition at the particle surface. While this condition is satisfied for a solid particle (as long as the flow field can be considered as a continuum), it may also be reasonable for a small droplet or a bubble, if there is a substantial contamination on the surface rendering it nearly immobile. The fluid stress force **S** results from the stress arising from the undisturbed fluid stress, and this gives two components: the first term is proportional to the Lagrangian fluid acceleration ($\mathrm{D}\mathbf{u}_{@p}/\mathrm{D}t$), which can be nonzero even in steady flow, and the second term is proportional to the hydrostatic pressure gradient, which in turn can be written as proportional to the displaced mass ($\rho_f V_p$) and hence is often called the buoyancy force. The added mass term (**A**) is slightly modified from the original Maxey–Riley equation as suggested by Maxey et al. (1997). The last term is the history force and assumes negligible relative velocity acceleration at $t = 0$, although Kim et al. (1998) give a proposed correction if this is not the case. Mei et al. (1991) noted that the above history force expression (**H**) is not valid for long times or noncreeping flow conditions. Thus, this equation invokes several assumptions.

Under certain conditions, some of the terms become secondary or tertiary and thus can be neglected in the particle dynamic equations. For example, the history force terms are often neglected since these corrections are typically small, numerically cumbersome, and not well posed, except for creeping-flow conditions of simple particle shapes. Furthermore, the case of very light particles (e.g., gas bubbles in a liquid where $\rho_p \ll \rho_f$) indicates that terms associated with ρ_p (e.g., F_{body} and $d\mathbf{v}/dt$) can be reasonably neglected under several (but not all) circumstances. By neglecting lift, yields the following Stokesian point-force expression for very light particles.

$$\rho_f V_p d\mathbf{v}/dt = -6\pi d\mu_f \mathbf{w} + 3\rho_f V_p D\mathbf{u}_{@p}/Dt - 2\mathbf{g}\rho_f V_p$$
$$- 3d^2(\pi\mu_f\rho_f)^{1\backslash 2}\int_0^t \left[\frac{d\mathbf{w}/d\tau}{\sqrt{t-\tau}}\right] d\tau + \mathbf{F}_{coll}, \qquad \rho_p \ll \rho_f \text{ and } Re_p \ll 1$$

For very heavy particles compared with the continuous-flow (e.g., drops or solid particles in a gas where $\rho_p \gg \rho_f$), many of the terms associated with ρ_f (e.g., **L**, **A**, **S**, and **H**) can be reasonably neglected under several (but not all) circumstances. Neglecting these terms, the Stokesian point-force expression for very heavy particles becomes

$$\rho_p V_p d\mathbf{v}/dt = -3\pi d\mu_f \mathbf{w} + \mathbf{g}\rho_p V_p + \mathbf{F}_{coll}, \qquad \rho_p \gg \rho_f \text{ and } Re_p \ll 1$$

There are a wide variety of other point-force equations (with both analytical and empirically derived force terms) that have been reported by researchers in order to take into account the particle aspects (such as interface conditions, nonspherical shapes, rotation, deformability, interior fluid motion, and mass transport) and the flow aspects (such as compressibility, turbulence, shear, and strain) as well as the presence of other particles or surfaces. In particular, empirical and semiempirical expressions are often used for conditions, that do not correspond to creeping flow past a simple shape. These empirical expressions are generally limited to specific regimes and may be subject to experimental uncertainties and bias.The various particle dynamic equations that are employed in the multiphase community are thus tailored to specific situations (based on the physics of interest, test conditions, and computational resources) and as such the particle equations appearing in the literature are extremely numerous. This nonuniqueness of multiphase flow equations indicates that there is no single standard equation that should be applied to all the conditions, and thus one must choose the appropriate equations as carefully as one chooses the appropriate numerical solution techniques.

13.1.4.2 Eulerian Approaches: Mixed-Fluid Versus Separated-Fluid Formulations

The Eulerian description applied to the dispersed phase generally assumes the characteristics of the particles (e.g., velocity or temperature) can be described as a continuum. This assumption allows the dispersed phase to be treated with the same discretization and similar numerical techniques as those used for the continuous phase. This is especially important when two-way coupling effects are present and can reduce the overall computational costs. The Eulerian treatment combined with a point-force assumption assumes that there are several particles per control volume, which can be described by a local number density (n_p) in the proper limit. To handle a variety of particle properties within a control volume, the particle characteristics can also be discretized using the multigroup approach, where the number density becomes a vector (n_{pi}), such that each group is identified by a particular characteristic range. For example, polydisperse particles can be separated into various bins, each with a specific particle diameter range (Crowe et al., 1998). In this case, transport equations are needed and computed for each Eulerian particle group.

The Eulerian techniques can be further subdivided into mixed- and separated-fluid approaches. The mixed-fluid approach assumes that the particles and the continuous phase are in local kinetic and thermal equilibrium, i.e., the relative velocities, and temperatures between the two phases are small in comparison to variations in the overall flowfield that are predicted. This approximation is the mixed-fluid method and distinguishes only the mass fractions of the particle and fluid phases in a mixed volume.

It has also been termed the locally homogeneous flow (LHF) by Faeth (1987). Thus, in this approach, the relative velocity (between the particle motion and the continuous-phase motion) is assumed to be negligible, so that one has

$$\mathbf{u}_m = \mathbf{u} = \mathbf{v} \quad (\mathbf{w} = 0) \quad \text{for mixed-fluid treatment}$$

Similarly, the temperature difference between the two phases is assumed to be negligible.

The use of the mixed-fluid approximation results in a single set of momentum conservation equations for the flow mixture (as opposed to one set for the continuous phase and one set of the dispersed phase). For example, the resulting equations of motion for a fluid mixture with a single velocity and temperature are shown in Table 13.2, where the particle volume fraction, α_p, is the ratio of volume occupied by the particle to the volume of the mixture of particles and the continuous phase, and where the continuous-phase void fraction is similarly defined, such that $\alpha_p + \alpha_f = 1$. This approximation allows strong numerical simplicity and can generally handle both dispersed and dense conditions. In addition, since it is based on volume averaging of both phases, the exact size and shape of the discontinuous phase is not needed for the flow simulation.

The separated-fluid approach for Eulerian description of the particle phase with the point-force assumption assumes that both the carrier fluid and the particles comprise two separate, but intermixed, continua. Therefore, two sets of momentum equations are required for a two-phase flow: one for the continuous phase and the other for the dispersed phase. The separated fluid method is also often called the two-fluid method, since two sets of PDEs and two sets of velocity fields are required (one for each phase):

$$\mathbf{w} \neq 0 \quad \text{for two-fluid treatment}$$

These equations will in general be coupled (e.g., one-way coupled means that the particle equations will depend on solution of the continuous-phase equations, and two-way coupled means that both sets of equations must be solved in companion).

In the coupling of these equations, the separated-fluid approach accounts for (and thus must formulate) the relative interphase mass, velocity, and temperature differences.

The interphase expressions that relate the mass, momentum, and energy of the different phases are then based on a point-force description. For example, the Eulerian separated-fluid PDEs with a point-force approach for the two phases assuming constant density, and viscosity for the continuous fluid may be represented as listed in Table 13.2. Alternatively, a probability distribution function (PDF) approach can be applied to the Eulerian equations to give the evolution of the ensemble-averaged properties. The resulting transport equations can take into account many of the effects incorporated into conventional Eulerian approaches, including near-wall behavior, particle evaporation, etc.

A key assumption regarding Eulerian treatments described above is that the particle concentration (e.g., α_p) is a variable, which is continuously differentiable, such that the PDE description is appropriate as given in Table 13.2. This is termed the particle-phase continuum assumption by Drew and Prassman (1998). From a deterministic point of view, this assumption is physically reasonable only considering control volume lengths that are much larger than the average particle spacing ($\Delta x \gg \Lambda_{p-p}$), i.e., the dispersed phase equations can be considered as a continuum when there are many particles within a single computational cell–volume so that the concentration variations do not induce significant discontinuities (as shown in Figure 13.9). In contrast, if only two particles are present in a computational cell and have different velocities, then refinement or particle convection which eliminates one of the particles from the cell, can cause a physically discontinuous change in the cell-averaged particle velocity $\mathbf{v}$. Therefore, Eulerian approaches are only deterministically reasonable when large amounts of particles are contained within each cell, and are not well posed for successive grid refinements.

This requirement of many particles per cell can be removed when a probabilistic point of view is considered based on some averaging. As such, a computational cell with 0.1 computational particles in its volume is equivalent to a 10% probability of a particle occurring in the volume at a given time, such that the Eulerian particle properties (α_p, $\mathbf{v}$, etc.) can be considered as the average of all possible realizations (Drew and Prassman, 1998).

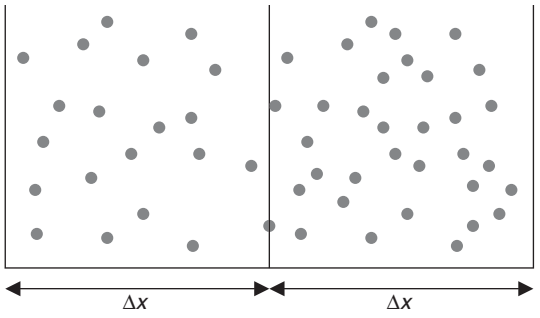

FIGURE 13.9 A two-dimensional description of discrete particles in two adjoining computational cells of an Eulerian grid where ($\Delta x \gg L_{p-p}$) and the continuum approximation can be employed.

However, the computational volume, it must still be much greater than the particle diameter ($\Delta x \gg d$) for the Eulerian continuum approach to be reasonable, if one includes a point-force approximation.

13.1.4.3 Lagrangian Versus Eulerian Point-Force Approaches

Since a variety of descriptions and treatments have been used for multiphase flows, the choice of which numerical approach to employ depends on the particle and fluid physics that are relevant and of interest (Loth, 2000). As discussed above, one of the key distinctions between the various multiphase numerical methods is that of Lagrangian vs. Eulerian representation of the particle characteristics (which include velocity, concentration, diameter, etc.).

Let us now compare the pros and cons of Lagrangian vs. Eulerian approaches for the point-force treatment of the particle fields. Lagrangian approaches are typically more physically robust if the following flow properties are of interest and importance: particle reflection from surfaces, particle breakup, particle–particle interactions (collisions and coalescence), counterflowing particles, and turbulent diffusion. In addition, nonphysical numerical diffusion of Eulerian particle density in regions of high gradients can be eliminated by employing Lagrangian particles due to their pointwise spatial accuracy. The Lagrangian method also allows particles to cross over the wake of other particles (as shown in Figure 13.8b), whereas steady-state Eulerian treatments do not allow this phenomenon. In addition, if the particles within the computational domain are not all of the same size or shape, the Lagrangian technique can employ statistical representations of the particle distributions to incorporate these effects. As the number of physical particles increases, such that individual tracking is prohibitive and collisions occur, the particles can be treated in groups for which probability of collisions are modeled and incorporated. Such techniques can use PDFs in simple homogeneous flows with simple geometries or Monte–Carlo methods, which employ random-number generators for more complex flows and domains. The latter is often called a random-walk approach and has been very successful for mean diffusion in homogenous turbulence, and has also shown some success in anisotropic nonhomogeneous turbulence (Bocksell and Loth, 2001).

In contrast, the Eulerian particle-phase approach describes particle properties as part of a continuum throughout the computational domain and has several distinct advantages. For particles distributed throughout the computational domain (instead of locally concentrated), the Eulerian description typically requires fewer degrees of freedom, i.e., less Eulerian nodes than Lagrangian nodes, especially if a stochastic diffusion model is employed for the Lagrangian case. Lagrangian methods can also be problematic if the parcel volume (Ω_p) is larger than the fluid averaging volume, whereas Eulerian methods have no equivalent restriction. In addition, an Eulerian approach allows both phases to be handled with a consistent numerical scheme and a consistent numerical grid. This discretization coincidence for an Eulerian treatment of the particles becomes a distinct accuracy advantage when one attempts to compute the effects of the particles on the continuous fluid for two-way coupling (Shrayber, 1979). For example, Sivier et al. (1996) examined Lagrangian and Eulerian representations of the particle field with respect to the prediction of shock attenuation of the continuous phase, and found that the Eulerian particle treatment

proved significantly more efficient (for the given accuracy levels) in terms of both computational memory and time.

13.1.4.4 Interphase Coupling

For either Lagrangian or Eulerian treatments, it should be noted that the two-way coupling requires description of the particle interphase coupling. This interaction occurs through the interface stresses between the two phases on the surface of the particle. In particular, the interphase coupling force ($\mathbf{F}_{\text{int},i}$) is the force acting on a single particle due to pressure and viscous stresses caused by the disturbed surrounding flow, owing to the boundary conditions at the bubble surface (Druzhinin and Elghobashi, 1998). It is equal in magnitude and opposite in direction to the hydrodynamic particle force acting on the continuous phase ($-\mathbf{F}_{\text{int},i}$). The interphase coupling force is effectively the hydrodynamic surface forces minus the contributions from the undisturbed flow stresses (i.e., minus the stress gradient forces, which occur independent of the presence of the partice):

$$\mathbf{F}_{\text{int}} = \mathbf{F}_{\text{surf}} - \mathbf{S} = \mathbf{F}_{\text{D}} + \mathbf{L} + \mathbf{A} + \mathbf{H}$$

For two-way coupling, the hydrodynamic force acting on a continuous-fluid computational volume is then $-n_{\text{p}}\mathbf{F}_{\text{int}}$.

For very heavy particles ($\rho_{\text{p}} \gg \rho_{\text{f}}$), the interphase force is often simplified to include only the particle drag (neglecting lift, added mass, and history effects, since they are proportional to ρ_{f}), i.e., $\mathbf{F}_{\text{int}} = \mathbf{F}_{\text{D}}$. For very light particles ($\rho_{\text{p}} \ll \rho_{\text{f}}$) with negligible collisions, the particle acceleration and body force can be neglected (as discussed in Section 13.1.4) θ, such that the interphase force can be conveniently written as $\mathbf{F}_{\text{int}} = -\mathbf{S}$ (Druzhinin and Elghobashi, 1998; Xu et al., 2002). In these two limits, the interaction force description is comparatively simple, which is particularly helpful for the Eulerian point-force treatment (see Table 13.2).

As the number of particles increase collisions become more important, leading to dense flows (Gidaspow, 1994). The key aspect for these flows is the proper incorporation of the particle–particle effects on the particle-phase fluid dynamics. In particular, the particle collision result in an effective stresses, which should be incorporated into the particle transport equation. These can be modeled with particle-phase viscosity, particle-pressure, granular temperature, etc., via a kinetic theory. For example, the Eulerian dense particle treatment will typically employ a gradient of the collisional pressure (p_{coll}) to capture this effect (see Table 13.2), while particle–particle momentum interactions are described via $\mathbf{F}_{\text{coll}}$ for an equivalent Lagrangian particle treatment. Eulerian formulations for the particle-phase generally model the integrated effect, and thus tend to be more empirical. However, such Eulerian formulation are independent of the number of particles, whereas the Lagrangian techniques become increasingly computationally intensive as the number of particles increases. Therefore, Eulerian formulation are most practical for collision-dominated conditions. (Crowe et al., 1998).

13.2 Direct Numerical Simulations

G. Tryggvason, Y. Tsuji, and S.E. Elghobashi

Direct simulation refers to the direct solution of the flow equations describing the two-phase mixture. Bubble and droplet motion are addressed first in which the deformation of the bubbles and/or droplets is included. The second section introduces the discrete element approach in which the details of particle-particle contact is addressed. The third section shows the application of the direct simulation of turbulence in fluid-particle flows.

13.2.1 Bubble and Droplet Motion and Deformation

G. Tryggvason

Understanding the dynamics of multiphase flows is of critical engineering and scientific importance and the literature is extensive. Much of what we know has, however, been obtained by experimentation and

scaling analysis. From a mathematical point of view, multiphase flow problems are notoriously difficult. In addition to the nonlinearity of the governing equations, the location of the phase boundary must generally be found as a part of the solution. Exact analytical solutions therefore exist only for the simplest of problems such as the steady state motion of bubbles and drops in Stokes flow, linear inviscid waves, and small oscillations of bubbles and drops. Experimental studies of multiphase flows are, however, not easy. For many flows of practical interests the length scales are small, the time scales are short, and optical access to much of the flow is limited. The need for numerical solutions of the governing equations has therefore been felt by the multiphase research community since the origin of computational fluid dynamics in the late 1950s and early 1960s. Although much has been accomplished, simulations of multiphase flows have remained far behind homogeneous flows where direct simulations have become a standard tool in turbulence research. Considerable progress has, however, been made in the last few years and it is clear that DNS will play a leading role in multiphase flow research in the next decade. Below we will first review briefly the various numerical techniques developed for computations of multiphase flows and then discuss results for disperse flows.

13.2.1.1 Simple Flows ($Re = 0$ and ∞)

In the limit of high and low Reynolds numbers, it is sometimes possible to simplify the flow description considerably by either ignoring inertia completely (Stokes flow) or by ignoring viscous effects completely (inviscid, potential flow). Most success has been achieved when the particles are undeformable spheres where in both these limits, it is possible to reduce the governing equations to a system of coupled ODES for the particle positions. For Stokes flow, the main contributor is Brady and collaborators (see Brady and Bossis (1988) for a review of early work), who have investigated extensively the properties of suspensions of particles in shear flows, and other problems. For inviscid flows, see Sangani and Didwania (1993) and Smereka (1993) for simulations of the motion of many bubbles in periodic domains.

For both Stokes flows as well as potential flows, deformable bubbles and drops can be simulated with boundary integral techniques. One of the earliest attempts was due to Birkhoff (1954), where the evolution of the interface between a heavy fluid initially on top of a lighter one (the Rayleigh–Taylor instability) was followed by a method where both fluids were assumed to be inviscid and irrotational, apart from baroclinic generation of vorticity at the interface. This allowed the evolution to be reformulated as an integral equation along the boundary between the fluids. Both the method as well as the problem later became a stable of multiphase flow simulations. A boundary integral method for water waves was presented by Longuet-Higgins and Cokelet (1976) and used to examine breaking waves. This paper was enormously influential and was followed by a large number of very successful extensions and applications, particularly for water waves (Baker et al., 1982; Vinje and Brevig, 1981; Schultz et al., 1994; and others). Other applications include the evolution of the Reyleigh–Taylor instability (Baker et al., 1980), the growth and collapse of cavitation bubbles (Blake and Gibson, 1981; Robinson et al., 2001), the generation of bubbles and drops due to the coalescence of bubbles with a free surface (Oguz and Prosperetti 1990; Boulton-Stone and Blake, 1993), the formation of bubbles and drops from an orifice (Oguz and Prosperetti, 1993), and the interactions of vortical flows with a free surface (Yu and Tryggvason, 1990), just to name a few. All boundary integral (or boundary element, when the integration is element based) methods for inviscid flows are based on following the evolution of the strength of surface singularities in time by integrating a Bernoulli-type equation. The surface singularities give one velocity component and Green's second theorem yields the other, thus allowing the position of the surface to be advanced in time. Different surface singularities allow for a large number of different methods (some that can only deal with a free surface and others that are suited for two-fluid problems) and different implementations multiply the possibilities even further. For an extensive discussion and recent progress see Hou, et al. (2001). Although continuous improvements are being made and new applications continue to appear, two-dimensional boundary integral techniques for inviscid flows are by now – a quarter century after the publication of the paper by Longuet–Higgins and Cokelet – a fairly mature technology. Fully three-dimensional computations are, however, still rare. Chahine and Duraiswami (1992) have computed the interactions of a few inviscid cavitation bubbles and Xue et al. (2001) have simulated a three-dimensional breaking wave.

The key to the reformulation of inviscid interface problems in terms of a boundary integral is the linearity of the field equations. In the opposite limit, where inertia effects can be ignored and the flow is dominated by viscous dissipation, the Navier–Stokes equations become linear (Stokes flow) and it is also possible to recast the governing equations into an integral equation on a moving surface. Boundary integral simulations of unsteady two-fluid Stokes problems appear to have originated with the work of Youngren and Acrivos (1976) and Rallison and Acrivos (1978) who simulated the deformation of a bubble and a drop, respectively, in an extensional flow. Subsequently, several authors have examined a number of problems. Pozrikidis and collaborators have examined several aspects of the suspension of drops, starting with a study by Zhou and Pozrikidis (1993) of the suspension of a few two-dimensional drops in a channel. Simulations of fully three-dimensional suspensions have been done by Loewenberg and Hinch (1996) and Zinchenko and Davis (2000). The method has been described in detail in the book by Pozrikidis (1992)and Pozrikidis (2001), gives a very complete summary of the various applications.

13.2.1.2 Finite Reynolds Number Flows

For intermediate Reynolds numbers, it is necessary to solve the full Navier–Stokes equations. Nearly 10 years after Birkhoff's effort to simulate the Rayleigh–Taylor problem by a boundary integral technique, the Marker-And-Cell (MAC) method was developed at Los Alamos by Harlow and collaborators. In Harlow and Welch (1965) the method was introduced and two sample computations of the so called dam breaking problem shown. Several papers quickly followed: Harlow and Welch (1966) examined the Rayleigh–Taylor problem and Harlow and Shannon (1967) studied the splash when a drop hits a liquid surface. As originally implemented, the MAC method assumed a free surface so there was only one fluid involved. This required boundary conditions to be applied at this surface and the fluid in the rest of the domain to be completely passive. The Los Alamos group quickly realized, however, that the same methodology could be applied to two-fluid problems. Daly (1969) computed the evolution of the Rayleigh–Taylor instability for finite density ratios and Daly and Pracht (1968) examined the initial motion of density currents. Surface tension was then added by Daly (1969) and the method again used to examine the Rayleigh–Taylor instability. The MAC method quickly attracted a small group of followers that used it to study several problems: Chan and Street (1970) applied it to free surface waves, Foote (1973, 1975) simulated the oscillations of an axisymmetric drop and the collision of a drop with a rigid wall, and Chapman and Plesset (1972) and Mitchell and Hammit (1973) simulated the collapse of a cavitation bubble. Although the MAC method was designed specifically for multifluid problems (hence the M for Markers!) it was also the first method to successfully solve the Navier–Stokes equation using the primitive variables (velocity and pressure). The staggered grid used was a novelty and today it is a common practice to refer to any method using a projection based time integration on a staggered grid as a MAC methods.

The next generation of methods for multifluid flow evolved gradually from the MAC method. It was already clear in the Harlow and Welch (1965) paper that the marker particles could cause inaccuracies, and among the number of algorithmic ideas explored by the Los Alamos group, the replacement of the particles by a marker function soon became the most popular alternative. Thus the volume-of-fluid (VOF) method was born. VOF was first discussed in a refereed journal article by Hirt and Nichols (1981), but the method apparently originated a few years earlier (DeBar, 1974; Noh and Woodward, 1976). The VOF method has been extended in various ways by a number of authors. It has also been distributed widely as the NASA SOLA-VOF code and as FLOW3D from Fluid Sciences Inc. In addition, many commercial computational fluid dynamics codes now include the option of simulating free surface or multiphase flows using the VOF method. For a review of VOF methods, see Scardovelli and Zaleski (1999). Other methods, based on similar ideas but advecting the marker function in a different way include the level set method (reviewed by Osher and Fedkiw, 2001; Sethian, 2001) and the CIP method of Yabe and collaborators (see Yabe et al., 2001, for a review).

While the MAC methodology and its successors were being developed, other techniques were also being explored. Hirt et al. (1970) describe one of the earliest use of structured boundary fitted Lagrangian grids. This approach is particularly well-suited when the interface topology is relatively simple and no

unexpected interface configurations develop. In a related approach, a grid line is aligned with the fluid interface, but the grid away from the interface is generated using standard grid generation techniques such as conformal mapping or other more advanced elliptic grid generation schemes. The method was used by Ryskin and Leal (1984), to compute the steady rise of buoyant, deformable, axisymmetric bubbles. Ryskin and Leal assumed that the fluid inside the bubble could be neglected, but Dandy and Leal (1989) and Kang and Leal (1987) extended the method to two-fluid problems and unsteady flows. Several authors have used this approach to examine relatively simple problems such as the steady state motion of single particles or moderate deformation of free surfaces. Fully three-dimensional simulations are relatively rare and it is probably fair to say that it is unlikely that this approach will be the method of choice for very complex problems, such as the three-dimensional unsteady motion of several particles.

A much more general approach to continuously represent a fluid interface by a grid line is to use unstructured grids to resolve the fluid motion. This allows grid points to be inserted and deleted as needed and distorted grid cells to be reshaped. While the grid was moved with the fluid velocity in some of the early applications of this method, the more modern approach is to either move only the interface points or to move the interior nodes with a velocity different from the fluid velocity in such a way that the grid distortion is reduced but adequate resolution is still maintained. A large number of methods have been developed that fall into this general category, but we mention only a few examples. Oran and Boris (1987) simulated the breakup of a two-dimensional drop; Shopov et al. (1990) examined the initial deformation of a buoyant bubble; and Fukai et al. (1995) did axisymmetric computations of the collision of a single drop with a wall.

Several hybrid methods combine the ideas discussed above in a variety of ways. Front-tracking methods where the interface is marked by connected marker points, but a fixed grid is used for the fluid within each phase have been particularly successful. In the method of Tryggvason and collaborators (Unverdi and Tryggvason, 1992; Tryggvason et al., 2001) the tracked front is used to advect a smoothed marker function and to compute the surface tension. The method is therefore very similar to methods that work directly with a grid-marker function, but the advection of the interface is greatly improved. Other methods have been designed to capture the interface more accurately. These include the method of Glimm and collaborators (Glimm and McBryan, 1985), where the fixed grid is modified near the front to make a grid line follow the interface, as well as more recent sharp-interface methods (such as Fedkiw et al., 1999; Ye et al., 1999; and Lee and LeVeque, 2003). The increased accuracy does, however, come at the cost of a considerably increased complexity and it is not clear at the time of this writing what the impact of these new methods will be on DNS of finite Reynolds numbers flows.

The most recent addition to the collection of methods capable of simulating finite Reynolds number multiphase flows is the Lattice-Boltzman method (LBM). Although there have been some doubts about the accuracy and correctness of the LBM, it seems now clear that they can be used to produce accurate results of accuracy comparable to more conventional methods. It is still not clear whether the LBM is significantly faster or simpler than other methods (as sometimes claimed), but most likely these methods are here to stay. For a discussion see, e.g., Shan and Chen (1993) and Sankaranarayanan et al. (2002).

Many reviews are available that discuss computational methods for multiphase flows. Early reviews include Hyman (1984) and Floyryan and Rasmussen (1989), and more recent reviews are given by Scardovelli and Zaleski (1999), who discuss volume of fluid methods, and Anderson et al. (1998), who review phase field methods. Several up-to-date articles about various aspects of computations of multiphase systems and related problems can be found in a special issue of the *Journal of Computational Physics* (Vol. 169, 2001). The book by Shyy et al. (1996) also discusses several aspects of computations of multiphase flows. For discussions of the role of numerical predictions for industrial problems, see Crowe et al. (1998), for example.

13.2.1.3 Disperse Flows

In many industrial and natural processes, multiphase flows consists of one phase in the form of well defined bubbles, drops, or solid particles dispersed in another continuous phase. Bubbly flows occur in boiling heat transfer, cloud cavitation, aeration, and stirring of reactors in water purification and waste

water treatment plants, bubble columns and centrifuges in the chemical industry, cooling circuits of nuclear reactors, the exchange of gases and heat between the oceans and the atmosphere, and explosive volcanic eruptions, just to name a few examples. Similarly, drops are found in sprays used in the atomization of liquid fuels, painting and coating, emulsions, and rain. Understanding the evolution and properties of *dispersed* flows is therefore of major technological as well as scientific interest.

For engineering applications with a large number of bubbles and drops, computational modeling relies on equations that describe the average flow field. The two-fluid model, where separate equations are solved for the dispersed and the continuous phase, is the most common approach. Since no attempt is made to resolve the unsteady motion of individual particles, closure relations are necessary for the unresolved motion and the forces between the particles and the continuous phase. Closure relations are usually determined through a combination of dimensional arguments and correlation of experimental data. The situation is analogous to computations of turbulent flows using the Reynolds averaged Navier–Stokes equations, where momentum transfer due to unsteady small-scale motion must be modeled. For details of two-fluid modeling, see Drew (1983), Ishii (1987) Drew and Lahey (1992), and Zhang and Prosperetti (1994). For the turbulent motion of single phase flows, direct numerical simulations, where the unsteady Navier–Stokes equations are solved on fine enough grids to fully resolve all flow scales, have had a major impact on closure modeling. The goal of direct numerical simulations of multiphase flows is similar. In addition to information about how the drift Reynolds number, velocity fluctuations, and bubble dispersion change with the properties of the system, the computations should yield insight into how bubbles and drops interact, both with each other and with the continuous phase. The simulations should show whether there is a predominant microstructure or interaction mode, and if the flow forms structures that are much larger than the size of the dispersed particles. Information about the microstructure is essential for the construction of models of multiphase flows and can also help to identify what approximations can be made.

Although the need for direct numerical simulations to help with the construction of reliable closure models has been recognized for a long time, it is only recently that major progress has been made. In the limit of high and low Reynolds numbers major simplifications are possible and the Stokesian dynamics method of Brady and collaborators (for a recent contribution, see Sierou and Brady (2002) for example) has been used to examine many aspects of solid suspensions. For invisic bubbles, Sangani and Didwania (1993) and Smereka (1993) simulated the motion of spherical bubbles in a periodic box and observed that the bubbles tended to form horizontal "rafts," particularly when the variance of the bubble velocities was small. As this rafting is generally not observed experimentally, the results cast considerable doubt on the utility of the potential flow approximation for the interactions of many bubbles. This is somewhat unexpected since for a single bubble this approximation is excellent (see, however Harper (1997) for a discussion of bubbles rising in-line). In both Stokes flows and potential flows, deformable bubbles and drops can be simulated using boundary integral techniques. For recent papers on Stokes flow see, for example, the study by Li and Pozrikidis (2000) of the dynamics of two-dimensional drops in a channel and the simulation of a few three-dimensional drops in a channel by Zinchenko and Davis (2000). While transient interactions of a few bubbles have been examined using boundary integral methods, no simulations of the long-time evolution of many deformable bubbles have been done, and given the failure of the potential flow approximation for rigid bubbles at high Reynolds numbers, it seems unlikely that such studies would be applicable to a large range of realistic situations.

For nondilute flows at intermediate Reynolds numbers it is necessary to solve the full unsteady Navier–Stokes equations. Such simulations for the unsteady motion of many bubbles or particles are relatively recent. Unverdi and Tryggvason (1992a, 1992b) computed the interactions of two, two- and three-dimensional bubbles and Esmaeeli and Tryggvason (1996) followed the evolution of a few hundred two-dimensional bubbles. Esmaeeli and Tryggvason (1998, 1999) simulated the unsteady motion of several two- and three-dimensional bubbles and Mortazavi and Tryggvason (2000) examined the motion of a periodic row of drops in a channel. More recently, Bunner and Tryggvason (1999, 2002a, 2002b, 2003) used a fully parallelized version of the method to examine three-dimensional systems with a much larger number of bubbles. Other studies of the motion and interactions of many bubbles have been done by several Japanese authors. Early work, using the VOF method to compute the motion of a single two-dimensional bubble can be found in Tomiyama et al. (1993) and more recent work on bubble interactions, using both VOF and the Lattice-Boltzman Method, is presented in Takada et al. (2000, 2001).

The numerical simulations of Tryggvason and collaborators have focused on homogeneous bubbly flows, modeled by fully periodic domains. The average bubble Reynolds number has generally been relatively modest, 20 to 30, so that each bubble is fully resolved by 20 to 30 grid points per diameter. Relatively low-order statistics, such as the average rise velocity of the bubbles and the pair probability distribution, converge rapidly with increasing size of the simulated domain and Bunner and Tryggvason (2002) found essentially no difference between the rise velocity of 12 and 216 nearly spherical bubbles. Other quantities, like the self-diffusion coefficient, converge much more slowly. For nearly spherical buoyant bubbles at modest Reynolds numbers, the simulations show that the dominant interaction mode is the "drafting, kissing, and tumbling" mechanism described by Fortes et al. (1987). Thus, a bubble behind another bubble is drawn into the wake of the bubble in front, once in the wake it catches up and collides with the one in front and the two bubbles then "tumble" and move apart. This collision mode is inherently a finite Reynolds number effect, since two buoyant bubbles in Stokes flow do not change their orientation unless acted on by the third bubble and bubbles in potential flow repeal each other if they are rising in an in-line configuration. The simulations have also shown that freely interacting bubbles rise considerably slower than bubbles constrained to remain in a fixed array. At very low Reynolds numbers the opposite is true as predicted theoretically for Stokes flow. While spherical bubbles remained nearly uniformly distributed, Bunner and Tryggvason (2003) found that deformable bubbles could gather into streams or chimneys and rise much faster than when they were uniformly distributed. Figure 13.10 shows the closeup of a few bubbles and the velocity field in a plane cutting through some of the bubbles, taken from a simulation of 27 freely rising bubbles at a void fraction of 6%, before they stream. The simulations are done using a cubic, fully periodic domain resolved by 192^3 grid points and for the particular set of parameters used here, the average rise Reynolds number of the bubbles is about 23.

Major progress has also been made in the simulation of finite Reynolds number suspension of rigid particles. Feng et al. (1994, 1995) simulated the two-dimensional, unsteady motion of one and two rigid particles, Hu (1996) computed the motion of a few hundred two-dimensional particles and fully three-dimensional simulations of 100 particles were presented by Johnson and Tezduyar (1997). Recent papers include simulations of over 1000 spheres by Pan et al. (2002) and a study of the fluidization of 300 circular particles in in plane Poiseuille flow by Choi and Joseph (2001). While there is, of course, some differences between the behavior of deformable bubbles and drops, development of direct numerical simulations for such systems have paralleled the capability for bubbly flows and lessons learned for one system often find applications in the other.

As computer power increases, it is possible to examine both larger and more complex systems. In Figure 13.11, one example of a relatively large-scale simulation of bubbles in a turbulent channel flow is shown. The bubbles and the streamwise velocity in two planes, one parallel to the lower wall and another

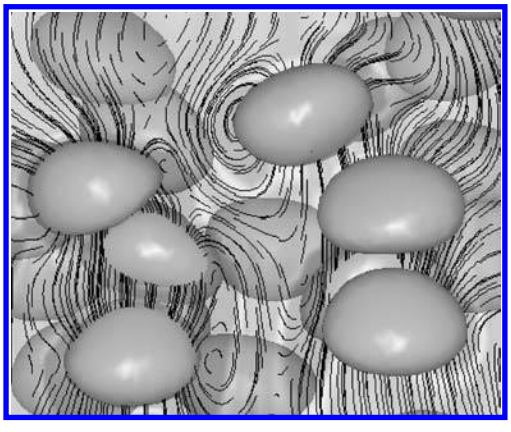

FIGURE 13.10 A closeup of the velocity field around a few interacting bubbles from a simulation of 27 buoyant bubbles in a fully periodic domain. The bubbles and the velocity in a plane cutting through the middle of the domain is shown. (Courtesy of Dr. Bernard Bunner.)

perpendicular to the walls, cutting through the middle of the channel, are plotted at a relatively early time. The domain is $2\pi \times \pi \times 2$ in the streamwise, spanwise, and wall-normal direction, respectively, resolved by a regular structured grid, stretched in the wall-normal direction to provide a finer resolution near the walls. The total number of grid points is $512 \times 256 \times 256$. The initial velocity field was taken from spectral simulations of turbulent channel flows to avoid having to simulate the transition, and the volume flux is kept constant by adjusting the pressure gradient. The turbulent flow was first evolved without bubbles to ensure that the finite-difference method used here correctly simulated the single-phase flow. Initially, 120 bubbles of diameter 0.3 are placed in the flow, next to the walls. The channel Reynolds number is 3000, giving a shear Reynolds number of 135 based on the shear velocity and the wall unit. The domain dimension are $848 \times 424 \times 270$ wall units, and in wall units the bubble diameter is 27.5. As the bubbles interact with the turbulent flow, they are dispersed and slowly migrate away from the walls. The goal of these simulations is to cast some light on how microbubble injection into turbulent boundary layers reduces drag. For the parameters used here, the effect of the bubbles on the wall drag is very small. For other work on this problem, see Kanai and Miyata (2001) and Kawamura and Kodama (2002).

13.2.1.4 Current Status

Direct numerical simulations of multiphase flows have come a long way during the last decade. It is now possible to follow the motion of hundreds of bubbles, drops, and particles at finite Reynolds numbers in simple geometries for sufficiently long time so that meaningful averages can be computed. Much remains to be done, however. At higher Reynolds numbers the number of grid points required to resolve each bubble and the flow around them increases and the cost of doing simulations with many bubbles increases. With larger computers such simulations will become increasingly more feasible. The formation of bubbles and drops as well as coalescence must also be addressed and except for a few simulations of the breakup of drops in well-defined flows, little has been done. These problems are, nevertheless, well within reach.

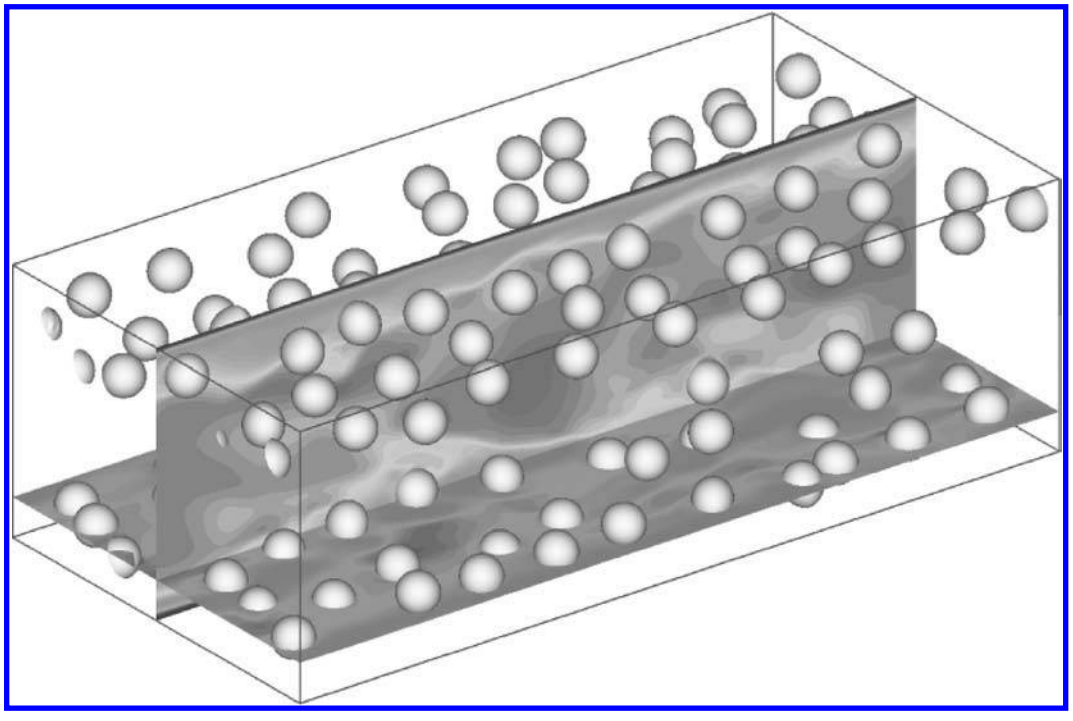

FIGURE 13.11 An example of a direct numerical simulation of bubbles in a turbulent channel flow. The bubbles and the streamwise velocity in a plane near the bottom wall and another one cutting through the middle of the domain is shown. (Courtesy of Dr. Jiacai Lu.)

As direct numerical simulations of multiphase flows become more common, the need for advances in the development of the theoretical framework for modeling such flows is also becoming more urgent. Current models have mostly been developed in an environment where relatively little has been known about the details of the flow, and for the most part these models are far behind what is available for single phase turbulent flows. While our abilities to simulate directly more and more complex multiphase systems will certainly increase dramatically in the next few years, it is important to realize that our desire to compute will always be ahead of what we can do by direct numerical simulations. Even if we could fully compute the behavior of a particular system, we can easily imagine, for example, that we might want to incorporate simulations into a real-time control algorithm that dynamically explored the consequences of several possible control actions. Thus, the condensation of knowledge obtained by direct numerical simulations into reduced or averaged models that allow faster predictions will remain at the core of multiphase flow research for a long time to come.

Although the opportunities for studies of two-fluid disperse systems are enormous, it is the longer-term development of the ability to compute the coupled motion of complex systems that will bring about the full impact of direct numerical simulations. Most engineering fluid systems include a large number of physical phenomena such as fluid flow, evaporation, solidification, and chemical reactions, and while the ability to examine each aspect in detail is important, simulations of the full system will allow unprecedented insight. Here, progress is just starting. A few investigators have simulated boiling flows (Son and Dhir, 1998; Juric and Tryggvason, 1998; Welch and Wilson, 2000; Shin and Juric, 2002; Esmaeeli and Tryggvason, 2003; Yoon et al., 2001), dendritic solidification in the presence of flow (Tonhardt and Amberg, 1988; Boettinger et al., 2002; Jeong et al., 2001; Al-Rawhai and Tryggvason, 2004), and a few other problems. The potential for complexity is virtually unlimited and even relatively simple systems will put considerable demand on computational resources and the solution methodology. Thus, for example, the effect of electric fields on the boiling of binary mixture requires the solution of the fluid flow, species conservation, the energy equation and phase change, as well as an equation for the electric field. It is also likely, as more and more complex problems are dealt with, that the difference between direct numerical simulations — where everything is resolved fully — and simulations where the smallest scales are modeled, will become blurred. Simulations of atomization where the evolution of thin films is computed by subgrid models and very small drops are included as point particles are a relatively obvious example of such hybrids. Other examples include possible couplings with microscopic simulations of moving contact lines, kinematic effects at a solidification interface, and thin flames. Simulations of non-Newtonian fluids, where the microstructure has to be modeled in such a way that the molecular structure is accounted for in some way also falls under this category.

13.2.2 Discrete Element Approach

Y. Tsuji

13.2.2.1 Introduction

The discrete element approach is known by various names, such as particle tracking approach, Lagrangian approach, single-particle approach, and so on. In the field of granular flows, the distinct element method (DEM) is a popular terminology used for expressing simulations employing the soft sphere model. In this approach, trajectories of all individual particles or sample particles of limited number are calculated by making use of the Newtonian equations of motion for a solid body. Equations of fluid motion are the same as those for single-phase flows in one-way coupling. In the two-way coupling the fluid–particle interaction term is added to the equation of fluid motion as external forces. In general, the calculation should be done based on the two-way coupling when the particle concentration is high. Under the condition of such high particle concentrations, not only the two-way coupling, but also the particle–particle interaction should be taken into account. The two-way coupling with the particle–particle interaction is the case in many industrial particle–fluid systems. If the particle concentration is sufficiently low, both fluid–particle and particle–particle interactions are neglected. Such a case corresponds to dilute-phase flow and is not described in this section.

The phenomena associated with particle–particle interaction are different depending on the degree of concentration. When the concentration is moderate, particles are dispersed in the fluid. In such a case,

the particle–particle interaction is different depending on the nature of fluid. If the fluid is a liquid, particles hardly touch due to the lubrication effect. If the fluid is a gas, the particle inertia force is dominant and the particles collide. When the concentration is extremely high, particles are not dispersed and they keep in contact with other particles. The case in which the lubrication effect is important is not described here. Therefore, this section deals with collision- and contact-dominated flow of gas–particle flows.

13.2.2.2 Equation of Motion

Concerning the particle motion, we use the well-known Newtonian equations of motion considering the effects of external forces such as gravitational force and fluid force. Individual particles have two types of motion: translation and rotation. The equations of translational and rotational motion are expressed as

$$\ddot{\mathbf{x}} = \frac{f_c + f_F}{m} + \mathbf{g} \tag{13.1}$$

$$\boldsymbol{\Omega} = \frac{M}{I} \tag{13.2}$$

where $\mathbf{x}$ is the position vector of the particle gravity center, m the particle mass, $\mathbf{f}_c$ the summation of contact forces, $\mathbf{f}_F$ the summation of fluid force, $\mathbf{g}$ the gravity acceleration vector, $\boldsymbol{\omega}$ the particle angular velocity vector, M the summation of torque, I the moment of inertia of the particle, and the $(\cdot)$ time derivative.

Needless to say, the contact force $\mathbf{f}_c$ is taken into account only when particles are in contact. The new velocity and position are calculated step by step by using an appropriate time step Δt:

$$\mathbf{v} = \mathbf{v}_0 + \ddot{\mathbf{x}}_0 \cdot \Delta t \tag{13.3}$$

$$\mathbf{x} = \mathbf{x}_0 + \mathbf{v} \cdot \Delta t \tag{13.4}$$

and

$$\Omega = \Omega_0 + \dot{\Omega}_0 \cdot \Delta t \tag{13.5}$$

where $\mathbf{v}$ is the particle velocity vector and the subscript (0) the value at the previous time.

The calculation method for the fluid motion can be classified into the following cases: (1) calculation of individual particle base and (2) calculation of local cell base.

In the first method, the instantaneous flow around each particle is found using the Navier–Stokes equation (Hu, 1996; Pan and Banerjee, 1997; Kajishima and Takiguchi, 2002; Pan et al., 2002) or the Lattice–Boltzman method (Qi, 2000) as shown in Figure 13.12. The fluid forces $\mathbf{f}_F$ acting on particles are obtained by integrating stresses on the surface of the particles, which are solutions of the basic equations. Thus, such coefficients as drag and lift are not needed. This method is most rigorous but it takes much computational time and large memory capability.

In the second method, a flow field is divided into cells as shown in Figure 13.13; the size of the cells should be larger than the particle size and smaller than the system size of flow. The effects of the presence of particles on fluid are taken into account by the volume fraction of each phase and momentum exchange through the drag force. This approach can be called "local averaging approach," proposed by Anderson and Jackson (1967).

The equations for fluid motion are given as follows:

$$\frac{\partial \varepsilon}{\partial t} + \frac{\partial (\varepsilon u_j)}{\partial x_j} = 0 \tag{13.6}$$

and

$$\frac{\partial (\rho \varepsilon u_i)}{\partial t} + \frac{\partial (\rho \varepsilon u_i u_j)}{\partial x_j} = -\varepsilon \frac{\partial p}{\partial x_i} + f_{si} + \varepsilon \frac{\partial \tau_{ij}}{\partial x_j} + \rho \varepsilon g \tag{13.7}$$

where u is the velocity, p the pressure, ρ the fluid density, ε the void fraction, f_{si} the force on fluid due to drag, and τ_{ij} the stress tensor.

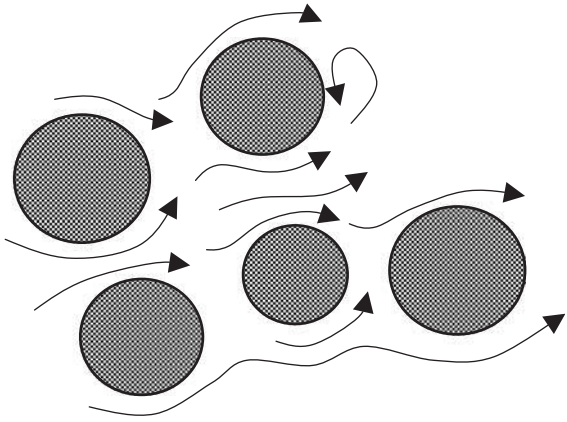

FIGURE 13.12 Treatment of individual particle base.

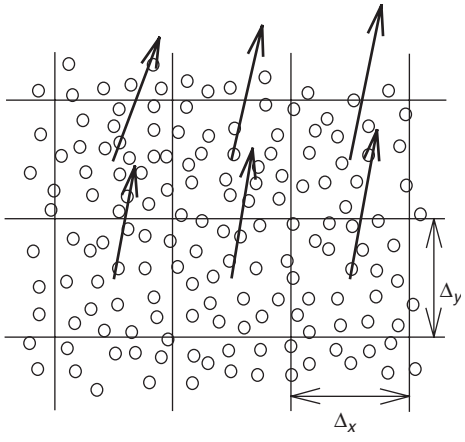

+FIGURE 13.13 Treatment of local cell base.

Equations (13.6) and (13.7) are the continuity equation and the momentum equations, respectively. Mass transfer is neglected in the above equations. Concerning the drag force, two different expressions are used depending on if the particle motion is collision or contact-dominated. The formula for the drag force acting on a single particle with modification of void fraction (Wen and Yu, 1966) is used for collision-dominated flows and an expression developed for particle beds, such as the Ergun equation (Ergun, 1952), is used for the contact-dominated flow. If the particles are coarse and the fluid is a gas, the particle inertia term is larger than the stress and gravitational terms which can be neglected. Tsuji et al. (1993) showed that calculation based on such simplifications leads to realistic results.

13.2.2.3 Collision-Dominated Flows

Once the external forces are given in Eqs. (13.1) and (13.2), the trajectory calculation is relatively simple during the period when the particle–particle collision does not occur. When a particle collides with another particle, values of particle velocities are reset. The postcollisional velocity can be obtained by the hard sphere model described in Section 12.4.1.1. These calculations are straightforward. The difficulty in the calculation of collision-dominated flows lies in finding collision pairs from a large number of particles in the flow field. There are two methods available for finding collision partners: (1) deterministic method and (2) stochastic method.

In the first method, the collision pairs are found deterministically from trajectories of individual particles. This method takes more computation time as the particle number is increased. The second method

is based on the probability of collision which has been developed in molecular flows. Oesterle and Petitjean (1993) proposed a method assuming the Maxwell distribution for particle fluctuating velocity. Kitron et al. (1990), Yonemura et al. (1993), and Tanaka et al. (1996) used the direct simulation Monte Carlo (DSMC) method. In the DSMC method, trajectory calculations are made only for sample particles; their number is much smaller than the actual number of particles.

The DSMC method is briefly explained below. Imagine that a very large number of particles exist in an actual flow field as shown in Figure 13.14a and all the particles have different velocity vectors. This actual field of particles is replaced with a simple field that consists of sample particles of a limited number with fixed velocity vectors. Figure 13.14b shows three such sample particles: white, black, and dotted. (In the figure, the number of sample particles shown is only 3; for simplicity of explanation, but in practical calculations, the number of sample particles should be much larger.) Each sample particle represents a group of particles with the same velocity vector, but it is invisible in Figure 13.14b. The invisible particles are assumed to be distributed at random. The actual field shown in Figure 13.14a is replaced with the field shown in Figure 13.14c, where particles that are invisible in Figure 13.14b are shown. The total number of particles in Figures 13.14a and 13.14c are set to be the same. Figures 13.14a and 13.14c appear similar but in Figure 13.14c, all the particles belong to a limited number of groups (here group 3). It can be proven mathematically that if the number of sample particles is sufficiently large, the statistical properties in Figures 13.14a and 13.14c are the same. Instead of the field shown in Figure 13.14a, we treat the field in Figure 13.14c. In this field it is easy to derive the collision probability, i.e., the collision probability can be expressed as a function of the relative velocity between both particle and number density. Once the collision probability is given, trajectory calculations are made in the field of Figure 13.14b, where only sample particles exist.

The next problem is to obtain the collision probability. If the relative velocity between two groups of particles distributed at random is known, the collision frequency P_{ij} at which a particle of the particle group i collides with particles of the particle group j within time Δt is given by

$$P_{ij} = n_j \cdot \pi d^2 \cdot G_{ij} \Delta t \tag{13.8}$$

where n_j is the number density of particle j, G_{ij} the relative velocity $v_i - v_j$, and d the particle diameter.

The next question is how to use this in the trajectory calculation. There are a few methods that have been proposed. Bird(1976) who developed the DSMC method proposed the time count method. Illner and Neunzert(1987) proposed the modified Nanbu (1980) method. The calculation process of the modified Nanbu is as follows.

As described earlier, trajectory calculations are made for sample particles with the time step Δt. Let us consider the motion of sample particle *i*. At every time step, a random number is produced to find the number of another sample particle, which is the candidate for the collision partner with the sample particle *i*. The number *j* chosen by the random number generator corresponds to many particles represented by the sample particle *j*. The possibility of collision between the sample particle *i* and one of particles represented by sample particle *j* depends on the collision probability given by Eq. (13.8). In the modified Nanbu method (Illner and Neunzert, 1987), one random number is used for finding a candidate of collision partner and for deciding if collision occurs. For details, refer to Tanaka et al. (1996).

13.2.2.4 Contact-Dominated Flows

The key idea for the discrete element approach of the contact-dominated flows is the model of the contact force. The soft sphere model described in Section 12. 4.1.2 is used for this purpose. Once the contact forces are given, trajectories of individual particles are obtained by Eqs. (13.1) to (13.3). To provide the readers with an image of how the discrete element approach for contact-dominated flows works, Figure 13.15 shows how particle motion is calculated by using the soft sphere model. Figure 13.15 also shows the case where particle *i* approaches particle *j* with a relative velocity $\mathbf{v}_i - \mathbf{v}_j$. Particle *j* is made stationary. Instead of considering deformation, the two particles are made to overlap. As the overlap distance increases, the contact force becomes larger and the particle velocity decreases. In the course of time, particle velocity changes direction and the overlap distance decreases. Finally the two particles separate. This process is calculated step-by-step by Eqs. (13.4)–(13.7). The time step Δt is much smaller than that for collision-dominated flows.

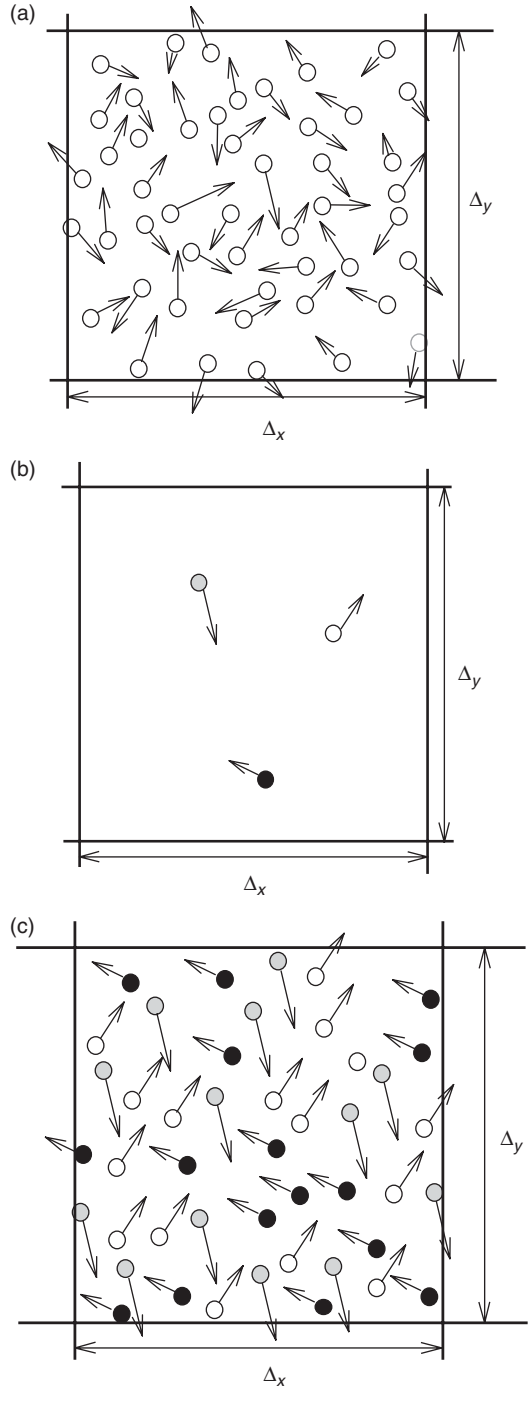

FIGURE 13.14 (a) Field of real particles; (b) sample particles; (c) field replacing.

13.2.2.5 Simulation Example

Figure 13.16 shows a snap shot of particle concentration and velocity vectors of particles and gas calculated by Yonemura et al. (1993), who used DSMC method. An interesting finding is that the in-elastic

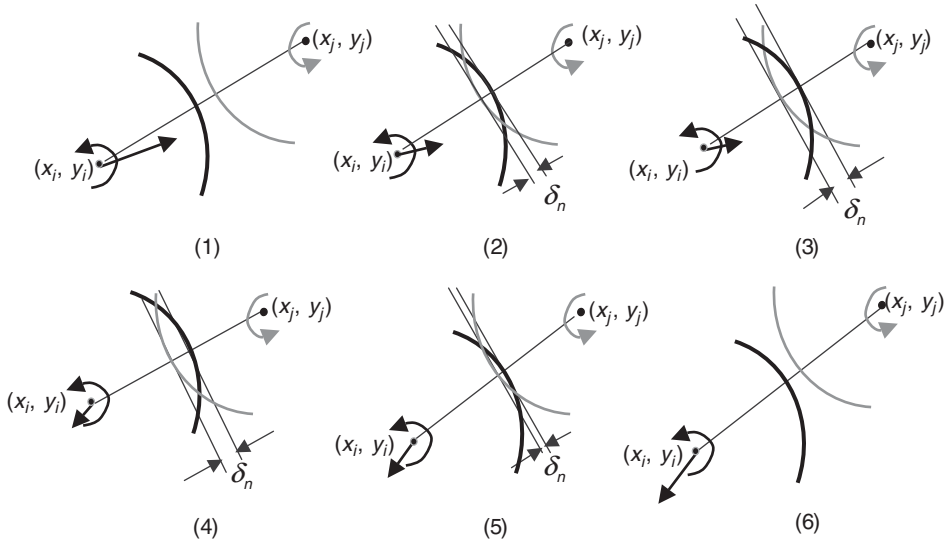

FIGURE 13.15 Calculation of particle motion based on soft sphere model.

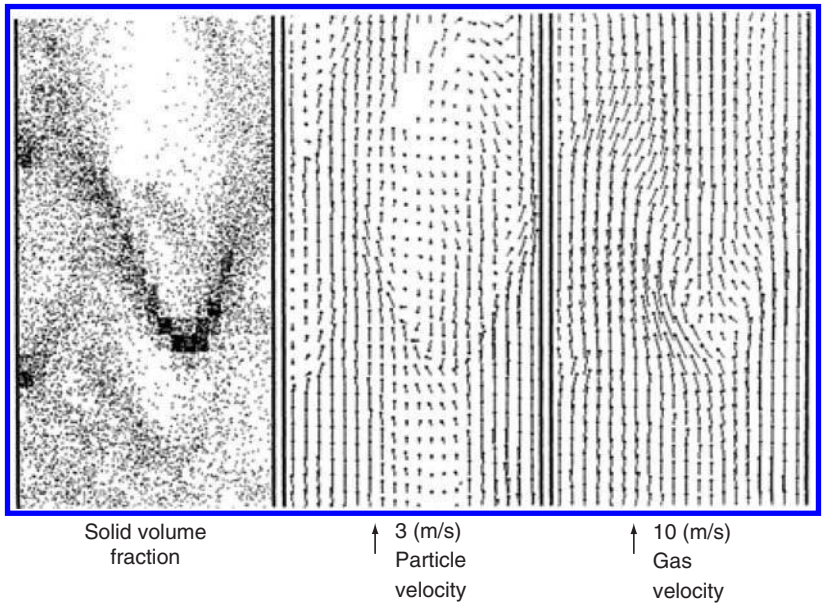

FIGURE 13.16 Collision-dominated flow. (From Yonemura et al., *ASME/FED Gas–Solid Flows*, 166, 303, 1993. With Permission)

particle-particle collision leads to the formation of clusters. The flow field of the clusters shows large-scale fluctuations. The structure of cluster has been investigated more in details by Tanaka et al. (2002)

The discrete element simulation using the soft sphere model DEM has very wide applicability in particle technology even if the fluid is neglected. The following examples are those to which the discrete element simulation has been applied to contact-dominated flows; gravity flows in hoppers and chutes,

rotary kiln, screw feeder, mixers (drum mixer and V-shape mixer), granulator, sieve, vibrating bed, shear flow, etc. Many scientists are engaged in the research of these particle flows; the research tends to deal with complicated cases. Some researchers take into account the effects of cohesion forces caused by a liquid bridge, some others nonsphericity, while few other include heat transfer.

If the effects of the fluid are included in the discrete particle simulation, the range of applications becomes larger. The first work of Tsuji et al. (1992) is a dense-phase pneumatic conveying example and the calculated results are shown in Figure 13.17. Tsuji et al. (1993) extended their work to the fluidized bed. The results for a bubble rising in the fluidized bed are shown in Figure 13.18. The velocity of the rising bubble agrees with experiments not only qualitatively but also quantitatively. A spouted bed (Figure 13.19) is another example to which the discrete element simulation has been applied. Recently, various complicated factors such as heat transfer (Rong et al., 2001; Liu et al., 2002) and cohesion forces (Mikami et al., 1998; Rhodes et al., 2001; Kuwagi and Horio, 2002) have been added by several workers for a more practical applications.

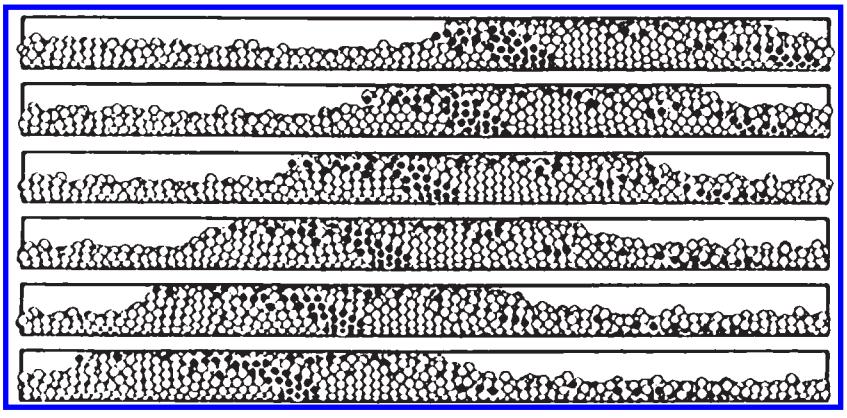

FIGURE 13.17 Plug conveying in horizontal pipe. (From Tsuji et al., *Powder Technol.*, 77, 79, 1993. With permission.)

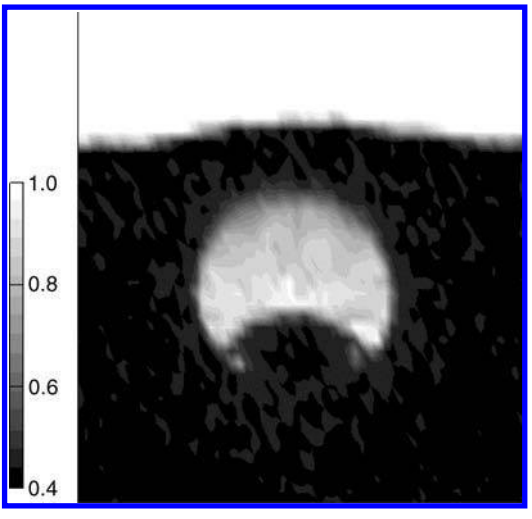

FIGURE 13.18 Single rising bubble in fluidized bed.

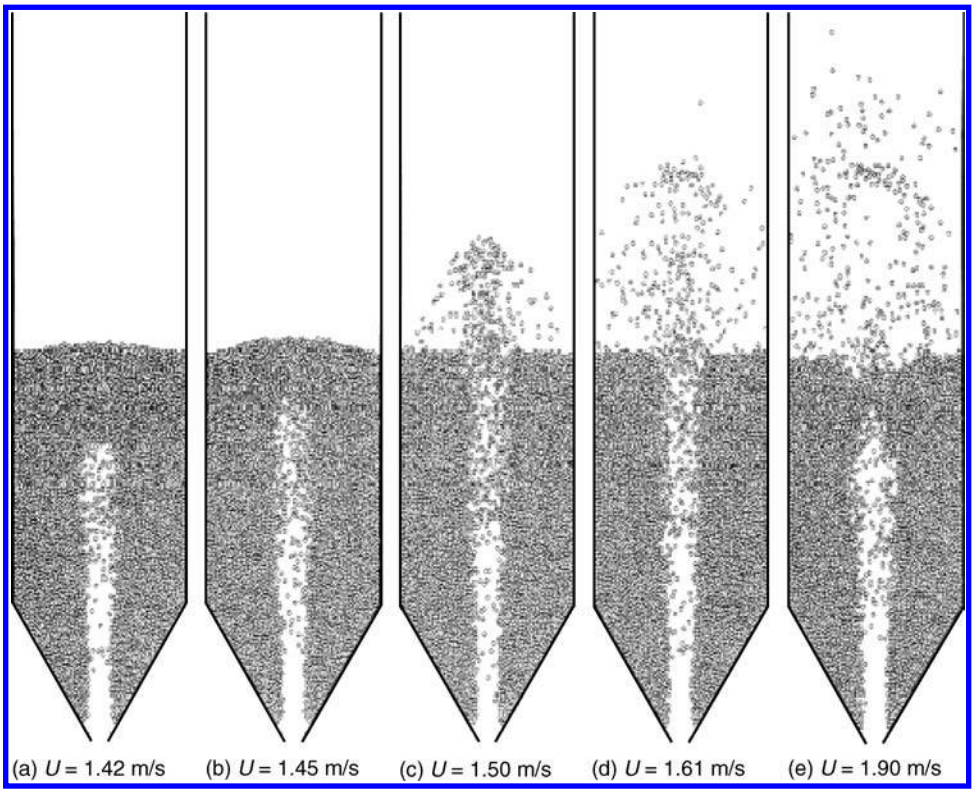

FIGURE 13.19 Spouted bed in cylinder. (From Kawaguchi et al., *Powder Technol.*, 109, 3, 2000. With permission.)

13.2.3 Direct Simulation of Turbulent Flows Laden with Dispersed Particles

S.E. Elghobashi

13.2.3.1 Introduction

DNS of turbulent flows laden with a large number (~10^8) of dispersed spherical (solid, liquid, or gas) particles requires the spatial and temporal resolution of all the relevant scales of the carrier fluid motion down to the Kolmogorov scales (η, τ_κ), and ideally, the simultaneous resolution of the flow around the surfaces of the individual particles. However, the resolution of the flow around each particle is infeasible at present and in the near future (i.e., the next 15 years; Jimenez, 2003). This infeasibility is only due *to* computer (memory and speed) limitations as demonstrated next. For example, consider a typical turbulent boundary layer flow of 0.01 m thickness over a flat plate of 1 m length and 0.5 m width (i.e., the fluid volume = 5×10^{-3} m^3 or 5 L), which contains dispersed particles of 50 μm diameter occupying a volume fraction (or concentration) of 10^{-3}. The number of these particles is thus more than 76×10^6. Now, in order to resolve the motion around each of these 76 million particles, we have to solve the unsteady, three-dimensional Navier–Stokes and continuity equations in a small domain surrounding each particle, at each time step of computing the carrier flow. If we assume that computing the flow around each particle requires only 10^3 CPU S (i.e., many orders of magnitude smaller than the currently required CPU time; Bagchi and Balachandar, 2003) on the fastest computer available, then we would need 76×10^9 sec/time step or 2443 CPU years/time step for a single processor. However, if we use 1024 parallel processors, this time can be reduced to 2.4 CPU years/time step; if we use 10, 000 processors, we can reduce this time further to 3 CPU months/time step, and at least 10^4 time steps are needed for a typical DNS run. Thus, it is evident that at present it is not possible to perform DNS of a turbulent flow laden with a large number of dispersed small particles while simultaneously resolving the flow around each

particle. This fact necessitates treating the dispersed particles in DNS as "*points*" whose motion and trajectories are governed by the appropriate differential equations. There are currently two approaches (namely, the Lagrangian–Eulerian or trajectory and the Eulerian–Eulerian or two-fluid) employed in DNS of particle-laden turbulent flows. These two approaches will be described in the two examples that are presented later in this chapter.

13.2.3.2 Classification Map of Particle-Laden Turbulent Flows

The classification map in Figure 13.20 is a slightly modified version of the original map proposed by Elghobashi (1994). The quantities appearing on the dimensionless coordinates are defined below:

- α volume fraction of particles$(=NV_p/V)$
- N total number of particles in the flow
- V_p volume of a single particle
- V total volume occupied by particles and fluid
- d diameter of particle
- τ_p particle response time $(=\rho_p d^2/(18\rho_f \nu)$ for Stokes flow
- τ_κ Kolmogorov time scale $(=(\nu/\varepsilon)^{1/2})$

In the above definitions, ρ is the material density, ν the kinematic viscosity of the fluid, and ε the dissipation rate of turbulence kinetic energy and the subscripts p and f denote, respectively, the particle and carrier fluid. For very low values of $\alpha(\leq 10^{-6})$, the particles have negligible effect on turbulence, and the interaction between the particles and turbulence is termed as *one-way coupling*. This means that particle dispersion, in this regime, depends on the state of turbulence but owing to the negligible concentration of the particles, the momentum exchange between the particles and the turbulence has an insignificant effect on the flow. In the second regime, $10^{-6} < \alpha \leq 10^{-3}$, the momentum exchange between the particles and turbulence is large enough to alter the turbulence structure. This interaction is called *two-way coupling*. Now, in this regime and for a given value of α, there are two zones (A and B), depending on the ratio τ_p/τ_κ where the transition from A to B occurs at about $\tau_p/\tau_\kappa = 10$. In zone A, the particle Reynolds number, R_p is ≤ 1, but within the range $0.01 \leq (\tau_p/\tau_\kappa) \leq 10$ and for a fixed α, the effects of the particles

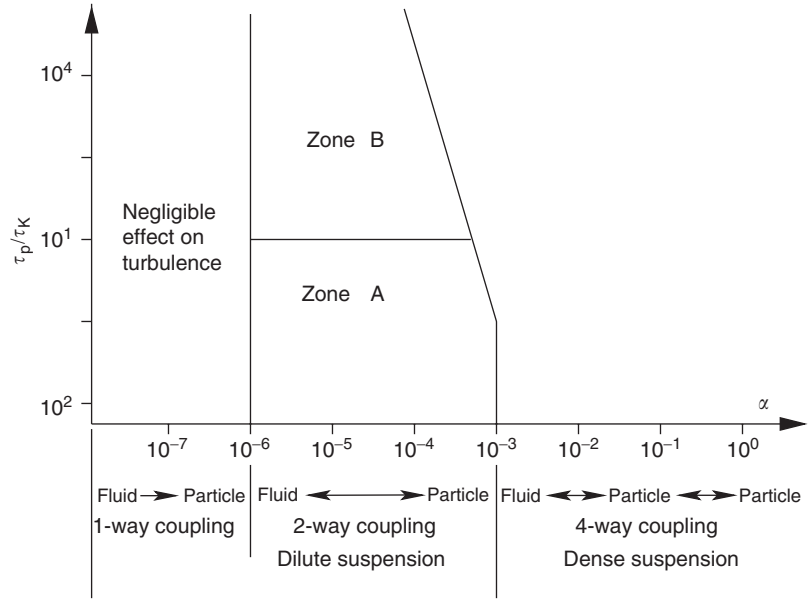

FIGURE 13.20 Classification map of dispersed two-phase flows.

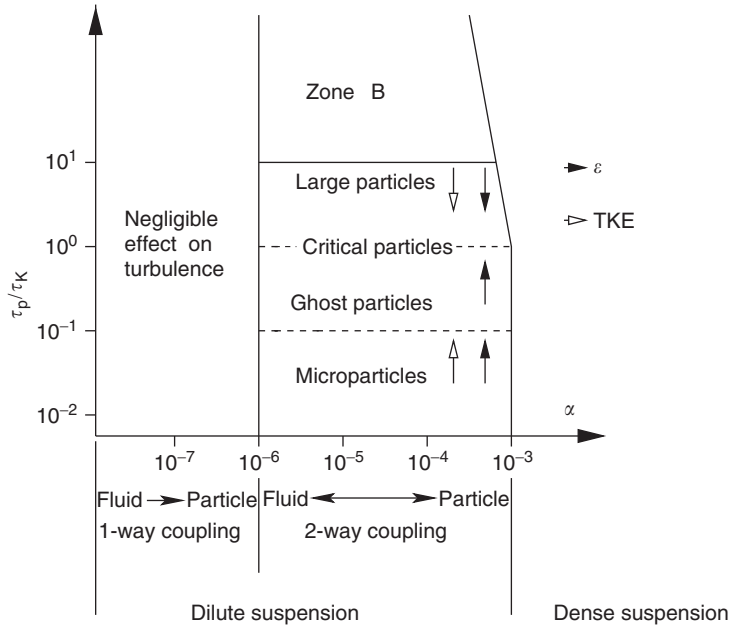

FIGURE 13.21 Classification map of dispersed two-phase flows details of Zone A.

on the turbulence vary significantly as function of (τ_p/τ_κ) as shown in Figure 13.21 and will be discussed later. In zone B, as τ_p increases (e.g., with an increase in the particle diameter) for the same α, the particle Reynolds number increases, and at values of $R_p \geq 400$, vortex shedding takes place resulting in an enhanced production of turbulence energy. In the third regime, due to an increase in particle loading , $\alpha > 10^{-3}$, flows are referred to as dense suspensions. Here, in addition to the two-way coupling between the particles and turbulence, particle–particle collision takes place, hence the term *four-way coupling*. As α approaches 1, we obtain a granular flow in which there is no fluid, and, therefore, the granular flow is beyond the scope of this chapter.

The line separating the two- and four-way coupling regimes is inclined to indicate the tendency of particle–particle collision to take place at higher values of τ_p/τ_κ, thus transforming the two- to four-way coupling regime even for $\alpha < 10^{-3}$.

The dispersion of particles (and their preferential accumulation) in turbulent flows with one-way coupling is reasonably understood, at least in unconfined homogeneous flows (Elghobashi and Truesdell, 1992, 1993; Ahmed and Elghobashi, 2001; Ferrante and Elghobashi, 2003). On the other hand, flows in the two- or four-way coupling regimes are still a challenge and require more studies to improve their understanding.

We restrict the present discussion to isothermal incompressible fluids without phase changes (e.g., vaporization) or chemical reaction. Also, the effects of particle–particle or particle–wall collisions are not considered here.

In the following subsections we will present two examples of DNS of particle- and bubble-laden turbulent flows and discuss the physical mechanisms of two-way coupling. These flows are: (1) isotropic turbulence laden with solid particles and (2) isotropic turbulence laden with bubbles.

13.2.4 The Physical Mechanisms of Two-Way Coupling in Particle-Laden Isotropic Turbulence

Since isotropic turbulence is the simplest homogeneous turbulent flow it has been the subject of a number of earlier DNS studies on the effects of particles on isotropic turbulence (Elghobashi and Truesdell,

1993; Squires and Eaton, 1990; Boivin et al., 1998; Sundaram and Collins, 1999; Druzhinin and Elghobashi, 1999b; Ferrante and Elghobashi, 2003).

The discussion in the following subsections is a condensed version of our paper (Ferrante and Elghobashi, 2003), whose objective was to analyze our DNS results for a detailed explanation of the main physical mechanisms responsible for the modification of isotropic turbulence by dispersed solid particles. The present study, in comparison with the previous DNS studies, has been performed with higher resolution ($Re_\lambda = 75$) and considerably larger number (80 million) of particles. One of the interesting results to be discussed is that in zero gravity, dispersed particles with $\tau_p/\tau_\kappa = 0.25$ (denoted here as '*Ghost particles*') modify the spectra of the turbulence kinetic energy and its dissipation rate in such a way that the decay rate of the turbulence energy is nearly identical to that of particle-free turbulence, and, thus, the two-way coupling effects of these ghost particles would not be detected, for example, in microgravity environment, by examining only the temporal behavior of the turbulence energy of the carrier flow either numerically or experimentally.

13.2.4.1 Mathematical Description

In this study we use the Eulerian–Lagrangian (or trajectory) approach, where the instantaneous, three-dimensional velocity and pressure fields of the fluid motion are computed on a fixed (Eulerian) mesh; whereas, the instantaneous trajectories of the dispersed particles are obtained by computing the instantaneous positions of the particles.

13.2.4.2 Governing Equations

The governing dimensionless equations for a particle-laden incompressible isotropic turbulent flow are the Navier–Stokes equations,

$$\frac{\partial u_j}{\partial t} + \frac{\partial (u_j u_k)}{\partial x_k} = -\frac{\partial p}{\partial x_j} + \nu \frac{\partial^2 u_j}{\partial x_k \partial x_k} - f_j \tag{13.9}$$

and the continuity equation,

$$\frac{\partial u_j}{\partial x_j} = 0 \tag{13.10}$$

where $j = 1,2,3$ for the three coordinate directions x_1, x_2, and x_3, respectively, and ν the dimensionless kinematic viscosity. In Eqs. (13.9) and (13.10) we neglect the volume occupied by the individual particles (in comparison with the volume of the carrier fluid) and thus they are treated as points moving in the flow according to Eq. (13.12). $-f_j$ is the net force per unit mass of fluid exerted in the x_j direction by M particles within the integration control volume and is computed from

$$f_j = \frac{1}{M_f} \sum_{\rho=1}^{M} f_{jp} \tag{13.11}$$

where f_{jp} is the drag force acting on particle p in the x_j direction and M_f the mass of fluid within the integration control volume.

The particle equation of motion (Maxey and Riley, 1983) can be written for large ratio (ρ_p/ρ) of the particle density to fluid density as

$$m_p \frac{dv_j}{dt_p} = m_p \frac{(u_j - v_j)}{\tau_p} + (m_p - m_f) g_j \tag{13.12}$$

where m_p is the mass of the particle, m_f the mass of fluid displaced by the particle volume, d/dt_p the time derivative following the moving particle, v_j the particle instantaneous velocity, u_j the instantaneous fluid velocity at the particle location, and g_j is the gravitational acceleration. The numerical solution method is described in detail in Ferrante and Elghobashi (2003) and, thus, will not be discussed here.

13.2.4.3 Results

13.2.4.3.1 Turbulence and Particles Parameters

We studied six cases to understand how particles with different inertia, τ_p,modify the decay rate of isotropic turbulence in both zero- and finite-gravity conditions. The flow parameters are listed in Table 13.3 and the particle properties in Table 13.4 Case A represents the particle-free flow, whereas cases B–E represent particle-laden flows with different inertia particles in zero gravity, and case F represents the particle-laden flow in finite gravity. It is important to note that all the five cases (B–F) of particle-laden turbulence have the same volume fraction of particles, $\alpha = 10^{-3}$, and the same mass loading ratio α_m=1.0 (for ρ_p/ρ=1000) and, thus, the differences between the resulting modifications of turbulence in these cases are only due to the different values of τ_p/τ_κ. We changed the particle diameter for each case to obtain a different ratio τ_p/τ_κ of the particle response time to the Kolmogorov time-scale at the injection time, for example., τ_p/τ_κ=0.1 in case B and τ_p/τ_κ=5.0 in case E. The effects of gravity are studied in case F where τ_p/τ_κ=0.25 (as in case C) and v_t/u_0^*=0.25, where v_t is the terminal velocity (v_t=$g\tau_p$) of the particle and u^*_0 is the rms velocity of the surrounding fluid at the injection time, and gravity is in the negative x_3 direction.

13.2.4.3.2 Turbulence Modification by Particles

In the following two subsections we describe briefly the temporal evolution of the turbulence kinetic energy (TKE) and its spectra, $E(k)$, for all the six cases (A–F). Then we discuss in detail the physical mechanisms of the two-way interaction in four of these cases. The details of the other cases are given by Ferrante and Elghobashi (2003).

13.2.4.3.2.1 Time evolution of turbulence kinetic energy. Figure 13.22 shows the temporal evolution of TKE normalized by its initial value, $E(t)/E_0$, for the zero gravity cases (A–E). The microparticles (case B) with $\tau_p/\tau_\kappa < 0.25$ initially ($1 < t \leq 2.1$) reduce the decay rate of TKE, resulting in TKE being larger than that of case A at all times, whereas particles with higher inertia (critical particles, case D, and large particles, case E), $\tau_p/\tau_\kappa < 0.25$, initially enhance the TKE decay rate considerably, resulting in TKE being smaller than that of case A at all times. Figure 13.22 also shows that particles with $\tau_p/\tau_\kappa = 0.25$ (case C) keep TKE nearly identical to that of case A at all times, with a percentage difference smaller than 0.6%. Thus we denote the particles in case C as ghost particles, since their effects on the turbulence cannot be detected by the temporal behavior of TKE, $E(t)$. However, as we will discuss later (Figure 13.23) these ghost particles do modify the spectrum of $E(\kappa)$ TKE. Figure 13.22 shows that at time $t = 5$, in comparison with TKE in case A, TKE in case B is larger by more than 5%; in case C is nearly identical; in case D is smaller by about 13%; in case E is smaller by about 30%.

TABLE 13.3 Flow Parameters (Dimensionless) at Initial Time ($t = 0$), Injection Time ($t = 1$), and for Case A at Time $t = 5$

t	u_o	ε	l	λ	η	Re_l	Re_λ	l/η	τ_k	τ_t
0.0	0.0503	7.4×10^{-4}	0.0684	0.0345	0.00202	150	75	33.8	0.177	1.36
1.0	0.0436	9.8×10^{-4}	0.0685	0.0259	0.00188	129	49	36.4	0.154	1.57
5.0	0.0233	2.0×10^{-4}	0.0891	0.0305	0.00280	90	31	31.9	0.338	3.83

TABLE 13.4 Particle Properties (Dimensionless) at Injection Time ($t = 1$) with α=10^{-3} and $\alpha_m = 1.0$ (for $\rho_p/\rho = 1000$)

Case	τ_p	τ_p/τ_l	τ_p/τ_k	d	d/l	d/η	d (μm)	M_c	M_r/M_c	$Re_{p,\max}$	v_t/u_0^*
A	–	–	–	–	–	–	–	–	0	–	–
B	0.0154	0.0098	0.1	0.80×10^{-4}	0.00117	0.043	30	80×10^6	46.7	0.11	0.0
C	0.0385	0.0245	0.25	1.26×10^{-4}	0.00185	0.067	47	80×10^6	11.8	0.31	0.0
D	0.1540	0.0979	1.0	2.53×10^{-4}	0.00369	0.134	94	80×10^6	1.5	1.34	0.0
E	0.7700	0.4895	5.0	5.66×10^{-4}	0.00825	0.300	211	10.6×10^6	1.0	5.33	0.0
F	0.0385	0.0245	0.25	1.26×10^{-4}	0.00185	0.067	47	80×10^6	11.8	0.32	0.25

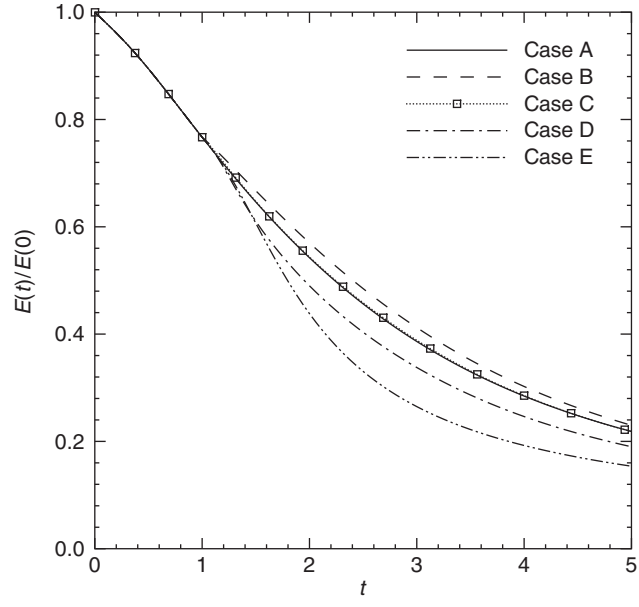

FIGURE 13.22 Time development of the turbulence kinetic energy.

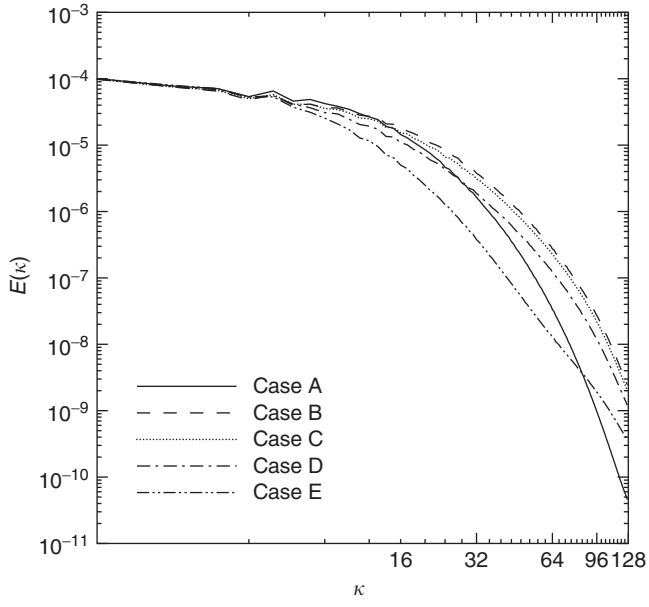

FIGURE 13.23 Three-dimensional spatial spectrum of energy $E(\kappa)$ at $t = 5.0$.

Figure 13.24 displays the effects of gravity on the time evolution of TKE by comparing cases C and F. The figure shows that in the presence of gravity (case F), particles reduce the decay rate of TKE as compared with both case C, the flow laden with ghost particles, and case A, the particle-free flow. The basic physical mechanisms that are responsible for the above-described modifications of $E(t)$ by the dispersed particles for cases B–F are discussed later in this section.

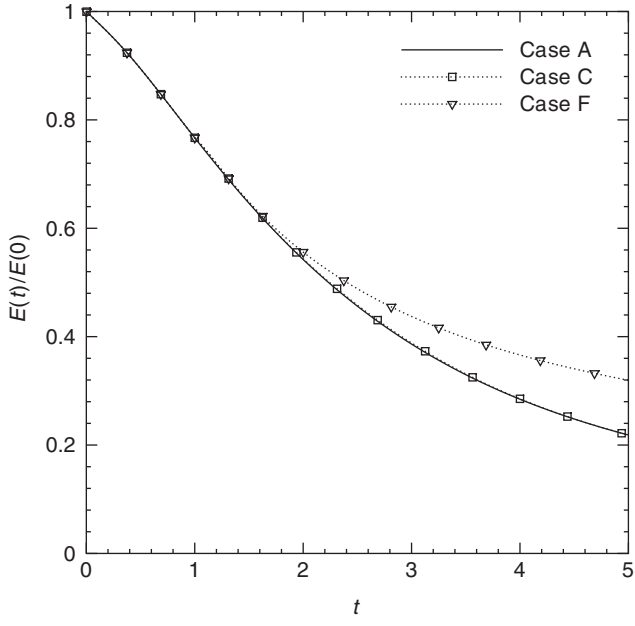

FIGURE 13.24 Time development of the turbulence kinetic energy normalized by its initial value showing the effect of gravity in case F.

13.2.4.3.2.2 Energy spectrum. Figure 13.23 shows the three-dimensional energy spectra $E(\kappa)$ for the five cases A-E at time $t = 5$. Microparticles (case B) increase $E(\kappa)$ relative to case A at wavenumbers $\kappa \geq 12$, and reduce $E(\kappa)$ relative to case A for $\kappa < 12$, such that $\int E(\kappa)\, d\kappa \equiv$ TKE in case B is larger than that in case A, as shown in Figure 13.22. For ghost particles (case C), although E(t) is nearly identical to that of case A at all times (Figure 13.22) it is clear in Figure 13.23, that the energy spectrum in case C differs from that in case A, but in such a unique way that its integral, TKE, is nearly identical to that in case A. Figure 13.23 shows that ghost particles reduce E(κ) relative to that of case A for $\kappa < 15$, and increase it above that of case A for $\kappa \geq 15$. Critical particles (case D) increase E(κ) above that of case A for $\kappa \geq 27$, and reduce it for smaller wavenumbers. In this case (case D) the modulation of E(κ) is such that its integral, TKE, is smaller than that in case A (Figure 13.22). Large particles (case E) contribute to a faster decay of TKE by reducing the energy content at almost all wavenumbers, except for $\kappa > 87$, where a slight increase of $E(\kappa)$ occurs.

In order to understand how the particles, $E(\kappa)$, modify we write the evolution equation of the three-dimensional energy spectrum:

$$\frac{\partial E(\kappa)}{\partial t} = T(\kappa) - \varepsilon(\kappa) + \Psi_p(\kappa) \tag{13.13}$$

Equation (13.13) states that in particle-laden isotropic turbulent flows, the rate of change of spectral turbulence kinetic energy at wavenumber κ is the net result of the spectral energy-transfer rate $\tau(\kappa)$, the spectral viscous dissipation rate $\varepsilon(\kappa)$, and the spectral two-way coupling (fluid–particle drag interaction) energy rate $\Psi_p(\kappa)$. A discussion on the behavior of $T(\kappa)$, $\varepsilon(\kappa)$, and $\Psi_p(\kappa)$ and their effects on $E(\kappa)$ is provided in the following section.

13.2.4.3.3 Mechanisms of Modification of Isotropic Turbulence by the Particles

In this section, we discuss the mechanisms responsible for the modification of decaying isotropic turbulence by the particles for four of the cases listed in Table 13.4: microparticles ($\tau_p/\tau_\kappa \ll 1$ in zero gravity; case B), critical particles with $\tau_p/\tau_\kappa \approx 1$ (case D), and ghost particles with $\tau_p/\tau_\kappa \approx 0.25$ (case C).

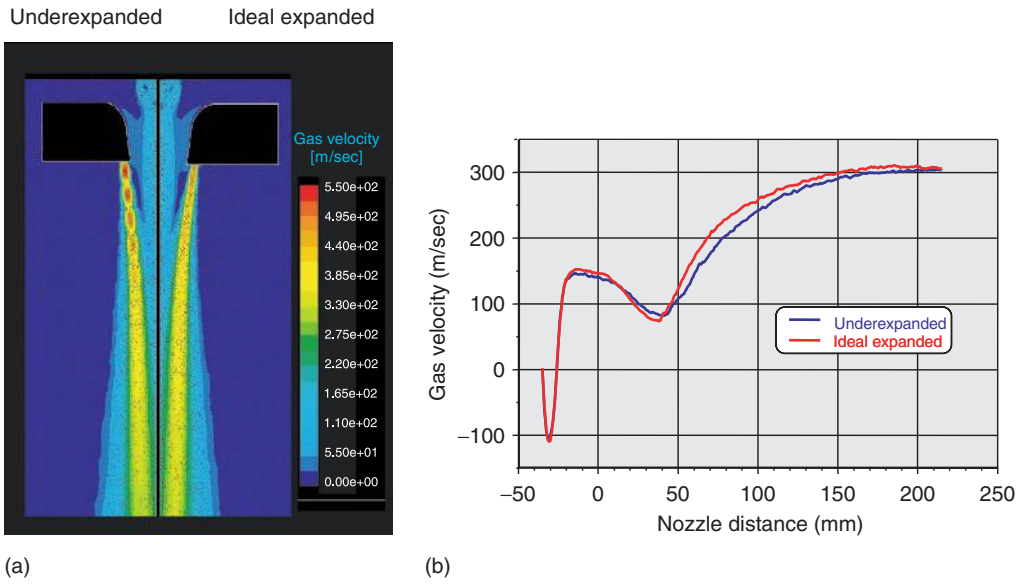

FIGURE 8.9 Gas flow field simulation for an external mixing (free-fall) atomizer: (a) gas velocity contours: underexpanded exit condition (left panel), and ideal expanded exit condition (right), (b) gas velocity on center line, comparison of under- and ideally expanded exit conditions. (From Heck, U., Ph.D. thesis, Universität Bremen, 1998. With permission.)

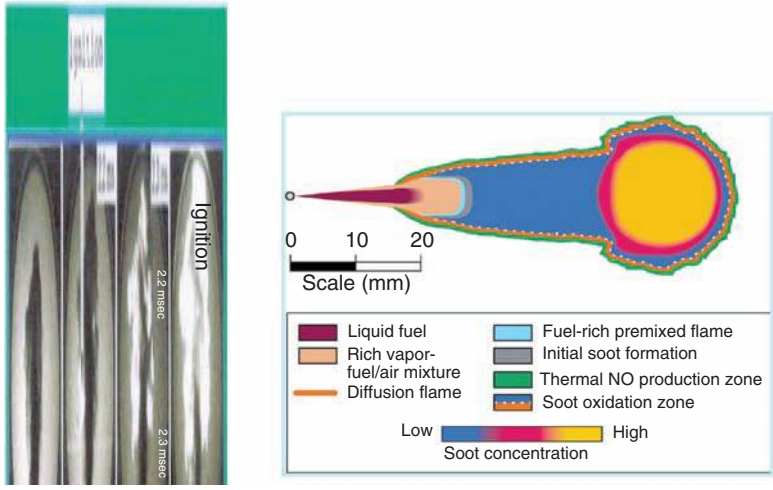

FIGURE 8.52 Diesel spray flame: photo of injection and ignition, principal stationary flame structure. (From Tao, F., Ph.D. thesis, Chalmers University of Technology, Sweden, 2003.)

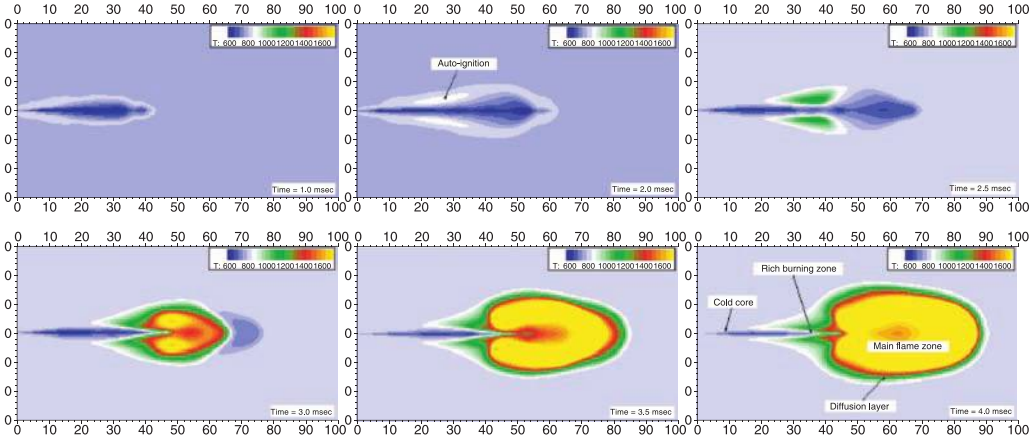

FIGURE 8.54 Simulation of a DI-diesel spray flame and temperature contours. (From Tao, F., Ph.D. thesis, Chalmers University of Technology, Sweden, 2003. With permission.)

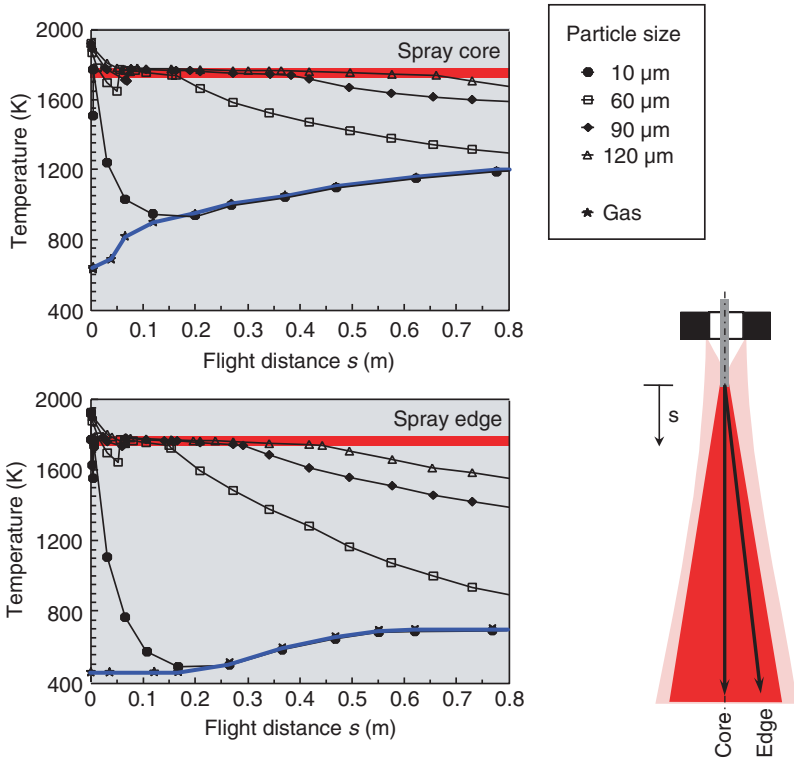

FIGURE 8.63 Modeling result for gas and particle temperature behavior on spray center line and edge in spray forming of steel. (From Bergmann et al., *Proceedings of the 2nd International Conference on Multiphase Flow*, Kyoto, Japan, April 3–7, 1995, Vol.1, pp. SP1–SP8. With permission.)

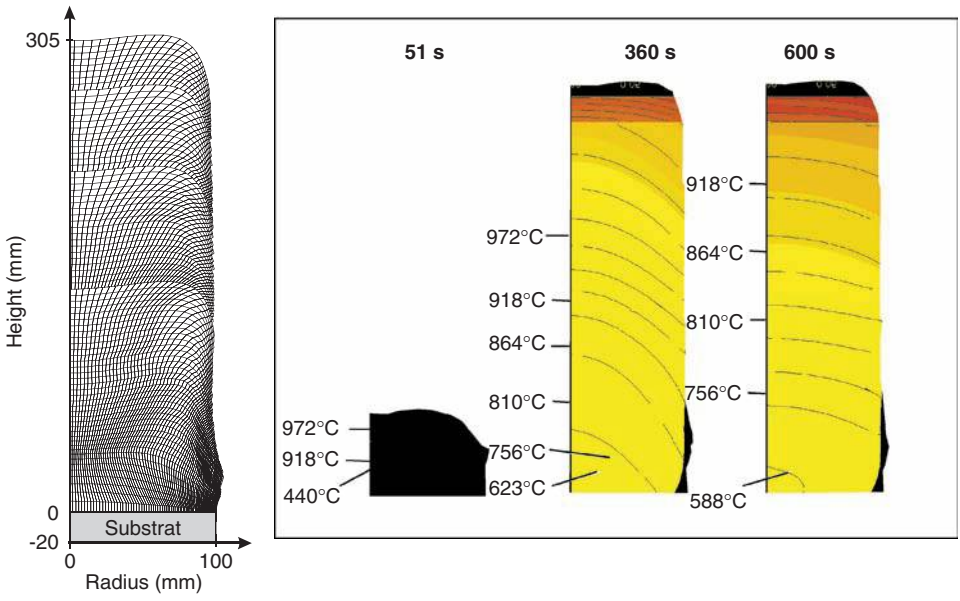

FIGURE 8.65 Temperature and solid content distribution during spray forming of a copper billet. (From Meyer et al., *Int. J. Thermal Sci.*, 42, 2003. With permission.)

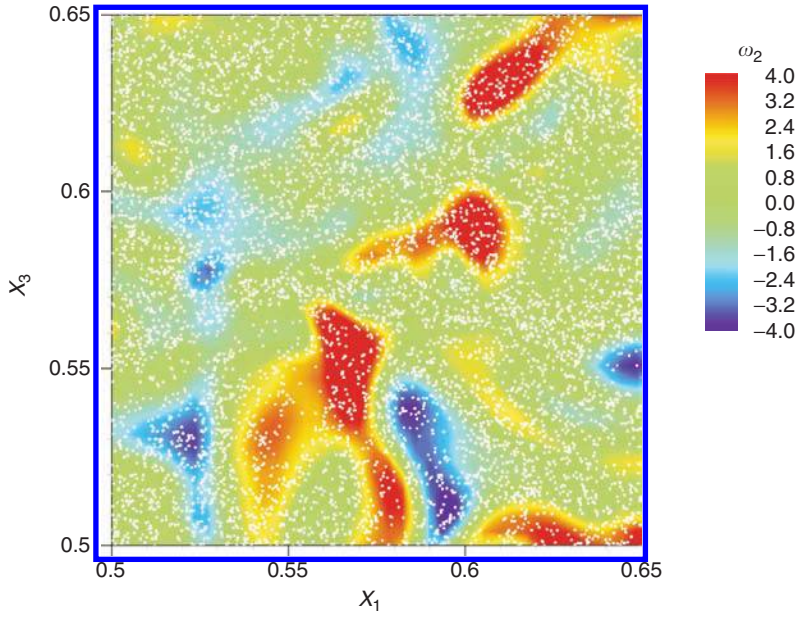

FIGURE 13.25 Case B: microparticles (white dots) superimposed on ω_2 (color contour) at $x_2 = 0.5$ and $t = 5.0$.

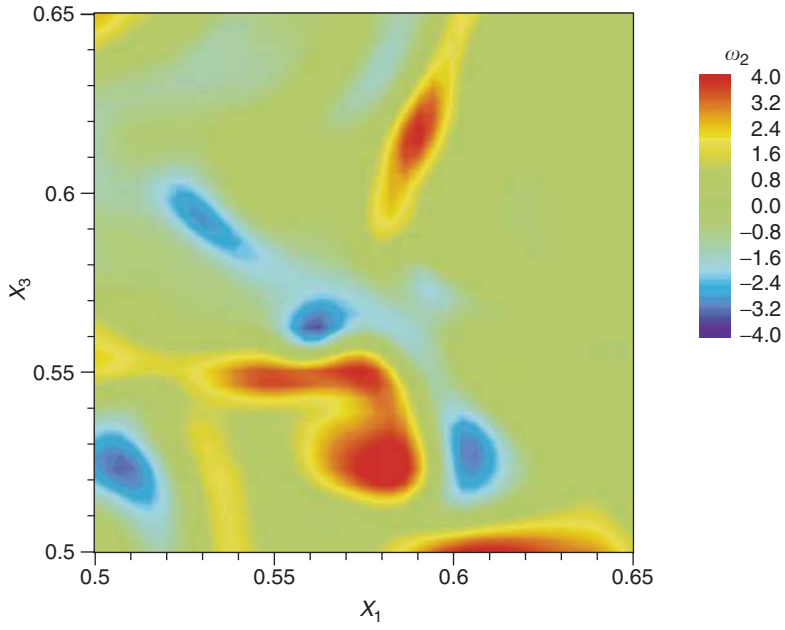

FIGURE 13.26 Case A: ω_2 (color contour) at $x_2 = 0.5$ and $t = 5.0$.

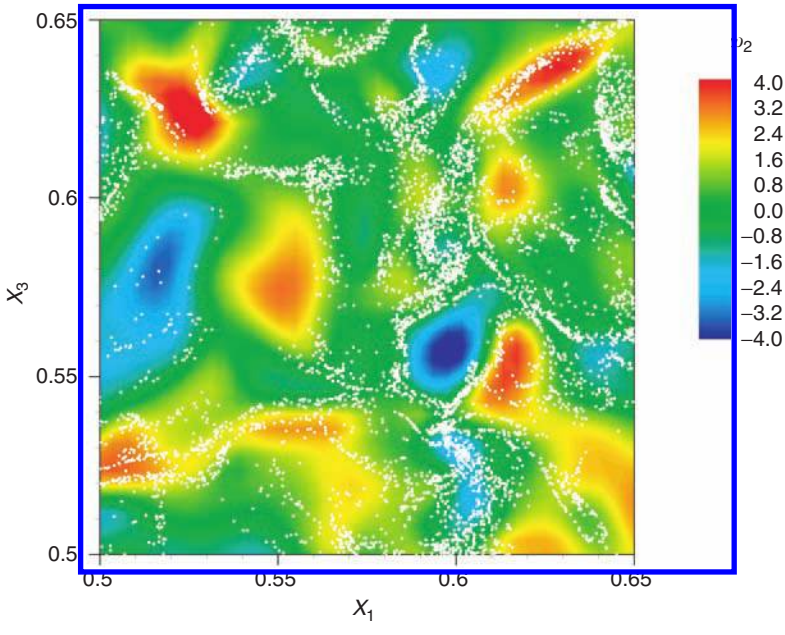

FIGURE 13.36 Case D: critical particles (white dots) superimposed on ω_2 (color contour) at $x_2 = 0.5$ and $t = 5.0$.

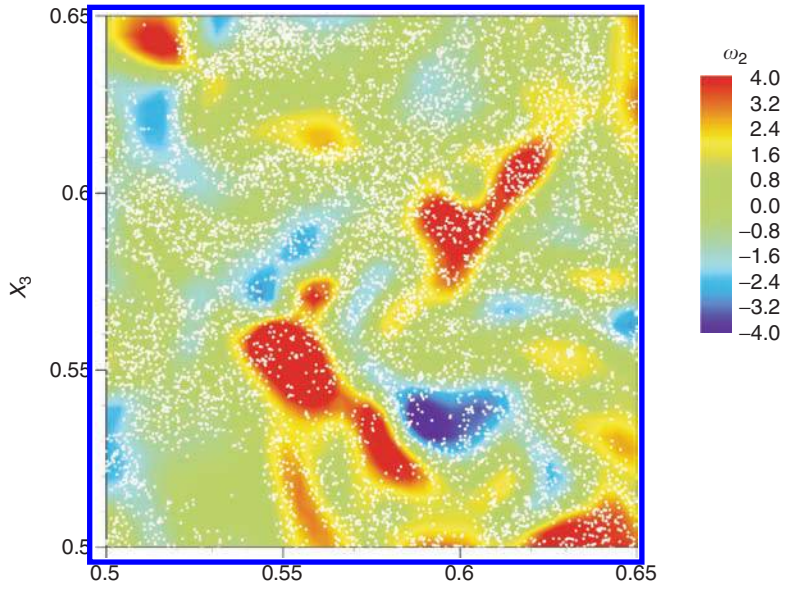

FIGURE 13.37 Case C: "ghost" particles in zero gravity (white dots) superimposed on ω_2 (color contour) at $x_2 = 0.5$ and $t = 5.0$.

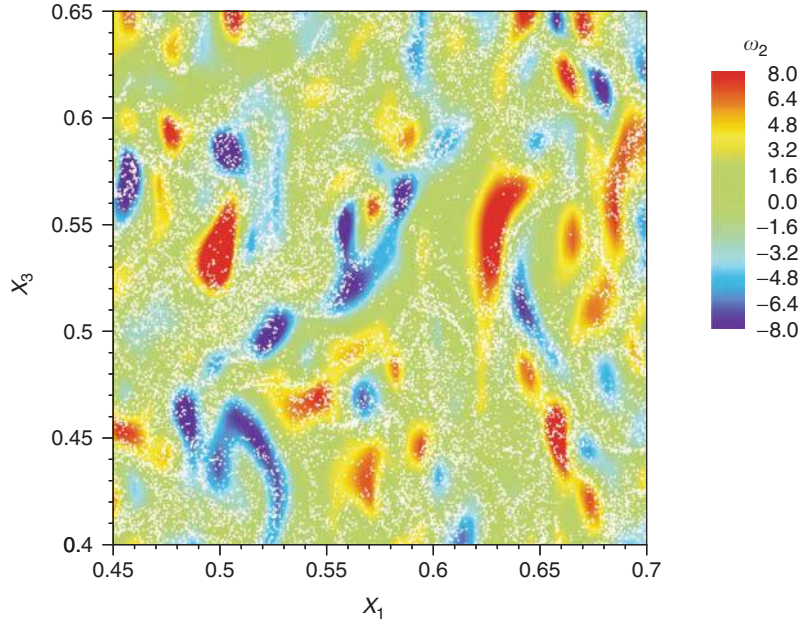

FIGURE 13.39 Case F: "ghost" particles in finite gravity (white dots) superimposed on ω_2 (color contour) at $x_2 = 0.5$ and $t = 5.0$.

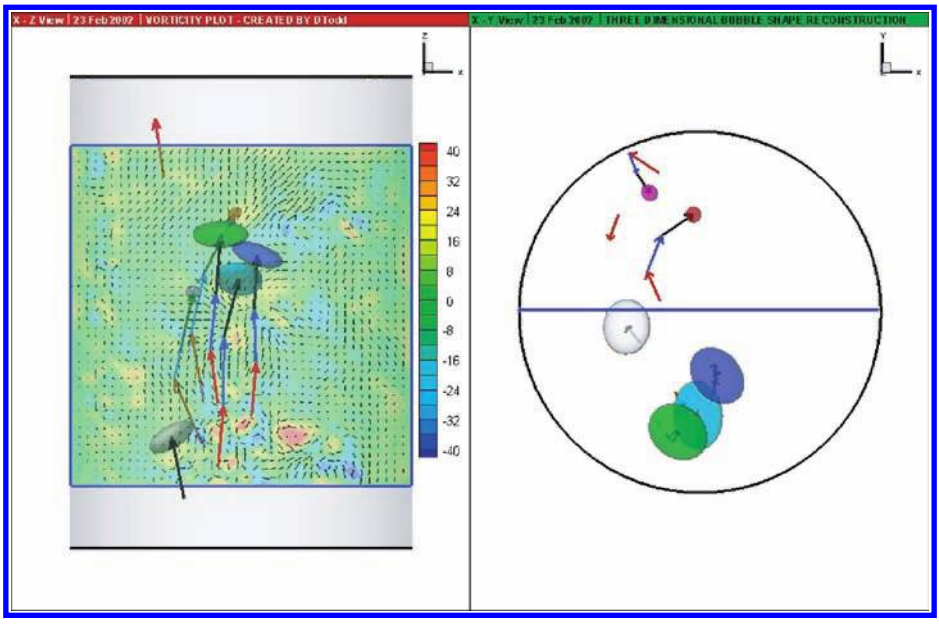

(a) time = t1

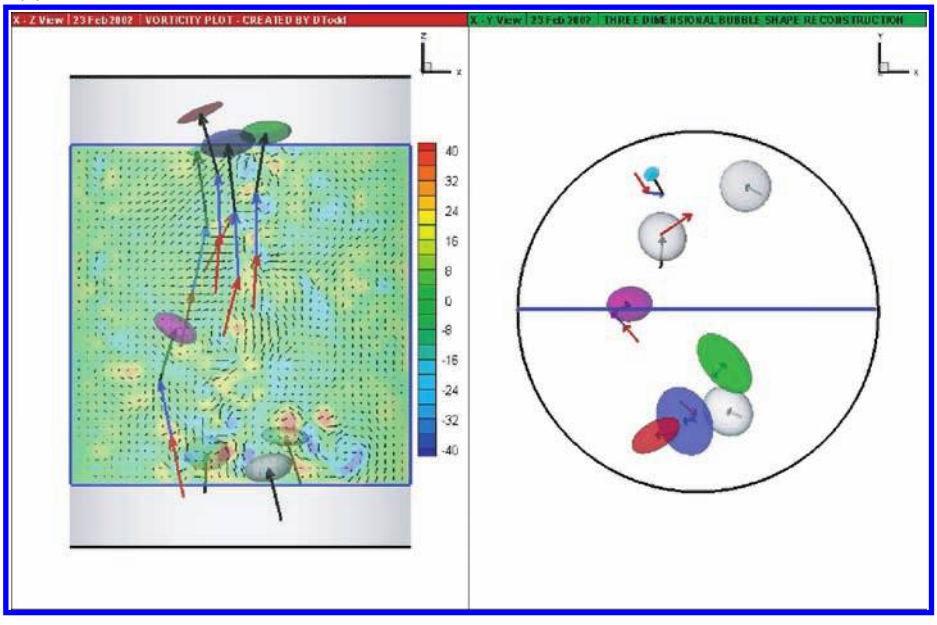

(b) time= t1 + 33.33 ms

FIGURE 14.85 Snapshots of interactions of the bubbles with the flow at two instants.

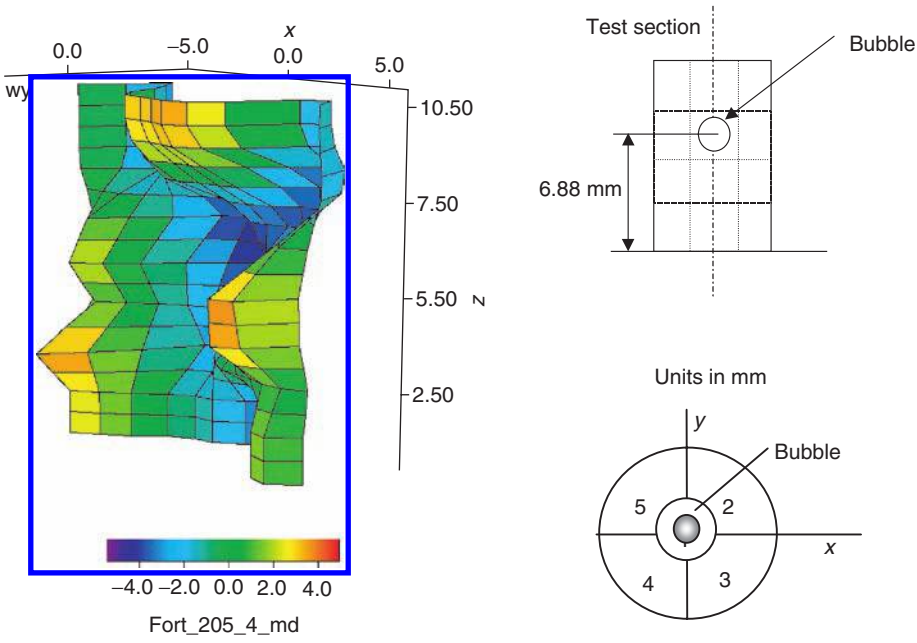

FIGURE 14.88 Surface plot of fluid vorticity component ω_y on X–Z plane, position $y = 0$, at $t = 33.3$ msec after the bubble has entered the viewing volume.

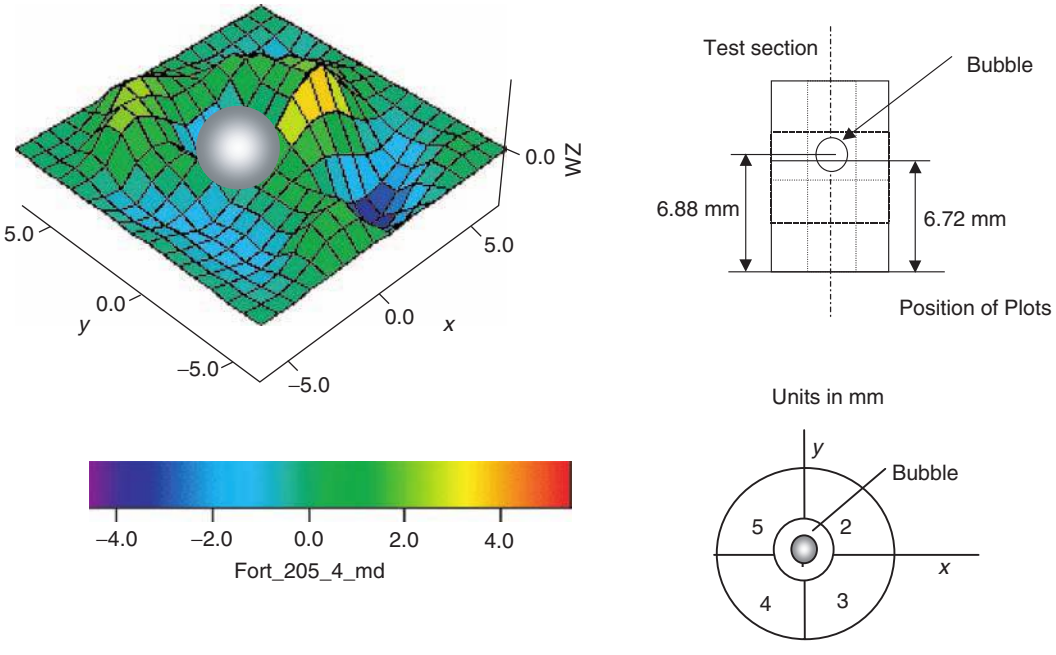

FIGURE 14.89 Surface plot of liquid vorticity component ω_z on X–Y plane, position $z = 6.72$, at $t = 33.3$ msec after the bubble has entered the viewing volume.

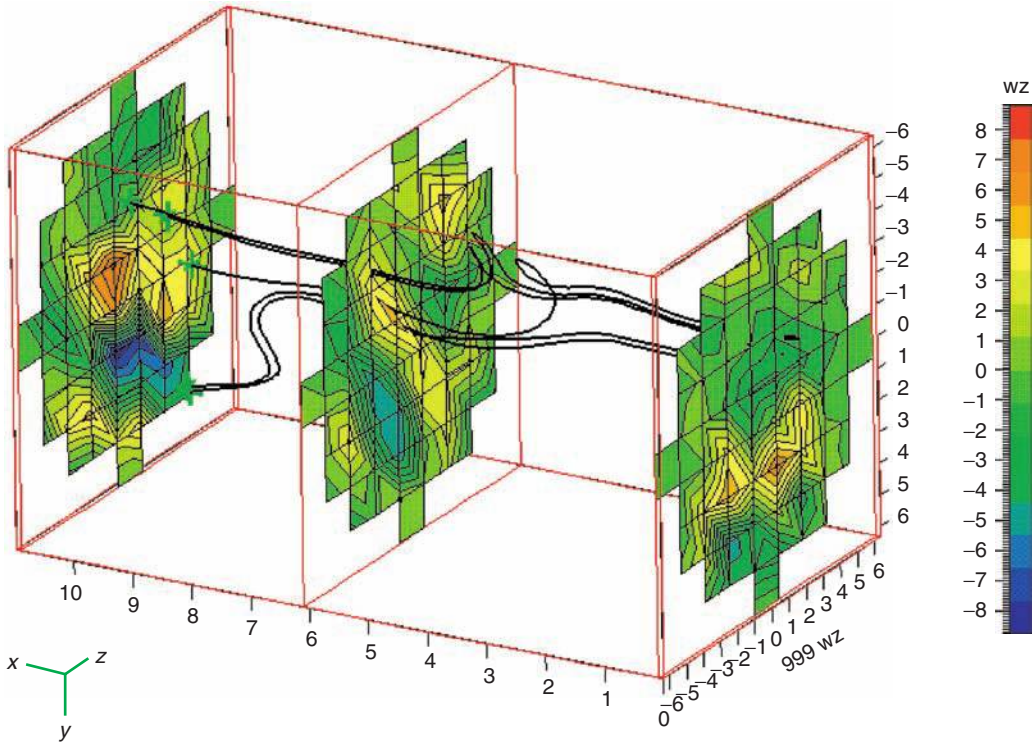

FIGURE 14.90 ω_z vorticity contours on Z-plane slices 16.6 msec after the bubble has departed from the viewing volume.

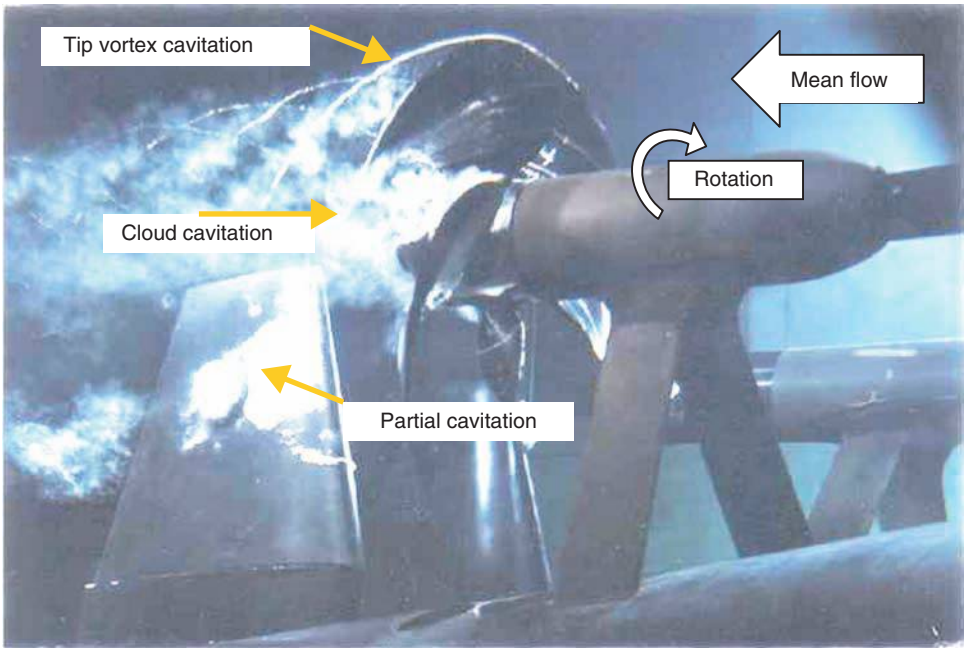

FIGURE 12.11 Tip vortex cavitation, cloud cavitation, and partial attached cavitation on a model of a marine propeller. (Courtesy of Dr. Y.T. Shen, Naval Surface Warfare Center-Carderock Division.)

13.2.4.3.3.1 Microparticles ($\tau_p/\tau_\kappa \ll 1$). Microparticles (case B) behave almost like flow tracers because their response time, τ_p, is much lesser than the Kolmogorov time scale, τ_κ, but since their material density, ρ_p, is much higher than that of the carrier fluid, ρ, they cause the fluid to behave like a 'heavy gas' (Saffman, 1962).

In order to explain the physical mechanism of the two-way coupling, we write the time evolution equation of TKE, which is obtained by multiplying Eq. (13.1) by u_j and ensemble averaging,

$$\frac{dE(t)}{dt} = -\varepsilon(t) + \Psi_p(t) \tag{13.14}$$

where $\varepsilon(t)$ is the viscous dissipation rate of $E(t)$ and $\Psi_p(t)$ the energy rate of change due to the particles drag force (Ahmed and Elghobashi, 2000):

$$\Psi_p(t) = \alpha_m \langle u_j(v_j - u_j)/\tau_p \rangle \tag{13.15}$$

and α_m is the mass loading ratio ($\alpha_m = \alpha\rho_p/\rho$).

Now we show how the microparticles contribute to both $\Psi_p(t)$ and $\varepsilon(t)$. Because of their fast response to the turbulent velocity fluctuations of the carrier flow, the microparticles are not ejected from the vortical structures of their initial surrounding fluid. Figure 13.25 shows contours of the instantaneous vorticity component ω_2 (in a small zone whose area is 2.25×10^{-2} of the vertical midplane, x_1x_3, of our computational domain) and particles locations at $t = 5$ for case B. It is seen that the solid particles are not ejected from the vortex cores, and that the contours of maximum positive and negative values of vorticity occupy a larger fraction (~ 18%) of that zone than in case A (~ 9%) in Figure 13.26. Furthermore, the inertia of the microparticles causes their velocity autocorrelation to be larger than that of their surrounding fluid $\langle v_j v_j \rangle > \langle u_j u_j \rangle$, Figure 13.27), indicating, as expected, that the microparticles retain their kinetic energy longer than the surrounding fluid. Since the microparticles trajectories are almost aligned with fluid points trajectories, and their kinetic energy is larger than that of their surrounding fluid, then the correlation $\langle u_j v_j \rangle$ remains higher than the fluid velocity autocorrelation $\langle u_j u_j \rangle$, (Figure 13.27). Consequently, Ψ_p provides a positive contribution to $dE(t)/dt$ in Eq. (13.14) as shown in Figure 13.28, and hence Ψ_p is responsible for the reduction of the decay rate of TKE relative to case A. On the other hand,

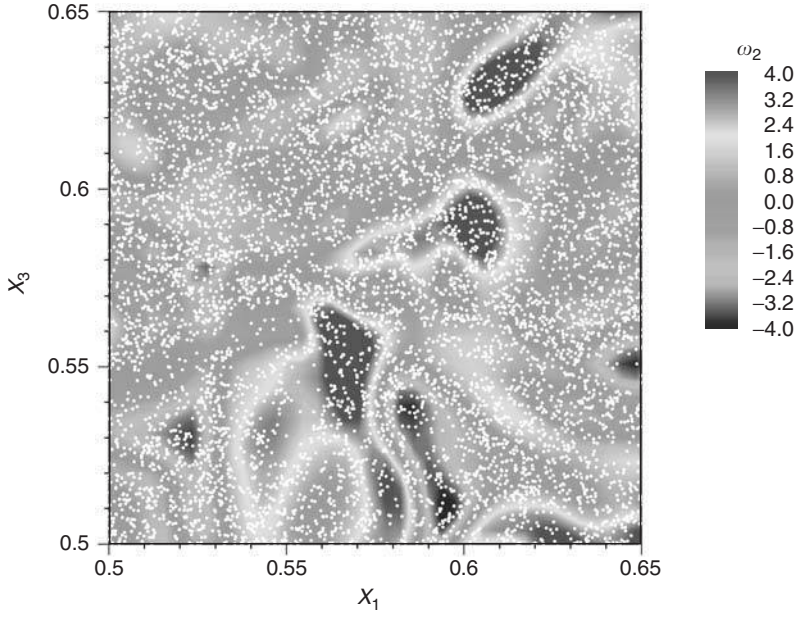

FIGURE 13.25 (Color insert follows page 13-40) Case B: microparticles (white dots) superimposed on ω_2 (color contour) at $x_2 = 0.5$ and $t = 5.0$.

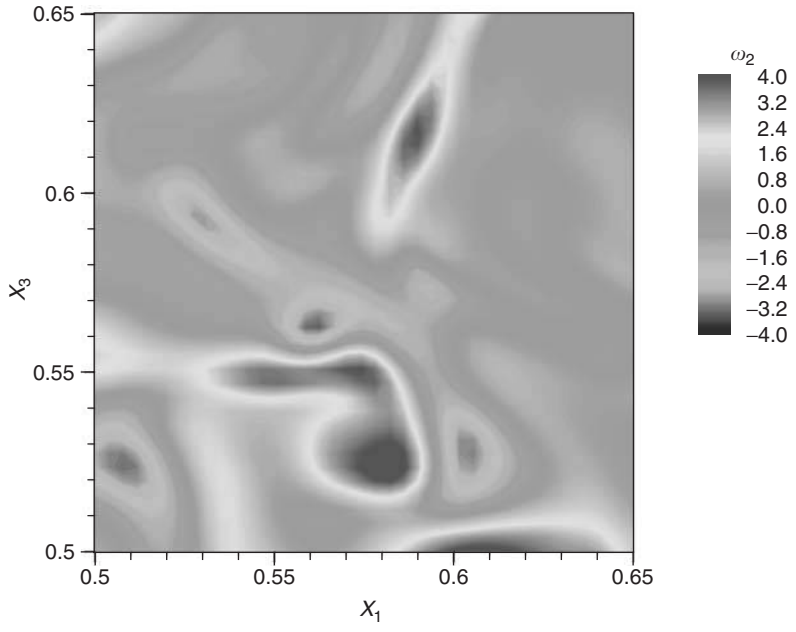

FIGURE 13.26 (Color insert follows page 13-40) Case A: ω_2 (color contour) at $x_2 = 0.5$ and $t = 5.0$.

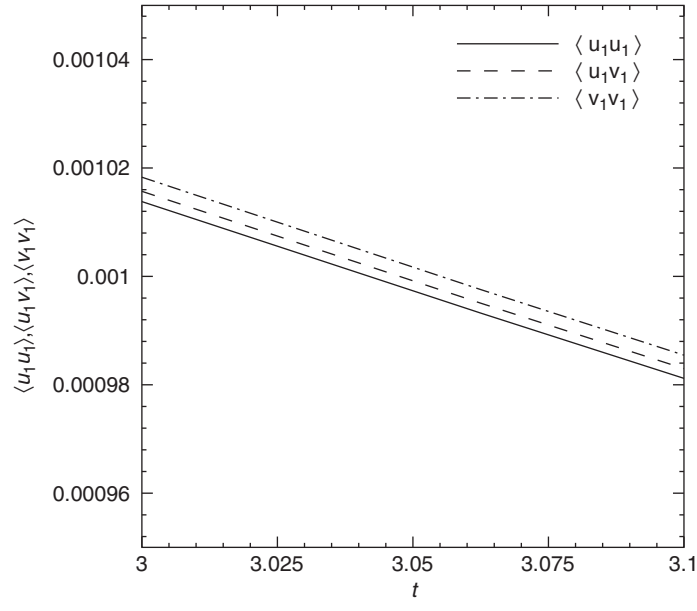

FIGURE 13.27 Case B: time development of fluid velocity autocorrelation $\langle u_1u_1\rangle$, correlation $\langle u_1v_1\rangle$ between the fluid velocity and particles velocity, and particle velocity autocorrelation $\langle v_1v_1\rangle$.

the microparticles increase the viscous dissipation rate, $\varepsilon(t)$, relative to that of case A (Figure 13.28). The reason is that microparticles remain in their initially surrounding vortices (Figure 13.25), and the correlation $\langle u_jv_j\rangle$ remains larger than $\langle u_ju_j\rangle$, as discussed above, thus causing the vortical structures to retain their initial vorticity and strain rates longer than the particle-free flow (case A). Table 13.5 shows that at time $t = 5$, the enstrophy in case B is about 86% larger than that in case A. Table 13.5 also shows that the

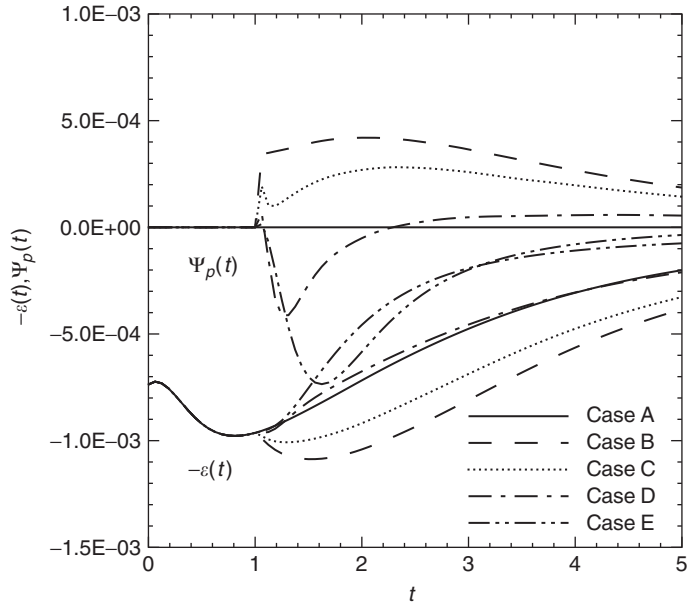

FIGURE 13.28 Time development of the negative of the energy dissipation rate $-\varepsilon(t)$ and the fluid–particle drag interaction energy rate $\Psi_p(t)$.

TABLE 13.5 Mean Values of Enstrophy and Strain Rate at Time $t = 5$

CASE	$\langle \omega^2 \rangle$	$\langle s_{ij} s_{ij} \rangle$
A–no particles	8.37	4.05
B–microparticles	15.6	7.26
C–ghost particles in zero gravity	13.1	6.20
D–critical particles	8.61	4.05
E–Large particles	3.13	1.52
F–ghost particles in finite gravity	33.6	15.6

mean square of the strain rate

$$S_{ij} = (\partial u_i/\partial x_j + \partial u_j/\partial x_i)/2 \tag{13.16}$$

for case B is nearly 80% higher than that in case A at $t = 5$. The square of the strain rate tensor is related to the three eigenvalues of S_{ij}: the extensional (α), intermediate (β), and compressive (γ) strain rates ($\alpha \geq \beta \geq \gamma$ and $\alpha + \beta + \gamma = 0$ due to incompressibility), through the relation

$$s_{ij} s_{ij} = \alpha^2 + \beta^2 + \gamma^2 \tag{13.17}$$

At time $t = 5$, Figures 13.29–13.31 confirm that the values of α, β, and γ in case B are larger than those in case A (i.e., the probability of finding a large value of α is higher in case B than in case A). The viscous dissipation rate is related to the strain rates via

$$\varepsilon(t) = 2\nu \langle s_{ij} s_{ij} \rangle = 2\nu \langle \alpha^2 + \beta^2 + \gamma^2 \rangle, \tag{13.18}$$

and thus the viscous dissipation rate in case B is larger than that in case A at all times as shown in Figure 13.28. This increase in $\varepsilon(t)$ is mainfested in the reduction of the growth rate of the Kolmogorov time-scale

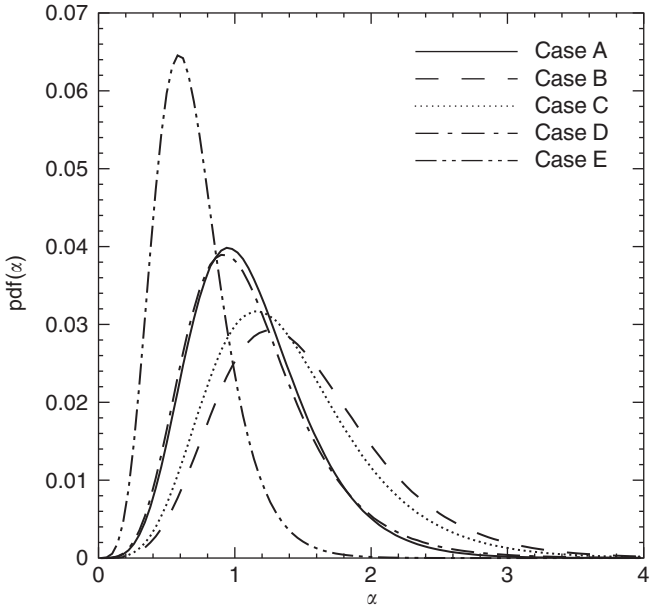

FIGURE 13.29 Probability distribution of the principal extensional strain rate α at $t = 5$.

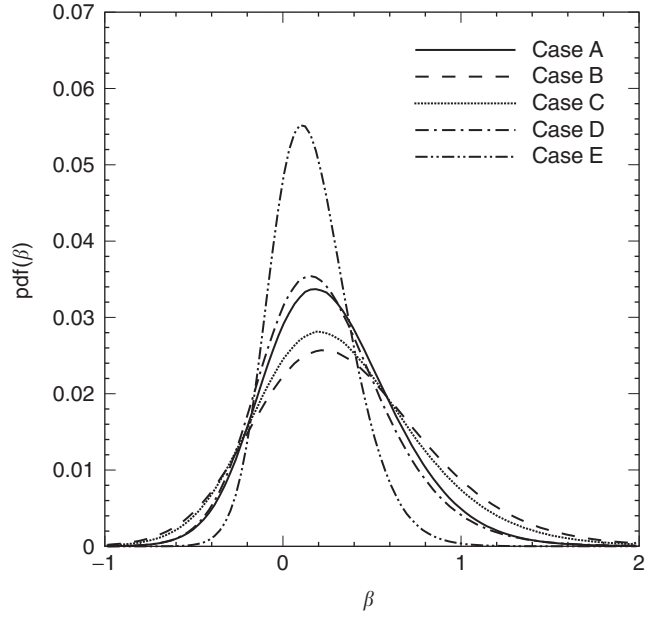

FIGURE 13.30 Probability distribution of the principal intermediate strain rate β at $t = 5$.

$\tau_\kappa(t)$ (not shown here). Figure 13.28 also shows that the magnitude of the increase in $\varepsilon(t)$ in case B relative to case A is less than the magnitude of increase in $\Psi_p(t)$ in the former with the net result of a reduction in the decay rate of $E(t)$ in case B according to Eq. (13.14) and is shown in Figure 13.22. Now we discuss the effects of the microparticles on the energy spectrum $E(\kappa)$ (Figure 13.23) of the carrier fluid. The time evolution of is governed by Eq. (13.13). Microparticles contribute to all the terms on the RHS

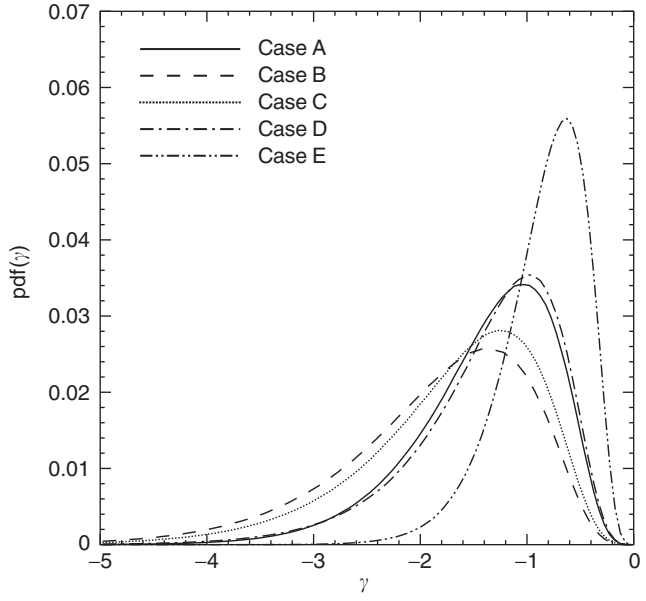

FIGURE 13.31 Probability distribution of the principal compressive strain rate γ at $t = 5$.

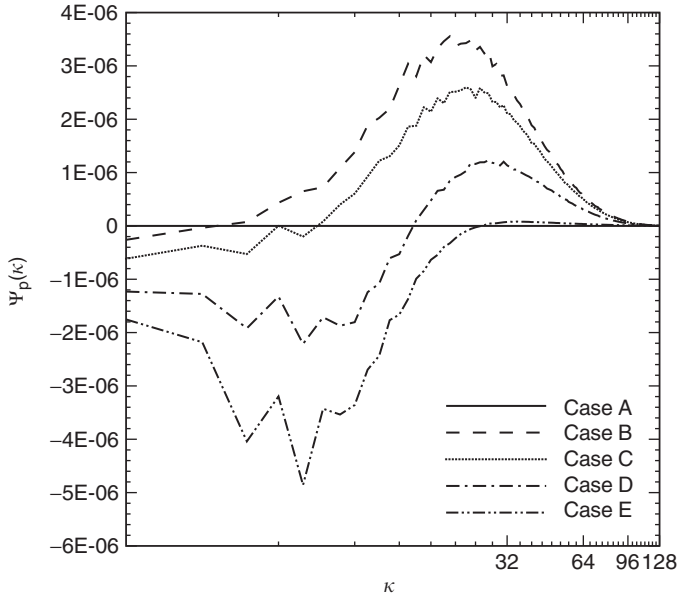

FIGURE 13.32 Three-dimensional spatial spectrum of two-way coupling fluid–particle drag interaction energy rate $\Psi_p(\kappa)$ at $t = 5.0$.

of Eq. (13.13) (Figures 13.32–13.34). The time evolution of $E(\kappa)$, not shown here, indicates that the microparticles first modify the high wave number portion of the spectrum, before the smaller wave numbers are affected as time increases. Because of their properties, microparticles ($d \ll \eta$ and $\tau_p \ll \tau_\kappa$) directly interact with the small scales of motion, augmenting their energy content. The triadic interaction of wave numbers then alters the energy content of the other scales of motion, such that after few integral

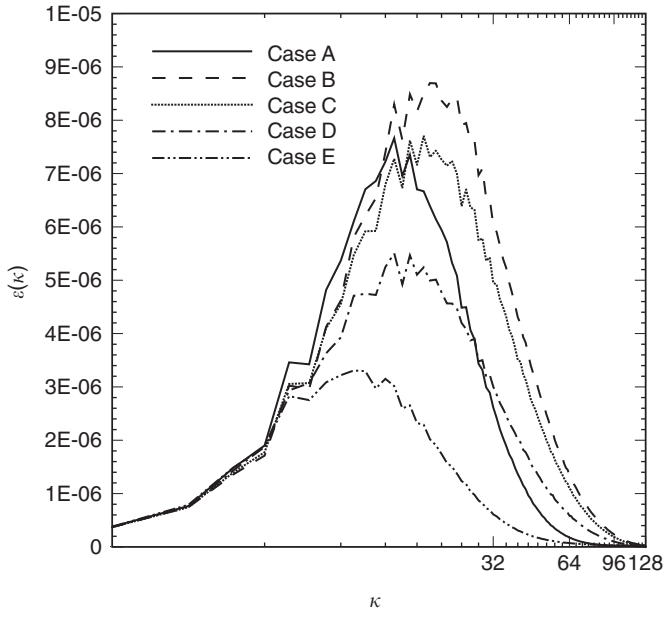

FIGURE 13.33 Three-dimensional spatial spectrum of energy dissipation rate $\varepsilon(\kappa)$ at $t = 5.0$.

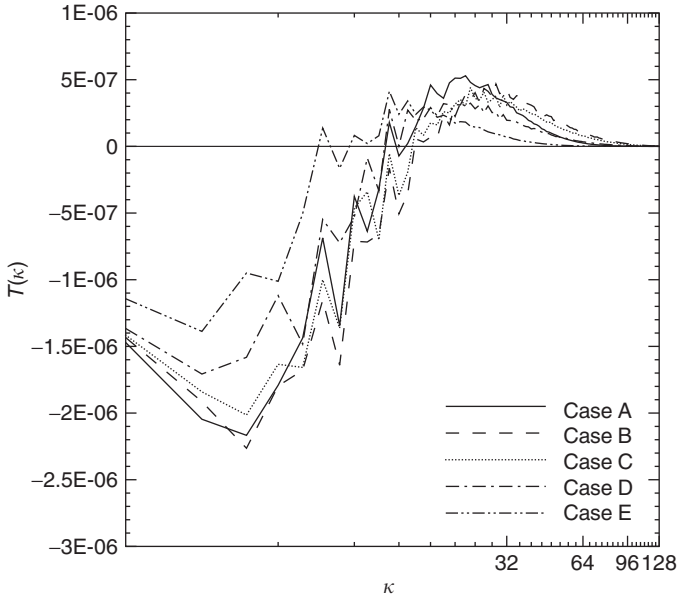

FIGURE 13.34 Three-dimensional spatial spectrum of nonlinear energy transfer rate $T(\kappa)$ at $t = 5.0$.

time scales, τ_l, $E(\kappa)$ modified at all the wave numbers as compared to the particle-free case (Figure 13.23). We have explained earlier in this section how microparticles produce a positive $\Psi_p(t)$ (Figure 13.28). Since $\Psi_p(t) = \int \Psi_p(\kappa)\, d\kappa$ at time t, in case B this integral should be positive. Figure 13.32 shows that $\Psi_p(\kappa)$ in case B is positive at almost all the wave numbers, and thus microparticles provide a positive two-way coupling contribution to $\partial E(\kappa)/\partial t$ (Eq. [13.13]).

On the other hand, we have explained how the microparticles increase the dissipation rate, $\varepsilon(t)$, in case B, as compared with the particle-free flow (Figure 13.28). Since $\varepsilon(t) = \int \varepsilon(\kappa)\, d\kappa$ at time t, $\int \varepsilon(\kappa)\, d\kappa$ in case B should be greater than that in case A (Figure 13.33). Also $\varepsilon(\kappa) = 2\nu\kappa^2 E(\kappa)$; thus, in accordance with $E(\kappa)$ in Figure 13.23, Figure 13.33 shows that $\varepsilon(\kappa)$ in case B is greater than that in case A at medium-high wave numbers. The increase in dissipation at high wave numbers causes a larger transfer rate of energy to the large κ value from the small κ value. The energy transfer rate $T(\kappa)$ is, thus, modified by shifting κ, at which $T(\kappa) = 0$ toward higher wave numbers for case B as compared with case A (Figure 13.34). Due to the increased transfer of energy from the small κ, the decay rate of $E(\kappa)$ at small κ is increased, and thus $E(\kappa)$ in case B is smaller than in case A at small κ (Figure 13.23).

13.2.4.3.3.2 Critical Particles ($\tau_p/\tau_\kappa \approx 1$). We label the particles in case D ($\tau_p/\tau_\kappa = 1$) as "critical" particles because of their property of maximum preferential accumulation in comparison to other particles as will be discussed later in this section. We will show that these particles are ejected from the large-vorticity cores of the eddies soon after injection, remain in certain orbits (Figure 13.36), and do not move from one eddy into another as larger particles do (case E).

Now we examine how these critical particles affect $\Psi_p(t)$ and $\varepsilon(t)$ to increase the decay rate of TKE with respect to case A (Figure 13.22). For critical particles, $\Psi_p(t)$ is negative after injection (Figure 13.28) and becomes positive at later times, $t > 2.3 \approx t_{\text{inj}} + \tau_l = 1 + \tau_l$, where τ_l is the turnover time of the large-scale motion (Table 13.3). At early times ($1 < t < 1 + \tau_l$) critical particles, similar to large particles, are centrifuged from their initial surrounding fluid and thus $\langle u_j v_j \rangle < \langle u_j u_j \rangle$. Consequently, according to Eq. (13.15), $\Psi_p(t)$ becomes negative (Figure 13.28) and thus contributes to the faster decay of TKE as compared to case A.

At later times ($t > 1 + \tau_l$), after they have been ejected from the cores of vortices, the critical particles do not have sufficient inertia to cross the convergence regions (of high-speed fluid between the counter-rotating vortices) and enter new eddies, similar to large particles, but rather, they accumulate in these regions of low vorticity and high strain (Maxey, 1987; Wang and Maxey, 1993b). The occurrence of preferential accumulation can be indicated by the time development of the D_c factor (Wang and Maxey, 1993b), which measures the sum of the squared differences between the actual probability of concentration, $P_c(C)$, and the probability of random distribution, $p_c^{\mu}(C)$,

$$D_c = \sum_{C=0}^{N_p} (P_c(C) - P_c^{\mu}(C))^2 \tag{13.19}$$

where N_p is the total number of computational particles (denoted by M_c in Table 13.4). Figure 13.35 shows the time development of D_c for the four cases (B–E). It is clear that in case D (critical particles), the preferential accumulation is much larger than in the other three cases. Figure 13.36 clearly shows the preferential accumulation of the critical particles in orbits outside the regions of large ω_2.

The higher inertia of the critical particles relative to the carrier fluid causes their velocity autocorrelation to be higher than that of the surrounding fluid, $\langle v_j v_j \rangle > \langle u_j u_j \rangle$, indicating that critical particles retain their kinetic energy longer than their surrounding fluid. Once these particles are in the high-velocity convergence regions, characterized by pathlines of small curvature, their trajectories become more aligned with those of the fluid points. Consequently, the correlation $\langle u_j v_j \rangle$ becomes larger than $\langle u_j u_j \rangle$ for $t > 1 + \tau_l$. Thus, $\Psi_p(t)$ becomes positive (Eq. [13.15]) for $t > 1 + \tau_l$ (Figure 13.28). Since the high vorticity cores are nearly free of particles, the two-way coupling force $f_\kappa \approx 0$ inside these cores, and thus the evolution equation of vorticity reduces to that of particle-free flow. Table 13.5 confirms that the value of mean enstrophy at time $t = 5$ in case D is nearly equal to that of case A, with a difference smaller than 3%.

Since the vortical structures in case D evolve nearly as that in case A, the growth rates of the turbulence scales are nearly identical in both cases ($\tau_{k_d}(t) \approx \tau_{k_A}(t)$)(not shown here). Consequently, the decay rate of the local velocity gradients will be the same in both the cases, resulting in a similar decay of the magnitude of the local strain rate. Table 13.5 shows that the strain rate for case D is identical to that of case A at $t = 5$. At time $t = 5$, Figures 13.29–13.31 confirm that the values of, α, β, γ and in case D are almost identical to those in case A. Accordingly, the viscous dissipation rates in these two cases are nearly the

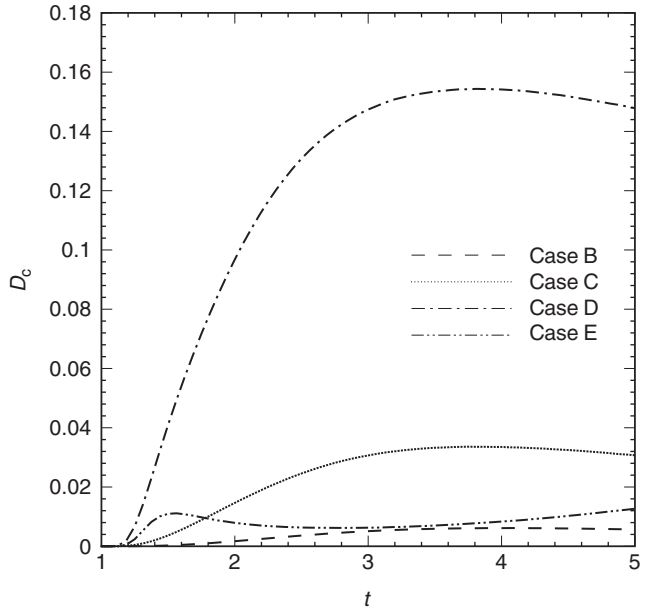

FIGURE 13.35 Time development of the D_c factor.

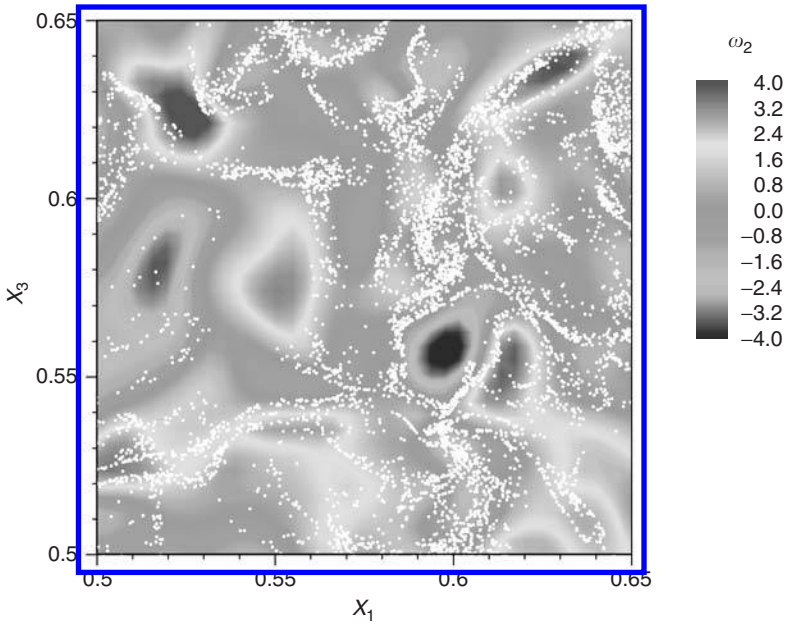

FIGURE 13.36 (Color insert follows page 13-40) Case D: critical particles (white dots) superimposed on ω_2 (color contour) at $x_2 = 0.5$ and $t = 5.0$.

same (see Figure 13.28). Thus, the net effect of the modifications of $\Psi_p(t)$ and $\varepsilon(t)$ in case D (Figure 13.28) is the reduction of $E(t)$ relative to case A. The modification of the energy spectrum $E(\kappa)$ of the carrier flow by the critical particles (case D) is displayed in Figure 13.23. It is seen that $E(\kappa)$ for case D lies between those of case B (microparticles) and case E (large particles). Accordingly, the magnitudes of

$\Psi_p(\kappa)$, $\varepsilon(\kappa)$, and $T(\kappa)$ of case D are intermediate between those of cases B and E (Figures 13.32–13.34). $\Psi_p(\kappa)$ is positive at large κ as for microparticles, and negative at small κ as for large particles. $\varepsilon(\kappa)$ is such that $\varepsilon(t) = \int \varepsilon(\kappa)\, d\kappa$ is nearly identical to that of case A (See Figure 13.28), as discussed above. The net result of these modifications is that, in case D, the crossover wave number of $E(\kappa)$ with that of the particle-free flow (case A) lies in between the crossover wave numbers of cases B and E.

13.2.4.3.3.3 Ghost particles in zero gravity. It is clear from Figure 13.22 and the discussion in the previous subsections that in comparison with the particle-free flow (case A), microparticles (case B, $\tau_p/\tau_\kappa = 0.1$) reduce the decay rate of TKE, and critical particles (case D, $\tau_p/\tau_\kappa = 1.0$) enhance this rate. These two opposing effects in cases B and D lead us to search for particles that have a neutral effect on that decay rate. More specifically, we searched for particles whose τ_p is in the range $0.1 < \tau_p/\tau_\kappa < 1.0$ and which maintain the decay rate of TKE as that of the particle-free flow (case A). Our DNS results show that particles with $\tau_p/\tau_\kappa = 0.25$ (case C) satisfy this condition at all times, as shown in Figure 13.22. Thus we denote these particles as ghost particles because their presence in the flow cannot be detected by examining only the temporal development of TKE. It is important to emphasize that the value of $\tau_p/\tau_\kappa = 0.25$ is not universal, but depends on $Re_{\lambda 0}$, α_m, and the magnitude of the gravitational acceleration (zero in our case). However, the significance of this finding is that dispersed particles are capable of modifying the turbulence energy spectrum (Figure 13.23) in such a unique way that the amount of energy gained by the turbulence at high wave numbers balances exactly the amount of energy lost at low wave numbers, with the net result of retaining the integral of the spectrum equal to that of the particle-free flow at all times (Figure 13.22).

Similar to microparticles, ghost particles are not ejected from the vortex cores (Figure 13.37), and thus they enhance the lifetime of the vortical structures, such that, at time $t = 5$, the enstrophy and the strain rate in case C are larger than those in case A by about 56 and 53%, respectively (Table 13.5). Since ghost particles have larger inertia than microparticles, their trajectories tend to deviate from those of their surrounding fluid points more than the trajectories of microparticles. Thus the magnitudes of $\Psi_p(t)$ and $\varepsilon(t)$ for the ghost particles (see Figure 13.28) are smaller than those for the microparticles. However, the magnitudes of $\Psi_p(t)$ and $\varepsilon(t)$ for the ghost particles are in a unique proportion, such that the positive $\Psi_p(t)$ is only equal to the increase ($\Delta\varepsilon(t)$) in the magnitude of $\varepsilon(t)$ with respect to case A, resulting in the net

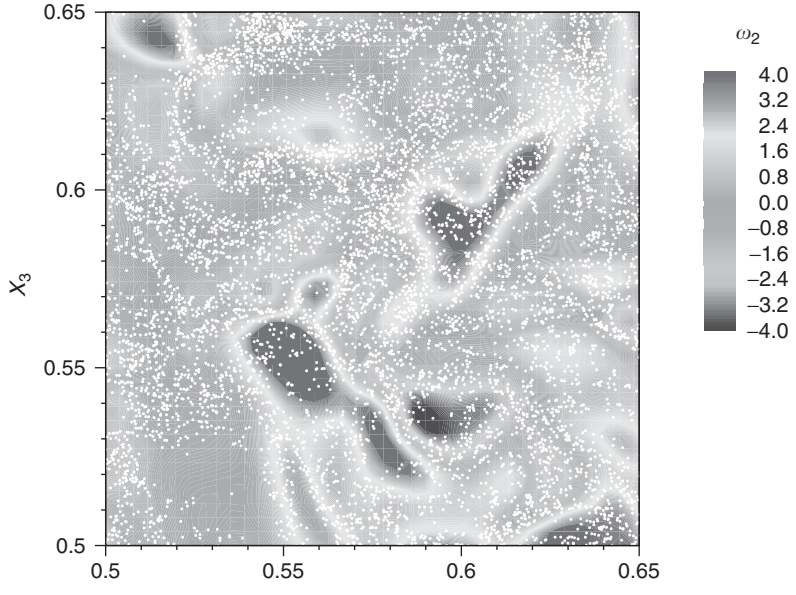

FIGURE 13.37 (Color insert follows page 13-40) Case C: "ghost" particles in zero gravity (white dots) superimposed on ω_2 (color contour) at $x_2 = 0.5$ and $t = 5.0$.

sum ($\Psi_p(t) - \Delta\varepsilon(t)$) being equal to $\varepsilon(t)$ of case A. Consequently, the decay rate of TKE in case C is the same as in case A.

13.2.4.3.3.4 Ghost particles in finite gravity. In case F, we study the effect of gravity on the two-way coupling between the ghost particles of case C ($\tau_p/\tau_\kappa = 0.25$) and decaying isotropic turbulence. A gravitational acceleration is imposed in the negative x_3 direction, and its magnitude is prescribed, such that (v_t/u_0) = 0.25 (Table 13.4).

Figure 13.24 shows that due to gravity, the particles in case F reduce the decay rate of TKE relative to cases A and C at all times. Figure 13.38 compares the temporal developments of the three rms velocity components, $u_{i,\mathrm{rms}}(t)$ of the fluid in both cases A and F. It is seen that only the decay rate of the velocity component in the x_3 direction, $u_{3,\mathrm{rms}}$, has been considerably reduced relative to the other components, i.e., the two-way coupling in the presence of gravity in the x_3 direction resulted in augmenting $u_{3,\mathrm{rms}}$. The mechanisms responsible for this modulation will be discussed below by comparing the vorticity fields in cases C (zero gravity) and F (finite gravity).

Figure 13.37 and Figure 13.39 display the contours of the instantaneous vorticity component ω_2 (in a small zone of the vertical midplane x_1x_3 of our computational domain) and particles locations at $t = 5$ for cases C and F, respectively. We see that most of the vortical structures in case F are stretched in the x_3 direction in a banana-like shape, and the values of maximum (positive and negative) vorticity are larger than in case C.

We also see that the particles in case F tend to accumulate in patches according to the mechanism of preferential sweeping described by Wang and Maxey (1993b). The solid particles, settling under the effect of gravity, tend to follow a path where the local fluid instantaneous velocity is in the direction of gravitational acceleration (negative x_3 direction). Figure 13.39 shows that the particles accumulate on the RHS of a vortical structure with positive (clockwise) vorticity (red color) or on the LHS of a structure with negative vorticity (blue color). This preferential accumulation or sweeping, as expected, creates zones that are nearly devoid of particles. Thus only the side of the vortical structure swept by the trajectories of the particles will be subjected to a drag force, $-f_3$, which is directed downward. As a consequence of this asymmetry of the force acting on the fluid, local gradients $\partial f_3/\partial x_1$ and $\partial f_3/\partial x_2$ are generated in the horizontal plane, increasing the magnitudes of the source terms, b_i, the horizontal components of vorticity, and ω_1 and ω_2, in addition to stretching the structures in the x_3 direction.

The results discussed above provided new information about the behavior of the TKE and its dissipation rate in Zone A of the classification map in Figure 13.20 as shown in Figure 13.21. Zone A includes

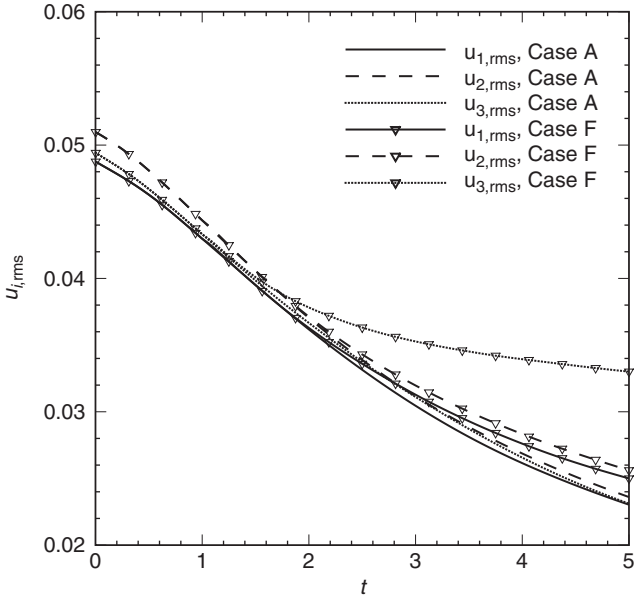

FIGURE 13.38 Time development of rms fluid velocity components.

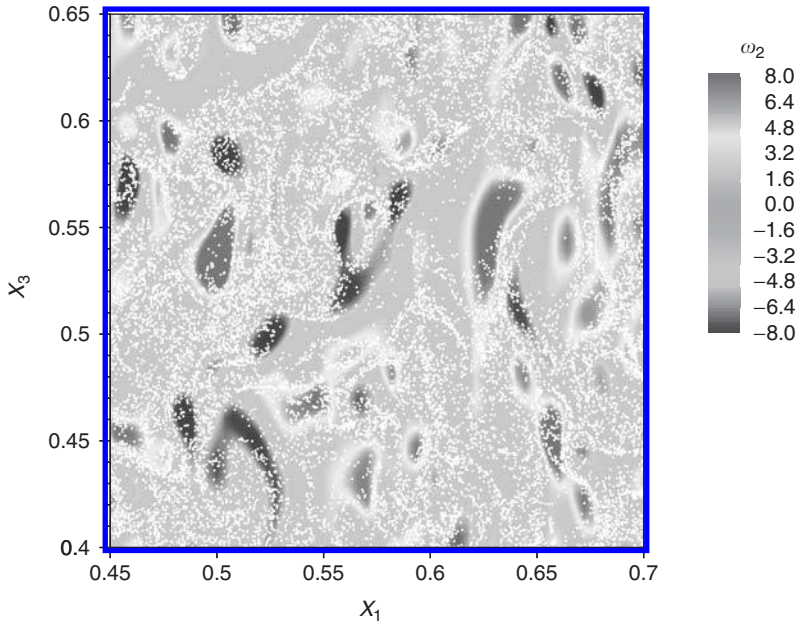

FIGURE 13.39 (Color insert follows page 13-40) Case F: "ghost" particles in finite gravity (white dots) superimposed on ω_2 (color contour) at $x_2 = 0.5$ and $t = 5.0$.

three regions:

- Microparticles ($\tau_p/\tau_\kappa \leq 0.1$) that cause both TKE and its dissipation rate, ε, to be larger than in the single-phase flow.
- Ghost particles ($0.1 < \tau_p/\tau_\kappa < 0.5$) that modify the energy spectrum $E(\kappa)$ in a manner such that TKE is unchanged but ε is larger than that of the single-phase flow.
- Large particles ($\tau_p/\tau_\kappa > 1$) that reduce both TKE and ε relative to their values in the single-phase flow.

13.2.5 DNS of Bubble-Laden Isotropic Turbulence Using the Two-Fluid Approach

In the preceding section we employed the Lagrangian–Eulerian approach to study the two-way coupling interactions between solid particles and isotropic turbulence. In the present section we use the alternative approach, known as the two-fluid or Eulerian–Eulerian approach (Elghobashi, 1994), which has been applied frequently with the Reynolds-averaged equations of motion (Elghobashi and Abou Arab, 1983). Recently Druzhinin and Elghobashi, 1998) employed the two-fluid approach in DNS of bubble-laden isotropic turbulence. This section provides a condensed version of this paper (Druzhinin and Elghobashi, 1998). In this approach, the governing equations are obtained by volume averaging the equations of motion of both the phases, (the carrier flow and bubbles) based on the assumption that the dispersed phase behaves as a continuum under certain conditions.

The objective of this section is to describe how DNS is performed using the two-fluid approach for bubble-laden homogeneous isotropic turbulence without applying force (i.e., decaying turbulence). It is important to point out that in employing the two-fluid approach a difficulty may arise due to the phenomenon of preferential accumulation of the dispersed particles. It is well known (Eaton and Fessler, 1994) that solid particles, due to their inertia, tend to accumulate in the low-enstrophy regions of the flow, whereas gaseous bubbles in a liquid flow tend to accumulate in a high-enstrophy regions (Druzhinin

and Elghobashi, 1998, 2001), generally associated with the centers of vortices. Preferential accumulation in homogeneous turbulence is most pronounced for particles with response times of the order of the Kolmogorov time scale τ_κ (Wang and Maxey, 1993b). This segregation creates regions devoid of particles neighboring regions of high particle concentration. Therefore, performing DNS using the two-fluid approach may generate high concentration gradients causing numerical resolution and stability problems, thus restricting the implementation of that approach. Druzhinin and Elghobashi (1999a) recently developed a numerical scheme that resolves the large gradients of particle velocity and concentration fields created by preferential accumulation.

In this section we show that the two-fluid approach is applicable to bubbles with diameter smaller than the Kolmogorov length scale, and accordingly their response time is much smaller than the Kolmogorov time scale. Thus, the effects of preferential accumulation of bubbles in the high-enstrophy regions of the carrier flow become less pronounced, so that DNS with the two-fluid approach can be successfully used.

13.2.5.1 Equations of Motion for the Bubble-Laden Flow

We consider spherical bubbles with diameter d_b to be much smaller than the characteristic length scale of the flow, L_f, and average the equations of motion of the fluid and bubble over a length scale λ, which is much smaller than L_f but much larger than the bubble diameter, $d_b \ll \lambda \ll L_f$. Thus the bubble phase can be treated as a continuum characterized by the velocity $V_i(\mathrm{r,t})$ and concentration (or volume fraction) $\alpha(\mathrm{r,t}) = \pi d_b^3 N_b(\mathrm{r,t})/6$, where $N_b(\mathrm{r,t})$ is the bubble number density.

We assume that the density of the gas and, consequently, the mass of the bubble are negligible compared with those of the surrounding fluid, $\rho_f \gg \rho_b = 0$. By taking into account the effect of the bubbles on the fluid flow in a unit volume of the mixture and neglecting the interactions between the bubbles, we write derive the following equations for the bubble-laden flow (Drew, 1983; Zhang and Prosperetti, 1997)
Fluid momentum equation:

$$(1-\alpha)\rho_f \frac{\mathrm{D}U_i}{\mathrm{D}t} = -(1-\alpha)\partial_i P + \partial_j(1-\alpha)\sigma_{ij} - \alpha F_i^d - (1-\alpha)\rho_f g\delta_{iz} \tag{13.20}$$

Fluid continuity equation:

$$-\partial_i\alpha + \partial_j(1-\alpha)U_j = 0 \tag{13.21}$$

Bubble-phase momentum equation:

$$0 = -\alpha\partial_i p + \partial_j\alpha\sigma_{ij} + \alpha F_i^d \tag{13.22}$$

Bubble-phase continuity equation:

$$\partial_i\alpha + \partial_j\alpha V_j = 0 \tag{13.23}$$

In the above equations, U_i is the fluid velocity, V_i the velocity of the bubble phase, σ_{ij} the viscous stress tensor, $\sigma_{ij} = \mu(\partial_j U_i + \partial_i U_j)$, the Lagrangian derivatives $\mathrm{D/D}t = \partial/\partial t + U_j\partial_j$ and $\mathrm{d/d}t = \partial/\partial t + V_j\partial_j$ are taken along the trajectories of the fluid point and bubble, respectively, and g the projection of the gravity acceleration on the z-axis, $g_i = -g\delta_{iz}$. F_i^d denotes the force acting on the bubble due to the pressure and viscous stresses caused by the disturbance flow U^d owing to the boundary conditions at the bubble surface. The details of the derivation of Eqs. (13.22)–(13.23) are given by Druzhinin and Elghobashi (1998).

Since we assume that the bubble mass is negligible, the sum of the forces acting on the bubble must vanish and thus the equation of the bubble motion becomes

$$F_i^0 + F_i^d = 0 \tag{13.24}$$

where F_i^0, the force exerted on the bubble by the undisturbed fluid flow U^0, is obtained by integrating both the pressure and viscous stresses of the undisturbed flow over the bubble surface. For small spherical bubbles with diameter much smaller than the flow length scale,

$$d_{\mathrm{b}} \ll L_f \tag{13.25}$$

and with Weber number less than unity, F_i^0 is given by

$$F_i^0 = \rho_f\left(\frac{\mathrm{D}U_i^0}{\mathrm{D}t} + g\delta_{\mathrm{iz}}\right) = -\partial_i P^0 + \partial_j \sigma_{ij}^0 \tag{13.26}$$

where P^0 and σ_{ij}^0 are the undisturbed pressure and viscous stresses fields, respectively. The boundary condition at the bubble surface is effectively equivalent to that for a solid sphere, rather than the stress free-condition needed for the Hadamard–Rybczynski formula (Batchelor, 1967). Thus, for bubbles with Reynolds number less than unity,

$$Re_{\mathrm{b}} = \frac{d_{\mathrm{b}}|U^0 - V|}{\nu} < 1 \tag{13.27}$$

the force due to the disturbance flow, F^{d}, can be calculated from the solution of the corresponding unsteady Stokes problem in the form

$$F_i^{\mathrm{d}} = \frac{18\mu}{d^2}(U_i^0 - V_i) + \frac{\rho_{\mathrm{f}}}{2}\left(\frac{\mathrm{D}U_i^0}{\mathrm{D}t} - \frac{\mathrm{d}V_i}{\mathrm{d}t}\right) \tag{13.28}$$

The first and second terms in Eq. (13.28) correspond to the Stokes drag and added-mass forces, respectively. From Eq. (13.24) we obtain an equivalent expression for the disturbance force:

$$F_i^{\mathrm{d}} = -F_i^0 \tag{13.29}$$

where F_i^0 is given by Eq. (13.26).

Therefore, the equation of the bubble motion Eq. (13.24) can be rewritten in the form

$$\frac{\mathrm{d}V_i}{\mathrm{d}t} = 3\frac{\mathrm{D}U_i}{\mathrm{D}t} + \frac{1}{\tau_{\mathrm{b}}}(U_{\mathrm{i}} - V_{\mathrm{i}} + W\delta_{\mathrm{iz}}) \tag{13.30}$$

where the bubble response time τ_{b} and terminal velocity w are defined as

$$\tau_{\mathrm{b}} = \frac{d^2}{36\nu} \tag{13.31}$$

and

$$W = 2\tau_{\mathrm{b}} g \tag{13.32}$$

In Eqs. (13.20)–(13.23), (13.30) and the following discussion, we omit the superscript "0" in the notation for the undisturbed fole U^0.

We assume that the bubble volume fraction, α, is small enough (i.e., $\alpha \leq 10^{-3}$), and therefore, neglect its contribution to the fluid inertia and continuity, i.e., we retain α only in the buoyancy term in the momentum equation of the carrier flow Eq. (13.20). This is analogous to the Boussinesq approximation in a stratified fluid with effective density $(1-\alpha)\rho_{\mathrm{f}}$.

By substituting the expression for the disturbance force obtained from Eqs. (13.29) and (13.26) into the equation for the fluid momentum Eq. (13.20), and using Eq. (13.20), we write equations of the conservation of the fluid- and bubble-phase momentum and mass in the form (Ruetsch and Meiburg, 1994):

$$\frac{\mathrm{D}U_i}{\mathrm{D}t} = -\frac{1}{\rho_f}\partial_i \widetilde{P} + \nu\Delta U_i + (\alpha - \langle\,\alpha\,\rangle)\mathrm{g}\delta_{iz} \tag{13.33}$$

$$\partial_j U_j = 0 \tag{13.34}$$

$$\frac{\mathrm{d}V_i}{\mathrm{d}t} = 3\frac{\mathrm{D}U_i}{\mathrm{D}t} + \frac{1}{\tau_\mathrm{b}}(U_i - V_i + W\delta_{iz}) \tag{13.35}$$

$$\frac{\partial \alpha}{\partial t} + \partial_j \alpha V_j = 0 \tag{13.36}$$

By using the analogy between the bubbly flow and a stratified flow with density $(1-\alpha)\rho_\mathrm{f}$, we remove the modified hydrostatic part in the pressure field in Eq. (13.33):

$$\widetilde{P} = P + \rho_\mathrm{f} g \int_0^z (1 - \langle \alpha \rangle)\, \mathrm{d}z \tag{13.37}$$

where $\langle \alpha \rangle$ is the ensemble-averaged bubble volume fraction. In the following discussion, we evaluate $\langle \alpha \rangle$ as an average over a horizontal (z) plane.

13.2.5.2 Numerical Method

The momentum conservation and continuity equations (13.33)–(13.36) for both phases are solved in a cubical domain with periodic boundary conditions. The equations are discretized in an Eulerian framework using a second-order finite-difference technique on a staggered grid containing 96^3 points equispaced within unit length in each of the three coordinate directions (x,y,z). The Adams–Bashforth scheme is used to integrate the equations in time. Pressure is obtained by solving the Poisson equation using fast Fourier transform. More details about the numerical method and its accuracy are discussed by Elghobashi and Truesdell (1993), Gerz et al. (1989), Schumann (1977) and Ferrante and Elghobashi (2003).

13.2.5.3 Results

In this section, we present the DNS results for bubble dispersion in isotropic decaying turbulence with one-way coupling.

13.2.5.3.1 Dispersion of Bubbles in Isotropic Decaying Turbulence (with One-Way Coupling)

DNS of bubble dispersion in isotropic decaying turbulence is performed with the initial conditions: $Re_{\lambda 0} = 25$, $U_0 = 0.05$, and $k_\mathrm{p}/k_\mathrm{min} = 5$, which correspond to the initial dissipation $\varepsilon(0) = 0.002584$, Taylor microscale $\lambda_0 = 0.027877$, Kolmogorov length scale $\eta_0 = 0.002861$, integral length scale $L_0 = 0.057815$, and viscosity $\nu = 5.57 \times 10^{-5}$. The dimensionless gravity constant g is assumed to equal unity. The reference length and time scales used in normalizing the above dimensionless quantities are $L_\mathrm{ref} = 0.098$ m and $T_\mathrm{ref} = 0.1$ s, respectively.

The initial bubble velocity and volume fraction (concentration) are prescribed as

$$V_\mathrm{i} = \delta_\mathrm{iz} W, \quad \alpha_0 = C_0 = 5 \times 10^{-4} \tag{13.38}$$

where the bubble terminal velocity W is given by Eq. (13.32).

The ability of the simulation to resolve the motion at the smallest turbulence scales is assured by the criterion $\eta k_\mathrm{max} > 1$, where $k_\mathrm{max} = N_\mathrm{g}\pi$ is the highest resolved wave number for the given number of grid points in each coordinate direction N_g (= 96 in the present case). Our simulations show that $1 \leq \eta k_\mathrm{max} \leq 2.65$ for $0.75 < \mathrm{t} < 10$.

The choice of the bubble response time is restricted by the conditions Eqs. (13.25) and (13.27), which can be rewritten in the form

$$d_\mathrm{b} < \eta \tag{13.39}$$

and

$$Re_\mathrm{b} = \frac{W d_\mathrm{b}}{\nu} < 1 \tag{13.40}$$

The first condition ensures that the bubble size is smaller than the characteristic flow scale, i.e., the Kolmogorov length scale $\eta = (\nu^3/\varepsilon)^{1/4}$ in the case of decaying isotropic turbulence. The second condition restricts the bubble Reynolds number, based on the bubble terminal velocity, to be less than one. Substituting the terminal velocity (13.32) and the bubble diameter ($d_b = (36\nu\tau_b)^{1/2}$) in Eq. (13.39) and Eq. (13.40), and using the equality $\eta^2 = \nu\tau_k$, we rewrite conditions (13.39) and (13.40) as

$$\frac{\tau_b}{\tau_k} < \frac{1}{36} \simeq 0.028 \tag{13.41}$$

and

$$\tau_b < \left(\frac{\nu}{144g^2}\right)^{1/3} = \tau_* \tag{13.42}$$

It should be emphasized that conditions (13.41) and (13.42) are essential for the derivation of the bubble motion equation (13.30). Thus, violating either of these conditions renders the equation of motion (13.30) invalid. Note that Wang and Maxey (1993a) and Maxey et al. (1994) performed DNS of isotropic turbulence laden with bubbles with $\tau_b = \tau_k$ using the Eulerian–Lagrangian approach and Eq. (13.30), i.e., violating the condition (13.41).

Also note that in the case of solid particles, the condition $d_p < \eta$ (which is also required for the derivation of the particle motion equation) is equivalent to $(\tau_p/\tau_k) < (\rho_p/18\ \rho_f)$, which allows (τ_p/τ_k) to be ≥ 1 for $\rho_p > 18\rho_f$.

In DNS of bubble-laden decaying turbulence we prescribe $\tau_b = 0.04\tau_{k0}$, where the initial dimensionless Kolmogorov time scale is $\tau_{k0} = 0.15$. The bubbles are added to the flow at time $t = 1$, when the magnitude of the skewness of the fluid velocity derivative reaches about 0.47, indicating an established rate of energy transfer across the energy spectrum. At that time, τ_k increases to 0.22, hence ratio $\tau_b/\tau_k = 0.027$ and the time $\tau_* = 0.0073$ (see Eq. [13.42]). Since τ_k increases monotonically in decaying turbulence, condition (13.41) is satisfied throughout the simulation. Thus both conditions Eqs. (13.41) and (13.42) are met for the prescribed value of τ_b. The corresponding bubble Reynolds number (13.40) equals 0.74 (i.e., of the order of unity) and the dimensional bubble diameter is $d_b \simeq 350\ \mu$m (for the bubble to remain spherical in liquid water, i.e., $d_b < 1$ mm). Therefore, the prescribed value of τ_b is close to the maximum limit for the validity of the equation set (13.33)–(13.36).

Figure 13.40 shows the time development of TKE $E(t)$, and its dissipation rate $\varepsilon(t)$, and the concentration variance $\langle\alpha'^2\rangle = \langle(\alpha - \langle\alpha\rangle)^2\rangle$calculated from the corresponding spectra $E(k,t)$ and $E_\alpha(k,t)$ as

$$E(t) = \sum_{k=1}^{N_k/2} E(k,\ t) \tag{13.43}$$

$$\epsilon(t) = 2\nu \sum_{k=1}^{N_k/2} k^2 E(k,\ t) \tag{13.44}$$

and

$$< \alpha'^2 > (t) = \sum_{k=1}^{N_k/2} E_\alpha(k,\ t) \tag{13.45}$$

normalized by the spective initial values $E(0)$, $\varepsilon(0)$ and $\alpha_0{}^2$. Both $E(t)$ and $\epsilon(t)$ decay in time due to the viscous dissipation. On the other hand, the bubbles concentration variance first increases from zero to $\langle\alpha'^2\rangle \simeq 5.1 \times 10^{-3}\alpha_0{}^2$ (for time $1 < t < 5$, where $t = 1$ is the time of injecting the bubbles into the flow), and then decays. The growth of the concentration variance is caused by the preferential accumulation of bubbles in the high-enstrophy regions of the flow. The effects of the bubble accumulation as well as the decay of the concentration variance for $t > 5$ are discussed below.

Figure 13.41 shows the spectra of the fluid kinetic energy, $E(k)$, the dissipation, $\varepsilon(k) = 2\nu k^2 E(k)$, and the bubble concentration fluctuations, $E_\alpha(k)$, at time $t = 3$ (here and below, for convenience, we omit the explicit reference to the time dependence of $E(k,t)$, $\varepsilon(k,t)$ and $E_{a\alpha}(k,t)$). At this time, the energy spectrum

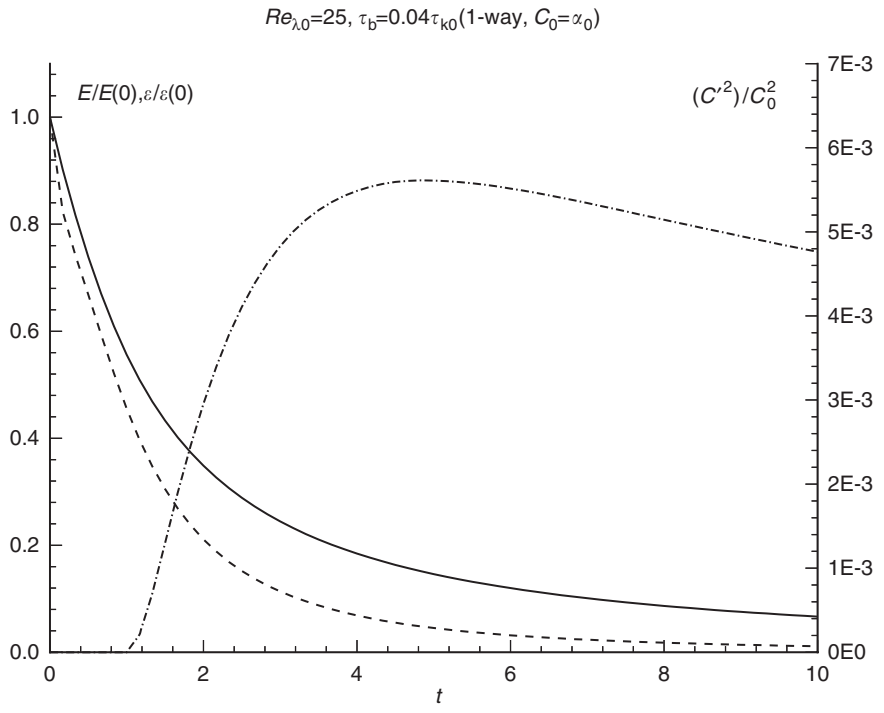

FIGURE 13.40 Time dependence of the normalized turbulence kinetic energy $E(t)/E(0)$ (solid curve), its dissipation rate $\varepsilon(t)/\varepsilon(0)$ (dashed curve) and variance of bubble volume fraction (concentration) $\langle\alpha'^2\rangle/\alpha_0^2 \equiv \langle C'^2\rangle/C_0^2$ (dash-dotted curve).

peaks at $k = 3$. Note that since the transport equation of bubble concentration is of the advection (Lagrangian) type, there is no molecular dissipation of the bubble concentration fluctuations. Thus there is no decay in the spectrum $E_\alpha(k)$ at high wave numbers, rather, the fluctuations intensity piles up at larger wave numbers (cf. Figure 13.41). Note however, that the concentration variance Eq. (13.45) remains finite and small, relative to the average concentration α_0^2, throughout the computations (cf. Figure 13.40). Figure 13.42 shows the DNS results obtained at $t = 3$ for the bubble concentration (gray scale) and flow enstrophy field (contour lines) in the (x,y) plane at $z = 0.5$. Although the bubble response time is much smaller than the Kolmogorov time scale, we still observe the accumulation of bubbles in the zones of maximum enstrophy (corresponding to the centers of intense vortices). This means that even for such small τ_b, the bubble inertia, owing to the added mass, influences the bubble motion and causes the preferential accumulation of bubbles in the high-enstrophy regions of the flow and the initial growth of the concentration variance. Note that the time interval $\Delta t = 2$ corresponds approximately to six characteristic vortex time scales, $\langle\omega^2\rangle^{-1/2}$, estimated as an average Kolmogorov $\overline{\tau}_k$ time for $1 < t < 3$, $\langle\omega^2\rangle^{-1/2}\,\overline{\tau}_k \simeq 0.3$.

In order to quantify the accumulation effects we calculated the enstrophy-conditioned average bubble concentration, $\langle\alpha\rangle_\omega$, and its variance, $\langle\alpha'^2\rangle_\omega$, defined as

$$\langle\alpha\rangle_\omega = \frac{1}{N(\omega^2)}\sum_{j=1}^{N(\omega^2)}\alpha_j/\alpha_0 \tag{13.46}$$

$$\langle\alpha'^2\rangle_\omega = \frac{1}{N(\omega^2)}\sum_{j=1}^{N(\omega^2)}(\alpha_j/\alpha_0 - \langle\alpha\rangle_\omega)^2 \tag{13.47}$$

where $N(\omega^2)$ is the number of grid points where the enstrophy value lies within the range $[\omega^2, \omega^2+\Delta\omega^2]$, and using the data shown in Figure 13.42 with the enstrophy increment $\Delta\omega^2 = 0.5$. Figure 13.43 shows the

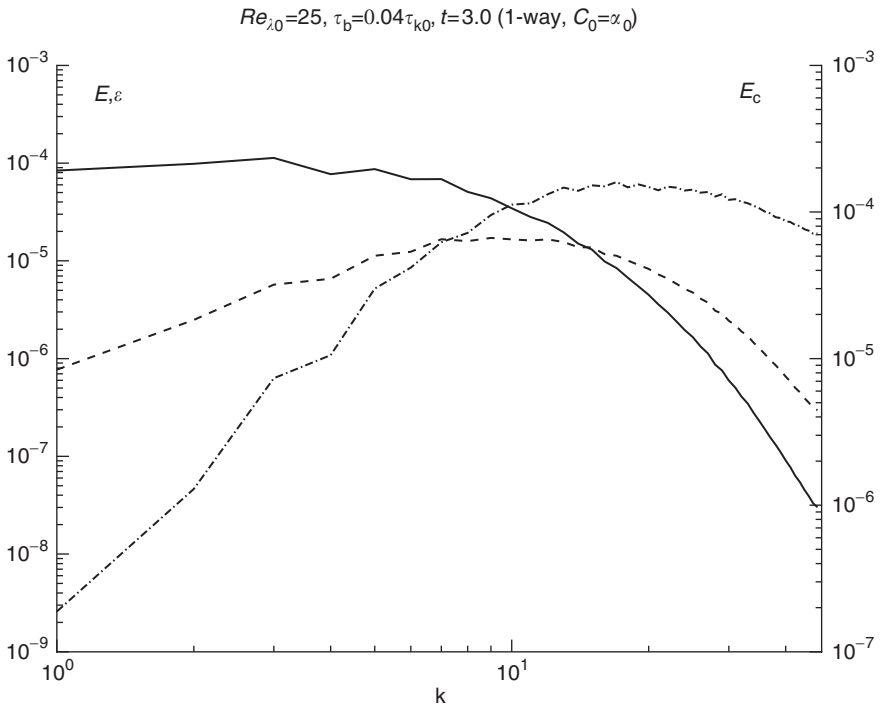

FIGURE 13.41 Spectra of the turbulence kinetic energy $E(k)$ (solid curve), dissipation $\varepsilon(k)$ (dashed curve) and bubble volume fraction (concentration) fluctuations $E_\alpha(k) \equiv E_c(k)$ (dash-dotted curve).

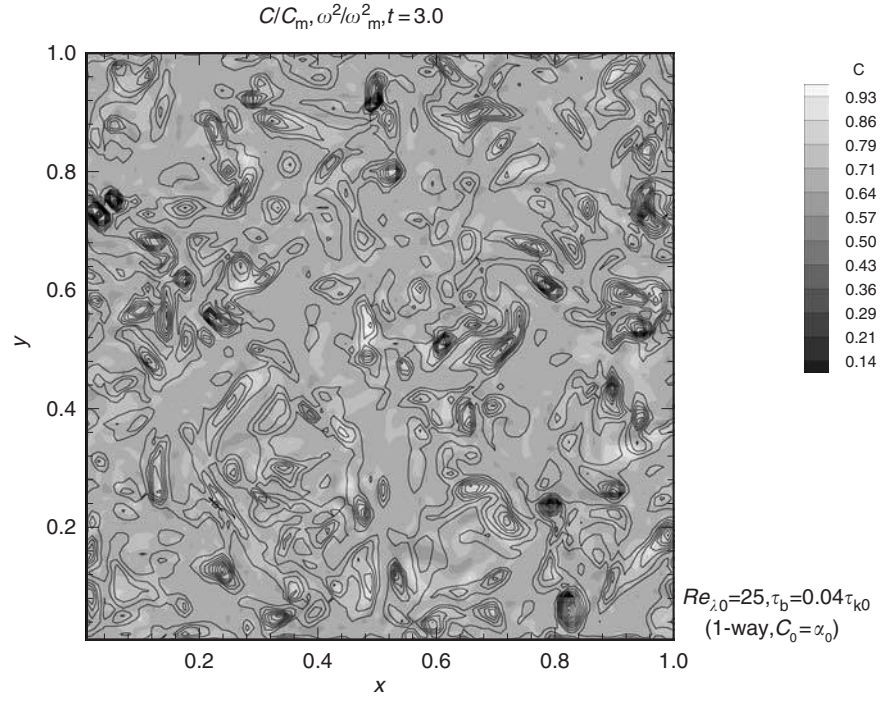

FIGURE 13.42 Turbulence enstrophy and bubbule volume fraction (concentration), $\alpha \equiv C$, normalized by the maximum values.

dependence of $\langle\alpha\rangle_\omega$ and $\langle\alpha'^2\rangle_\omega$ on ω^2. As in the case of bubble dispersion in the Taylor–Green (TG) vortex discussed in Druzhinin and Elghobashi (1998), both $\langle\alpha\rangle_\omega$ and $\langle\alpha'^2\rangle_\omega$ increase in the high-enstrophy regions of the flow. However, since the bubble response time is much smaller than the Kolmogorov time scale, the bubble preferential accumulation is significantly reduced compared with the TG-vortex case (Druzhinin and Elghobashi, 1998), where $\tau_b \simeq \tau_f$. Also note also that fluctuations of both $\langle\alpha\rangle_\omega$ and $\langle\alpha'^2\rangle_\omega$ grow as the enstrophy increases, which shows the intermittent nature of the high-enstrophy regions in turbulence.

Now, we introduce a mathematical model to explain how the ratio τ_b/τ_k governs the preferential accumulation process and the growth of the local concentration gradients in isotropic turbulence.

Let us consider a single vortex with a radius of the order of the Kolmogorov length scale η and core vorticity $\omega_0 = 1/\tau_k$. Assume that the bubble response time is much smaller than the Kolmogorov time scale, $\tau_b/\tau_k \ll 1$. Then, the local accumulation rate can be estimated from the solution for the bubbles concentration in the TG vortex (Druzhinin and Elghobashi, 1998) as

$$\frac{\partial\alpha/\partial t}{\alpha_0} \simeq \tau_b\omega_0^2 \simeq \frac{\tau_b}{\tau_k^2} \tag{13.48}$$

Thus the difference in bubble concentration between the inside and the outside of the vortex, $\Delta\alpha = \alpha_i - \alpha_o$, related to (τ_b/τ_k) via

$$\frac{\Delta\alpha}{\alpha_o} \simeq \frac{\tau_b}{\tau_k} \tag{13.49}$$

and the corresponding concentration gradient is

$$\frac{|\nabla\alpha|}{\alpha_o} \sim \frac{\Delta\alpha}{\alpha_o\eta} \sim \frac{\tau_b}{\eta\tau_k} \tag{13.50}$$

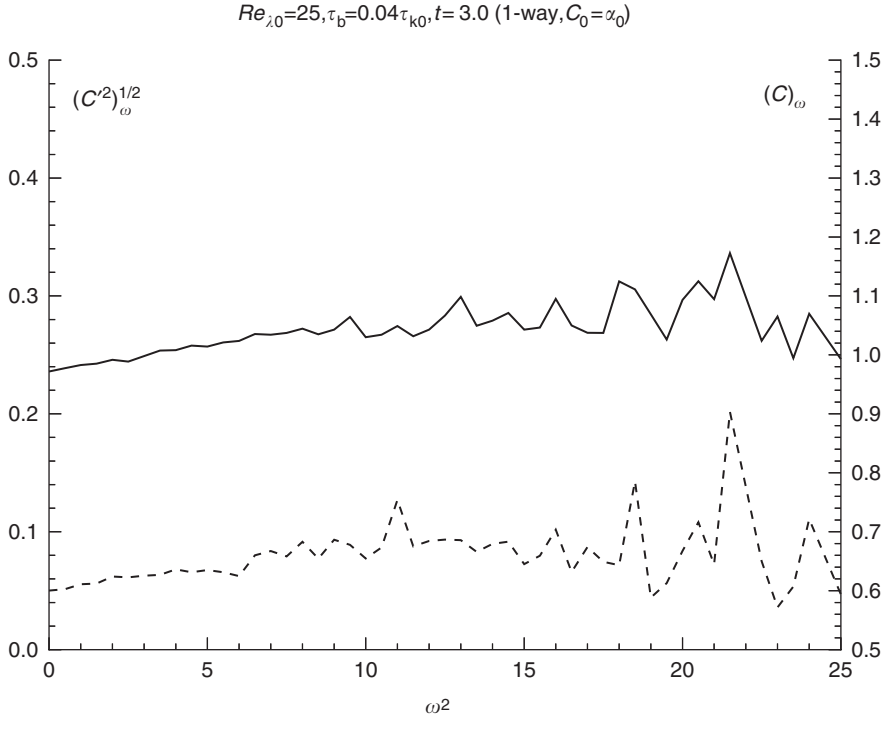

FIGURE 13.43 Dependence of the enstrophy-conditioned average bubble volume fraction (concentration), $\langle\alpha\rangle_\omega \equiv \langle C\rangle_\omega$, (solid curve) and its variance $\langle\alpha'^2\rangle_\omega \equiv \langle C'^2\rangle_\omega$ (dashed curve) on the enstrophy.

Note that according to Eq. (13.49), the variance of the concentration fluctuations is proportional to the ratio $(\tau_b/\tau_k)^2$, which decreases with time in decaying turbulence, since the Kolmogorov time scale increases monotonically. This prediction agrees with our DNS results for $\langle \alpha'^2 \rangle$ given in Figure 13.40, which shows that the concentration variance decays with time after the initial transient ($1 < t < 5$).

It should be noted that both the accumulation of bubbles and the absence of the diffusivity in the transport equation for the bubble concentration Eq. (13.36) may lead to instabilities in the numerical solution due to the development of steep gradients in the concentration field. The occurrence of this numerical instability depends on the initial distribution of the bubble concentration, the flow Reynolds number, and the bubble response time. In the DNS, we chose the initial microscale Reynolds number $\mathrm{Re}_{\lambda 0} = 25$, so that at the time of the injection of bubbles ($t = 1$), the small-scale motions are resolved, i.e., $k_{\max}\eta \geq 1$, where $k_{\max} = N_g\pi$ is the maximum wave number for the given grid resolution N_g=96. The numerical instability may occur for higher-inertia bubbles, i.e., for τ_b of the order of the Kolmogorov time scale τ_k. However, prescribing $\tau_b \simeq \tau_k$ would violate the condition $d_b < \eta$, which is necessary for deriving Eq. (13.35) of bubble motion.

In our DNS we prescribe $\tau_b = 0.04\tau_{k0} = 0.006$, for which the bubble diameter ($d_b \simeq 3.47 \times 10^{-3}$) is smaller than the Kolmogorov length scale at the time of bubble injection ($\eta \simeq 3.5 \times 10^{-3}$ at $t = 1$) (both d_b and η are dimensionless here), to remain within the validity limit of Eq. (13.35). No instability occurs in our DNS under these conditions, for both the cases of the initially uniform and the initially linear bubble concentration fields. This is evident in Figure 13.44 which shows the instantaneous concentration variance spectra, obtained from our DNS for the initially uniform bubble distribution, at four different times. The time evolution of the concentration spectrum in Figure 13.44 and the corresponding concentration variance $\langle \alpha'^2 \rangle$ (dash-dotted curve in Figure 13.40) show that no numerical instability occurs. The spectrum $E_C(k)$ at high wave numbers approaches an asymptotic form at $t = 10$ (Figure 13.44). The high wave-number range in the spectrum (i.e., $k \geq 40$) would detect any numerical instability if it existed. Furthermore, Figure 13.40 shows that the concentration variance $\langle \alpha'^2 \rangle$, decays with time for $t > 5$.

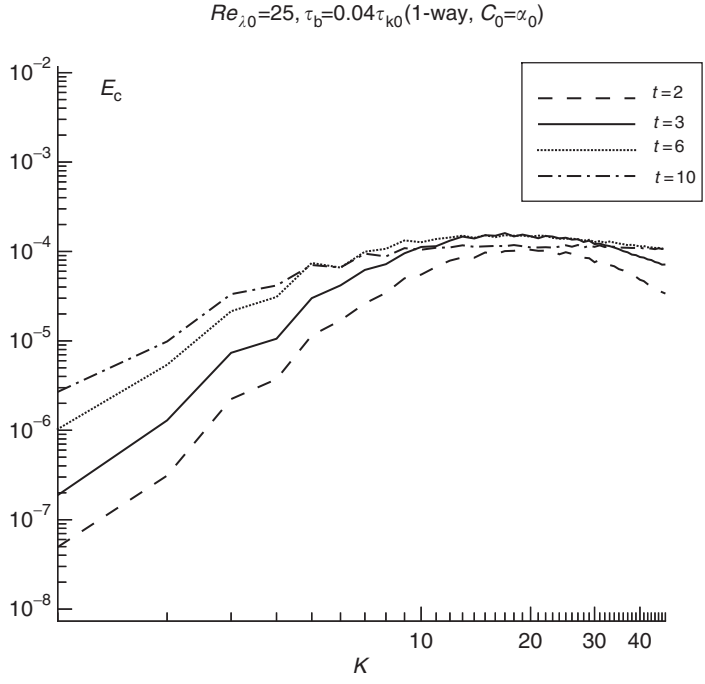

FIGURE 13.44 Instantaneous spectra of the bubble volume fraction (concentration) fluctuations $E_\alpha(k) \equiv E_c(k)$ at four different times (with one-way coupling).

The reason for the absence of the instability is that the fluctuations of the bubble concentration, caused by the preferential accumulation, are proportional to the ratio τ_b/τ_k, which decreases with time (~$1/t$) in decaying turbulence, as discussed above.

13.2.6 DNS of Turbulent Shear Flows Laden by Dispersed Solid Particles or Bubbles

In the above subsections we described our DNS studies for nonsheared turbulent flows. Here we describe briefly two recent DNS studies on turbulent shear flows, one homogeneous shear and the other inhomogeneous, laden with particles or bubbles.

13.2.6.1 The Mechanisms of Modifying the Structure of Turbulent Homogeneous Shear Flows by Dispersed Solid Particles

This study (Ahmed and Elghobashi, 2000) is concerned with answering the question: what are the physical mechanisms responsible for the modification of the turbulence structure by solid particles dispersed in a homogeneous shear flow? We employ DNS to examine the effects of the two-way interaction between the two phases on the turbulence structure. Our results indicate that particles affect the rate of production of turbulence energy via modifying the vorticity dynamics. It is known that regions of large production rate of turbulence energy are sandwiched between counterrotating vortices whose vorticity, ω_s, is aligned with the axes of the longitudinal vortex tubes. These longitudinal vortex tubes are strongly inclined toward the streamwise direction due to the imposed mean shear. The stronger ω_s is the longer the production rate. The dispersed solid particles modify the alignment of the local vorticity vector, ω, with the axis of the longitudinal vortex tube. Increasing this alignment, increases the ω_s, which in turn augments the turbulence production rate, and vice versa. In addition, due to the enhanced strain rate of the carrier fluid by the particles, the dissipation rate of turbulence energy is always increased. The particles also reduce the alignment of the vorticity vector with the intermediate eigenvector (β) of the strain rate tensor. This reduction in alignment is due to an increase in the rotational term and particle-source term in the governing equation of the cosine of the angle between the vorticity vector and the intermediate strain eigenvector.

13.2.6.2 DNS of a Microbubble-Laden, Spatially Developing Turbulent Boundary Layer over a Flat Plate

The objective of the present section (Ferrante and Elghobashi, 2004) is to explain in as much detail as possible, the physical mechanisms responsible for the reduction of skin friction in a microbubble-laden, spatially developing turbulent boundary layer over a flat plate, for $Re_\theta = 1430$. Our DNS results with microbubbles volume fraction ranging from $\alpha = 0.001$ to 0.02 show that the presence of bubbles results in a *local* positive divergence of the fluid velocity, $\nabla \cdot \mathbf{U} > 0$, creating a positive mean velocity normal to (and away from) the wall, which in turn reduces the mean streamwise velocity and displaces the quasi-streamwise longitudinal vortical structures away from the wall.

This displacement has two main effects:

(1) it increases the spanwise gaps between the wall streaks associated with the sweep events and reduces the streamwise velocity in these streaks thus reducing the skin friction by up to 20.2% for $\alpha = 0.02$;

(2) it moves the location of peak Reynolds stress production away from the wall to a zone of a smaller transverse gradient of the mean streamwise velocity (i.e., smaller mean shear), thus reducing the production rate of TKE and enstrophy.

13.3 Continuous-Phase Equations

Clayton T. Crowe

Unlike the flow of a single-phase liquid or gas, the carrier phase of a dispersed-phase flow contains dispersed particles or droplets. For analysis, the ideal situation would be to solve the governing conservation

(continuity, momentum, and energy) equations for the carrier phase by accounting for the boundary conditions imposed by each and every particle or droplet in the field. This would provide a complete description of the carrier phase throughout the mixture.

Computationally, this would require a grid dimension at least as small as the smallest particle in the field. Such a solution is beyond current computer capability. Solutions have been obtained in limited cases with a finite number of particles in a low Reynolds number (Stokes) flow (Brady, 1993). Also numerical solutions have been obtained for flows in which the particles occupy no volume but produce a drag force on the flow (Elghobashi and Truesdell, 1992; Squires and Eaton, 1991). These solutions are also limited to low Reynolds numbers. In general, however, one must resort to the use of equations based on the average properties in a flow.

The purpose of this section is to introduce the averaging procedures and to present the equations in volume average form suitable for numerical model development. The equations for kinetic energy of turbulence are presented and discussed at the end of this section

13.3.1 Averaging Procedures

In essence, there are three approaches to averaging the continuous phase equations: time, volume, and ensemble averaging.

13.3.1.1 Time Averaging

The time average is the result of averaging the flow properties over time at a point in the flow as shown in Figure 13.45. This type of measurement corresponds to a hot-wire or laser-Doppler anemometry, which has been used extensively to obtain average and fluctuation properties in single-phase flows. The time average of property B of the fluid is defined as

$$\hat{B} = \frac{1}{T}\int_0^T B\,\mathrm{d}t \tag{13.51}$$

where T is the averaging time.

Assume that the velocity of each phase is measured as particles and fluid pass the measuring point. The signal may appear as shown in Figure 13.46. Obviously, the averaging time must be large compared with the local fluctuation time, t', in order to define an average value. Yet, the averaging time must be smaller than the time associated with the system change, T'.

$$t' \ll T \ll T'$$

In many transient flow systems, this condition may not be realizable. A true time average can only be obtained in a steady flow system and is given by

$$\hat{u} = \lim_{T\to\infty} \frac{1}{T}\int_0^T u\,\mathrm{d}t \tag{13.52}$$

A more detailed discussion on temporal averaging is provided by Ishii (1975).

13.3.1.2 Volume Averaging

Volume averaging is carried out by averaging properties at an instant in time over a volume and ascribing the average value to a point in the flow. For example, the volume-averaged property B would be defined as

$$\overline{B} = \frac{1}{V}\int_V B\,\mathrm{d}V \tag{13.53}$$

where V is the averaging volume. Assume that the distribution of the dispersed-phase mixture appears as shown in Figure 13.47, where ℓ is the nominal distance between the particles and L is a distance that

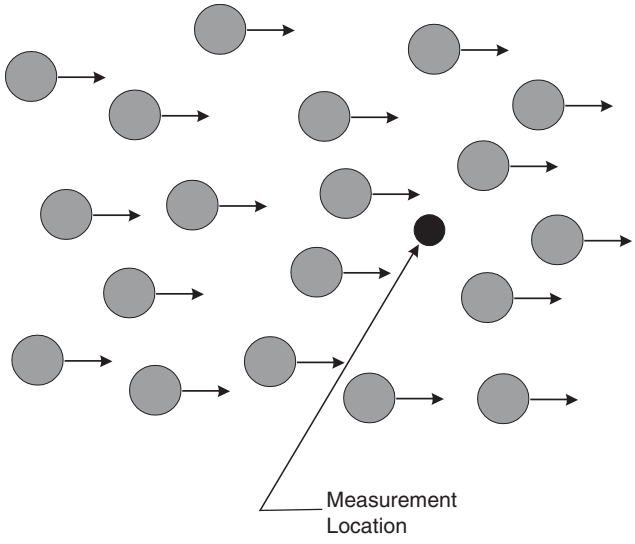

FIGURE 13.45 Measurement location in a multiphase flow field.

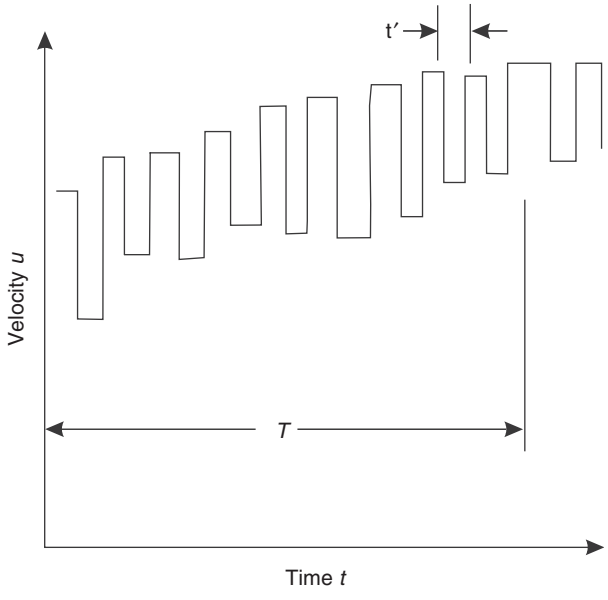

FIGURE 13.46 Velocity variation with time at measurement point.

characterizes the spatial change in mixture properties. Obviously, in order to obtain a near stationary average (an average which does not change with a change in the size of the averaging volume), the averaging volume must be much larger than ℓ^3. However, in order that the average provide a local value for B in the field, the averaging volume must be much less than L^3. Thus the constraints on the averaging volume are

$$\ell^3 \ll V \ll L^3 \tag{13.54}$$

This constraint is essential to approximate spatial derivatives of $\overline{B}$ in the flow field. An accurate volume average is only possible for a homogeneous mixture.

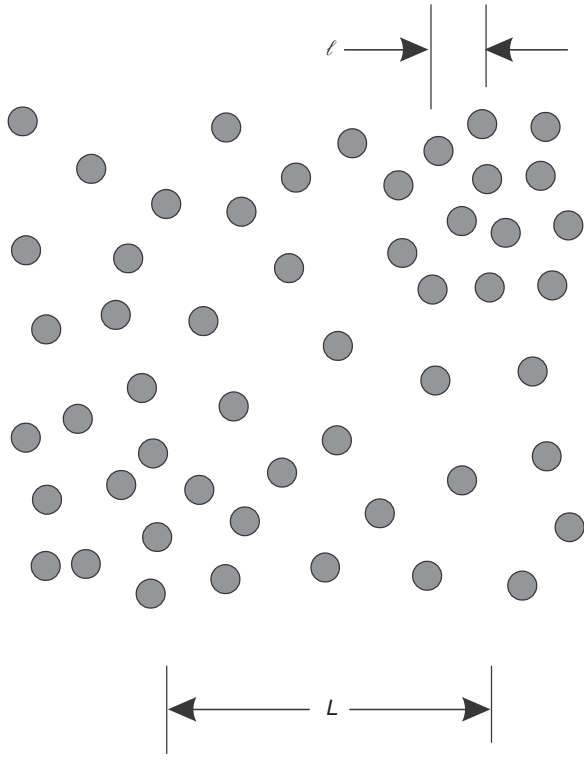

FIGURE 13.47 Spatial distribution of particles in spatial averaging field

Besides the volume average defined by Eq. (13.53), there is also a phase average, which is the average over the volume occupied by the phase:

$$\{\mathrm{B}\} = \frac{1}{V_c}\int_{V_c} B\,\mathrm{d}V \tag{13.55}$$

where V_c is the volume associated with the continuous phase. This defines the phase average for the continuous phase. If B is the density of the continuous phase, then $\{\rho_c\}$ is the average material density of the continuous phase. If the density is constant, then $\{\rho_c\}=\rho_c$. The relationship between the volume-averaged property and the phase average for the continuous phase is $\{B\}=\alpha_c\overline{B}$.

Several authors have used the volume averaging approach to derive the equations for the continuous phase in a mixture. Drew (1983) introduced a phase function

$$X_k(x_i, t) = \begin{cases} 1 & \text{if } x_i \text{ is in phase } k \text{ and time } t \\ 0 & \text{otherwise} \end{cases} \tag{13.56}$$

The basic equations are then multiplied by $X_k(x_i,t)$ and averaged including the discontinuity at the surfaces between the dispersed and continuous phases.

Crowe (1998) used the formulation, introduced by Slattery (1972), to relate the volume average of the derivative to the derivative of the volume average

$$\overline{\frac{\partial B}{\partial x_i}} = \frac{\partial}{\partial x_i}\{B\} - \frac{1}{V}\int_{S_d} Bn_i\,\mathrm{d}S \tag{13.57}$$

where the integral is taken over the interface, S_d, between the continuous and dispersed phase. The property B can be a scalar or a vector. Another relation used in the analysis is for the volume average of the time derivative

$$\overline{\frac{\partial B}{\partial t}} = \frac{\partial}{\partial t}\{B\} - \frac{1}{V}\int_{S_d} B\dot{r}\, dS \tag{13.58}$$

where $\dot{r}$ is the local regression rate of the surface with respect to coordinates moving with a dispersed-phase element. The equations presented in this section are based on this approach. Special attention is given to the disperse-phase elements that are severed by the control surface. These are referred to as boundary elements.

Another approach to volume and temporal averaging has been developed by Roco and Shook (1985) and has been applied to liquid–solid flows.

13.3.1.3 Ensemble Averaging

Ensemble averaging avoids the shortcomings of time and volume averaging, but is much more difficult to implement. Ensemble averaging is based on the probability of the flow field being in a particular configuration at a given time. For example, assume that the distribution of the fluid density over a region is measured many times. It is found that there are N different configurations and that the distribution in each configuration (realization) at a given time t is

$$\rho\varepsilon_c = f_\eta(x_i, t) \tag{13.59}$$

where η is one realization of the N configurations (ensemble). Assume that $n(\eta)$ is the number of times that configuration $f_\eta(x_i,t)$ occurred. The ensemble average is then defined as

$$\langle\rho_c\rangle = \frac{\sum_N f_\eta(x_i, t)n(\eta)}{\sum_N n(\eta)} \tag{13.60}$$

In the limit of an infinite number of realizations, the above equation becomes

$$\langle\rho_c\rangle = \int_0^1 f(x_i, t, \mu)\, d\mu \tag{13.61}$$

where μ is the probability that the realization $f(x_i,t)$ will occur. Obviously, ensemble averaging is not limited by volume or time constraints.

Joseph et al. (1990) applied ensemble averaging techniques to develop the equations for an incompressible fluid–particle suspension. They used an indicator function for both the solid and the fluid. The ensemble average of the indicator functions give volume fractions. The resulting equations differed from those postulated from mixture theory, particularly the form of the stress terms.

Hinch (1977) utilized ensemble averaging to find the relationship between bulk stress and bulk strain rate for force-free particles.

Zhang and Prosperett (1994) addressed ensemble averaging of a mixture of identical particles in an inviscid, incompressible fluid. They defined a function ζ^N representing a specific configuration of a system with position vectors and velocities. They also defined an indicator function χ_C which is unity for the continuous phase and zero otherwise. Relationships were developed for the ensemble averages of the time and spatial derivatives in terms of the time and spatial derivatives of the ensemble averages. These relationships were then used to develop the ensemble-averaged form of the conservation equations. In 1997, Zhang and Prosperetti extended the model to viscous Newtonian flows. The authors continued their work (Machioro et al., 1999) to address the mixture pressure and shear stress.

The conservation equations presented in this section are based on volume averaging. The detailed derivations for the continuity and momentum equations can be found in Crowe et al. (1998). The majority of numerical models for multiphase flows are based on volume discretization. Also, the volume-averaging approach is amenable to Large Eddy Simulation (LES).

13.3.2 Mass Conservation

The general statement for mass conservation is that the net efflux of mass from a control volume plus the rate of accumulation of mass flow in the volume is zero. Starting with the continuity equation for the continuous phase,

$$\frac{\partial \rho_c}{\partial t} + \frac{\partial}{\partial x_i}(\rho_c u_i) = 0 \tag{13.62}$$

Taking the volume average yields

$$\overline{\frac{\partial \rho_c}{\partial t}} + \overline{\frac{\partial}{\partial x_i}(\rho_c u_i)} = 0 \tag{13.63}$$

Applying Eqs. (13.57) and (13.58) yields (Crowe et al., 1998)

$$\frac{\partial}{\partial t}(\alpha_c\{\rho_c\}) + \frac{\partial}{\partial x_i}(\alpha_c\{\rho_c u_i\}) = -\frac{1}{V}\sum_k \dot{m}_k \tag{13.64}$$

where $\dot{m}_k$ is the rate of change of mass of the dispersed-phase element (droplet) k and the summation is carried out over every element in the averaging volume. This is the mass source term or the mass coupling term.

$$S_{\text{mass}} = -\frac{1}{V}\sum_k \dot{m}_k \tag{13.65}$$

For evaporating droplets, $\dot{m}_k < 0$, hence mass coupling term would be positive. If all the droplets evaporate at the same rate, the mass source term simplifies to $S_{\text{mass}} = -n\dot{m}$.

For convenience, the mass-averaged velocity, defined by

$$\tilde{u}_i = \frac{\{\rho_c u_i\}}{\{\rho_c\}} \tag{13.66}$$

will be used. If the density of the continuous phase is constant, the volume average and mass average velocities are the same. If, however, the continuous-phase density is nearly constant over the averaging volume, then $\tilde{u}_i \simeq \{u_i\}$. Thus the continuity equation is written as

$$\frac{\partial}{\partial t}(\alpha_c\{\rho_c\}) + \frac{\partial}{\partial x_i}(\alpha_c\{\rho_c\}\tilde{u}_i) = S_{\text{mass}} \tag{13.67}$$

All averaging techniques yield the same form of the continuity equation. Some derivations do not include the mass coupling term. For numerical models that treat the dispersed phase as point (no volume) elements, the volume fraction of the continuous phase, α_c, is set equal to unity and the continuity equation simplifies to

$$\frac{\partial}{\partial t}\{\rho_c\} + \frac{\partial}{\partial x_i}(\{\rho_c\}\tilde{u}_i) = S_{\text{mass}} \tag{13.68}$$

which is the same as the continuity equation for single-phase flow, except for the mass coupling term.

If the continuous phase is a gas, which consists of component chemical species, then the continuity equation for species A would be

$$\frac{\partial}{\partial t}(\alpha_c\{\rho_c\}\omega_A) + \frac{\partial}{\partial x_i}(\omega_A\{\rho_c\}\alpha_c\tilde{u}_i) = \omega_{A,S}S_{\text{mass}} + \frac{\partial}{\partial x_i}\left(\alpha_c\{\rho_c\}\mathfrak{D}_A\frac{\partial \omega_A}{\partial x_i}\right) + \dot{R}_A \tag{13.69}$$

where ω_A is the mass fraction of species A, $\omega_{A,s}$ is the mass fraction of species A at the droplet surface, $\mathfrak{D}_A$ the diffusion coefficient, and $\dot{R}_A$ the mass generation rate of species A per unit volume due to a chemical reaction. In this equation, $\tilde{u}_i$ is the mass-averaged velocity for the mixture.

13.3.3 Momentum Conservation

The momentum equation for the continuous phase is

$$\frac{\partial}{\partial t}(\rho_c u_i) + \frac{\partial}{\partial x_j}(\rho_c u_i u_j) = -\frac{\partial p}{\partial x_i} + \frac{\partial \tau_{ij}}{\partial x_j} + \rho_c g_i \tag{13.70}$$

where τ_{ij} is the shear stress tensor and g_i the acceleration due to gravity. Taking the volume average of each term and accounting for the boundary elements yields

$$\frac{\partial}{\partial t}(\alpha_c\{\rho_c\}\tilde{u}_i) + \frac{\partial}{\partial x_j}(\alpha_c\{\rho_c\}\tilde{u}_j\tilde{u}_i) = -\frac{\partial\{p\}}{\partial x_i} - \frac{1}{V}\sum_k v_{k,i}\dot{m}_k \tag{13.71}$$

$$+ \frac{\partial}{\partial x_j}\{\tau_{ij}\} - \frac{\partial}{\partial x_j}(\alpha_c\{\rho_c u_i' u_i'\}) - \frac{1}{V}\sum_k F_{i,k} + \alpha_c\{\rho_c\}g_i$$

where $v_{k,i}$ is velocity of the dispersed phase element k and $F_{k,i}$ is the hydrodynamic force produced by the continuous phase on particle k. The velocity u_i' is

$$u_i' = u_i - \tilde{u}_i$$

or the deviation of the local velocity in the averaging volume from the mass-averaged value.

The term $-1/v\sum_k v_{k,i}\dot{m}_k$ is the momentum coupling term due to addition of mass (and momentum) to the continuous phase and will be identified by

$$S_{\text{mom},\dot{m}} = -\frac{1}{V}\sum_k v_{k,i}\dot{m}_k \tag{13.72}$$

If all the dispersed-phase elements are moving at the same velocity, v_i, then

$$S_{\text{mom},\dot{m}} = v_i S_{\text{mass}} \tag{13.73}$$

If all the dispersed-phase elements are losing mass at the same rate, $\dot{m}$, then

$$S_{\text{mom},\dot{m}} = -\dot{m}\{v_i\}n \tag{13.74}$$

The term $-(\partial/\partial x_i)(\alpha_c\{\rho_c u_i' u_j'\})$ is analogous to the Reynolds stress in a single-phase flow. The flow does not have to be turbulent to create this stress, because velocity deviations can occur by the flow around individual particles. In order to evaluate the shear stress terms, constitutive models are necessary to relate the shear stress to the properties of the conveying phase. One approach is to define an effective stress

$$\{\tau_{ij}\}^e = -\{\rho_c u_i' u_j'\} \tag{13.75}$$

and to assume that the effective shear stress can be represented by

$$\{\tau_{ij}\}^e = \mu_e\left(\frac{\partial\tilde{u}_i}{\partial x_j} + \frac{\partial\tilde{u}_j}{\partial x_i}\right) \tag{13.76}$$

where μ_e becomes the effective viscosity. This is referred to as the Boussinesq approximation. The effective shear stress is related to the turbulence parameters of the flow. It is a common practice to use the k–ε methodology, common to single-phase flows, to estimate the effective shear stress. It is unlikely that this approach is useful since the gradients in the average velocity do not capture the local gradients imposed by the presence of the particles.

The hydrodynamic force on dispersed-phase element k is the integral of the pressure forces and shear stress acting on the particle surface, S_k.

$$F_{k,i} = \int_{S_k}(-pn_i + \tau_{ij}n_j)\,dS \tag{13.77}$$

expressing the pressure as $p=\{p\}+\delta p$ and $\tau_{ij}=\{\tau_{ij}\}+\delta\tau_{ij}$, the force becomes

$$F_{ij} = -V_a\frac{\partial\{p\}}{\partial x_i} + V_d\frac{\partial\{\tau_{ij}\}}{\partial x_j} + \int_{S_k}(-\delta p n_i + \delta\tau_d n_j)\,\mathrm{d}S \tag{13.78}$$

$$= -V_d\frac{\partial\{p\}}{\partial x_i} + V_d\frac{\partial\{\tau_{ij}\}}{\partial x_j} + L_{k,i}$$

The last term, $L_{k,i}$, represents the sum of all the other forces: the lift force, the steady-state drag, the virtual mass, and Basset term. Substituting this equation into Eq. (13.69) for the force yields

$$\frac{\partial}{\partial t}(\alpha_c\{\rho_c\}\tilde{u}_i) + \frac{\partial}{\partial x_j}(\alpha_c\{\rho_c\}\tilde{u}_j\tilde{u}_i) = -\alpha_c\frac{\partial\{p\}}{\partial x_i} + S_{\mathrm{mom},\dot{m}} \tag{13.79}$$

$$+ \alpha_c\frac{\partial}{\partial x_j}\{\tau_{ij}\} - \frac{\partial}{\partial x_j}(\alpha_c\{\rho_c u_i' u_i'\}) - \frac{1}{V}\sum_k L_{i,k} + \alpha_c\{\rho_c\}g_i$$

This is nearly the same form as obtained using ensemble averaging (Zhang and Prosperetti, 1997). With ensemble averaging, there is one additional term relating to the momentum transfer associated with the flow around individual particles. This effect is in the Reynolds stress term, which is not singled out by volume averaging.

If the $L_{k,i}$ force consists only of steady-state drag, the momentum equation becomes

$$\frac{\partial}{\partial t}(\alpha_c\{\rho_c\}\tilde{u}_i) + \frac{\partial}{\partial x_j}(\alpha_c\{\rho_c\}\tilde{u}_j\tilde{u}_i) = -\alpha_c\frac{\partial\{p\}}{\partial x_i} + S_{\mathrm{mom},\dot{m}} \tag{13.80}$$

$$+ \alpha_c\frac{\partial}{\partial x_j}\{\tau_{ij}\} - \frac{\partial}{\partial x_j}(\alpha_c\{\rho_c u_i' u_i'\}) - \frac{1}{V}\sum_k 3\pi\mu_c d_k f_k(u_i - v_{i,k}) + \alpha_c\{\rho_c\}g_i$$

where f_k is the ratio of the drag to Stokes drag for particle k. If all the dispersed-phase elements have the same size and move at the same speed, v_i, then the momentum equation simplifies to

$$\frac{\partial}{\partial t}(\alpha_c\{\rho_c\}\tilde{u}_i) + \frac{\partial}{\partial x_j}(\alpha_c\{\rho_c\}\tilde{u}_j\tilde{u}_i) = -\alpha_c\frac{\partial\{p\}}{\partial x_i} - n\dot{m}v_i \tag{13.81}$$

$$+ \alpha_c\frac{\partial}{\partial x_j}\{\tau_{ij}\} - \frac{\partial}{\partial x_j}(\alpha_c\{\rho_c u_i' u_i'\}) - \alpha_d\rho_d\frac{f}{\tau_v}(u_i - v_i) + \alpha_c\{\rho_c\}g_i$$

In the case of bubbles, the steady-state drag is not the most important force and other forces, such as virtual mass, must be included.

If the dispersed-phase elements occupy no volume (point particles), then

$$\frac{\partial}{\partial t}(\{\rho_c\}\tilde{u}_i) + \frac{\partial}{\partial x_j}(\{\rho_c\}\tilde{u}_j\tilde{u}_i) = -\frac{\partial\{p\}}{\partial x_i} - n\dot{m}v_i \tag{13.82}$$

$$+ \frac{\partial}{\partial x_j}\{\tau_{ij}\} - \frac{\partial}{\partial x_j}(\{\rho_c u_i' u_i'\}) - \overline{\rho}_d\frac{f}{\tau_v}(u_i - v_i) + \{\rho_c\}g_i$$

where $\overline{\rho}_d$ is the bulk density of the dispersed phase.

In DNS of multiphase flows, averaging is not used. In the case of point particles, the equation of motion for the continuous phase is

$$\frac{\partial}{\partial t}(\rho_c u_i) + \frac{\partial}{\partial x_j}(\rho_c u_i u_j) = -\frac{\partial p}{\partial x_i} + \frac{\partial\tau_{ij}}{\partial x_j} + \rho_c g_i + f_{p,i} \tag{13.83}$$

where $f_{p,i}$ is the force acting at the point due to the neighboring the dispersed-phase elements. Some of the examples of DNS are provided in Section 13.2.3. Further, examples using DNS and LES with point particles can be found in Boivin et al. (2000)

13.3.4 Energy Equation

There are two forms for the energy equation: the total energy equation that includes the kinetic energies, and the thermal energy equation, which addresses the change of thermal properties of the fluid. The thermal energy equation is obtained by subtracting the dot product of the local velocity and the momentum equation from the total energy equation. The result is

$$\frac{\partial}{\partial t}(\rho_c i_c) + \frac{\partial}{\partial x_i}(\rho_c u_i i_c) = -p\frac{\partial u_i}{\partial x_i} + \tau_{ij}\frac{\partial u_i}{\partial x_j} - \frac{\partial \dot{q}_i}{\partial x_i} \tag{13.84}$$

where i_c is the internal energy of the continuous phase and $\dot{q}_i$ is the heat transfer rate to the continuous phase. If the fluid is incompressible, then $\partial u_i/\partial x_i = 0$ and the first term on the RHS disappears. The second term is the dissipation term, which is always positive, and represents the irreversible conversion of mechanical into thermal energy. This term will be represented by ϕ. The equation reduces to

$$\frac{\partial}{\partial t}(\rho_c i_c) + \frac{\partial}{\partial x_i}(\rho_c u_i i_c) = \phi - \frac{\partial \dot{q}_i}{\partial x_i} \tag{13.85}$$

Performing the volume-averaging operation on this equation yields

$$\frac{\partial}{\partial t}(\alpha_c\{\rho_c\}\tilde{i}_c) + \frac{\partial}{\partial x_i}(\alpha_c\{\rho_c u_i i_c\}) \tag{13.86}$$

$$= -\frac{1}{V}\sum_k \dot{m}_k i_{s,k} + \alpha_c\{\phi\} + \frac{\partial}{\partial x_i}\left(k_{\text{eff}}\frac{\partial\langle T_c\rangle}{\partial x_i}\right) + \sum_k \dot{q}_k$$

where the first term on the RHS is the energy input due to mass transfer from the dispersed phase carried out over all elements in the control volume. This term will be designated as $S_{\text{ener},\dot{m}}$.

The third term is the conductive heat transfer through the mixture where k_{eff} is the thermal conductivity for the mixture. A first-order model for k_{eff} would be

$$k_{\text{eff}} = \alpha_c k_c + \alpha_d k_d \tag{13.87}$$

where k_c and k_d are the thermal conductivities of the continuous and dispersed phases, respectively. The last term is the conductive heat transfer from the dispersed-phase elements to the continuous phase. It would be evaluated by

$$\sum_k \dot{q}_k = \pi k_c \sum_k Nu_k d_k (T_{d,k} - \{T_c\}) \tag{13.88}$$

where Nu_k is the Nusselt number and the summation is carried out over all elements in the control volume.

The convection term on the LHS of the Eq. (13.85) can be rewritten as

$$\frac{\partial}{\partial x_i}(\alpha_c\{\rho_c u_i i_c\}) = \frac{\partial}{\partial x_i}(\alpha_c\{\rho_c\}\{u_i\}\tilde{i}_c) + \frac{\partial}{\partial x_i}(\alpha_c\{\rho_c\}\{u_i' i_c'\}) \tag{13.89}$$

where u_i' and i_c' are the deviation in velocity and internal energy from the averaged values. The additional term can be regarded as the heat transfer due to turbulent fluctuations, analogous to Reynolds stress, and possibly may be modeled as

$$\{\rho_c\}\{u_i''i_c''\} \simeq k_t \frac{\partial\{T_c\}}{\partial x_i} \tag{13.90}$$

where k_t is the heat transfer coefficient due to turbulence, which may be determined from the experiment or, possibly, PDF methodologies. By Reynolds analogy, one can make an estimate for k_t using $k_t \simeq \mu_e c_m$, where c_m is the specific heat of the mixture and μ_e is defined by Eq. (13.76).

Taking the internal energy as the product of the temperature and specific heat allows one to write the energy equation as

$$\frac{\partial}{\partial t}(\alpha_c\{\rho_c\}c_m\{T_c\}) + \frac{\partial}{\partial x_i}(\alpha_c\{\rho_c\}\tilde{u}_i c_m\{T_c\}) \tag{13.91}$$

$$= S_{ener,\dot{m}} + \alpha_c\{\phi\} - \frac{\partial}{\partial x_i}\left[(\alpha_c c_m \mu_e + k_{eff})\frac{\partial\{T_c\}}{\partial x_i}\right]$$

$$+ \pi k_c \sum_k N u_k d_k (T_{d,k} - \{T_c\})$$

In actual applications of this equation, order or magnitude analyses would be useful to eliminate terms, that can be neglected. The form of the equation is similar to that reported in Zhang and Prosperetti (1997).

13.3.5 Turbulence Equations

Several derivations of the equations for the turbulent energy of the continuous phase have appeared in the literature. Most of the derivations (e.g., Elghobashi and Abou-Arab, 1973; Chen and Wood, 1975), begin with the momentum equation in the form

$$\frac{\partial}{\partial t}(\alpha_c\rho_c u_i) + \frac{\partial}{\partial x_j}(\alpha_c\rho_c u_j u_i) = -\alpha_c\frac{\partial p}{\partial x_i} + \alpha_c\frac{\partial}{\partial x_j}\tau_{ij} - f_i + \alpha_c\rho_c g_i \tag{13.92}$$

where f_i is the force of the disperse phase on the continuous phase per unit volume of mixture. The derivations proceed using a Reynolds decomposition to develop the equations for turbulence energy in the same manner as for single-phase flows. The above equation implies that the velocities are defined at a point, which is not the case for averaged equations. This equation can only be regarded as a short-hand notation for the actual momentum equation (13.79) where the velocities are volume–averaged. Reynolds decomposition using volume (or ensemble)-averaged velocities does not yield the fluctuation velocity

$$\{u_i\} - \widehat{\{u_i\}} \neq u_i' \tag{13.93}$$

Unfortunately, there is a whole body of literature based on this misconception (Crowe, 2000).

Another approach (Crowe, 1998) is to start with the mechanical energy equation for the continuous phase obtained, by taking the dot product of the momentum equation and the velocity. The resulting equation is

$$\frac{\partial}{\partial t}\left(\rho_c\frac{u_i u_i}{2}\right) + \frac{\partial}{\partial x_j}\left(\rho_c u_j\frac{u_i u_i}{2}\right) = -u_i\frac{\partial p}{\partial x_i} + u_i\frac{\partial\tau_{ij}}{\partial x_j} + \rho_c u_i g_i \tag{13.94}$$

By taking the volume average of this equation and subtracting the dot product of Eq. (13.79) and $\{u_i\}$, one obtains an equation for the turbulence kinetic energy

$$k_c = \left\{\frac{u_i' u_i'}{2}\right\} \tag{13.95}$$

in the form

$$\frac{\partial}{\partial t}(\alpha_c\rho_c k_c) + \frac{\partial}{\partial x_i}(\alpha_c\rho_c\{u_i\}k_c) \tag{13.96}$$

$$= \frac{\partial}{\partial x_i}\left(\sigma_c \frac{\partial k_c}{\partial x_i}\right) - \alpha_c \rho_c \{u_i' u_j'\} \frac{\partial \{u_i\}}{\partial x_j}$$

$$+ \alpha_d \rho_d \frac{f}{\tau v} |\{u_i\} - \{v_i\}|^2 + \alpha_d \rho_d \frac{f}{\tau v} (\{v_i' v_i'\} - \{u_i' v_i'\})$$

$$- \alpha_c \varepsilon$$

where the unsteady forces on the disperse phase have been neglected and all dispersed-phase elements are assumed to have the some size. This equation has the same terms as for single-phase flow. The first two terms on the RHS are the diffusion and generation of turbulence and the last term on the RHS is the dissipation. The dissipation is given by

$$\varepsilon = \left\{ \frac{\partial u_i'}{\partial x_j} \frac{\partial u_i'}{\partial x_j} \right\} \tag{13.97}$$

There are two additional terms that account for the presence of the dispersed phase. The third term on the RHS is the turbulence generation due to particle drag. The fourth term relates to the kinetic energy transfer between phases and is generally much smaller than the third term. Similar forms of the turbulence energy equation have been reported by Liljegren and Fosslein (1994), Hwang and Shen (1993), Kataoka and Serizawa (1989), and Kashiwa and VanderHeyden (2000).

Equations for the dissipation of turbulence are generally adhoc extensions of the dissipation equations used for single-phase flow. More developments with the dissipation equation can be found in Kashiwa and VanderHeyden (2000).

More information on multiphase turbulence is provided in Section 12.6.

13.4 Dispersed Phase Equations

A. Berlemont, Clayton T. Crowe, M. Reeks, and O. Simonin

There are essentially three approaches to modeling the particle flow field. One approach to follow individual particles or sample particles. This is the Lagrangian approach. Another technique is to treat the particles as a cloud with continuum-like equations. This is the Eulerian approach. Another approach is to use particle ditribution functions (PDF approach) to describe the particle flow properties.

13.4.1 Lagrangian Approach

A. Berlemont and Clayton T. Crowe

The Lagrangian approach is applicable to both dilute and dense flows. In dilute flows, the time between particle–particle collisions is larger than the response time of the particles (or droplets), so the motion of the particles is controlled by the particle fluid interaction, body forces, and particle-wall collisions. In a dense-phase flow, the response time of the particles is longer than the time between collisions; thus particle–particle interaction not only controls the dynamics of the particles, but is also influenced by the hydrodynamic and body forces as well as particle–wall interaction. If the flow is steady and dilute, a form of the Lagrangian approach known as the *trajectory method* (Crowe et al., 1977) is easy to implement. If the flow is unsteady and dense, a more general *discrete element approach* is necessary.

13.4.1.1 Trajectory Method

The trajectory approach can be explained best with reference to an example. Consider a nozzle spraying a liquid at a steady rate into the chamber shown in Figure 13.48. Assume, that the flow is steady, so the spatial distribution of the carrier flow properties is invariant with time. The flow field is subdivided into a series of computational cells as shown. The inlet stream is discretized into a series of starting

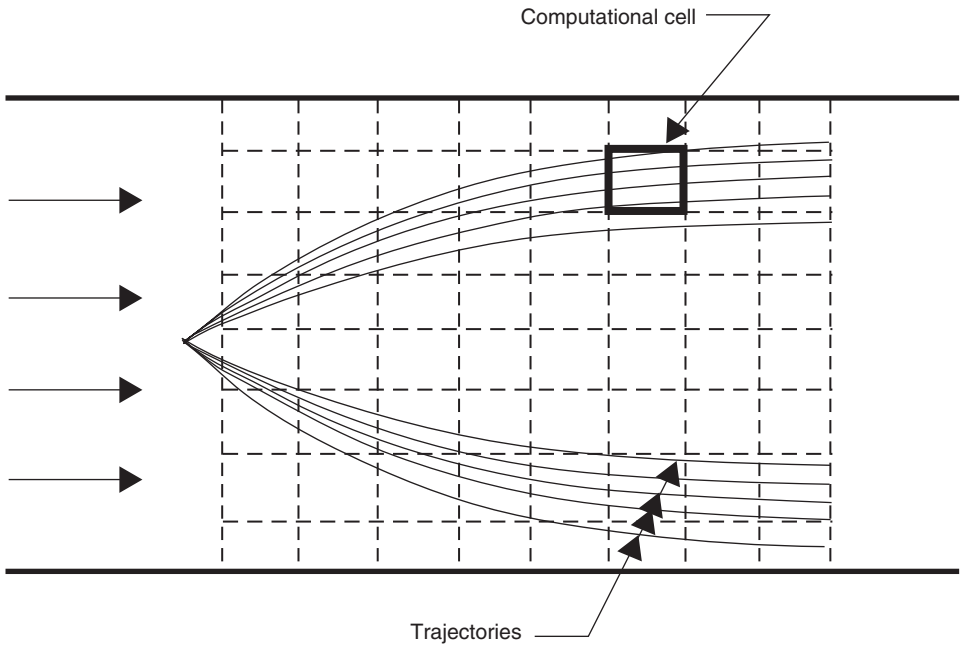

FIGURE 13.48 Droplet trajectories in a spray.

trajectories. If the initial droplet velocity and mass are known, the droplet velocity can be calculated by solving the droplet motion equation (Section 1.4) in the flow field, namely,

$$\frac{\mathrm{d}\mathrm{v}}{\mathrm{d}t} = \frac{\mathbf{F}_\mathrm{f}}{m} + \mathrm{g} \tag{13.98}$$

where $\mathbf{F}_\mathrm{f}$ is the fluid forces (form and friction forces) acting on the droplet of mass m and g, the gravity vector. The trajectory is obtained from

$$\frac{\mathrm{d}\mathrm{x}_\mathrm{p}}{\mathrm{d}t} = \mathrm{v} \tag{13.99}$$

where x_p is the droplet position. The integration scheme to be used depends on the desired accuracy and computational efficiency.

Concurrently, the droplet temperature history can be calculated using

$$\frac{\mathrm{d}T_\mathrm{d}}{\mathrm{d}t} = \frac{1}{mc_\mathrm{d}}(\dot{Q}_\mathrm{d} + \dot{m}h_\mathrm{L}) \tag{13.100}$$

where $\dot{Q}_\mathrm{d}$ is the sum of both the convective and radiative heat transfer to the particle or droplet. If the Biot number of the droplet is large, this equation must be modified to account for the fact that the surface temperature is not the average temperature in the droplet.

The droplet mass transfer must also be calculated along the trajectory according to the relations given in Section 1.4. Evidently, the droplet diameter must be adjusted to conform with the droplet mass unless the application is the drying of a porous particle.

Assume that the mass flow entering from the atomizer is discretized into j trajectories and the mass flow associated with each trajectory is $\dot{M}(j)$. Then the number flow rate along trajectory j would be

$$\dot{n}(j) = \frac{\dot{M}(j)}{(\pi/6)\rho_\mathrm{d} d_0^3} \tag{13.101}$$

where ρ_d is the material density of the droplet and d_0 the initial droplet diameter. If no droplet breakup or coalescence occurs, the flow rate number will be invariant along each trajectory. Of course, more detail is possible obtained by discretizing the starting conditions according to a size distribution as well. For example, if $\tilde{f}_m(D_s)$ is the fraction of particle mass associated with size D_s (see Chapter 3), then the number flow rate associated with size D_s on trajectory j would be

$$\dot{n}(j, D_s) = \frac{\tilde{f}_m(D_s)\dot{M}(j)}{(\pi/6)\rho_d D_s^3} \tag{13.102}$$

Obviously more detail requires more trajectories and increased computational time. In an axisymmetric flow, if the starting locations are discretized to a series of concentric rings, the mass flow rate on each ring must be weighted with the ring radius.

Once all the trajectories are calculated, the properties of the particle cloud in each computational cell can be determined. The particle number density is found using

$$n = \frac{\sum_{\text{traj}} \dot{n}\Delta t_j}{V} \tag{13.103}$$

where Δt_j is the time required for the particle to traverse the cell on trajectory j and V the volume of the computational cell. The summation is carried out over all trajectories which traverse the cell. The particle volume fraction in each computational cell can be determined from

$$\alpha_d = \frac{\sum_{\text{traj}} \dot{n}_j \overline{V}_d \Delta t_j}{V} \tag{13.104}$$

where $\overline{V}_d$ is the average droplet volume along trajectory j in the cell. Other properties such as bulk density, particle velocity, and temperature can be determined in the same way. Thus, the properties of the cloud can be determined once all the trajectories have been calculated.

Particle or droplet wall collisions are included in the calculation by continuing the trajectory after wall collision, according to the models presented in Section 12.4.2. New velocities are established depending on the nature of the collision. In the case of a droplet impact, the droplet may splatter on the surface and the trajectory is terminated or the trajectory is restarted with smaller droplets. In the case of annular mist flows, one would model reentrainment by initializing trajectories of droplets from the liquid layer on the wall. The specific conditions depend on the model selected for the problem.

The Lagrangian method has been the basis of many numerical simulations of gas–particle and gas-droplet flows.

13.4.1.2 Discrete Element Method

If the flow is unsteady and dense (particle–particle collisions are important), the more general discrete element method is required. In this approach, the motion and position (as well as other properties) of individual particles, or representative particles, are tracked with time. Ideally, one would like to track each and every particle, but this may not be computationally feasible. For a gas laden with 100 μm particles at a mass concentration of unity, there would be an order of 10^9 particles/m^3. If the flow field of interest were one tenth of a cubic meter, then 10^8 particles would have to be tracked through the field. This is impractical, so a smaller number of computational particles are chosen to represent the actual particles. For example, if 10^4 computational particles were chosen, then each computational particle would represent 10^4 physical particles. This computational particle is regarded as a parcel of particles. It is assumed then that the parcel of particles moves through the field with the same velocity and temperature, as a single particle (physical particle). Of course, size distribution effects can be included by specifying parcels with a specific particle size. The parcel is identified as a discrete element. In some simulations, such as fluidized beds, it may not be possible to use parcels of particles without forgoing the details necessary to simulate the system, so the dynamics of each individual particle must be considered.

The equation for particle motion now assumes the form

$$\frac{\mathrm{dv}}{\mathrm{d}t} = \frac{\mathbf{F}_\mathrm{f} + \mathbf{F}_\mathrm{c}}{m} + \mathrm{g} \tag{13.105}$$

where $\mathbf{F}_\mathrm{c}$ is the force due to particle–particle (and particle–wall) contact.

Establishing the initial conditions for the discrete elements, depends on the problem. For the example shown in Figure 13.49, a parcel could be the droplets emerging along a starting trajectory j in time interval Δt_p. Thus, the number of droplets in the parcel would be $N_\mathrm{p} = \dot{n}(j, d_\mathrm{s})\ \Delta t_\mathrm{p}$, and the initial velocity would be determined from other information. For modeling a fluidized bed, the initial state may be all the particles at rest as a packed bed, and the interstitial gas flow initiates the motion.

The motion of each parcel over one time interval is obtained by integrating the particle motion equation. At the same time, the particle temperature, spin, and other properties can be calculated. A field with a distribution of sample particle parcels is shown in Figure 13.49. During the time step, there may be particle–particle collisions that alter the trajectories and change the distribution of the parcels in each computational cell.

At every time step, the properties of the droplet cloud can be determined by summing over all the particles in a computational volume. For example, the number density would be

$$n = \frac{\sum_p N_p}{V} \tag{13.106}$$

where the summation is carried out over all the parcels in the computational cell. Also the particle volume fraction would be

$$\alpha_\mathrm{d} = \frac{\sum_p N_p V_{\mathrm{d},p}}{V} \tag{13.107}$$

where $V_{\mathrm{d,p}}$ is the volume associated with an individual particle and N_p the number of particles in parcel p. The calculation of other properties such as bulk density and particle velocity is obvious. The distribution of

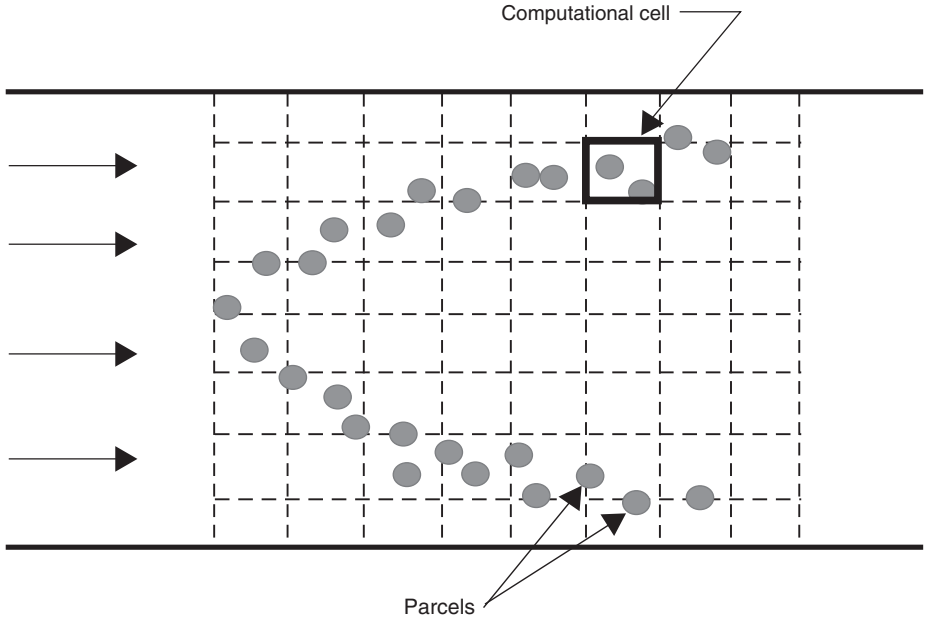

FIGURE 13.49 Distribution of droplet parcels in a spray field.

the volume fraction of the solid phase is important in calculating the interstitial flow field. If each discrete element is an individual particle, then N_p in the above equations is unity.

13.4.1.3 Source Term Evaluation

The mass source term for a computational cell is simply the sum of the mass added by every droplet in the cell:

$$S_{\text{mass}} = -\sum_k \dot{m}_k \tag{13.108}$$

where $\dot{m}_k$ is the rate of change of mass of droplet k and the summation is carried out over every droplet in the cell. The minus sign indicates that a droplet losing mass is adding mass to the carrier phase. The mass source term using the trajectory approach is evaluated by

$$S_{\text{mass}} = -\sum_{\text{traj}} \dot{n}_j \overline{\dot{m}}\, \Delta t_j \tag{13.109}$$

where $\overline{\dot{m}}$ is the average mass evaporation rate of the droplet during its traverse through the cell. The mass source term is evaluated using the discrete element approach by

$$S_{\text{mass}} = -\sum_p N_p \dot{m}_p \tag{13.110}$$

where summation is carried out over all parcels, which occupy the cell at the given time and $\dot{m}_p$ is the mass evaporation (or condensation) rate of the individual droplets in the parcel. The mass source term per unit volume is

$$S_{\text{mass}} = \frac{S_{\text{mass}}}{V} \tag{13.111}$$

where V is the volume of the computational cell.

The momentum source term in the i direction is given by

$$S_{\text{mom}} = -\sum_k (\mathrm{F}_{\text{f},k} + \mathrm{v}_k \dot{m}_k) \tag{13.112}$$

where $F_{\text{f},k}$ is the fluid forces acting on the droplet and v_k the velocity of droplet k. The force would include both a lift and drag force, but would not include the forces due to pressure gradient, shear stress gradient, and body forces. For the case in which the transient drag forces and lift forces are unimportant, the momentum source term for the trajectory approach becomes

$$S_{\text{mom}} = -\sum_{\text{traj}} \dot{n}_j \Delta t_j \left[m_j \frac{f_j}{\tau_{v,j}} (\mathrm{v}_j - \mathrm{u}) - \dot{m}_j \mathrm{v}_j \right] \tag{13.113}$$

where v_j is the average velocity of droplets, f_j the drag factor and $\tau_{v,j}$ is the velocity response time for the particles on trajectory j. The corresponding momentum source term for the discrete element approach is calculated by

$$S_{\text{mom}} = \sum_p N_p \left[m_p \frac{f_p}{\tau_{\text{v},p}} (\mathrm{v}_p - \mathrm{u}) - \dot{m}_p \mathrm{v}_p \right] \tag{13.114}$$

where the subscript p refers to particles or droplets in the packet. Note that the body force due to gravity is not included in this expression.

The source term for the total energy equation using the trajectory approach is

$$S_{\text{ener}} = -\sum_{\text{traj}} \dot{n}_j \Delta t_j \left[\dot{Q}_j + \dot{m}_j \left(h_{\text{s},j} + \frac{|\mathrm{v}|_j^2}{2} \right) + \mathrm{F}_{\text{f},j}\, \mathrm{v}_j \right] \tag{13.115}$$

where $h_{\text{s,j}}$ is the enthalpy of the carrier phase at the surface of the droplet on trajectory j and $\dot{Q}_k$ the convective heat transfer to the droplet (radiative heat transfer is not included). The corresponding source

term for the discrete element method is

$$S_{\text{ener}} = -\sum_{\text{p}} N_p \left[\dot{Q}_p + \dot{m}_p \left(h_{\text{s},p} + \frac{|\text{v}|_p^2}{2} \right) + \text{F}_{\text{f},p}\, \text{v}_p \right] \tag{13.116}$$

If the transient drag forces and lift forces are unimportant, the energy source term due to the dispersed phase is

$$S_{\text{ener}} = \sum_{\text{p}} N_p \left[\frac{Nu_p}{2} \frac{m_p c_{\text{d}}}{\tau_{T,p}} (T_{\text{d},p} - T_{\text{c}}) - \dot{m}_p \left(h_{\text{s},p} + \frac{|\text{v}|_p^2}{2} \right) + m_p \frac{f_p}{\tau_{v,p}} (\text{v} - \text{u})_p\, \text{v}_p \right] \tag{13.117}$$

The source terms for the thermal energy equation can be evaluated in the same fashion.

Source terms can also be evaluated for the turbulence energy and dissipation depending on the models used.

13.4.1.4 Calculation of Particle–Droplet Trajectories in Dilute Turbulent Flows

In ditute two-phase flows the particle motion is controlled by the fluid–particle interaction. The relationships for calculating the trajectories is given by Eqs. (13.98) and (13.99). The force on the particle involves the lift and drag which depends on the fluid velocity at the particle position, $\text{u}_p = f(\text{x}_p, t)$. In turbulent flow, the fluid velocity is the instantaneous velocity, the accurate prediction of which is the primary difficulty in Lagrangian tracking. The instantaneous velocity is decomposed into a mean value (interpolated on particle position) and a fluctuating part, u'_p. Developing techniques to generate the fluctuating part is the primary problem.

Methods based on DNS provide an accurate simulation of turbulence in simple flows (Yeung and Pope, 1989; Elghobashi and Truesdel, 1993; Wang and Maxey, 1993; Eaton and Fessler, 1994) but are limited to small Reynolds numbers and are not useful for practical applications. LES can handle more complex flows (Squires and Eaton, 1990; Wang and Squires, 1996; Boivin et al., 2000) but the majority of models for engineering problems are based on complete stochastic modeling. This section will address RANS modeling, such as the k–ε model, supplemented with algebraic models to account for anisotropy or Reynolds stress models for more accurate prediction of Reynolds stress.

A significant problem in evaluating the fluid velocity at the particle location derives from the fact that the particle does not follow the fluid path. There are three aspects to this problem.

When no body force is included, particle motion is controlled by the particle mass and drag force. The key parameter is the particle relaxation time, τ_V, that describes the particle response to any fluctuation of the surrounding fluid. For turbulent flow, the relevant scale for fluctuating velocities is the Lagrangian integral time scale, τ_L, and the time scale ratio τ_L/τ_V quantifies the influence of turbulence on the particle motion.

In the presence of a body force such as gravity, a relative mean velocity is generated between the discrete particle and the carrier fluid. In this case, it is obvious that the discrete particle no longer follows the same fluid element or eddy, but is continuously crossing several eddies on its trajectory. This behavior is called crossing trajectory effects as first described by Yudine (1959) and Csanady (1963) and experimentally studied by Wells and Stock (1983). It has been observed that the fluid velocity correlation along the particle trajectory is overestimated by the time scale τ_L, and particle dispersion is correspondingly reduced.

The third effect that can also modify the particle behavior is due to the continuity of the fluid turbulence. The fluid mass conservation equation implies that an eddy that is crossing a plane parallel to the mean flow direction must be replaced by an eddy crossing the same plane in the opposite direction. The net result of this effect is the occurrence of positive and negative fluid velocity correlations in the corresponding direction along the particle trajectory, and thus a decrease in particle dispersion. The continuity effect is a consequence of the difference on the Eulerian fluid velocity correlation with respect to the average velocity. It is known from turbulence theory that if there are no negative loops in the longitudinal correlation, then negative loops will be involved in the transverse correlation.

From the work of Csanady (1963) on stationary homogeneous turbulence with gravity, an integral time scale along the discrete particle trajectory that takes into account crossing trajectory effects and continuity effects can be derived in the form

$$\tau_L^p = \frac{\tau_L}{\sqrt{1 + \beta^2\xi^2}} \tag{13.118}$$

in the direction parallel to the gravitational force and

$$\tau_L^p = \frac{\tau_L}{\sqrt{1 + 4\beta^2\xi^2}} \tag{13.119}$$

in the direction normal to the gravitational force. β is the ratio between the Lagrangian integral time scale and the Eulerian time scales and ξ the ratio between the discrete particle mean velocity (here the free fall velocity) and the fluid velocity rms. It will be shown further that these scales can be used in a one-step approach.

13.4.1.4.1 Eddy Lifetime Model

Historically, the first approach to the stochastic modeling of turbulence was developed by Gosman and Ioannides (1981) and has been used widely in engineering calculations. It is referred to as the eddy lifetime model. In this scheme, the particle is assumed to interact with a succession of eddies. Each eddy is characterized by a velocity (fluctuating), a time scale (lifetime), and length scale (size). The fluctuation velocity is randomly sampled from a Gaussian PDF with variance determined from the turbulence kinetic energy, k. The eddy lifetime is related to the integral time scale, τ_L, and the length scale is defined by

$$l_e = b\frac{k^{3/2}}{\varepsilon} \tag{13.120}$$

where ε is the dissipation rate and b is an empirical constant ranging from 0.16 to 0.46. The time for a particle to traverse an eddy is calculated from the particle velocity (at the beginning of the time step) and length scale

$$\tau_e = -\tau_v \ln\left(1 - \frac{l_e}{\tau_v|\mathbf{v} - \mathbf{u}_p|}\right) \tag{13.121}$$

The particle is assumed to interact with the eddy for a time that is the minimum of the eddy lifetime and the eddy transit time, τ_c. During the interaction time, the fluctuating fluid velocity is assumed constant. Following the interaction time, a new fluctuating velocity is sampled and the process is repeated. Note that in the limit of very small particles that identify fluid particles, the process generates a linear decrease for the fluid Lagrangian correlation function from 1 to 0 in a time delay equal to $2\tau_L$.

The original scheme has been extended in order to include inertia, continuity, and crossing trajectory effects. An analysis of the performance of variants of the eddy lifetime model has been investigated by Graham (1998).

13.4.1.4.2 Coupled Fluid and Particle Trajectories

This method is based on the simultaneous realization of a fluid trajectory and a particle trajectory. Originally developed by Ormancey (1984), the method has been adapted by Zhou and Leschziner (1991), Burry and Bergeles (1993), and Pascal and Oesterlé (2000), among others.

Figure 13.50 presents an overview of the method. Initially the fluid particle and discrete particle are at the same location. Then the fluid particle F is moved to location $x_F\ (t + \delta t)$ using a one-step stochastic procedure with respect to the fluid Lagrangian integral time scale. In the particular case of fluid particles, the stochastic scheme implies an exponential decrease in the fluid Lagrangian correlation. The discrete particle trajectory P is calculated using the particle equation of motion. The fluid velocity is then transferred from the fluid position to the particle position $x_p\ (t + \delta t)$ according to the Eulerian correlation. The process is then repeated.

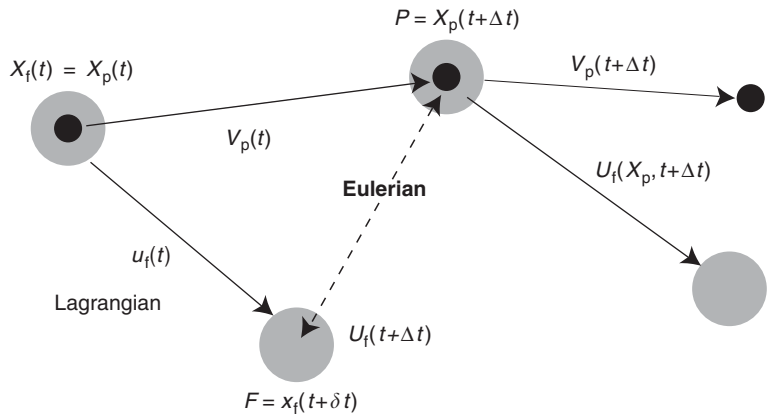

FIGURE 13.50 Coupled fluid and particle trajectories in one-time step.

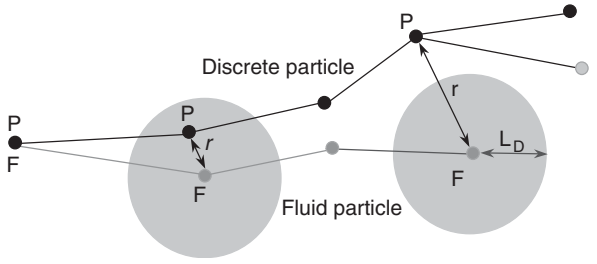

FIGURE 13.51 Coupled fluid and particle trajectories and correlation domain.

This approach has been extended by Berlemont et al. (1990) and includes the correlation matrix method for fluid trajectories in order to handle any kind of correlation. The method is depicted on Figure 13.51. The locations of the fluid particle and discrete particle are calculated simultaneously for several time steps. The fluid velocity at the particle location is determined by the use of Eulerian correlations. This process is carried out until the discrete particle leaves a correlation domain corresponding to the fluid particle. When the distance r between the two particles is greater than the correlation length scale L_D, a new fluid particle is sampled on the discrete particle location and the process is repeated. This scheme accounts for the crossing trajectory effects in a very physical way. It also allows one to incorporate the continuity effect through the Eulerian correlation. It is apparent that whatever method is chosen, the essential problem is the determination of the fluid velocity at the position of the discrete particle.

Using the same ideas with a spatial correlation of a random process for the temporal correlation, it is assumed that the fluid velocity at point P can be expressed as (in one dimension)

$$u'_P = \gamma u'_F + \eta y \tag{13.122}$$

where

$$\gamma = \frac{\langle u'_P u'_F \rangle}{\sqrt{\langle (u'_P)^2 \rangle \langle (u'_F)^2 \rangle}}$$

and

$$\eta = \langle (u'_F)^2 \rangle^{1/2} \sqrt{1 - \gamma^2}$$

When anisotropy of the flow is involved, a change of coordinate system is first carried out, where the first unit vector direction is the direction from x_F to x_P. The above relation is extended to 3D case through the equivalent expression:

$$\mathbf{u}'_P = \{\gamma\}\mathbf{u}'_F + \{\eta\}\mathbf{y}_s \tag{13.123a}$$

$$\{\gamma\} = \langle \mathbf{u}'_P \mathbf{u}'^T_F \rangle \langle \mathbf{u}'_F \mathbf{u}'^T_F \rangle^{-1} \tag{13.123b}$$

$$\{\eta\}\{\eta\}^T = \langle \mathbf{u}'_F \mathbf{u}'^T_P \rangle - \{\gamma\}\langle \mathbf{u}'_F \mathbf{u}'^T_F \rangle \{\gamma\}^T \tag{13.123c}$$

Any kind of relation can be used for the correlation coefficients. For example, the Frenkiel function may be used where the loop parameters n_i and n_{ij} can be specified:

$$\langle u'_{i,F} u'_{i,P} \rangle = \sqrt{\langle u'^2_{i,F} \rangle}\sqrt{\langle u'^2_{i,P} \rangle} \exp\left[\frac{-r}{(n_i^2 + 1)L_{E_i}} \right] \cos\left[\frac{n_i r}{(n_i^2 + 1)L_{E_i}} \right] \tag{13.124a}$$

and

$$\langle u'_{i,F} u'_{j,P} \rangle = \langle u'_{i,F} u'_{j,F} \rangle \exp\left[\frac{-r}{(n_{ij}^2 + 1)L_{E_{ij}}} \right] \cos\left[\frac{n_{ij} r}{(n_{ij}^2 + 1)L_{E_{ij}}} \right] \tag{13.124b}$$

The loop parameter n_i can help to introduce the continuity effect in the Eulerian correlation, namely, by choosing $n_i = 0$ in the main flow direction and $n_i = 1$ in the transverse directions. When no information is available on the length scales, the following relations can be used:

$$L_{E_{ii}} = \sqrt{\langle u'^2_i \rangle}\tau_{L_i} \tag{13.125}$$

where

$$\tau_{L_i} = C\text{ste}\frac{\langle u'^2_i \rangle}{\varepsilon}$$

and *C*ste ranges between 0.2 and 0.6. Also

$$L_{E_{ij}} = C_{ij}\tau_{L_{ij}}\sqrt{|\langle u'_i u'_j \rangle|} \tag{13.126}$$

where

$$\tau_{L_{ij}} = C_{L_{ij}} \frac{|\langle u'_i(t) u'_j(t) \rangle|}{\varepsilon}$$

and $C_{ij} = C_{L_{ij}} = 1$.

13.4.1.4.3 One-Step Scheme

Another approach, based on a one-step stochastic process, is to approximate the fluid velocity at the particle location with respect to the time scale viewed by the fluid along the particle path. It means that the Lagrangian step and the Eulerian step of the previous method are mixed to give a simpler stochastic scheme. The key issue is then the approximation of the time and length scales T^*, which characterize the fluid viewed by the particles. A Langevin equation is used:

$$u'_{pi}(t + \delta t) = a u'_{pi}(t) + b y_i \tag{13.127}$$

where

$$a = \exp\left(-\frac{\delta t}{T_i^*} \right)$$

and

$$b = \langle u'^2_{pi}(t)\rangle^{1/2}\sqrt{1-a^2}$$

Different expressions can be found in the literature for scales and for the fluid velocity correlation along discrete particle trajectory. By assuming gravity is in the third dimension, Wang and Stock (1992) proposed

$$R_{33}(\tau) = \exp\left\{-\frac{\tau}{T^p_{\rm f}}\sqrt{1+\left(\frac{v_d T^p_{\rm f}}{L_{\rm f}}\right)^2}\right\} \tag{13.128a}$$

$$T^*_3 = \frac{T^p_{\rm f}}{\sqrt{1+\left(\frac{v_{\rm d}T^{\rm p}_{\rm f}}{L_{\rm f}}\right)^2}} \tag{13.128b}$$

$$R_{11}(\tau) = R_{22}(\tau) = \left(1-\frac{v_{\rm d}\tau}{2L_{\rm f}}\right)R_{33}(\tau) \tag{13.128c}$$

and

$$T^*_1 = T^*_2 = \frac{T^p_{\rm f}}{1+(v_d T^p_{\rm f}/L_{\rm f})^2}\left[\sqrt{1+\left(\frac{v_{\rm d}T^p_{\rm f}}{L_{\rm f}}\right)^2}-\frac{v_{\rm d}T^p_{\rm f}}{2L_{\rm f}}\right] \tag{13.128d}$$

where the fluid integral time scale along the particle path depends on Stokes number:

$$T^p_{\rm f}(Stk) = T_{\rm mE}\left[1-\frac{1-T_{\rm L}/T_{\rm mE}}{(1+Stk)^{0.4/(1+0.01Stk)}}\right] \tag{13.129}$$

where $v_{\rm d}$ is the drift velocity, $T_{\rm mE}$ is the Eulerian time scale, Stk the Stokes number, and $L_{\rm f} = \sigma_{\rm f}T_{\rm mE}$.

Applying the same philosophy, Pozorski and Minier (1998) proposed in a Langevin model:

$$T^*_3 = \frac{T^*_{\rm L}}{1+(v_{\rm d}T^*_{\rm L}/\sigma_{\rm f}T_{\rm E})} \tag{13.130}$$

and

$$T^*_1 = T^*_2 = \frac{T^*_{\rm L}}{1+2(v_{\rm d}T^*_{\rm L}/\sigma_{\rm f}T_{\rm E})} \tag{13.131}$$

where $T^*_{\rm L}$ is given by

$$\frac{1}{T^*_{\rm L}} = \frac{x}{\tau_{\rm L}} + \frac{1-x}{T_{\rm E}} \tag{13.132}$$

with

$$x = \frac{\sigma_{\rm p}}{\sigma_{\rm f}}$$

The problem is the evaluation of x. One possible approach is to assume that Tchen's theory is valid (stationary isotropic turbulence) and x satisfies

$$x = \sqrt{\frac{1}{1+\tau_v/\tau_{\rm L}}} \tag{13.133}$$

Another version of the one-step method is that introduced by Sommerfeld et al. (2001). In this model, the component of fluid velocity fluctuation in the i direction, at the new particle position, u'_{in+1}, is correlated with the old position through a correlation function by

$$u'_{i,n+1} = u'_{i,n}R_{p,i}(\Delta t,\Delta r) + \sigma\sqrt{1-R^2_{p,i}(\Delta t,\Delta r)}\xi_i \tag{13.134}$$

where $R_{p,i}(\Delta t, \Delta r)$ is the correlation function, σ the mean fluctuation velocity of the fluid at the particle position, and ξ_i a Gaussian random number selected for the i direction with zero mean and standard deviation of unity. The mean fluid fluctuation velocity is obtained from the kinetic energy k by

$$\sigma^2 = 2k/3 \tag{13.135}$$

The correlation function in the i direction is decomposed into a Lagrangian and Eulerian part according to

$$R_{p,i}(\Delta t, \Delta r) = R_{\mathrm{L}}(\Delta t) \times R_{\mathrm{E},i}(\Delta r) \tag{13.136}$$

where the exponential form

$$R_{\mathrm{L}}(\Delta t) = \exp\left(-\frac{\Delta t}{T_{\mathrm{L}}}\right) \tag{13.137}$$

is selected for the Lagrangian part. The Lagrangian time scale is determined from

$$T_{\mathrm{L}} = c_{\mathrm{T}}\frac{\sigma^2}{\varepsilon} \tag{13.138}$$

where ε is the dissipation rate.

The spatial correlation function can be obtained from Eulerian correlation tensor (Von Karman and Horwarth, 1938)

$$R_{\mathrm{E},ij}(\Delta r) = \{f(\Delta r) - g(\Delta r)\}\frac{r_i r_j}{r^2} + g(\Delta r)\delta_{ij} \tag{13.139}$$

where $f(\Delta r)$ and $g(\Delta r)$ are exponential functions of the separation distance and the integral length scales. Generally, only the three main components of the tensor are used and the integral length scales are related to the T_{L} and σ.

These different schemes have been compared extensively with theoretical and experimental results. But it is important to keep in mind that all these schemes are very sensitive to scale approximation and particle dispersion is roughly proportional to the turbulence time and length scales.

13.4.1.5 Calculation of Particle Motion in Dense Flows

In dense flows, the particle motion is controlled by particle–particle collisions. Different approaches can be developed to study and to understand the underlying physical processes. Simulations on the basis of tracking several particles simultaneously (Tanaka and Tsuji, 1991; Chang, 1998; Berlemont et al., 1998) have been developed. Also Lagrangian simulations have been proposed based on single-particle tracking with stochastic process for collisions (Oesterlé and Petitjean, 1993; Sommerfeld, 1995, 2001; Berlemont and Achim, 1999; 2001; Berlemont et al., 2001).

In the multiple-particle method, several particles are tracked simultaneously and particle pairs are examined on each time step in order to determine if any collision is taking place. Since the number of simultaneous trajectories is limited by computational constraints, the simulation is carried using several starting points for a given number of particles. They are initially randomly distributed in a box, the size of which is established by the mean distance between particle centers derived from the initial concentration and geometry for the case under study. The multiple-particle method is obviously quite expensive in CPU time. Moreover, the multiple-particle method is unrealistic for industrial purposes. In addition, it was found that the overall particle–particle velocity correlation (referring to the two colliding particles) induced by the surrounding fluid is an important parameter requiring particular attention.

In the stochastic approach for particle collisions, a collision probability is defined and a random process is used to first decide if a collision occurs. Several successive random processes are then involved in order to characterize the collision partner in terms of velocity, concentration, impact location, and diameter when polydispersed particles are considered.

13.4.1.5.1 The Stochastic Collision Model

Using the classical one-particle Lagrangian approach, a stochastic particle–particle collision model is needed, as described by Sommerfeld (2001) and Berlemont et al. (2001). The model first requires information on the collision frequency. It is assumed that the fluctuating motion of the discrete phase is similar to the thermal motion of molecules in a gas. A collision frequency can then be estimated by analogy with the kinetic theory.

Consider two particle classes, which are identified through the diameters d_1 and d_2 (radius r_1 and r_2), the instantaneous velocities v_1 and v_2, and the number of particles per unit of volume, n_{p1} and n_{p2}. The collision frequency with which particle 1 collides with particle 2 is

$$f_{\text{coll}} = \frac{\pi}{4}(d_1 + d_2)^2 n_{p2} \int_{-\infty}^{+\infty} |v_{\text{rel}}| f_p^{(2)} \, \mathrm{d}v_1 \, \mathrm{d}v_2 \tag{13.140}$$

where $|v_{\text{rel}}| = |v_2 - v_1|$,

The most important term in the above equation is the particle–particle pair distribution function $f_p^{(2)}$. If is assumed that the colliding particle velocities are independent (molecular chaos assumption), then the particle velocity distribution is Gaussian:

$$f_p^{(1)} = \frac{1}{(2\pi\langle v'^2\rangle)^{3/2}} \exp\left(-\frac{v^2}{2\langle v'^2\rangle}\right) \tag{13.141}$$

and the particle–particle pair distribution function is the product of the two distribution functions. The collision frequency then reduces to (Abrahamson, 1975; Gourdel et al., 1999)

$$f_{\text{coll}} = \frac{\pi}{4}(d_1 + d_2)^2 n_{p2} \|v_{\text{rel}}\| H(z) \tag{13.142}$$

with

$$H(z) = \frac{\exp(-z)}{\sqrt{\pi z}} + \operatorname{erf}\sqrt{z}\left(1 + \frac{1}{2z}\right)$$

and

$$z = \frac{1}{2} \frac{\|v_{\text{rel}}\|^2}{\langle v_1^2\rangle + \langle v_2^2\rangle}$$

The variable z represents the ratio between the mean particle relative velocity and the particle turbulent fluctuation velocity. For large values of z (high drift velocity), $H(z)$ tends to unity, hence:

$$f_{\text{coll}} = \frac{\pi}{4}(d_1 + d_2)^2 n_{p2} \|\langle v_1\rangle - \langle v_2\rangle\| \tag{13.143}$$

and the collision frequency depends essentially on mean particle relative velocity. Using a Taylor expansion for $H(z)$ for small values of z (low drift velocity) leads to

$$f_{\text{coll}} = \frac{2^{3/2}\pi^{1/2}}{4}(d_1 + d_2)^2 n_{p2} \|\langle v_1^2\rangle + \langle v_2^2\rangle\| \tag{13.144}$$

which means that the collision frequency depends primarily on the particle agitation.

The collision probability p_{12} of particle 1 to collide with particle 2 then reads:

$$p_{12} = f_{\text{coll}} \Delta t \tag{13.145}$$

where the time step Δt is assumed to be small enough (of the order of $\tau_c/10$ where $\tau_c = 1/f_{\text{coll}}$). To decide whether there is a collision or not, a uniform random number (between 0 and 1) is sampled and the collision occurs when it is smaller than the collision probability. Velocities of a fictitious collision partner are then sampled from the local properties.

When two particles collide, the first problem is to determine the point of contact on the particle surfaces. A coordinate system $(Ox'y'z')$ is moved such that the main axis (Ox') is in the v_{rel} direction and O is the center of the tracked particle (Figure 13.52a). A uniformly distributed random number β between 0 and 1 is used to obtain the normalized impact parameter b ($b = B/(r_1 + r_2) = \sqrt{\beta}$) and another uniform random number is then chosen to get the α angle, with $0 \leq \alpha \leq 2\pi$ (Figure 13.52b). The new coordinate system $(Ox''y''z'')$ is now used with Ox'' at the particle center direction (Figure 13.52c), and Ψ and Φ angles are defined by

$$\Psi = \arctan\left(\frac{b\sin\alpha}{\sqrt{1 - b^2\sin^2\alpha}}\right) \quad \text{and} \quad \Phi = \arctan\left(\frac{-b\cos\alpha}{\sqrt{1 - b^2}}\right) \tag{13.146}$$

When the point of impact is located, the change in particle velocity has to be calculated. These relation ships for doing so are provided in Section 12.4.1. Returning to the initial coordinate system completes the process.

When comparing the stochastic approach with LES results, it is found that the molecular chaos assumption was not satisfied. The scheme has to account for the correlation between the fluctuating motion of the colliding particles caused by the surrounding fluid. In order to overcome this problem, Sommerfeld (2001) has recently proposed correlating the fictitious particle velocities with velocities of the real particle through the following relation:

$$v_{2,i} = R(Stk)v_{1,i} + \sigma_i\sqrt{1 - R(Stk)^2}\xi \tag{13.147}$$

where σ_i is the rms value of the velocity component i, ξ a Gaussian random number, and $R(Stk)$ given (comparing model calculations to LES results) by

$$R(Stk) = \exp(-0.55Stk^{04}) \tag{13.148}$$

This relation improves the results but is still based on empiricism.

Another approach utilizes an exact relation for the particle–particle pair distribution function $f_p^{(2)}$ which is not the product of two independent distributions $f_p^{(1)}$ for correlated velocities. The correlation between the colliding particle velocities in the turbulent eddy through which they are moving has to be introduced in the distribution function. This important consideration was first stated and solved by Lavieville et al. (1995) for two identical particles. Pigeonneau (1998) proposed an extension for particles with different diameters with no empiricism required. Berlemont et al. (2001) recently proposed to use that approach for particle Lagrangian tracking with particle collisions. The results are limited to nondeformable spherical particles. When the interface between the two phases is not rigid, interface tracking

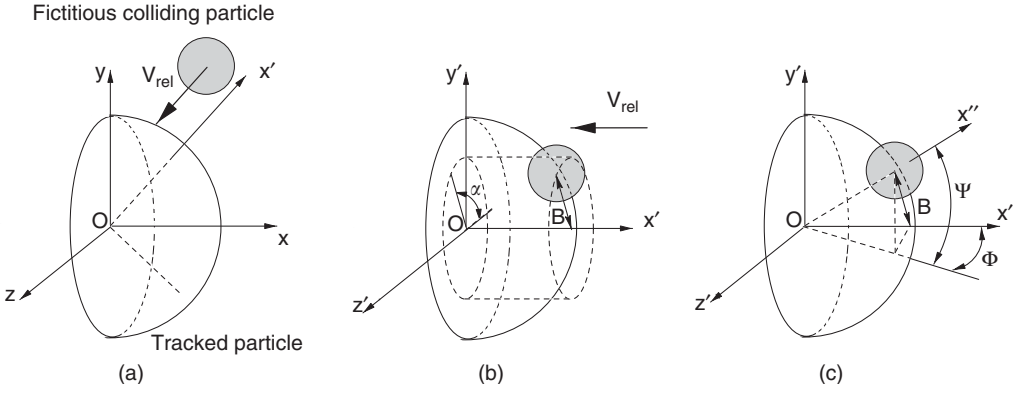

FIGURE 13.52 Sampling point of contact in particle collision.

methods are then used, namely, the volume of fluid method, or the front tracking method, or the Level set method. The examples of calculations with dense-phase flows are provided in Section 13.2.2.

13.4.2 Eulerian Approach

Clayton T. Crowe

In the Eulerian approach, the particle or droplet cloud is treated as a continuous medium with properties analogous to those of a fluid. For example, the bulk density, or mass of particles per unit volume of mixture, is regarded as a continuous property. The particle velocity is the average velocity over an averaging volume. The purpose of this section is to develop and present the governing equations for the Eulerian approach. In that the continuous phase is a fluid, the use of the Eulerian approach for the dispersed phase is commonly referred to as the two-fluid or Eulerian–Eulerian approach. The terms will be used interchangeably here.

A significant advantage of the Eulerian approach is that the equations for both phases have the same form so the same solution techniques can be used for each phase.

There are several levels of description for the Eulerian approach. If the Stokes number is sufficiently small, the particles and carrier fluid will have the same velocity (velocity equilibrium). If the characteristic time used in the definition of the Stokes number is a time representative of the carrier-phase turbulence, a small Stokes number implies that the particles will move with and disperse at the same rate as the carrier flow. In this case, the two-phase mixture can be regarded as a single phase with modified properties (density, thermal capacity, etc.). If the Stokes number is based on some characteristic time of the flow field, a small Stokes number implies that the particles will move with the mean motion of the carrier flow but may not disperse at the same rate due to turbulence.

Of more practical interest is the situation where the velocities of the carrier fluid and particles are not the same. This could be the result of velocity gradients in the mean flow field, turbulent fluctuations, and body forces acting on the particles. The local particle velocity is regarded as the average velocity of particles in an averaging volume

$$\{\mathrm{v}\} = \frac{\sum_k \mathrm{v}_k}{N} \tag{13.149}$$

where N is the number of particles in the volume and $\{\ \}$ is used to denote volume averaging. Another possibility would be the mass-averaged velocity defined by

$$\tilde{\mathrm{v}} = \frac{\sum_k m_k \mathrm{v}_k}{\sum_k m_k} \tag{13.150}$$

where m_k is the mass of particle k in the averaging volume. This type of averaging is referred to as Favre averaging.

The Eulerian dispersed-phase equations are obtained by summing the conservation equations for individual particles (or droplets) over all particles in the control volume to obtain equations for a particle cloud. A cloud of particles or droplets in a Cartesian control volume is shown in Figure 13.53. The fundamental finite-difference equations are derived by taking into account the flux of properties over all faces. The finite-difference equations are then divided by the control volume and the limit is taken as the volume approaches the limiting value. More details are available in Crowe et al. (1998). Index notation is used throughout.

13.4.2.1 Continuity Equation

The basic continuity equation for each dispersed-phase element is $\mathrm{d}m/\mathrm{d}t = \dot{m}$. Summing the rate of mass change of all the elements in the computational cell and equating it to the net efflux of droplet mass through the control surfaces plus the rate of change of mass in the cell yields

$$\frac{\partial}{\partial t}(\alpha_\mathrm{d}\rho_\mathrm{d}) + \frac{\partial}{\partial x_\mathrm{i}}(\alpha_\mathrm{d}\rho_\mathrm{d}\tilde{v}_\mathrm{i}) = \sum_k \dot{m}_k / V \tag{13.151}$$

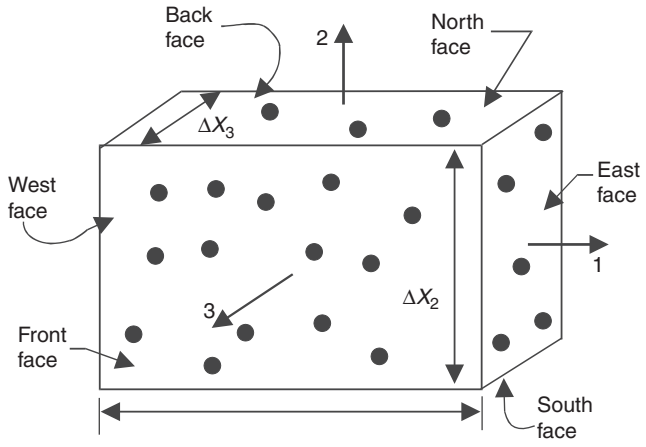

FIGURE 13.53 Three-dimensional control volume for dispersed-phase elements.

where $\tilde{v}_i$ is the mass-averaged velocity of the dispersed phase, α_d the volume fraction of the dispersed phase, and ρ_d the material density of the dispersed phase. The summation is carried out over all droplets in the control volume *V*. The last term in the equation is the mass source term for the dispersed phase, which can be written as $-S_{mass}$. The minus sign comes from the fact that S_{mass} is the mass source term for continuous phase that is negative for the dispersed phase.

If the simple average velocity is used *in lieu* of the mass-averaged velocity, the continuity equation has to be formulated differently. In this case, the velocity in the averaging volume is expressed as

$$v_i = \{v_i\} + v_i' \tag{13.152}$$

where v_i' is the deviation of the velocity from the averaged value. Similarly, the bulk density, ρ_d, is written as

$$\overline{\rho}_d = \overline{\rho}_{d,0} + \overline{\rho}_d' \tag{13.153}$$

where $\overline{\rho}_{d,0}$ is the bulk density at the central point and $\overline{\rho}_d'$ the deviation in bulk density at adjacent points, so the average mass flux is

$$\langle \overline{\rho}_d v_i \rangle = \langle \overline{\rho}_d \rangle \langle v_i \rangle + \langle \overline{\rho}_d' v_i' \rangle \tag{13.154}$$

The additional term can be regarded as a mass diffusion term. In a flow with homogeneous bulk density or uniform particle velocities, this term would be zero. Turbulence, however, will produce a distribution of particle velocities, which will give rise to a net mass flux in nonhomogenous particle density fields.

The gradient transport model is used in the two-fluid formulation to simulate dispersion of particles in turbulent flows. With reference to Fick's law it is assumed that

$$\langle \tilde{\rho}_d v_i' \rangle = -D_d \frac{\partial \overline{\rho}_d}{\partial x_i} \tag{13.155}$$

where D_d is the dispersion coefficient for the dispersed phase. The value for the dispersion coefficient has to be determined from experiment or through some auxiliary analysis. Picard et al. (1986) predicted a dispersion coefficient based on an early analysis of particle motion in turbulence reported by Tchen (1949). Adjustments are necessary to account for crossing trajectory effects. Rizk and Elghobashi (1989) employed a semiempirical correlation suggested by Picard et al. Unfortunately, there are no simple analyses or models, which will provide D_d as a function of particle properties and flow turbulence, so the choice of an appropriate value depends on finding or reducing a value from an experiment which is

considered representative of the flow field to be simulated. Reeks has shown through the PDF approach (Section 13.4.3) that the gradient diffusion model is not universally applicable.

A further problem exists with boundary conditions. If the particles bounce specularly from a wall, it is probably appropriate to set the gradient of the bulk density normal to the wall equal to zero. If the bouncing is not specular, another approximation must be made. If droplets impact the wall and there is no reentrainment, setting bulk density equal to zero at the wall does not represent a realistic boundary condition for the bulk density field. The choice of suitable boundary conditions is addressed in Section 13.4.3 for reflecting and perfectly absorbing walls.

The final form for the two-fluid continuity equation using the volume-averaged velocity is

$$\frac{\partial}{\partial t}(\alpha_{\mathrm{d}}\rho_{\mathrm{d}}) + \frac{\partial}{\partial x_i}(\alpha_{\mathrm{d}}\rho_{\mathrm{d}}\{v_i\}) = \frac{\partial}{\partial x_i}\left(D_{\mathrm{d}}\frac{\partial \overline{\rho}_{\mathrm{d}}}{\partial x_i}\right) - S_{\mathrm{mass}} \tag{13.156}$$

If F_{avre} (mass averaging) is used, the diffusion term is eliminated.

13.4.2.2 Momentum Equation

The momentum equation for an individual dispersed-phase element of mass m is

$$m\frac{\mathrm{d}v_i}{\mathrm{d}t} = F_i + mg_i \tag{13.157}$$

This equation is valid for an reacting droplet, provided the mass is leaves the surface uniformly. That is, it does not contribute to the momentum of the droplet. Adding $\dot{m}v_i$ to each side gives

$$\frac{\mathrm{d}mv_i}{\mathrm{d}t} = \dot{m}v_i + F_i + mg_i \tag{13.158}$$

The forces acting on the element are

$$F_i = -V_{\mathrm{d}}\frac{\partial\{p_{\mathrm{c}}\}}{\partial x_i} + V_{\mathrm{d}}\frac{\partial\{\tau_{\mathrm{c},ij}\}}{\partial x_j} + L_i \tag{13.159}$$

where $\{p_{\mathrm{c}}\}$ and $\{\tau_{\mathrm{c},ij}\}$ are the average pressure and shear stress in the continuous phase, respectively. The force L_i includes all the other forces including the lift force, the steady-state drag, the virtual mass force, and the Basset force. In flows with heavy particles, only the steady-state drag may be important.

The momentum equation can also be developed by summing over every dispersed-phase element in the computational cell. The resulting differential equation is

$$\frac{\partial}{\partial t}(\alpha_{\mathrm{d}}\rho_{\mathrm{d}}\tilde{v}_i) + \frac{\partial}{\partial x_j}(\alpha_{\mathrm{d}}\rho_{\mathrm{d}}\tilde{v}_i\tilde{v}_j) = \sum_k \dot{m}_k v_{i,k}/V - \alpha_{\mathrm{d}}\frac{\partial p}{\partial x_j} \tag{13.160}$$

$$\alpha_{\mathrm{d}}\frac{\partial}{\partial x_i}\tau_{ij} + \sum_k L_{i,k} + \alpha_{\mathrm{d}}\rho_{\mathrm{d}}g_i - \alpha_{\mathrm{d}}\frac{\partial}{\partial x_j}\left(\sum_k \overline{\rho}_{\mathrm{d},k}v'_i v'_{k,j}\right)$$

where $\tilde{v}_i$ is the mass-averaged velocity and the fluctuation velocity $v'_{i,k}$ is the deviation of the velocity of the kth particle from the mass average velocity.

The first term on the RHS of Eq. (13.158) is the momentum source due to mass exchange between phases. This term is expressed as $-S_{\mathrm{mom},i}$, namely,

$$-\sum_k \dot{m}_k v_{\mathrm{i},k}/V = -S_{\mathrm{mom},i} \tag{13.161}$$

This term represents the momentum associated with the mass issued from the surface of the droplets moving at velocity $V_{i,k}$. The negative sign is chosen so that momentum addition to the carrier phase is defined as positive.

The last term is analogous to a Reynolds stress

$$\tau^{\mathrm{R}}_{\mathrm{d},ij} = -\sum_k \overline{\rho}_{\mathrm{d},k}v'_{k,i}v'_{k,j} \tag{13.162}$$

and is identified as the dispersed-phase Reynolds stress. This term arises because the mass-averaged velocity is not a momentum-averaged velocity. Traditionally, the dispersed-phase Reynolds stress has been modeled using the Boussinesq approximation (stress proportional to the rate of strain):

$$\tau_{ij}^{R} = \mu_s \left(\frac{\partial v_i}{\partial x_j} + \frac{\partial v_j}{\partial x_i} \right) - \frac{2}{3} \mu_s \frac{\partial v_k}{\partial x_k} \delta_{ij} \tag{13.163}$$

where μ_s is an *solids viscosity*. It is very difficult to select a solids viscosity, since the particle velocity fluctuations depend not only on local turbulence but also on the particle properties and particle history. Chung et al. (1986) related the solids viscosity to the eddy viscosity of the carrier fluid through a function, which depends on the Stokes number based on the integral time scale of the carrier-phase turbulence. Rizk and Elghobashi (1989) simply used a constant ratio between the solids viscosity and the fluid eddy viscosity. The problem with the Boussinesq approximation is that one can visualize a Reynolds stress without a gradient in the mean velocity field (no rate of strain), because the turbulent fluctuations of particles will give rise to a nonzero value for the dispersed-phase Reynolds stress.

The momentum equation, Eq. (13.158), is also valid for a field of bubbles. In the same way, the Reynolds stress term relates to the fluctuations in bubble velocity. A similar form of the dispersed-phase momentum equation is presented in Zhang and Prosperetti (1997).

If the forces acting on the particles or droplets are only the drag forces and the unsteady terms can be neglected, then the momentum equation becomes

$$\frac{\partial}{\partial t}(\alpha_d \rho_d \tilde{v}_i) + \frac{\partial}{\partial x_j}(\alpha_d \rho_d \tilde{v}_i \tilde{v}_j) = -\alpha_d \frac{\partial p}{\partial x_i} - S_{mom,i} + \alpha_d \frac{\partial}{\partial x_j}(\tau_{ij}) + \frac{3\pi\mu_c}{V} \sum_k d_k f_k (u_i - v_i)_k + \alpha_d \rho_d g_i + \alpha_d \frac{\partial}{\partial x_j} \tau_{d,ij}^{R} \tag{13.164}$$

where m_k is the mass of particle k, λ_k the ratio of the drag to Stokes drag, and τ_V the velocity response time. If all the droplets have the same mass and evaporate at the same rate, the momentum equation reduces to

$$\frac{\partial}{\partial t}(\alpha_d \rho_d v_i) + \frac{\partial}{\partial x_j}(\alpha_d \rho_d v_i v_j) = -\alpha_d \frac{\partial p}{\partial x_i} + n\dot{m} v_i + \alpha_d \frac{\partial}{\partial x_j}(\tau_{ij} + \tau_{d,ij}^{R}) + n 3\pi\mu_c d f (u_i - v_i) + \alpha_d \rho_d g_i \tag{13.165}$$

The dispersed-phase Reynolds stress can arise from several sources, particle velocity fluctuations due to the carrier-phase turbulence, and particle–particle collisions. Even with no carrier-phase turbulence or collisions, the Reynolds stress term would appear due to particle velocity variations arising from a distribution in particle size. Such a situation would occur for a particle-laden flow at the throat of a venturi, where the smaller particles would tend to move at a velocity near the local fluid velocity, while the larger particles would exhibit a larger velocity lag. In this special case, the Reynolds stress due to velocity variation could be circumvented by introducing a momentum equation for each particle size category.

Kinetic theory models have been used to derive relationships for the solids viscosity and other parameters for dense phase flows. An additional equation is included for the kinetic energy of the fluctuating motion of the particulate phase. Because of the similarities between particle–particle interactions and molecular interactions in a gas, the concepts from kinetic theory can be used to develop the governing equations for dense-phase flows. This approach is nominally credited to Bagnold (1954), who derived an equation for repulsive pressure in uniform shear flow. Many others, particularly Savage (1983), have further contributed to this approach. Complete details of the derivations and applications to dense-phase flows can be found in Gidaspow (1994). The basic concept is that particle–particle collisions are responsible for momentum and energy transfer in the dense-phase flow in the same way as the molecular interactions are responsible for pressure wave propagation and viscosity in a single-phase fluid.

The kinetic energy associated with the particle velocity fluctuations is called the granular temperature and defined as

$$\Theta = \frac{1}{3}\langle C^2 \rangle \tag{13.166}$$

where C is the fluctuational velocity of the particle motion. Granular temperature can be produced by a shearing action in the granular flow and by hydrodynamic forces. Dissipation can occur through inelastic particle–particle and particle–wall collisions and dissipation in the fluid. Granular temperature can also be diffused in the same manner as heat. The stress term in the momentum equation based on kinetic theory becomes (Gidaspow, 1994)

$$\tau_{d,ij} = \left[-p_s + \xi_s \frac{\partial v_k}{\partial x_k} \right] \delta_{ij} + \mu_s \left(\frac{\partial v_j}{\partial x_i} + \frac{\partial v_i}{\partial x_j} \right) - \frac{2}{3} \frac{\partial v_k}{\partial x_k} \delta_{ij} \tag{13.167}$$

where p_s is the solids pressure, ξ_s the solids phase bulk viscosity, and μ_s the solids shear viscosity. These three parameters are functions of the granular temperature as well as the particle restitution coefficient, particle diameter, material density, and volume fraction. The solids pressure is

$$p_s = \rho_d \alpha_d \Theta [1 + 2(1 + e) g_o \alpha_d] \tag{13.168}$$

where g_o is referred to as a radial distribution function

$$g_o = \frac{3}{5} \left[1 - \left(\frac{\alpha_d}{\alpha_{d,max}} \right)^{1/3} \right]^{-1}$$

The solids-phase bulk viscosity assumes the form

$$\xi_s = \frac{4}{3} \alpha_d^2 \rho_s d g_o (1 + e) \left(\frac{\Theta}{\pi} \right)^{1/2} \tag{13.169}$$

and the shear viscosity is

$$\mu_s = \frac{2\mu_{s,dil}}{(1 + e) g_o} \left[1 + \frac{4}{5} (1 + e) g_o \alpha_d \right]^2 + \frac{4}{5} \alpha_d^2 \rho_s d g_o (1 + e) \left(\frac{\Theta}{\pi} \right)^{1/2} \tag{13.170}$$

where $\mu_{s,dil}$ is the solids-phase dilute viscosity given by

$$\mu_{s,dil} = \frac{5\sqrt{\pi}}{96} \rho_d d \Theta^{1/2} \tag{13.171}$$

An additional equation is needed for Θ which relates the change in Θ to the generation by velocity gradients, the dissipation with collisions and the diffusion due to gradients in Θ. The details are available in Gidaspow (1994).

Several numerical models have been implemented for dense-phase flows using the two-fluid models based on granular temperatures. These include flow in chutes, fluidized beds, and sedimentation. Sinclair and Jackson (1989) have used the two-fluid model for modeling dense flows in vertical tubes. Section 13.5.3 provides an application of two-fluid modeling for predicting flow in a fluidized bed using kinetic theory for the constituitive equations. There are several advantages in using the two-fluid model for dense-phase flows. The most significant advantage is that there is no need to consider the dynamics of individual particles, so large systems can be modeled. Also, the numerical formulations used for single-phase flows can be applied to the two-fluid equations for the solid phase. However, there is a level of empiricism that must be introduced in establishing the constitutive equations. Also, features such as particle–particle sliding, particle rotation, and particle size distribution are not included.

The granular temperature model should also extend to dilute flows. In this case, the hydrodynamic effects on particle oscillation in turbulence would have to be more accurately modeled. Extensions of the two-fluid model to dilute flows have been reported by Bolio and Sinclair (1996). In dense flows, the particle–particle contribution to particle fluctuation energy is more significant than that due to local turbulence in the continuous phase.

The PDF approach introduced in Section 13.5.3 provides a more rational approach to evaluating the particle-phase Reynolds stress due to carrier-phase turbulence and particle–particle collisions. This approach, still in development, will yield more reliable models for the Reynolds stress with minimal empiricism.

13.4.2.3 Thermal Energy Equation

The energy equation for an individual dispersed-phase element is

$$\frac{\mathrm{d}}{\mathrm{d}t}(mi_{\mathrm{d}}) = -\dot{m}\frac{p_{\mathrm{s}}}{\rho_{\mathrm{d}}} - \frac{\mathrm{d}}{\mathrm{d}t}(S_{\mathrm{d}}\sigma) + \dot{m}h_{\mathrm{s}} + \dot{Q}_{\mathrm{d}} \tag{13.172}$$

where p_{s} is the pressure at the surface, S_{d} the surface area of the element, σ the surface tension, h_{s} the enthalpy of the matter leaving the surface, and $\dot{Q}_{\mathrm{d}}$ the heat transfer rate to the dispersed-phase element, including both conductive and radiative heat transfer. The first term on the RHS is usually small and neglected.

The Eulerian thermal energy equation for the droplet cloud can be derived in the same way as the continuity and momentum equations by summing up the droplets in a control volume. By following the development in Crowe et al. (1998), the multidimensional thermal energy equation is

$$\frac{\partial}{\partial t}(\alpha_{\mathrm{d}}\rho_{\mathrm{d}}\tilde{\imath}_{\mathrm{d}}) + \frac{\partial}{\partial x_i}(\alpha_{\mathrm{d}}\rho_{\mathrm{d}}\tilde{v}_{\mathrm{in}}\tilde{\imath}_{\mathrm{d}}) = -\frac{\partial}{\partial x_j}\left(\sum_k \tilde{\rho}_{\mathrm{d},k}v'_{j,k}i'_{\mathrm{d},k}\right) \tag{13.173}$$

$$-\sum_k \dot{E}_{\sigma,k}/V + \sum_k \dot{m}_k h_{\mathrm{s},k}/V + \frac{2\pi k_{\mathrm{c}}}{V}\sum \lambda_k d_k (T_{\mathrm{c}} - T_{\mathrm{d}})_k + \sum_k \dot{Q}_{r,k}/V$$

where $\tilde{\imath}_{\mathrm{d}}$ is the mass-averaged droplet internal energy. The first term on the RHS, $\sum_k \tilde{\rho}_{\mathrm{d},k}v'_{j,k}i'_{\mathrm{d},k}$ is analogous to the Reynolds stress term and has to be modeled based on, for example, a gradient diffusion term.

$$-\frac{\partial}{\partial x_j}\left(\sum_k \tilde{\rho}_{\mathrm{d},k}v'_{j,k}i'_{\mathrm{d},k}\right) = \frac{\partial}{\partial x_j}\left(k_{\mathrm{s,eff}}\frac{\partial T_{\mathrm{d}}}{\partial x_j}\right) \tag{13.174}$$

where T_{d} is the dispersed-phase temperature and $k_{\mathrm{s,eff}}$ the effective thermal conductivity, which, currently, must be chosen empirically or through kinetic theory for dense flows. In future, PDF modeling will provide more accurate models for this term. The second term is the energy change associated with the surface tension; the third term is the energy (enthalpy) flux from the droplet surface, where $h_{\mathrm{s},k}$ is the enthalpy of the matter emerging at the surface of droplet k and is equal to $-S_{\mathrm{mass}}h_{\mathrm{s}}$; the fourth term is the convective heat transfer between the droplets and the carrier fluid, where

$$\lambda_k = Nu_k/Nu_o \tag{13.175}$$

is the ratio of the Nusselt number to the Nusselt number at zero Reynolds number ($\nu_o = 2$ with no free convection effects) and $\tau_{\mathrm{T},k}$ the thermal response time of particle k; the last term is the radiative heat transfer. In specific applications, many of these terms can be neglected. Particularly, the first and third terms on the RHS are zero for solid particles. These terms would generally be small compared with

convective heat transfer for droplet flows. For nonreactive particles, the source term associated with mass flux from the dispersed-phase surface would also be zero. Also, for many applications, radiative heat transfer may not be significant.

The internal energy is the product of both temperature and specific heat, so the energy equation written in terms of dispersed-phase temperature is

$$\frac{\partial}{\partial t}(\alpha_d \rho_d c_d T_d) + \frac{\partial}{\partial x_i}(\alpha_d \rho_d \tilde{v}_i c_d T_d) = \frac{\partial}{\partial x_j}\left(k_{s,\text{eff}} \frac{\partial T_d}{\partial x_j}\right) - S_{\text{mass}} h_s \tag{13.176}$$

$$-\sum_k \dot{E}_{\sigma,k}/V + \frac{2\pi k_c}{V} \sum \lambda_k d_k (T_c - T_d)_k + \sum_k \dot{Q}_{r,k}/V$$

where c_d is the specific heat of the dispersed-phase. If all the elements have the same size, same specific internal energy, and evaporation rate, and if the first and third terms are neglected, the thermal energy equation becomes

$$\frac{\partial}{\partial t}(\alpha_d \rho_d c_d T_d) + \frac{\partial}{\partial x_i}(\alpha_d \rho_d v_i c_d T_d) = -S_{\text{mass}} h_s + 2\pi n k_c \lambda d (T_c - T_d)$$

$$+ \frac{\partial}{\partial x_j}\left(k_{s,\text{eff}} \frac{\partial T_d}{\partial x_j}\right) + n\dot{Q}_r \tag{13.177}$$

where n is the number density. In dense flows there is also a heat transfer due to particle–particle contact, which is not included here.

13.4.2.4 Advantages and Disadvantages of the Two-Fluid Model

In general, the advantages are:

1. The numerical scheme used for the carrier phase can be used for the dispersed phase, so the two-fluid model may be more computationally efficient.
2. The model is limited by modeling large numbers of particles or droplets.

The disadvantages are:

1. The constituitive equations, which include the effects of carrier-phase turbulence, particle–particle collisions, and size distribution, are not well established.
2. The boundary conditions for mass, momentum, and energy are not straightforward.
3. The equations are not applicable as the flow becomes increasingly dilute.

As PDF methods and similar analyses are forthcoming, the disadvantages will be minimized.

13.4.3 PDF Models

M. Reeks and O. Simonin

13.4.3.1 Introduction

The PDF approach has proved very useful in studying the behavior of stochastic systems. Examples of its usage occur in the study of Brownian motion (Chandrasekhar, 1943) and in the kinetic theory of gases (Chapman and Cowling, 1952). In more recent times, it has been used extensively by Pope and others to model both turbulence (Pope, 1985) and turbulent-related phenomena such as combustion (Pope, 1991) and atmospheric dispersion (MacInnes and Bracco, 1992). In this section, the use of PDF approaches to

model the behavior of a particle-laden turbulent gas is described, where like kinetic theory for modeling gas flows, it may be regarded as a rational approach. This means : first there exists an underlying equation (a master equation) containing terms that can be traced back in a rational manner to the underlying equations of motion of the individual particles themselves. Second, this master equation, in a strictly formal way, can be used to derive both the continuum equations and constitutive relations of a gas or dispersed phase of particles while at the same time handle the natural boundary conditions at the wall (the so-called near-wall behavior). In kinetic theory, the master equation is the well-known Maxwell–Boltzmann equation, while in dispersed flows, it is known as the PDF equation.

There are currently two forms of the PDF equation in use. In the first form, the PDF, as in kinetic theory, refers to the probability density that a particle has a certain velocity and position at a given time. This PDF approach is referred to as the kinetic method (KM). Originated by Buyevich (1971, 1972a, 1972b), and has been developed since by a number of workers, most notably Reeks (1980, 1991, 1993), Hyland et al. (1999a, 1999b), Swailes and Darbyshire (1997), Derevich and Zaichik (1988), Zaichik (1991), Pozorski and Minier (1998) as well as Zhou and Li (1996) . In all these developments the PDF approach was restricted to inert, nonreactive particles. More recently, this approach has been extended to reactive condensing or evaporating particles in a turbulent gas (Pandya and Mashayek, 2001, 2003) and in polydispersed combusting sprays (Laurent and Massot, 2001).

In contrast, the second form of the PDF equation, first proposed by Simonin et al. (1993), is a more general PDF which includes the velocity of the carrier flow local to the particle as a phase-space variable as well as the particle position and velocity. It is a development of the PDF approach used by Haworth and Pope (1986) based on a generalized Langevin model (GLM) for the equation of motion of the carrier flow encounterd by a particle. It is referred here as the GLM approach.

As far as two-fluid modeling is concerned, the application of the PDF approach is different from what has been discussed earlier. In the past, for instance, it has been traditional to assume that the particle phase behaves as a simple Newtonian fluid (Elghobashi and Abou Arab, 1983), i.e., the particle Reynolds stresses are assumed to be proportional to the mean symmetric rate of strain of the particle flow via some particle eddy viscosity that is related to that of the carrier flow in some empirical way. Now, using the PDF approach, one can examine the validity of these assumptions within the context of a more reliable and complete framework using techniques that are well tested and understood and ultimately replace them with more legitimate relationships that do not rely on intuition and empiricism. Perhaps, more importantly, an approach that is crucial to the formulation of particle–wall interactions is now available. The particle–wall interactions are referred to here as the natural boundary conditions of a gas–particle flow.

In this section, it is shown how the PDF approach deals with both aspects of a two-fluid model with and without interparticle collisions; namely, how it generates the equations for mass, momentum and energy (the so-called continuum equations) and constitutive relations for the dispersed phase (that would be appropriate for the far-wall solution of a gas–particle flow) and how it generates near-wall solutions that take into account the inhomogeneity of the flow and the natural boundary conditions.

The section has been divided into two parts. The first part deals with a dilute suspension of particles in a turbulent gas and the second part with a dense suspension where interparticle collisions play an equally important part as the underlying turbulence of the gas. In the first part, a basic introduction to PDFs and PDF equations is provided and how they are derived in principle from the underlying particle equations of motion. This introduces the problem of closure of PDF equations, which is the essential problem of all stochastic systems involving turbulence. As an example, it is shown how this has been tackled for the particular case of nonreactive particles in a turbulent gas, examining how it has been dealt with as a closure approximation in the KM approach or through a model for the carrier flow velocity fluctuations encountered by a particle in the case of the GLM approach. This important aspect constitutes the subject of Section 13.4.3.2.

Section 13.4.3.3 deals with the continuum equations and constitutive relations derived from the PDF equations, where the focus is on transport equations for the particle velocity covariance (kinetic stresses)

and the particle fluid covariances. In either case, there is a need for closure approximations for the particle turbulent kinetic energy flux and that of the particle-fluid covariance flux which are tackled using the Chapman–Enskog approach. Predictions are compared with measurements of the particle dispersion of particles in nonuniform unbounded flows, where the local strain rate of the continuous phase introduces a strong anisotropy in the particle kinetic stresses.

Section 13.4.3.4 is concerned with the application of the PDF approach to the prediction of near-wall behavior; in particular, natural boundary conditions involving partial absorption and both specular and diffuse reflection are considered. Finally, the solutions for the well-known problem of particle deposition in a turbulent boundary layer with perfectly absorbing walls are addressed (this is a much studied system both theoretically and experimentally) which highlights the break down of so-called gradient transport due to both strong inhomogeneity of the flow near the wall and the strong departure of the velocity distribution at the wall compared with that in the far wall (bulk flow).

The remaining part of the section is devoted to the treatment of interparticle collisions using the PDF approach and follows largely the approach adopted by Lavieville et al. (1995).

13.4.3.2 PDFs and PDF Equations

As an example of how PDFs and their equations are obtained, consider the motion of evaporating or condensing particles in a dilute suspension in which there are no inter-particle collisions. Let $\mathbf{X}(t)$ be the phase-space vector at time t of a single particle as it moves through phase space. So in this case,

$$\mathbf{X} = [m, \Theta, \mathbf{v}, \mathbf{x}] \tag{13.178}$$

where m is the mass of the particle, Θ the temperature, and $\mathbf{v}$, $\mathbf{x}$ are the velocity and position of the particle center of mass at time t. The number n of independent variables that defines the phase-space dimension is thus $n = 8$. For a single realization of the underlying carrier flow velocity field $\mathbf{u}(\mathbf{x}, t)$ and temperature field $T(\mathbf{x}, t)$, the number of particles in an elemental volume $d^n\mathbf{X}$ of phase space located at $\mathbf{X}$ will be given by $W(\mathbf{X}, t)d^n\mathbf{X}$, where $W(\mathbf{X}, t)$ is the phase-space density, i.e., the number of particles per unit volume in phase space. So for conservation of particle number within that elemental volume at $\mathbf{X}$ with respect to W, one has

$$\frac{\partial W}{\partial t} + \frac{\partial}{\partial \mathbf{X}}[W\dot{\mathbf{X}}] = 0 \tag{13.179}$$

So, for the case of the evaporating droplet one would have explicitly

$$\dot{\mathbf{X}} = [\dot{m}, \dot{\Theta}, \dot{v}, \dot{\mathbf{x}}] \tag{13.180}$$

where the components of $\dot{\mathbf{X}}$ represents the *particle equations of motion* in the most general sense and are derived from the mass, momentum and energy conservation equations for an individual particle-droplet. However, because the underlying carrier flow field is turbulent, $\dot{\mathbf{X}}$ has a random component, so one can only usefully refer to the PDF corresponding to a set of values $\mathbf{X}$ at any given time. This is represented by the ensemble average of W over all realizations of the system, symbolically as $\langle W \rangle$. The equation for $\langle W \rangle$ (the PDF equation) can be found by ensemble averaging the conservation equation for W (Liouville equation). For convenience, the instantaneous components of $\dot{\mathbf{X}}$ are separated into their mean $\langle \dot{\mathbf{X}} \rangle$ and fluctuating components $\dot{\mathbf{X}}'$, noting that $\dot{\mathbf{X}} = \mathbf{v}$, so the explicit PDF equation for the evaporating-condensing particle is

$$\frac{\partial \langle W \rangle}{\partial t} + \left(\frac{\partial}{\partial m}\langle \dot{m} \rangle + \frac{\partial}{\partial \Theta}\langle \dot{\Theta} \rangle + \frac{\partial}{\partial \mathbf{x}}\cdot\mathbf{v} + \frac{\partial}{\partial \mathbf{v}}\cdot\langle \dot{\mathbf{v}} \rangle \right)\langle W \rangle \tag{13.181}$$

$$= -\frac{\partial}{\partial m}\langle \dot{m}' W \rangle - \frac{\partial}{\partial \Theta}\langle \dot{\Theta}' W \rangle - \frac{\partial}{\partial \mathbf{v}}\cdot\langle \dot{\mathbf{v}}' W \rangle$$

where on the LHS one has the convective part (the transport in the absence of the turbulence) and on the RHS, the dispersive part involving the gradients of the net fluxes due to the turbulence. To close the equation, one needs to relate the turbulent fluxes in some way, directly or indirectly, to $\langle W \rangle$ and its derivatives. Thus, there is a closure problem to resolve, which is the most important element of the PDF approach.

To illustrate the way in which the values of $\dot{\mathbf{X}}$ depend upon the properties of the particle and the underlying carrier flow, consider the case of the evaporating droplet in more detail. From mass conservation of a spherical droplet of diameter dp evaporating in a gas of mass density ρ_g, the general relationship is (see Section 1.4)

$$\dot{m} = \pi \rho_g d_p D_v Sh(Re_p, S_c) \ln\left[\frac{1 - \alpha_v}{1 - \alpha_{vs}}\right] \tag{13.182}$$

where α_v is the mass fraction of vapor emitted by the particle in the locally undisturbed gas flow, α_{vs} the (saturated) vapor mass fraction at the droplet (or particle) surface assumed to be in equilibrium with the particle (so it depends directly on the temperature Θ of the particle), D_v the molecular diffusion coefficient of the vapor, and Sh the droplet Sherwood number for mass transfer of vapor to or from the droplet which is a function of the vapor Schmidt number, and the local particle Reynolds number Re_p given by

$$Re_p = \frac{d_p|\mathbf{v} - \mathbf{u}|}{\nu_g}, \quad Sc = \frac{D_v}{\nu_g}$$

where ν_g *is* the kinematic viscosity of the gas.

Similarly, the changes in particle-droplet velocity and temperature also depend on the local particle Reynolds number. A point to note here is that the equations of motion are all coupled and all depend upon the instantaneous particle Reynolds number which, in turn, depends on the relative velocity between particle and locally undisturbed gas.

13.4.3.2.1 PDF Equation for Inert Particles

As stated previously, there are currently two PDF approaches in use: the KM and GLM. To illustrate the differences and similarities between these approaches, let us consider the simplest case of the transport of inert nonreacting solid particles in a turbulent gas flow. To simplify the situation still further the drag acting on the particle is linearized with respect to the relative velocity, i.e.,

$$\mathbf{F}_A \cong \underline{\overline{\eta}}(\mathbf{u} - \mathbf{v}) \tag{13.183}$$

where $\underline{\overline{\eta}}$ is the net friction coefficient and given by

$$\underline{\eta} = \frac{1}{2}\rho_g A C_D(\overline{Re}_p)|\overline{\mathbf{u}} - \overline{\mathbf{v}}| \tag{13.184}$$

where $\overline{\mathbf{v}}$ is the net particle velocity and $\overline{Re}_p$ the value of the particle Reynolds number based on net relative velocity between particle and local carrier flow. The equations of motion for a particle are

$$\frac{\mathrm{d}\mathbf{x}}{\mathrm{d}t} = \mathbf{v} \tag{13.185a}$$

and

$$\frac{\mathrm{d}\mathbf{v}}{\mathrm{d}t} = \underline{\beta} \cdot (\mathbf{u} - \mathbf{v}) \tag{13.185b}$$

where $\underline{\beta}$ is the inverse particle response tensor and given by $m^{-1}\underline{\overline{\eta}}$ for a particle of mass m. In the case of Stokes drag, the elements of $\underline{\beta}$ are constants of the motion and those of β_{ij}^{-1} are the corresponding particle response times to changes in flow. In addition to the particle equations of motion, the equation of

motion of the carrier flow velocity **u** along a particle trajectory is included, namely,

$$\frac{\mathrm{d}u_i}{\mathrm{d}t} = F_i(\mathbf{v}, \mathbf{u}, \mathbf{x}, t) \tag{13.186}$$

In the KM approach, one considers the continuum equations derived from an equation for the phase-space density $W(\mathbf{v},\mathbf{x},t)$, in which $\mathbf{u}(\mathbf{x},t)$ is a random function of $\mathbf{x}$, t, and $\mathbf{v}$ and $\mathbf{x}$ the independent random variables. In the GLM approach, the continuum equations are derived from a conservation equation for the phase-space density $P(\mathbf{v},\mathbf{u},\mathbf{x},t)$, where $\mathbf{v},\mathbf{u},\mathbf{x}$ form a set of independent variables. The transport-conservation equations for $W(\mathbf{v},\mathbf{x},t)$ and $\mathrm{P}(\mathbf{v},\mathbf{x},\mathbf{u},t)$ are, respectively,

$$\left\{\frac{\partial}{\partial t} + \frac{\partial}{\partial x_i}\mathbf{v}_\mathrm{i} + \frac{\partial}{\partial \mathbf{v}_i}\beta_{ij}(u_j(\mathbf{x}, t) - v_j)\right\}W(\mathbf{v}, \mathbf{x}, t) = 0 \tag{13.187}$$

and

$$\left\{\frac{\partial}{\partial t} + \frac{\partial}{\partial x_i}\mathbf{v}_i + \frac{\partial}{\partial \mathbf{v}_i}\beta_{ij}(u_j - \mathbf{v}_j) + \frac{\partial}{\partial u_i}F_i(\mathbf{v}, \mathbf{u}, \mathbf{x}, t)\right\}P(\mathbf{v}, \mathbf{u}, \mathbf{x}, t) = 0 \tag{13.188}$$

Note that integrating the equation for P over all u gives the equation for W. The functions $u_i(\mathbf{x},t)$ and $F_i(\mathbf{v},\mathbf{u},\mathbf{x},t)$ are resolved into mean and fluctuating parts:

$$u_i = \langle u_i\rangle + u_i'', \quad F_i = \langle F_i\rangle + F_i''$$

where $\langle ....\rangle$ represents an ensemble average. Then, the transport equations for mean values of W and P, namely, $\langle W\rangle$ and $\langle P\rangle$, are

$$\left\{\frac{\partial}{\partial t} + \frac{\partial}{\partial x_i}\mathbf{v}_i + \frac{\partial}{\partial \mathbf{v}_i}\beta_{ij}(\langle u_j\rangle - \mathbf{v}_j)\right\}\langle W\rangle = -\frac{\partial}{\partial v_i}\beta_{ij}\langle u_j'' W\rangle \tag{13.189}$$

$$\left\{\frac{\partial}{\partial t} + \frac{\partial}{\partial x_i}\mathbf{v}_i + \frac{\partial}{\partial v_i}\beta_{ij}(u_j - \mathbf{v}_j) + \frac{\partial}{\partial u_i}\langle F_i\rangle\right\}\langle P\rangle = -\frac{\partial}{\partial u_i}\langle F_i'' P\rangle \tag{13.190}$$

When suitably normalized, $\langle W\rangle$ and $\langle P\rangle$ represent the probability density at time t, for which a particle has $(\mathbf{v},\mathbf{x})$ and $(\mathbf{v},\mathbf{u};\mathrm{x})$, respectively. To solve these equations, closure relations for $\langle u_i'' W\rangle$ and $\langle F_i'' P\rangle$ are required. For simplicity, only the case where $\beta_{ij} = \beta\delta_{ij}$ will be considered.

13.4.3.2.2 Closure Approximation for a Nonreactive Gas–Particle Flows

13.4.3.2.2.1 Kinetic model. Based on either the LHDI approximation (Reeks, 1993) or the Furutsu–Novikov formula (Swailes and Darbyshire, 1997), the closure approximation for the net flux $\langle u_i'' W\rangle$ for particles with velocity $\mathbf{v}$ and position $\mathbf{x}$ at time t, is given by

$$\langle u_i'' W\rangle = -\left(\frac{\partial}{\partial u_j}\langle u_i(\mathbf{x}, t)\Delta\mathbf{v}_j\rangle + \frac{\partial}{\partial x_j}\langle u_i(\mathrm{x}, t)\Delta\mathbf{v}_j\rangle\right)\langle W\rangle - \left\langle\frac{\partial u_i''}{\partial x_j}\Delta x_j\right\rangle\langle W\rangle \tag{13.191}$$

where explicitly $\Delta x_j(\mathbf{x},\mathbf{v},t|0)$ and $\Delta\mathrm{v}_j(\mathbf{x},\mathbf{v},t|0)$ denote changes in the particle position and velocity for a particle starting somewhere in the particle phase space at some initial time $s=0$ and arriving at the point $\mathbf{v},\mathbf{x}$ at time $s=t$ The result is exact for a process in which the displacements $\Delta x_j(\mathbf{x},\mathbf{v},t|0)$, $\Delta v_j(\mathbf{x},\mathbf{v},t|0)$ form a Gaussian process. The averages $\langle u_i(\mathbf{x},\mathrm{t})\Delta x_j\rangle$ and $\langle u_i(\mathbf{x},\mathrm{t})\Delta v_j\rangle$ shall be referred to as the fluid-particle dispersion coefficients for spatial and velocity gradient diffusion in phase space.

The value of the dispersion coefficients in uniform shear flow are used as approximate values for the general case of nonuniform flows by choosing the local shearing of the flow at $\mathbf{x}$ in the flow and assuming the turbulence is quasi-homogeneous. In this instance, one can express $\Delta\mathbf{v}$ and $\Delta\mathbf{x}$ in Eq. (13.187) in

terms of a set of response functions $G_{ji}(s)$ which are the displacements of the particle in the $\hat{x}_i$ direction in response to an impulsive force $\underline{\delta}(s)$ applied in the $\hat{x}_j$ direction of the mean flow (in the absence of the turbulence). Thus if $\mathbf{u}''(s)$ is the fluctuating value of the carrier flow velocity with respect to its mean encountered by a particle along its trajectory measured at time s, then

$$\Delta x_i(t) = \beta \int_0^t u_j''(s) G_{ji}(t-s)\,\mathrm{d}s\ ;\ \Delta \mathbf{v}_i(t) = \beta \int_0^t u_j''(s)\dot{G}_{ji}(t-s)\,\mathrm{d}s \tag{13.192}$$

because the mean flow field is linear in $\mathbf{x}$, and where $G_{ji}(t)$ *is* the solution of the equation

$$\dot{G}_{ji} + \beta \dot{G}_{ji} - \beta \dot{G}_{jk} S \frac{\partial \langle u_i \rangle}{\partial x_k} = \delta_{ji}\delta(t) \tag{13.193}$$

13.4.3.2.2.2 Generalized Langevin model (*GLM*). Simonin and Deutsch, Minier (SDM) (1993) derive an equation of motion for the fluid velocity along a particle trajectory by starting from the Langevin equation that Pope (Harworth and Pope, 1986) has used as the analog of the Navier–Stokes equation for fluid point motion. Thus along a fluid point trajectory

$$\frac{\mathrm{d}u_i}{\mathrm{d}t} = \alpha_{ij}(\mathbf{X})(\langle u_i \rangle - u_j) + f_i(\mathbf{X}) + f_i''(t) \tag{13.194}$$

where $f_i(\mathbf{x})$ is the net viscous and pressure force per unit mass of fluid and $f_i''(t)$ is a white noise function of time. Both SDM and Pope consider the equation of motion in differential form because the white noise is assumed to be nondifferentiable. For convenience, it is assumed that the white-noise, like all turbulence related functions is differentiable. The equation of motion has white-noise properties simply because it has a time scale much shorter than the time scale over which $\mathbf{u}(t)$ varies along a fluid point trajectory $O(\alpha^{-1})$. For future reference it is noted that

$$f_i(\mathbf{x}) = \frac{\mathrm{D}_f \langle u_i \rangle}{\mathrm{D}t} + \frac{\partial \langle u_j'' u_i'' \rangle}{\partial x_j} \tag{13.195}$$

where

$$\frac{\mathrm{D}_f}{\mathrm{D}t} = \frac{\partial}{\partial t} + \langle u_j \rangle \frac{\partial}{\partial x_j} \tag{13.196}$$

SDM use this relationship to derive an equation of motion for the fluid velocity along a particle trajectory. Hence if $\mathrm{d}_p/\mathrm{d}t$ is the time derivative of the fluid velocity along a particle trajectory and similarly if $\mathrm{d}_f/\mathrm{d}t$ is along a fluid point trajectory, then

$$\begin{aligned}\frac{\mathrm{d}_p u_i}{\mathrm{d}t} &= \left(\frac{\partial}{\partial t} + \mathrm{v}_j \frac{\partial}{\partial x_j}\right) u_i(\mathbf{x}, t) \\ &= (\mathrm{v}_j - u_j)\frac{\partial u_i(x,t)}{\partial x_j} + \frac{\mathrm{d}_f u_i}{\mathrm{d}t} \\ &= (\mathrm{v}_j - u_j)\frac{\partial u_i(x,t)}{\partial x_j} \\ &\quad + \alpha_{ij}(\langle u_j \rangle - u_j) + f_i(\mathbf{x}) + f_i''(t)\end{aligned} \tag{13.197}$$

SDM consider only the contribution from the gradient of the mean fluid velocity in this equation of motion for the fluid velocity along a particle trajectory i.e., they consider the equation

$$\frac{\mathrm{d}_p u_i}{\mathrm{d}t} = (v_j - u_j)\frac{\partial \langle u_i(\mathrm{x}, t) \rangle}{\partial x_j} + \alpha_{ij}(\langle u_j \rangle - u_j) + f_i(\mathbf{x}) + f_i''(t) \tag{13.198}$$

In effect, this is equivalent to assuming that the contribution of the fluctuating fluid velocity gradient is absorbed into the white-noise function $f_i''(t)$. By using the white-noise function , the equation for $\langle P\rangle$ can be closed exactly, namely,[1]

$$\langle F_i''(\mathbf{x}, t)P(\mathbf{v}, \mathbf{x}, \mathbf{u}, t)\rangle = \langle f_i''(t)P(\mathbf{v}, \mathbf{u}, \mathbf{x}, t)\rangle \tag{13.199}$$

$$= -\int_i^\infty \langle f_i''(0)f_i''(s)\rangle \, \mathrm{d}s \frac{\partial\langle P\rangle}{\partial u_j}$$

Then from Eq. (13.193), the equation for $\langle P\rangle$ used by SDM is:

$$\frac{\partial\langle P\rangle}{\partial t} + \frac{\partial}{\partial x_i}\mathrm{v}_i\langle P\rangle + \frac{\partial}{\partial \mathrm{v}_i}\beta_{ij}(u_j - \mathrm{v}_j)\langle P\rangle \tag{13.200}$$

$$+ \frac{\partial}{\partial u_i}\left[\alpha_{ij}(\langle u_j\rangle - u_j) + f_i(\mathrm{x}) + (\mathrm{v}_j - u_j)\frac{\partial\langle u_i\rangle}{\partial x_j}\right]\langle P\rangle$$

$$= -\int_i^\infty \langle f_i''(0)f_j''(s)\rangle \, \mathrm{d}s \frac{\partial^2\langle P\rangle}{\partial u_i u_j}$$

13.4.3.3 Continuum Equations and Constitutive Relations for the Dispersed Phase (Without Collisions)

The continuum equations refer to the transport equations of mass, momentum, and kinetic stress of the particle phase and can be generated from the PDF equations for $\langle P\rangle$ or $\langle W\rangle$ by multiplying them by an appropriate power of $m\mathrm{v}'^p\mathrm{v}'^q\mathrm{v}'^r$ and then integrating overall u and v (for $\langle P\rangle$) and over all v (for $\langle W\rangle$), where m is the mass of a particle (assuming that all the particles for the sake of simplicity have the same mass m) and v_i' the fluctuating value of v_i relative its mean density weighted value $\bar{\mathrm{v}}_i$. Thus

$$\mathrm{mass}(\langle\rho\rangle) = m\int\langle P\rangle(\mathrm{v}, \mathrm{u}, \mathrm{x}) \, \mathrm{dv} \, \mathrm{du} \tag{13.201a}$$

$$\mathrm{momentum}\langle\rho\rangle\bar{\mathrm{v}}_i = m\int\langle P\rangle(\mathrm{v}, \mathrm{u}, \mathrm{x}) \, \mathrm{dv} \, \mathrm{du} \tag{13.201b}$$

and

$$\text{kinetic stress}\langle\rho\rangle\overline{\mathrm{v}_i'\mathrm{v}_j'} = m\int\langle P\rangle(\mathrm{v}, \mathrm{u}, \mathrm{x})\mathrm{v}_i'\mathrm{v}_j' \, \mathrm{dv} \, \mathrm{du} \tag{13.201c}$$

So the quantities $\bar{\mathrm{v}}_i$ and $\overline{\mathrm{v}_i'\mathrm{v}_j'}$ are the particle mass density weighed mean and covariance of the particle velocities at (x,t). The continuum equations are from Eq. (13.189):

$$\frac{\partial\langle\rho\rangle}{\partial t} + \frac{\partial}{\partial \mathrm{x}_i}\langle\rho\rangle\bar{\mathrm{v}}_i = 0 \tag{13.202a}$$

$$\langle\rho\rangle\frac{\mathrm{D}_p}{\mathrm{D}t}\bar{\mathrm{v}}_i = -\frac{\partial}{\partial x_j}\langle\rho\rangle\overline{\mathrm{v}_i'\mathrm{v}_j'} + \langle\rho\rangle\beta_{ij}(\langle u_j\rangle - \bar{\mathrm{v}}_j) + \beta_{ij}\langle\rho\rangle\overline{u_j''} \tag{13.202b}$$

and

$$\langle\rho\rangle\frac{\mathrm{D}_\mathrm{p}}{\mathrm{D}t}\overline{\mathrm{v}_i'\mathrm{v}_j'} = -\frac{\partial}{\partial x_k}\langle\rho\mathrm{v}_k'\mathrm{v}_j'\mathrm{v}_i'\rangle + \rho\overline{\mathrm{v}_j'\mathrm{v}_k'}\frac{\partial\bar{\mathrm{v}}_i}{\partial x_k} + \langle\rho\rangle\overline{\mathrm{v}_j'\mathrm{v}_k'}\frac{\partial\bar{\mathrm{v}}_i}{\partial x_k} \tag{13.202c}$$

$$-\langle\rho\rangle\beta_{ik}(\overline{\mathrm{v}_k'\mathrm{v}_j'} + \overline{\mathrm{v}_k'\mathrm{v}_j'} + \overline{\mathrm{v}_k'\mathrm{v}_j'})$$

[1]Note the closure is also exact if $f''(t)$ is Gaussian nonwhite but will include gradients of $\langle P\rangle$ in x and v as well.

where $u_i' = u_i - \overline{u}_i$ and D_p/D_t is the particle substantial derivative i.e.,

$$\frac{D_p}{D_t} = \frac{\partial}{\partial t} + \overline{\mathrm{v}}_j \frac{\partial}{\partial x_j} \tag{13.203}$$

Closed expressions are required for:

1. $\overline{u_i''}$ the average fluid velocity relative to $\langle u \rangle$ encountered by a particle
2. $\overline{u_k' v_j'}$ the carrier-particle velocity covariances
3. $\langle \rho v_k' v_j' v_i' \rangle$ the turbulent kinetic energy flux

Note the distinction here between variables u_i'' and u_i'. Herein after, double prime and prime refer to random variables relative to $\langle u \rangle$ and density-weighted averages, respectively, For example, $v'' = v - \langle u \rangle$; and $v' = v - \overline{v}$.

13.4.3.3.1 Constitutive Relations Based on Kinetic Model

By using Eq. (13.189) with Eq. (13.191), and suitably integrating it over all particle velocities to form transport equations for the particle phase momentum and particle kinetic stresses, and comparing the resulting equations with Eqs. (13.202b) and (13.202c), one obtains the identities

$$\overline{u_i''}\langle \rho \rangle = -\frac{\partial}{\partial x_j}(\langle u_i''(\mathrm{x}, t)\Delta x_j(\mathrm{x}, t/0)\rangle\langle \rho \rangle) - \left\langle \frac{\partial u_i''}{\partial x_j}\Delta x_j \right\rangle \langle \rho \rangle \tag{13.204}$$

$$\overline{u_i' \mathrm{v}_j'} = \langle u_i''(\mathrm{x}, t)\Delta \mathrm{v}_j(\mathrm{x}, t/0)\rangle - \langle u_i''(\mathrm{x}, t)\Delta x_m(\mathrm{x}, t|0)\rangle \frac{\partial \overline{\mathrm{v}}_j}{\partial x_m} \tag{13.205}$$

where the displacements $\Delta \mathrm{v}$ and $\Delta \mathrm{x}$ refer to all particle trajectories arriving at x at time t irrespective of their velocity. The average $\langle u_i''(\mathrm{x}, t)\Delta \mathrm{v}_j(\mathrm{x}, t/0)\rangle$ is the fluid–particle velocity diffusion coefficient and $\langle u_i''(\mathrm{x}, t)\Delta x_j(\mathrm{x}, t/0)\rangle$ is the fluid–particle spatial diffusion coefficient.

It is apparent from Eq. (13.191) that the turbulent interfacial momentum transfer term $\beta.\overline{\mathrm{u}''}\langle \rho \rangle$ will contribute an interfacial surface force to the particle-phase momentum equation, which combines with the particle Reynolds stresses to give a pressure tensor ρ whose components are expressible in terms of an equation of state, namely, at x:

$$p_{ji}/\langle \rho \rangle = \langle v_i' v_j' \rangle + \beta_{ik}\langle u_k''(\mathrm{x}, t)\Delta x_j(\mathrm{x}, t|0)\rangle \tag{13.206}$$

where v' is the particle velocity fluctuation relative to the mean $\overline{\mathrm{v}}$ at x. Equation (13.206), in turn, encapsulates a fundamental relationship between the components of p and a set of particle diffusion coefficients ε_{ij}, leading to the relationships

$$p_{ji}/\langle \rho \rangle = \beta_{ik}\ \varepsilon_{kj} = \langle \mathrm{v}_i' \mathrm{v}_j' \rangle + \beta_{ik}\langle u_k''(\mathrm{x}, t)\Delta x_j(\mathrm{x}, t|0)\rangle \tag{13.207}$$

It is clear from the momentum equation that when the intertial term $\mathrm{D}\overline{v}_i/\mathrm{D}_t$ is small compared with the other terms, the transport is described by a simple convection gradient transport equation, in which the diffusion coefficients are identical to ε_{ij} and the convection velocity is given by

$$\underline{\mathrm{v}}_\mathrm{D} = \beta^{-1}\mathrm{F} + \underline{\mathrm{v}}_\mathrm{d} \tag{13.208a}$$

$$\underline{\mathrm{v}}_\mathrm{d} = \beta^{-1}\left\{ \frac{\partial}{\partial \underline{\mathrm{x}}}\overline{\mathrm{v}'\mathrm{v}'} + \right\} - \left\langle \left(\frac{\partial}{\partial \mathrm{x}}\Delta \mathrm{x}(\mathrm{x}, t|0) \right) u''(\mathrm{x}, t) \right\rangle \tag{13.208b}$$

The first term on the RHS of Eq. (13.208b) has sometimes been referred to as the turbophoretic or stressphoretic velocity (Reeks, 1993; Ramshaw, 1979). The additional contribution from the second term is entirely due to the structure of the flow and should be zero for inertialess particles which follow the flow. According to this approach, gradient diffusion is always the case for particles, which follow the flow.

In fact, the set of diffusion coefficients ε_{ij} reduces to the local average

$$\varepsilon_{ij} = \langle u_i''(\mathrm{x},\, t)\Delta x_j(\mathrm{x},\, t|0)\rangle \tag{13.209}$$

One should note that these are not the same as the diffusion coefficients D_{ij} for the dispersion in a simple linear shear flow. For particles injected at the center of the shear with zero velocity in simple linear shear flow, the dispersion can be described as

$$\frac{\partial\langle\rho\rangle}{\partial t} = \frac{\partial}{\partial x_i}\mathrm{D}_{ij}(t)\frac{\partial}{\partial x_j}\langle\rho\rangle + \delta(\mathrm{x})\,\delta(t) \tag{13.210}$$

In these rather special cases, the convection term $\langle\rho\rangle\langle\mathbf{u}\rangle$ (for the case of inertialess particles following the flow) behaves like a diffusive term when the particles are released from the center of the shear with a diffusion coefficient, which adds to the diffusion coefficients ρ_{ij} to give the total diffusion coefficient D_{ij}. However, this result is only true for particles that follow the flow. For particles with inertia, while the process is still diffusive (for particles released from the center of the shear) the inertial acceleration term in the particle-phase momentum equation, Eq. (13.202b), also makes a finite contribution to D_{ij} along with normal gradient diffusion term. Indeed, for particles with small relaxation times, this term dominates the diffusion as time increases, especially in the case of the rotating flow.

The carrier–particle velocity covariances $\overline{u'_k v'_j}$ are given by

$$\overline{u'_i v'_j} = \langle u_i''(\mathbf{x},\, t)\Delta \mathrm{v}_j(\mathbf{x},\, t|0)\rangle - \langle u_i''(\mathbf{x},\, t)\Delta x_m(\mathbf{x},\, t|0)\rangle\frac{\partial \overline{\mathrm{v}}_j}{\partial x_m} \tag{13.211}$$

where the displacements $\Delta\mathbf{v}$ and $\Delta\mathbf{x}$ refer to all particle trajectories arriving at $\mathbf{x}$ at time t irrespective of their velocity.

Substituting the expressions for the carrier–particle velocity covariances in Eq. (13.211) into transport Eq. (13.202.c) for the particle Reynolds stresses gives

$$\begin{aligned}\langle\rho\rangle\frac{\mathrm{D}}{\mathrm{D}t}\overline{\mathrm{v}'_m\mathrm{v}'_n} = &-\frac{\partial}{\partial x_i}\langle\rho\mathrm{v}'_i\mathrm{v}'_m\mathrm{v}'_n\rangle + \langle\rho\rangle\left\{\frac{\partial \overline{\mathrm{v}}_n}{\partial x_l}\rho_m + \frac{\partial \overline{\mathrm{v}}_m}{\partial x_l}\rho_n\right\}\\ &-\langle\rho\rangle\left\{\beta_{nl}\overline{\mathrm{v}'_l\mathrm{v}'_m} + \beta_{mi}\overline{\mathrm{v}'_i\mathrm{v}'_n}\right\}\\ &+\langle\rho\rangle\left\{\beta_{ml}\langle u_l''(\mathrm{x},\, t)\Delta \mathrm{v}_n(\mathrm{x},\, t|0)\rangle + \beta_{nl}\langle u_l''(\mathrm{x},\, t)\Delta \mathrm{v}_m(\mathrm{x},\, t|0)\rangle\right\}\end{aligned} \tag{13.212}$$

Referring to the terms on the RHS of the equation, the second term in brackets represent "viscous" losses from the action of surface forces P (as defined in Eq. (13.207) in changing the shape and size of an elemental volume of the dispersed flow as it moves through the mean shear gradients of that flow. The third and fourth terms are net loss and production terms arising from an internal volume dissipative force $-\beta\mathbf{v}'$ (third term) and driving force $\beta\boldsymbol{u}''(\mathrm{x},\, t)$ (fourth term). One note that at equilibrium in homogeneous turbulence,

$$\overline{\mathrm{v}'^2} = \langle u_i''(\mathbf{x},\, t)\Delta \mathrm{v}_i(\mathbf{x},\, t|0)\rangle \tag{13.213}$$

all other terms being zero. Using the appropriate form for Δv_i (x, t|0) gives the correct analytic form (Reeks, 1997)

$$\overline{\mathrm{v}'^2} = \beta\int_0^\infty \mathrm{e}^{-\beta s}\langle u''(0)u''(s)\rangle\,\mathrm{d}s \tag{13.214}$$

where $u''(s)$ is the fluctuating aerodynamic driving force along a particle trajectory. Thus, the Reynolds stresses depend explicitly on the shearing of the dispersed phase (the term in square brackets in Eq. (13.212) and the shearing of the carrier flow (terms involving $\langle u_i''(\mathbf{x},\mathrm{t})\,\Delta\mathbf{v}_n\,(\mathbf{x},\mathrm{t}|0)\rangle$ in Eq. (13.212).

To illustrate this behavior still further, let us represent $\langle \mathbf{u}''(\mathbf{x},t)\,\Delta\mathbf{v}(\mathbf{x},t|0)\rangle$ by $\boldsymbol{\zeta}$ and divide it into a homogeneous part $\boldsymbol{\zeta}^{(0)}$ (as if the flow was uniform and independent of the shearing of the carrier flow) and a deviatoric part $\delta\zeta$ linear in the local shearing of the carrier flow. Likewise, divide the particle Reynolds stress into similar components. Consider the case when $\beta^{-1}$is very small (almost fluid point motion). Only a balance of the terms of order β are important in the Reynolds stress equation, so by taking β to be isotropic for simplicity, one has

$$-2\delta\overline{\mathrm{v}'_n\mathrm{v}'_m} + \left\{\delta\zeta_{mn} + \delta\zeta_{nm}\right\} - \varepsilon_{mi}\frac{\partial \bar{\mathrm{v}}_n}{\partial x_i} - \varepsilon_{ni}\frac{\partial \bar{\mathrm{v}}_m}{\partial x_i} = 2\overline{v'_n\mathrm{v}'_m}^{(0)} - \left\{\zeta^{(0)}_{mn} + \zeta^{(0)}_{mn}\right\} \tag{13.215}$$

The terms on the LHS contain all the deviatoric terms and the terms of the RHS are all the homogeneous terms. The whole equation must express the fact that in this limit, the particle velocity covariances are the same as the carrier flow covariances: this is consistent with the bracketed terms containing all the homogeneous forms and the deviatoric terms being both zero. The implication for the sum of the deviatoric terms being zero is that

$$2\delta\overline{\mathrm{v}'_n\mathrm{v}'_m} = -\varepsilon_{mi}\frac{\partial}{\partial x_i}(\bar{v}_n - \bar{u}_n) - \varepsilon_{ni}\frac{\partial}{\partial x_i}(\bar{v}_m - \bar{u}_m)\,\beta^{-1} \to 0 \tag{13.216}$$

The particle deviatoric Reynolds stresses in the limit of very small particles are linear in the relative shearing between the carrier and dispersed phases. In the case of very large particles, the contribution from the interfacial momentum transfer term to the deviatoric particle Reynolds stresses drops to zero with no explicit dependence on the shearing of the carrier flow, i.e., the contribution is entirely viscous.

13.4.3.3.1.1 The turbulent kinetic energy flux $\langle \rho \mathrm{v}'_k \mathrm{v}'_j \mathrm{v}'_i \rangle$. An evaluation of the turbulent kinetic energy flux is based on an application of the Chapman–Enskog approximation in which the nonequilibrium state of the dispersed phase is approximated by slight deviations from the equilibrium state (Chapman and Cowling, 1952). The analysis presented is based on that found in Buyevich (1972), where an equation similar to the classical Fokker–Planck equation was examined. It is also similar to that given by Swailes and Sergeev (1998). As a first step, the KM PDF equation is used, Eq. (13.189), with Eq. (13.191) to calculate the equilibrium distribution function, $\langle W\rangle^{(0)}$ This is found by setting all the time and space derivatives to zero in the equation, and further assuming that the carrier phase is homogeneous, such that the equation for $\langle \mathrm{W}\rangle^{(0)}$ is

$$\frac{\partial}{\partial \mathrm{v}'_i}\left(\beta_{ij}\mathrm{v}'_j\langle W\rangle^{(0)}\right) + \frac{\partial^2}{\partial \mathrm{v}'_i\partial \mathrm{v}'_j}\left(\beta_{ik}\langle u''_k\Delta\mathrm{v}_j\rangle\langle W\rangle^{(0)}\right) = 0 \tag{13.217}$$

$\widetilde{\langle W\rangle}^{(0)}(\mathbf{k})$ is the Fourier transform of $\langle W\rangle^{(0)}(\mathrm{v})$. If then

$$\widetilde{\langle W\rangle}^{(0)} = \langle n\rangle \exp\left\{-\frac{1}{2}\langle u''_i\Delta v_j\rangle A_{\mathrm{mn}}k_ik_{\mathrm{n}}\right\} \tag{13.218}$$

Now consider a state of the system that differs slightly from equilibrium. In this new state, the variables describing the mean flow, are now functions of time and position, and consequently, unlike in the equilibrium state, their derivatives are not identically zero. As in Chapman and Cowling (1952), it is assumed that the deviation from the equilibrium solution is sufficiently small so a solution can be sought for the nonequilibrium state in the form of a series solution with a small parameter, ξ, being employed to distinguish between the various orders of approximation (see also Buyevich, 1972). It should be remarked that the parameter ξ has been introduced only for convenience as a way of ordering terms. Obviously, it must be set equal to unity at the end of the calculations. To proceed, the KM-PDF equation is now written in the form

$$M(\langle W\rangle = L\langle W\rangle \tag{13.219}$$

where

$$M = M\left(\frac{\mathrm{D}}{\mathrm{D}t'}\frac{\partial}{\partial \mathrm{x}'}, \bar{\mathrm{v}}, \overline{\mathrm{v}'\mathrm{v}'}, \langle u''\Delta \mathrm{x}\rangle\right) L = L\left(\frac{\partial}{\partial \mathrm{v}'}\langle u''\Delta \mathrm{v}\rangle\right)$$

and following both Chapman and Cowling (1952) and Buyevich (1972), $\langle W\rangle$ and L are both expanded in terms of a small parameter ξ, namely,

$$\langle W\rangle = \frac{1}{\xi}\sum_{m=0}^{\infty}\xi^m\langle W\rangle^{(m)} \tag{13.220a}$$

$$L\langle W\rangle = \frac{1}{\xi}\sum_{m=0}^{\infty}\xi^m L^{(m)} \tag{13.220b}$$

with

$$L^{(r)} = L\langle W\rangle^{(r)} = \frac{\partial^2}{\partial \mathrm{v}'_i \partial \mathrm{v}'_j}\left(\beta_{jk}\langle u''_k \Delta v_i\rangle\langle W\rangle^{(r)}\right) + \frac{\partial}{\partial \mathrm{v}'_i}\left(\beta_{jk}\mathrm{v}'_j\langle W\rangle^{(r)}\right)$$

and with a similar expansion carried out for M ⟨W⟩. Substituting these expansions into Eq. (13.219) gives

$$\overline{\mathrm{v}'_i\,\mathrm{v}'_j\,\mathrm{v}'_k} - \varepsilon_{\mathrm{li}}\frac{\partial}{\partial x_l}\overline{\mathrm{v}'_j\mathrm{v}'_k} - \varepsilon_{lj}\frac{\partial}{\partial x_l}\overline{\mathrm{v}'_i\mathrm{v}'_k} - \varepsilon_{lk}\frac{\partial}{\partial x_l}\overline{\mathrm{v}'_i\mathrm{v}'_j} \tag{13.221}$$

where the diffusion coefficients ε_{ij} are the same as those defined in Eq. (13.207). See Swailes and Sergeev (1998) for precise details.

13.4.3.3.2 Constitutive Relations Based on GLM

The closure expressions in this case are transport equations for $\overline{\mathbf{u}''}$ and $\overline{\mathrm{u}'_k\mathrm{v}'_j}$ derived from the GLM-PDF equation for $\langle P\rangle$ (Eq. [13.200]). Multiplying Eq. (13.200) by u_i and integrating over all **v** and **u** yields

$$\frac{\partial}{\partial t}\langle\rho u_i\rangle + \frac{\partial}{\partial x_j}(\rho \mathrm{v}_j u_i) = \left\{f_i(\mathbf{x}) - \alpha_{ij}\overline{u''_j} + (\bar{\mathrm{v}}_k - \bar{u}_k)\frac{\partial\langle u_i\rangle}{\partial x_k}\right\}\langle\rho\rangle \tag{13.222}$$

The **LHS** can be rewritten as

$$\frac{\partial}{\partial t}\langle\rho u_i\rangle + \frac{\partial}{\partial x_j}(\rho \mathrm{v}_j u_i) = \langle\rho\rangle\frac{\mathrm{D}_p}{\mathrm{D}t}\langle u_i\rangle + \langle\rho\rangle\frac{\mathrm{D}_p}{\mathrm{D}t}\overline{u''_i} + \frac{\partial}{\partial x_j}\overline{\mathrm{v}'_j u'_i}\langle\rho\rangle \tag{13.223}$$

Also from Eq. (13.196) and resolving the velocity into mean and fluctuating parts

$$\left(\frac{\partial}{\partial t} + \bar{u}_j\frac{\partial}{\partial x_j}\right)\langle u_i\rangle = \frac{\mathrm{D}_f}{\mathrm{D}t}u_i + \overline{u''_j}\frac{\partial\langle u_i\rangle}{\partial x_j} \tag{13.224}$$

Finally by using the relationship given in Eq. (13.196) gives the transport equation for $\overline{u''_i}$, namely,

$$\langle\rho\rangle\frac{\mathrm{D}_p}{\mathrm{D}t}\overline{u''_i} = -\frac{\partial}{\partial x_j}\overline{\mathrm{v}'_j u'_i}\langle\rho\rangle + \langle\rho\rangle\frac{\partial}{\partial x_j}\langle u''_j u''_i\rangle) \tag{13.225}$$

$$-\left\{\frac{\partial\langle u_i\rangle}{\partial x_j} + \alpha_{ij}\right\}\overline{u''_j}\langle\rho\rangle$$

A transport equation for $\overline{u'_k v'_j}$ can also be obtained by transforming the GLM-PDF equation into an equation for $P(\mathrm{v}', \mathrm{u}', \mathrm{x}, t)$, multiplying the resulting equation by $u'_i v'_j$ and then integrating over all u′ and v′.

This gives

$$\langle\rho\rangle\frac{\mathrm{D}_p}{\mathrm{D}t}\overline{u'_i v'_j} = -\frac{\partial}{\partial x_k}\langle\rho\rangle\overline{u'_i v'_j v'_k} - \langle\rho\rangle\overline{v'_j v'_k}\frac{\partial u''_i}{\partial x_k} \tag{13.226}$$

$$-\left(\langle\rho\rangle\overline{u'_i v'_k}\frac{\partial \overline{v}_j}{\partial x_k} + \langle\rho\rangle\,\overline{v'_j l u'_k}\frac{\partial \overline{u}_j}{\partial x_k}\right)$$

$$-\langle\rho\rangle\beta\left(\overline{u'_i v'_j} - \overline{u'_i u'_j}\right)$$

$$+\langle\rho\rangle\alpha_{ik}\overline{u'_k v'_j}$$

13.4.3.3.3 Fluid-Particle Velocity Correlation Models

The general form of $\boldsymbol{\alpha}$ in Popes GLM model is assumed to be linear in the local strain rates of the carrier flow, i.e.,

$$\alpha_{ij} = \alpha_{ij}^{(0)} + \beta_2\frac{\partial \overline{u}_i}{\partial x_j} \tag{13.227}$$

where $\alpha_{ij}^{(0)}$ is the homogeneous (strain-rate independent) component and β_2 a constant whose value is obtained from measured values of one-point statistics. In the case of the SDM model, the values of $\alpha_{ij}^{(0)}$ are dependent on the particle itself, since they refer to fluid time scales viewed by the particle. In particular, SDM account for the influence of crossing trajectories by choosing the following form for $\alpha_{ij}^{(0)}$:

$$\alpha_{ij}^{(0)} = \frac{\delta_{ij}}{\tau_{fp,\perp}} + \left[\frac{1}{\tau_{fp,\|}} - \frac{1}{\tau_{fp,\perp}}\right]\hat{n}_i\hat{n}_j \tag{13.228}$$

where $\tau_{\mathrm{fp},\perp}$ and $\tau_{\mathrm{fp},\|}$ are the turbulent characteristic time scale of the fluid velocity fluctuations viewed by the particles in the direction normal and parallel to the mean relative velocity vector $\overline{\mathbf{v}}_\mathrm{r}$ between particle and carrier flow. Adopting the same approach as Csanady for gravitational settling, the direction cosines for the relative velocity are given by

$$\tau_{\mathrm{fp},\,\|} = \tau_\mathrm{f}(1 + C\zeta_r^{\,2})^{-1/2}\tau_{\mathrm{fp},\,\perp} = \tau_\mathrm{f}(1 + 4C\zeta_\mathrm{r}^{\,2})^{-1/2}$$

where

$$\zeta_\mathrm{r}^{\,2} = \frac{3\left|\overline{\mathbf{V}}_\mathrm{r}\right|^2}{\langle u'.u'\rangle}$$

For closure of the transport equation for the fluid–particle covariances in Eq. (13.226) need a closed expression for fluid–particle velocity $\langle\overline{\rho u'_i v'_j v'_k}\rangle$ turbulent flux. In the case of the scalar particle fluid covariance $\mathbf{u}'\cdot\mathbf{v}'$, Simonin (1996) has used a Boussinesq approximation

$$\langle\rho\mathrm{u}'.\mathrm{v}'\mathrm{v}'_\mathrm{i}\rangle = -\langle\rho\rangle\nu_\mathrm{fp}^\mathrm{t}\frac{\partial}{\partial x_i}\langle\mathrm{u}'.\mathrm{v}'\rangle \tag{13.229}$$

where $\nu_\mathrm{fp}^\mathrm{t}$ is referred to as the fluid–particle turbulent viscosity written in terms of the time scale of the fluid along a particle trajectory τ_fp, namely

$$\nu_\mathrm{fp}^\mathrm{t} = \frac{1}{3}\langle\mathbf{u}'\cdot\mathbf{v}'\rangle\tau_\mathrm{p} \tag{13.230}$$

Using this gradient approximation for the particle fluid velocity fluxes and the expressions for α_{ij}, the transport equation can, in principle, be solved for the linear form for α_{ij} in Eq. (13.227). Fevrier and Simonin (1998), from a computational point of view, have derived an algebraic model for the off-diagonal particle–fluid covariances, which they then use in conjunction with a transport model for of the scalar

fluid–particle covariance, $\langle \mathbf{u}' \cdot \mathbf{v}' \rangle$. This algebraic model is derived from Eq. (13.226) by assuming equilibrium of the fluid–particle turbulent velocity correlation tensor in single-phase flow, namely,

$$\langle u'_m v'_m \rangle \left[\frac{\mathrm{d}}{\mathrm{d}t} \langle u'_i v'_j \rangle - D_{ij} \right] = \langle u'_i v'_j \rangle \left[\frac{\mathrm{d}}{\mathrm{d}t} \langle u'_m v'_m \rangle - D_{mm} \right] \tag{13.231}$$

where D_{ij} refer to the diffusive component (gradient of the fluid–particle velocity flux) in the transport equation for the fluid–particle covariance. Then from the fluid–particle correlations transport, Eq. (13.226), one obtains the algebraic model

$$\begin{aligned} \langle u'_i v'_j \rangle = {} & \frac{1}{3} \langle \mathbf{u}' \cdot \mathbf{v}' \rangle \delta_{ij} + \frac{\langle u' \cdot v' \rangle}{\langle u'^2 \rangle} \left[\langle u'_i u'_j \rangle - \frac{1}{3} \langle u'^2 \rangle \delta_{ij} \right] \\ & - \frac{1}{2\beta \langle u'^2 \rangle} \left[\langle \mathbf{u}' \cdot \mathbf{v}' \rangle \left\{ \langle u'_i v'_k \rangle \frac{\partial \overline{v_j}}{\partial x_k} + (1 - \beta_2) \langle u'_i v'_k \rangle \frac{\partial \overline{u_j}}{\partial x_k} \right\} \right. \\ & \left. - \langle u'_i v'_j \rangle \left\{ \langle u'_m v'_n \rangle \frac{\partial \overline{v_m}}{\partial x_n} + (1 - \beta_2) \langle v'_m u'_n \rangle \frac{\partial \overline{u_m}}{\partial x_n} \right\} \right] \end{aligned} \tag{13.232}$$

where $\langle u'^2 \rangle = \langle \mathbf{u}' \cdot \mathbf{u}' \rangle$. For practical applications, this algebraic expression may be used with the transport equation for the fluid particle covariance $\langle \mathbf{u}' \mathbf{v}' \rangle$ obtained directly from Eq. (13.226). Fevrier and Simonin go further and derive an even simpler model than the algebraic model by assuming that the fluid–particle covariance tensor anisotropy is small, so that, for instance, certain ratios in the algebraic model equation can be replaced by their local quasi homogeneous values. Thus

$$\frac{\langle \boldsymbol{u}' \cdot \mathbf{v}' \rangle}{\langle u'^2 \rangle} = \frac{\beta_{\tau fp}}{1 + \beta_{\tau fp}}$$

This sort of approximation gives a Boussinesq or eddy–viscosity model for the fluid–particle velocity covariance, namely,

$$\begin{aligned} \langle u'_i v'_j \rangle = {} & \frac{1}{3} \langle \boldsymbol{u}' \mathbf{v}' \rangle \delta_{ij} + \frac{\beta_{\tau \mathrm{fp}}}{1 + \beta_{\tau \mathrm{fp}}} \left\{ \langle u'_i v'_j \rangle - \frac{1}{3} \langle \mathbf{u}' \cdot \mathbf{v}' \rangle \right\} \\ & - \frac{\nu^t_{fp}}{1 + \beta_{\tau fp}} \left\{ \frac{\partial \overline{\mathrm{v}_j}}{\partial x_i} - \frac{\delta_{ij}}{3} div \overline{\mathrm{v}} + (1 - \beta_2) \left(\frac{\partial \overline{u_\mathrm{i}}}{\partial x_j} - \frac{\delta_{ij}}{3} div\, \overline{u} \right) \right\} \end{aligned} \tag{13.233}$$

In the following section, predictions for the dispersion of particles in particle laden jet are compared with experimental results.

13.4.3.3.4 Comparison of Predictions with Experimental Results for Nonuniform Unbounded Flows

Here the GLM approach is used to predict the concentration, mean velocity and velocity covariances of a dilute suspension of particles in a nonuniform flow as where near-wall behavior is not a feature. This is the case for a particle-laden round turbulent jet, where the flow is strictly unbounded. It represents one of the many examples where a comparison between model predictions and experimental measurements have been made (see Simonin [2000] for details). However, it does provide very good examples of the application of the transport equation for the particle kinetic stresses where the work done by the mean shear of either phase introduces a significant anisotropy into the particle velocity covariance as is the case of dispersion in a simple shear. The results are taken from Fevrier and Simonin (1998) for dispersion in a particle-laden coaxial jet with properties: mean particle diameter = 80 μm, density ratio $\rho_\mathrm{p}/\rho_\mathrm{f} = 237$, particle relaxation time $\beta^{-1} = 5 \times 10^{-3}$sec, mass loading $= 3.3 \times 10^{-2}$, and mean volume fraction 1.4×10^{-4}. In such a flow, the fluid modulation by the particles and particle–particle collisions are negligible. Computations were made on a 31×51 mesh using the full second-order model involving the transport of the particle kinetic stress equation, Eq. (13.202), and the scalar fluid–particle covariance

(derived from Eq. (13.226) together with the algebraic models for the off-diagonal particle-fluid velocity covariances (Eq. [13.232]). The results are also given using the eddy viscosity model for the fluid–particle velocity covariances Eq. (13.233). The inlet conditions on the fluid and particle mean velocity and fluctuations are taken from the experimental data of Hishida and Maeda (1990). As experimentally observed, the particle normal kinetic stresses are much more anisotropic than the corresponding values of the carrier flow, due to the significant increase in the shearing of the flow in the axial direction than in as radial direction (see Figures 13.54 and 13.55). Application of the algebraic model accurately predicts the values in the particle velocity fluctuations in both the axial and radial directions for all measured axial locations . The fluid–particle eddy–viscosity model is reasonably accurate in predicting the radial velocity fluctuations but clearly underpredicts the axial values.

13.4.3.3.5 Accuracy and Reliability of PDF Models

The PDF equation in its simplest and most practical form is an equation for the particle phase space distribution in which the random force due to the turbulence along a particle trajectory is a Gaussian process or, more appropriately, the velocity and spatial displacements $\Delta\mathbf{v}(\mathbf{x},t|\mathbf{v}',0)$ and $\Delta\mathbf{x}(\mathbf{x},t|\mathbf{v}',0)$ about a given point $\mathbf{x}$, t for a particle with an initial velocity of $\mathbf{v}'$ are Gaussian. This leads to a simple advection diffusion equation (ADE) for the net turbulent driving force in particle phase space. It is possible to extend this further to non-Gaussian processes, but in doing so, we would require more knowledge; more statistics on the displacements and ultimately on the forces that produce them information we rarely posses. Although the ADE approximation is used, it is applied at the simplest level of the dynamics in which the underlying Liouville equation, upon which the PDF equation is based, is a linear equation. This leads to a better chance of success. Indeed, one might say that the PDF approach is more reliable than other approaches from several points of view:

1. Simple closure based on a Gaussian process for turbulent driving force is used at a more basic level of the dynamics. This leads to a non-Gaussian spatial ADE process, which admits all the higher order gradient diffusion terms that are contained in an ADE process for a compressible non-Gaussian random particle velocity field.
2. Provides valid criteria for the application of simple gradient diffusion (simple ADE) and in cases, where this is not valid, a method of solution involving a hierarchy of continuum (moment) equations closed at a suitable level using closure approximations based on formal solutions to the PDF equation itself.

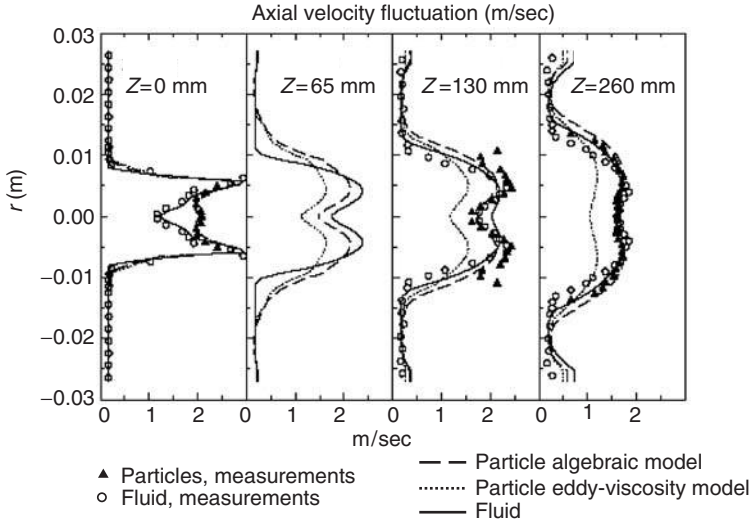

FIGURE 13.54 Radial profiles of axial fluctuations at different locations downstream of a nozzle for a coaxial round jet.

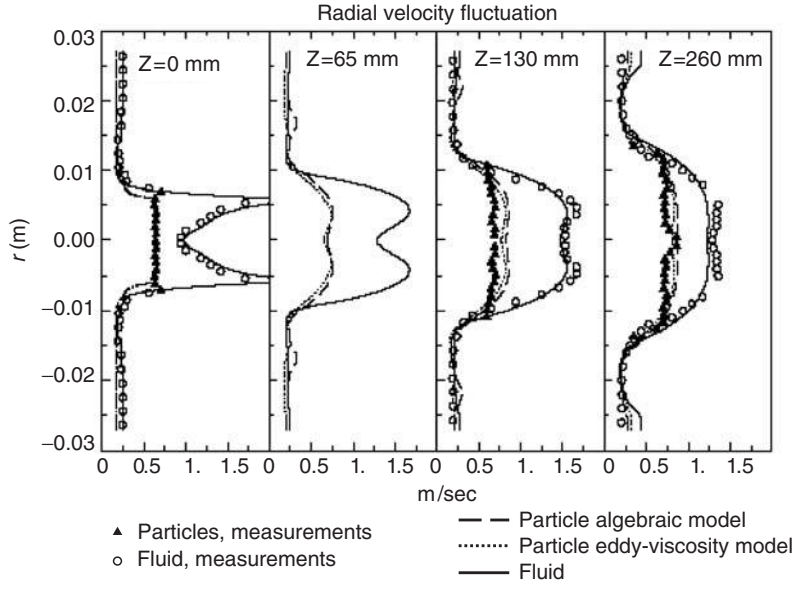

FIGURE 13.55 Radial profiles of radial fluctuations at different locations downstream of a nozzle for a coaxial round jet.

3. The PDF equation, or more appropriately the closure approximation involved, is asymptotically exact in the limit of high inertia particle when the process is similar to Brownian motion.
4. Implementation of natural boundary condition, e.g., absorbing/partially absorbing surfaces is an integrable part of the approach, where solution of the PDF equations is carried out directly near and at the depositing wall. This is the subject of the following section.

13.4.3.4 Near–Wall Behavior

In this section the works of Devenish et al. (1999), Reeks and Swailes (1997), Swailes and Reeks (1994), and Darbyshire and Swailes (1996) on the application of the PDF approach to near-wall behavior and the influence of natural boundary conditions are briefly reviewed. The natural boundary conditions involve some change in particle velocity together with possible deposition–absorption at the boundary and cannot be prescribed in the standard two-fluid formulation. Only using a PDF method explicitly involving the particle velocity distribution at the wall can this be achieved. Furthermore, the steep change in the level of turbulence at the wall means that only for very small particles are the two-fluid equations (mass momentum and energy) likely to apply i.e., the particle distribution of velocities at any position within the turbulent boundary layer will not be locally related to the turbulence. Depending on its size, a particle will retain some memory of its behavior in the far wall or bulk flow. More precisely, this depends on the variation of the turbulence over a particle mean free path defined as the distance a particle travels in a time equal to its correlation time ε/v'. The same type of conditions apply to a gas at low pressure when the dimensions of the container are comparable to the molecular mean free path. Under such circumstances the so-called continuum theory no longer applies. It is to be noted that even without the steep change in turbulence, the boundary conditions at the wall are by themselves likely to invalidate the two-fluid model equations simply because the particle–wall distribution is very much different from the normal distribution.

13.4.3.4.1 General Boundary Conditions at Wall

Referring to Figure 13.56, the general boundary condition for a particle impacting at a wall at x with velocity u and rebounding with a range of possible velocities **v** is the flux condition

$$\mathrm{v}P(\mathrm{v}, \mathrm{x}, t) = \int_{\mathrm{u.n}\le 0} \mathbf{u}P(\mathbf{v}, \mathbf{u}, t)\Theta(\mathbf{v}|\mathbf{u})\, \mathrm{du} \tag{13.234}$$

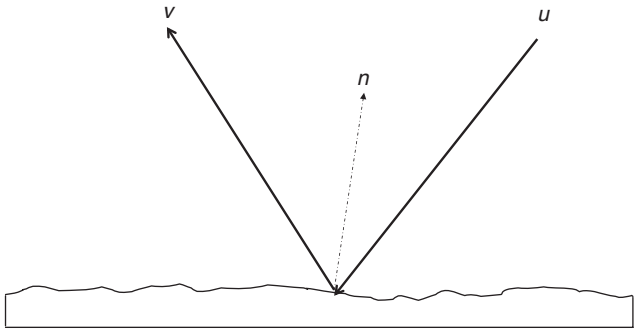

FIGURE 13.56 Diffuse scattering from a rough surface where n is the unit vector normal to the surface at the point of impact with the surface.

where **n** is the direction normal to the wall at x, and $\Theta(\mathrm{v} \mid \mathrm{u})$ the transition or scattering probability density that a particle will rebound with a velocity v after impacting the surface with velocity **u**. The velocities **u** and **v** are related deterministically (specular reflection) or stochastically (diffuse scattering as in the case of a microscopically rough surface). Swailes and his co-workers (Darbyshire and Swailes, 1996; Reeks and Swailes, 1997; Devenish et al., 1999) have obtained solutions for the PDF equation for simple flows in both these cases. Both the cases involve duct flow, in which the turbulence is regarded as homogeneous with uniform mean velocity in the streamwise direction. In these cases, therefore, the particle's response time is sufficiently large that it does not respond to the spatial variations in the mean flow and the turbulence, especially near the wall. Also, it is the boundary conditions themselves which determine the near-wall behavior, where the continuum equations are inappropriate and the behavior can be approximated well by a simple steady-state solution of the PDF equation in 1D in **x** and in **v** The conditions for particle response times are consistent with the second gradients flux term in Eq. (13.191) being set to zero, in which case the PDF equation can be normalized in a universal form under steady conditions as (Swailes and Reeks, 1994)

$$\left(\mathrm{v}\frac{\partial}{\partial y} - \frac{\partial}{\partial \mathrm{v}}\mathrm{v} + g\frac{\partial}{\partial \mathrm{v}} + \frac{\partial^2}{\partial \mathrm{v}^2}\right)\langle W(y, \mathrm{v})\rangle = 0 \tag{13.235}$$

In this equation, y is the normal distance from the wall ($y = 0$) and positive velocities are directed toward the wall, particles are acted upon by a gravitational force g directed toward the wall and velocities and distances are normalized on the particle rms velocity at equilibrium (perfectly reflecting walls) and on the particle mean free path ε/v'.

In the simple flows considered by Swailes and Reeks (1994) and Reeks and Swailes (1997), the flow is divided into a far-wall region, which acts as a constant source of particles entering the near-wall region. The interface is set at some distance Y from the wall in particle mean free paths where the spatial distribution of the particles is uniform. It follows from Eq. (13.235) that this distribution will be Gaussian

$$w(0, \mathrm{v}) = (2\pi)^{-1/2}\exp\left(-\frac{1}{2}\mathrm{v}^2\right) \quad \text{for } v > 0 \tag{13.236}$$

13.4.3.4.2 Method of Solution

The PDF equation is solved numerically using a spectral expansion in terms of Hermite polynomials, looking for solutions in the form

$$w(y, \mathrm{v}) \approx \sum_{n=0}^{N} \phi_n(y)\Psi_n(\mathrm{v}) \tag{13.237}$$

where the Ψ_n are orthonormal functions based on the Hermite polynomials H_n. They are

$$\Psi_n(\mathrm{v}) = \left(\frac{b}{2^n n!\sqrt{\pi}}\right)^{1/2} \exp\left(-\frac{1}{2}(b\mathrm{v})^2\right) \mathrm{H}_n(b\mathrm{v}) \tag{13.238}$$

The inclusion of the scaling factor b allows the placement of a set of collocation points v_j $(j = 0, 1, N)$, to be optimized. At these collocation points, the approximation in Eq. (13.237) is exact. In this problem, the collocation points are taken to be the zeros of the function $\Psi_{\mathrm{N+1}}$, which provide discrete orthonormal properties for $\Psi\mathrm{n}(\mathrm{v}_s)$. Substituting the approximation Eq. (13.237) into Eq. (13.235) and making it exact at these collocation points, one gets a system of first-order equations

$$\frac{\mathrm{d}}{\mathrm{d}y}\mathrm{W} = A\mathrm{W} \tag{13.239}$$

where W is column vector whose elements are values of the PDF at the collocation points and A is a matrix whose elements are functions of Ψ_n^s.

The boundary conditions given by Eqs. (13.234) and (13.236) are discretized at the points v_j. If N^* is defined to be the integer such that $\mathrm{v}j < 0$ for $j < N^*$ and $\mathrm{v}_j = 0$ for $j \geq N^*$, then the boundary condition at the interface $y = Y$ can be written as

$$\sum_{n=0}^{N} \zeta_{jn} w_{\mathrm{n}} = 1, \quad j \geq N^* \tag{13.240}$$

where $w_n = w(\mathrm{v}_n, Y)$ and

$$\zeta_{jn} = \delta_{jn}(2\pi)^{1/2} \exp\left(\frac{1}{2}\mathrm{v}_j^2\right), \quad j \geq N^*$$

The boundary condition at the wall $y = 0$ is

$$\sum_{n=0}^{N} \zeta_{\mathrm{jn}} w_n = 0, \quad j < N^* \tag{13.241}$$

where

$$\zeta_{jn} = \delta_{jn}\mathrm{v}_n + h_n^{-1} \sum_{m=0}^{N} \Psi_m^n I_m(\mathrm{v}_j), \quad j \geq N^*$$

with

$$I_m(\mathrm{v}_j) = \int_0^\infty \Psi_m(u) u \Theta(\mathrm{v}_j|\mathbf{u})\, \mathrm{d}u$$

The interface and wall boundary conditions represent standard two-point boundary conditions for the solutions of Eq. (13.239) and can be solved by a standard numerical method. Figures 13.57–13.59 show some of the results obtained by Swailes (Darbyshire et al., 1996; Reeks and Swailes, 1997) for the particle deposition at a wall with or without gravity for specific examples of the wall scattering function $\Theta(v_j|u)$. In each case, results are compared with those obtained from a random walk simulation that simulates the system precisely. In this case it was assumed that upon impact there was energy loss that was conveniently described by defining a critical impact velocity v_c below which a particle adheres upon impact but above which a particle will rebound with a prescribed rebound velocity $\mathbf{v} = \Theta(\mathbf{u})$. Thus $\Theta(\mathbf{v}|\mathbf{u})$ for specular reflection is

$$\Theta = \begin{cases} 0 & \text{for } 0 < \mathrm{v} \leq \mathrm{v}_c \\ \delta(\mathrm{v} - \theta(u) & \text{for } v > \mathrm{v}_c \end{cases} \tag{13.242}$$

Modeling the dependence of $v = \theta(\mathrm{u})$ from a constant energy loss upon impact as

$$\mathrm{v} = -\sqrt{u^2 - \mathrm{v}_c^2} \quad \text{for } u > \mathrm{v}_c \tag{13.243}$$

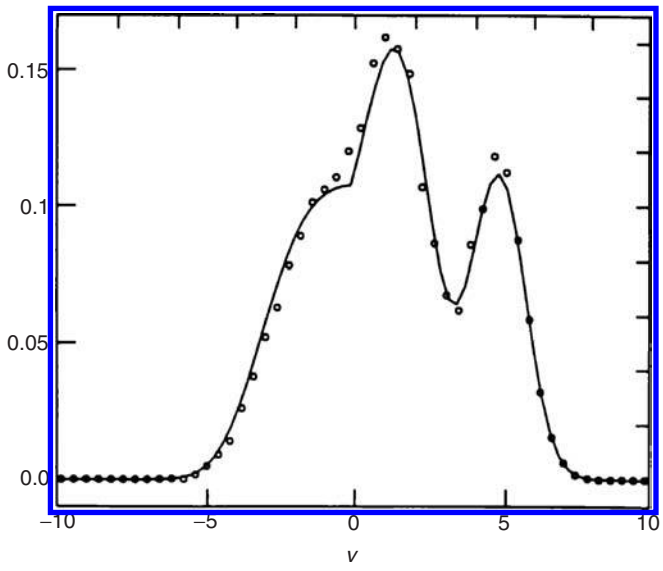

FIGURE 13.57 Particle–wall velocity distrubution for particles falling under gravity with reflection and absorption; normalized critical impact velocity v_c=5, gravitational settling velocity=5.

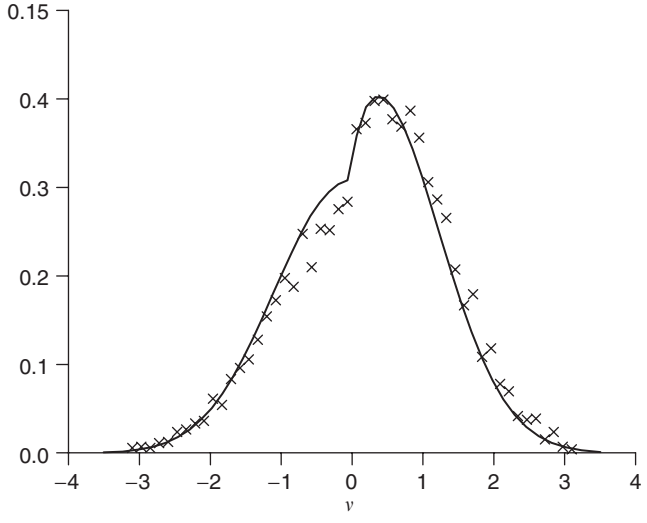

FIGURE 13.58 Wall distribution of velocities for specular reflection; $\gamma = 0°$, $v_c = 1$.

gives the simple form

$$W(\mathrm{v},0) = W(\mathrm{u},0) \text{ for } \mathrm{u} > \mathrm{v}_{\mathrm{c}}, \tag{13.244}$$

where v and u are related by Eq. (13.243). It is noted that $v_c = 0$ (no absorption and energy loss) gives the perfect reflection boundary condition $w(v,0) = w(-v,0)$, while letting $\mathrm{v_c} \to \infty$ gives the perfect absorption case $w(v,0) = 0$, $v < 0$. The results were obtained for a range of values of the gravitational settling velocity $\mathrm{v_g}$ and critical impact velocities $\mathrm{v_c}$. Figure 13.57 shows the results of solving the PDF equation(13.235) compared with those obtained from the simulation for the velocity distribution at the

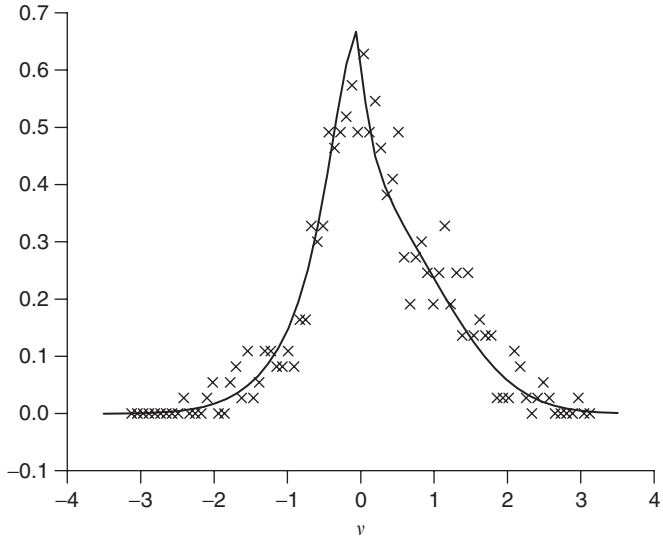

FIGURE 13.59 Wall distribution of velocities for specular reflection; $\gamma = 75°$, $v_c = 1$.

wall for the specific case of a partially absorbing wall with $v_c = 5$ and $v_g = 5$ (in normalized units). Note there are two peaks, one centerd at $v = v_g$ and the other with its center slightly displaced from the origin. The relative heights of these peaks depend upon the the ratio of v_c/v_g. For $v_c/v = 0$ (zero absorption) the latter peak has a maximum value $v = 0$, with no contribution from the peak at $v = v_g$. In contrast, the opposite is the case when $v_c/v_g \to \infty$.

13.4.3.4.3 Diffuse Reflection with Deposition

As an illustration, suppose that particles arriving at the surface are still reflected with a deterministic speed, but now, the velocity vector is directed at some random angle α to the surface. Since only with particle transport in the direction normal to the wall is of concern, the rebound velocity can be taken as $v = -r \cos \alpha$ where, as in Eq. (13.243), the deterministic speed is. $r = \sqrt{u^2 - v_c^2}$. If $u < v_c$ then the particle is considered to adhere.

A variety of distributions $\Theta(v|u)$ can be constructed depending on the prescribed distribution of α. For the purpose of illustration, Darbyshire and Swailes (1996) considered the simple case, where the reflection angle α is uniformly distributed on $(-\gamma,\gamma)$ in which case

$$\Theta(\mathrm{v}|u) = \begin{cases} \gamma^{-1}(u^2 - a^2)^{-1/2} & \text{for } a \le u \le c \\ 0 & \text{otherwise} \end{cases} \tag{13.245}$$

where $a(v) = \sqrt{v_c^2 + v^2}$ and $c(v) = \sqrt{v_c^2 + v^2 \sec^2 \gamma}$.

Predictions for the velocity distribution at the wall compared with those obtained from random walk simulations are shown in Figure 13.59 for $\gamma = 75°$. Compare this distribution with that for specular reflection with the same critical impact velocity shown in Figure 13.58, which illustrates the essential effect of diffuse reflection, namely, the reduction near the wall of the normal component of the particle rms velocity, the effect becoming more pronounced with increasing γ. These features are accompanied with an increase in particle–wall concentration as γ increases.

13.4.3.4.4 Particle Deposition in a Turbulent Boundary Layer to a Perfectly Absorbing Wall

Analysis of near-wall behavior in this circumstance is dominated by both the boundary conditions that give rise to a wall PDF, which is far from Gaussian. Steep gradients of the turbulence near to the wall imply that for a particle with inertia the assumption of local equilibrium (as if the flow was locally

homogeneous) is invalid, i.e., even with perfectly reflecting boundary conditions, continuum approximations for particle transport is inappropriate. The influence of boundary conditions and changes in the turbulence within the near-wall region is covered by the single condition that variations in PDF over a particle mean free path must be small for the application of a traditional two-fluid model. It is therefore not surprising to find that gradient diffusion models for particle deposition in a turbulent boundary layer give generally poor agreement with experimental results, even the gradient diffusion is assumed to apply up to one particle stop distance away from the wall (the so-called gradient diffusion/free-flight models). See, for example the review by Papavergos and Hedley (1984). Reeks and Swailes (1993) have made predictions of the deposition velocity as a function of τ^+ (particle response time in wall units) by solving the PDF equations using the same wall functions as in the particle tracking model of Kallio and Reeks (1989). Values for k^+ were calculated from the asymptotic form of the PDF for large times downstream of the initial injection point of particles in the channel. In this case, the spectral collocation technique was used to solve a time-dependent PDF equation of the form (Kallio and Reeks, 1989):

$$\left(\frac{\partial}{\partial t} - v\frac{\partial}{\partial y} - \beta \frac{\partial}{\partial v} v - \mu(y)\frac{\partial^2}{\partial v^2} + \lambda(y)\frac{\partial^2}{\partial y \partial v} \right) \langle W(v, y, t) \rangle = 0 \tag{13.246}$$

in which the occurrence of spurious drift has been eliminated. The symbol y is the distance from the wall in wall units and v the particle velocity (normalized with respect to the friction velocity) at y toward the wall (in the $-y$ direction) and

$$\mu(y) = \beta \langle u(y, t) \Delta v(y, t|0) \rangle \quad \lambda(y) = \beta \langle u(y, t) \Delta v(y, t|0) \rangle$$

are based on their homogeneous forms, by using the same forms for the turbulence intensity and time scales normal to the wall used in Kallio and Reeks (1989). The predictions for κ^+ versus τ^+ compared favorably with the experimental results of Liu and Agarawal (1974) shown in Figure 13.60. An important point to note is that while gradient transport is inappropriate in a traditionally based two-fluid model, it is acceptable in a PDF equation.

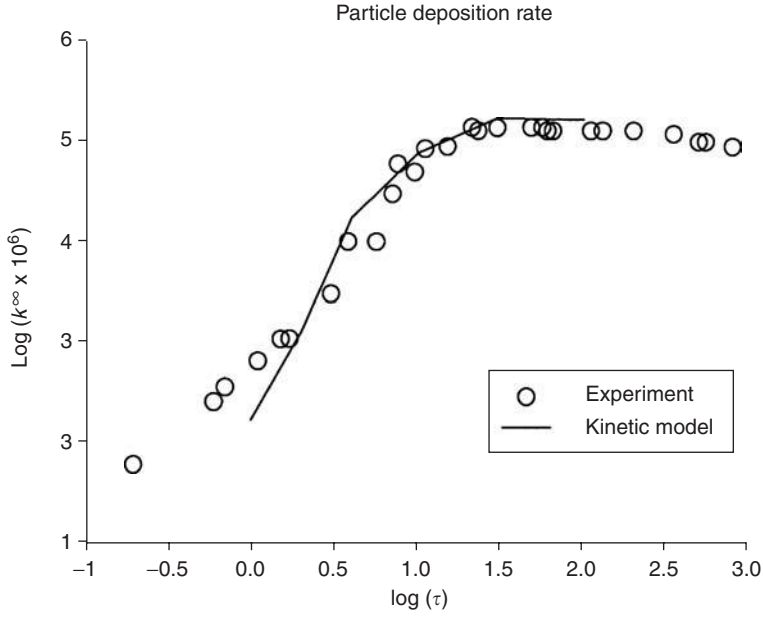

FIGURE 13.60 Particle deposition in turbulent pipe flow.

13.4.3.5 Particle Dispersion with Interparticle Collisions

Experimental and numerical simulations have indicated that inert particle collisions have a measurable influence on coarse particle transport properties in gas–solid turbulent flows, even for small values of the dispersed-phase volume fraction ($\alpha_p < 0.01$). In addition, detailed modelling of the interparticle collision rate is needed for accurate prediction of coalescence–agglomeration processes in dilute flows. By neglecting hydrodynamic interaction, hard sphere kinetic theory can be used to account for interparticle inelastic collisions in a PDF approach to particle flows. Thus, referring to Figure13.61 for an inelastic collision between two identical spherical particles labeled 1 and 2,

$$\mathbf{v}_1' = \mathbf{v}_1 + e_c(\mathbf{v}_{21}\hat{\mathbf{k}})\hat{\mathbf{k}}, \quad \mathbf{v}_2' = \mathbf{v}_1 - e_c(\mathbf{v}_{21}\hat{\mathbf{k}})\hat{\mathbf{k}} \tag{13.247}$$

where $\mathbf{v}_1'$ and $\mathbf{v}_2'$ are the velocities of particles 1 and 2 after the collision related to the velocities $\mathbf{v}_1$ and $\mathbf{v}_2$ before the collision , involving the coefficient of restitution e_c, the unit vector $\hat{\mathbf{k}}$ directed from the center of the first colliding sphere to the center of the second at impact and $\mathbf{v}_{21}$ is the relative velocity of particle 2 with respect to that of particle 1 at impact. Note that there is no interparticle friction.

While there are certain obvious similarities between molecular collisions and particle collisions in a turbulent flow, there are, however, fundamental differences because the continuous-phase turbulence plays an important role in the particle transport in a dilute mixture while dissipation induced by inelastic collision controls the particle kinetic energy in a dense flow. Indeed, in the kinetic theory of dilute gases, the statistics of binary collisions are derived by assuming that the velocities and positions of any two particles are independent of each other (the molecular chaos assumption), whereas, in gas–solid flow, the probable positions and velocities of colliding particles will definitely be correlated through their interaction with the same surrounding turbulent flow. In this section, we first describe the original approach due to Simonin (1991), which ignores this correlation, and then the approach proposed by Lavieville et al. (1995) that attempts to take it into account. A detailed description of the modelling approach can be found in He and Simonin (1994), Lavieville et al. (1995) and more recently in Simonin et al. (2002), and Vermorel et al. (2003).

13.4.3.5.1 Collision Integrals

If particle–particle interactions in which more than two particles take place are assumed to be negligible in number and effect, the collisional PDF rate of change may be written in terms of particle–particle pair

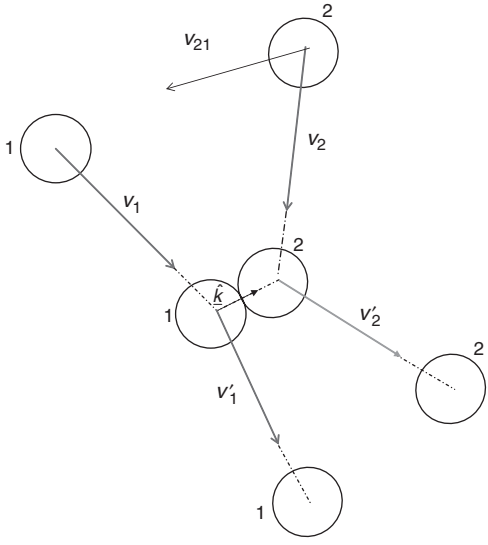

FIGURE 13.61 Kinematics of two colliding spherical particles.

distribution functions $\rho(2)(\mathbf{v}_1,\mathbf{x}_1,\mathbf{x}_1,\mathbf{x}_2,t)$ for particle 1 with velocity $\boldsymbol{v}_1$ at position $\boldsymbol{x}_1$ and particle 2 with velocity $\boldsymbol{v}_2$ at $\boldsymbol{x}_2$, for which special closure assumptions are needed:

$$\left(\frac{\partial P}{\partial t}\right)_{\text{collisions}} = d_p^2 \int\int_{\mathbf{v}_{21}\hat{\boldsymbol{k}}>0} \Delta\rho_2\left(\mathbf{v}_1, \mathbf{x}, \mathbf{x} + d_p\hat{\boldsymbol{k}}, t\right) \mathbf{v}_{21}\, \mathrm{d}\, \hat{\boldsymbol{k}}\, \mathrm{d}\mathbf{v}_2 \tag{13.248}$$

Where $\rho = (\mathrm{v}, \mathrm{x}, \mathrm{t}) = <\mathrm{w}, \mathrm{v}, \mathrm{x}, \mathrm{t}>$

$$\Delta\rho_{(2)}\left(\mathbf{v}_1, \mathbf{x}, \mathbf{v}_2, \mathbf{x} + d_p\hat{\boldsymbol{k}}, t\right) = \frac{1}{e_c^2}\rho_{(2)}\left(\mathbf{v}_1^+, \mathbf{x}, \mathbf{v}_2^+, \mathbf{x} + d_p\hat{\boldsymbol{k}}, t\right) - \rho_{(2)}\left(\mathbf{v}_1, \mathbf{x}, \mathbf{v}_2, \mathbf{x} + d_p\hat{\boldsymbol{k}}, t\right)$$

and

$$\mathbf{v}_1^+ = \mathbf{v}_1 + \frac{1 + e_c}{2e_c}(\mathbf{v}_{21}.\hat{\boldsymbol{k}})\hat{\boldsymbol{k}}, \quad \mathbf{v}_2^+ = \mathbf{v}_2 + \frac{1 + e_c}{2e_c}(\mathbf{v}_{21}.\hat{\boldsymbol{k}})\hat{\boldsymbol{k}}$$

assuming that both particles are identical spherical particles with diameter d_p. The mean collisional rate of change for some property ψ, e.g., kinetic energy, is the integral over all possible binary collisions of the change in ψ in a particular collision multiplied by the probable frequency of such a collision and can be written as

$$c(\psi) = d_p^2 \int\int\int_{\mathbf{v}_{21}\hat{\boldsymbol{k}}>0} (\psi_2^+ - \psi_2) p_2\left(\mathbf{v}_1, \mathbf{x}, \mathbf{v}_2, \mathbf{x} + d_p\hat{\boldsymbol{k}}, t\right) \mathbf{v}_{21}.\hat{\boldsymbol{k}}\, \mathrm{d}\, \mathrm{d}\mathbf{v}_2\, \mathrm{d}\mathbf{v}_1 \tag{13.249}$$

13.4.3.5.2 Collision Models

By using the approach adopted in kinetic theory, the pair distribution functions in the collision integral is simply written in terms of the single-distribution function, assuming that colliding particle velocities are completely independent; namely,

$$\rho_{(2)}\left(\mathbf{v}_1, \mathbf{x}, \mathbf{v}_2, \mathbf{x} + d_p\hat{\boldsymbol{k}}, t\right) = P\left(\mathbf{v}_1, \mathbf{x}, t\right) P\left(\mathbf{v}_2, \mathbf{x} + d_p\hat{\boldsymbol{k}}, t\right)$$

$$\tau_p \gg \tau_e \quad \text{(eddy lifetime)} \tag{13.250}$$

The above assumption has been retained in the derivation of the collision integral used by Simonin (1991) and is referred to as the random collision model.

This is also the assumption implicitly used by Oesterle and Petijean (1993) and Sommerfeld (1995). However, this assumption is valid only when the particle response time is much larger than the eddy–particle interaction time. In contrast, when the particle response time is of the same order or smaller than this interaction time, the approaching particle velocities will be correlated through interaction with the same eddy.

To account for correlation between colliding particles, an extended collision model is developed by expressing the particle pair distribution function $\rho_{(2)}(\mathbf{v}_1,\mathbf{x},\mathbf{v}_2,\mathbf{x}+d_p\hat{\boldsymbol{k}},t)$ in terms of the joint fluid–particle–particle distribution function $\rho_{(2)}(\mathbf{u}_1,\mathbf{v}_1,\mathbf{x},\mathbf{v}_2,\mathbf{x}+d_p\hat{\boldsymbol{k}})$ by assuming that the particle–particle velocity correlation is induced by particle interaction with the large-scale fluid turbulent motion. By definition

$$\rho_{(2)}\left(\mathbf{v}_1, \mathbf{x}, \mathbf{v}_2, \mathbf{x} + d_p\hat{\boldsymbol{k}}\right) = \int \rho_{(12)}\left(\boldsymbol{u}, \mathbf{v}_1, \mathbf{x}, \mathbf{v}_2, \mathbf{x} + d_p\hat{\boldsymbol{k}}, t\right) \mathrm{d}u \tag{13.251}$$

and

$$\rho_{(2)}\left(\mathbf{v}_1, \mathbf{x}, \mathbf{v}_2, \mathbf{x} + d_p\hat{\boldsymbol{k}}\right) = \rho_{(2)}\left(\mathbf{v}_1, \mathbf{x}, |\, \boldsymbol{u}, \mathbf{v}_2, \mathbf{x} + d_p\hat{\boldsymbol{k}}\right) \rho_{(2)}\left(\mathbf{v}_2, \mathbf{x} + d_p\hat{\boldsymbol{k}} |\, \boldsymbol{u}, \mathbf{x}\right) \rho_{(12)}\left(\boldsymbol{u}, \mathbf{x}\right) \tag{13.252}$$

where (|) denotes a conditional PDF and explicitly $p_{12}(\boldsymbol{u},\boldsymbol{x})$ is the probability density of finding a carrier flow velocity $\boldsymbol{u}$ conditioned upon there being any particle at $\boldsymbol{x}$. By using these relationships, it is assumed that

$$\rho_{(2)}\left(\mathbf{v}_1, \mathbf{x}, |\, \boldsymbol{u}, \mathbf{v}_2, \mathbf{x} + d_p\hat{\boldsymbol{k}}\right) = \rho_{(2)}\left(\mathbf{v}_1, \mathbf{x}, |\, \boldsymbol{u}, \mathbf{x}\right) \tag{13.253}$$

and, if the characteristic length scales of the carrier flow turbulence is larger than the particle diameter, then

$$\rho_2\left(\mathbf{v}_2, \mathbf{x} + d_p\hat{k} \middle| \mathbf{u}, \mathbf{x}\right) \approx \rho_2\left(\mathbf{v}_2, \mathbf{x} + d_p\hat{k} \middle| \boldsymbol{u}, \mathbf{x} + d_p\hat{k}\right) \tag{13.254}$$

By using the relationship

$$\rho_2\left(\mathbf{v}_1, \mathbf{x}, \middle| \boldsymbol{u}, \mathbf{x}\right)\ \rho_{1/2}\left(\boldsymbol{u}, \mathbf{x}\right) = \rho_{12}\left(\boldsymbol{u}, \mathbf{v}, \mathbf{x}\right) \tag{13.255}$$

the particle–particle pair distribution function may be written in terms of the fluid–carrier flow-particle joint PDF as

$$\rho_{(2)}\left(\mathbf{v}_1, \mathbf{x},\ \mathbf{v}_2, \mathbf{x} + d_p\hat{k}\right) = \int \rho_{(2)}\left(\boldsymbol{u}, \mathbf{v}_1, \mathbf{x}\right) \rho_{(2)}\left(\boldsymbol{u}, \mathbf{v}_2, \mathbf{x} + \hat{k}d_p\right) \rho_{1/2}\left(\boldsymbol{u}, \mathbf{x}\right)\ \mathrm{d}u \tag{13.256}$$

13.4.3.5.3 Third-Order Moment Expansion (Grad's Theory)

Following Grad's theory of rarefied gases (1949), the distribution function in the collision term may be approximated by its third-order expansion in Hermite polynomials:

$$P(\underline{v}, \underline{x}, t) = \left[1 + \frac{a_{2,ij}}{2T_2^2}\mathrm{v}'_i\mathrm{v}'_j + \frac{a_{2,ijk}}{6T_2^3}\mathrm{v}'_i\mathrm{v}'_j\mathrm{v}'_j - \frac{a_{2,ijj}}{2T_2^2}\mathrm{v}'_i\right]P^0(\underline{v}, \underline{x}, t) \tag{13.257}$$

where using q^2 to denote the mean the particle kinetic energy per unit particle mass

$$T_2 = \frac{2}{3}q^2, \quad a_{2,ij} = \left(\overline{u'_{k,i}u'_{k,j}}\right)_2 - \frac{2}{3}q^2\delta_{ij}, \quad a_{2,ijk} = \langle \mathrm{v}'_i\mathrm{v}'_j\mathrm{v}'_k\rangle$$

$P(\underline{v},\underline{x},t)$ is the equilibrium PDF, the product of the local spatial density and a Maxwellian distribution for the particle velocities i.e.,

$$P^0(\underline{v}, \underline{x}, t) = \frac{<p(\underline{x}, t)>}{(4\pi q^2/3)^{3/2}}\ \exp\left(-\frac{v'^2}{4q^2/3}\right) \tag{13.258}$$

By using the hard sphere collision model, Jenkins and Richman (1985) derived the following collisional terms in the transport equations for the particle mass (m), momentum ($m\mathrm{v}$), kinetic stresses ($1/2m\mathrm{v}'^2$), and kinetic energy flux, ($m\mathrm{v}'_i\mathrm{v}'_j\mathrm{v}'_k$) respectively:

$$C(m) = 0 \tag{13.259a}$$

$$C(m\mathrm{v}) = 0 \tag{13.259b}$$

$$C(m\mathrm{v}'_i\mathrm{v}'_j) = -<\rho>\frac{\sigma_c}{\tau_c}\left(\langle \mathrm{v}'_i\mathrm{v}'_j\rangle - \frac{2}{3}q^2\delta_{ij}\right) - <\rho>\frac{(1 - e_c^2)}{2\tau_c^2}\ \frac{2}{3}q^2\delta_{ij} \tag{13.259c}$$

$$C(m\mathrm{v}'_i\mathrm{v}'_j\mathrm{v}'_k) = \frac{5}{12}\ <\rho>\frac{\xi_c}{\tau_c}(9a_{ijk} - a_{ill}\delta_{jk} - a_{jll}\delta_{ik} - a_{mll}\delta_{ij}) \tag{13.259d}$$

where τ_c is the time between particle collisions and $\sigma_c = (1 + e_c)(3 - e_c)/5$ and $\xi_c = (1 + e_c)(49 - 3e_c)/100$. The collisional term in the kinetic stress transport equation is written as a return to isotropy term analogous to the Rotta term in the Reynolds stress transport turbulence modeling approach. Elastic collisions ($e_c = 1$) lead to a destruction of the off-diagonal correlations and redistribution of energy among the various normal stresses without modifying the total kinetic energy. The extension to inelastic collisions leads to a linear dissipation rate in the kinetic stress transport equations proportional to the collision frequency and a function of the coefficient of restitution.

Following Lavieville (1997), Grad's theoretical approach may also be used for correlated collisions by performing a Hermite polynomial expansion for the fluid–particle joint PDF. This eventually leads to a generalized form for the collisional source term in the kinetic stress transport equation:

$$C(mv'_i v'_j) = <\rho> \frac{\sigma_c}{\tau_c} \left(a_{2,ij} + \frac{q_{12}^2}{4q_1^2} a_{1,ij} - \frac{q_{12}}{q_1^2} a_{12,ij} \right) - <\rho> \frac{(1 - e_c^2)}{3\tau_c^2} (1 - \xi_{12}^2) \qquad (13.260)$$

where

$$a_{k,ij} = \left(\overline{u'_{k,i} u'_{k,i}} \right) - \frac{2}{3} q_k^2 \delta_{ij}$$

$$2a_{12,ij} = \left(\overline{u'_{1,i} u'_{2,j}} \right) + \left(\overline{u'_{1,j} u'_{2,i}} \right) - \frac{2}{3} q_{12} \delta_{ij}$$

$$\xi_{12}^2 = \frac{q_{12}^2}{4q_1^2 q_2^2}$$

with $k = 1$ referring to the continuous phase and $k = 2$ the dispersed phase and $u'_{k,i}$, is the fluctuating velocity component of phase k with respect to its mean value. Likewise q_k^2 is the turbulent kinetic energy of phase k and q_{12} are the particle fluid covariance $\left(\overline{u'_{1,i} u'_{2,i}} \right)$.

13.4.3.5.4 Interparticle Collision Time

The interparticle collision frequency can be computed in terms of the binary particle distribution function as

$$\frac{1}{\tau_c} = \frac{n d_p^2}{n} \int\int \left| \underline{v}_1 - \underline{v}_2 \right| p_2(\underline{v}_1, \underline{v}_2) \, \mathrm{d}\underline{v}_1 \, \mathrm{d}\underline{v}_2$$

where n is the particle number density. Using the form for $p_2(\underline{v}_1, \underline{v}_2)$ derived for correlated collisions gives

$$\tau_c = \tau_c^k (1 - \xi_{12}^2)^{-1/2}$$

where τ_c^k is the standard kinetic theory interparticle collision time based on the molecular chaos assumption and given explicitly by

$$(\tau_c^k)^{-1} = n\pi d_p^2 \sqrt{\frac{16}{\pi} \frac{2}{3} q_2}$$

The above equations show that the effective interparticle collision rate based on the correlated collision model is always smaller than the one given by standard kinetic theory and decreases with respect to the ratio of the eddy–particle interaction time to particle relaxation time as a result of the increase of correlation coefficient ξ_{12}. This behavior was observed by Lavieville et al. (1995) in LES-Lagrangian simulations in homogeneous isotropic turbulent flows showing that neighboring particles have correlated turbulent velocities.

13.4.3.6 Conclusions and Future Developments

The PDF approach provides a rational framework in which the behavior of a flow of dispersed particles can be formulated. The focus here is on the PDF equation itself, how it is derived and how it is used to obtain the continuum equations and constitutive relations for the dispersed phase in a two-fluid model. In addition, the approach can also be used to deal with the near wall behavior by incorporating the influence of boundary conditions in a natural and complete way. The example considered here was of particles impacting the wall with rebound and absorption (impact adhesion or sticking). This poses serious problems in the traditional two-fluid approach not only because the boundary conditions have to be cast in an artificial form (based on certain adhoc assumptions about the particle velocity distribution at the wall), but also because the continuum equations break down close to the wall. Furthermore, the traditional two-fluid approaches make certain assumptions about the properties of the dispersed phase; i.e., it behaves as a simple Newtonian fluid, which is strictly a heuristic assumption.

It is important to appreciate also that closure approximations for the PDF equations are necessarily carried out in particle-phase space (particle velocity and position in the inert particle cases considered here). This means that a single closure approximation in phase space implies closure at all levels of the moment equations (i.e., closure of the continuum equations and higher order moment equations). All these important features were discussed in the subsection on accuracy and reliability of PDF approaches.

In this section, the focus was on dilute flows and dense flows (through the influence of interparticle collisions). The problem of two-way coupling and turbulence modification by the dispersed phase was not discussed. It is clear, however, that the closure terms in the mass, momentum, and Reynolds stress transport equations for the continuous phase bear a relationship to two-way coupling and turbulence modification. However, the crucial problem on how the particles influence the turbulence dissipation in the continuous phase in terms of closure has not been dealt with adequately. This is all bound up with the way particles interact with turbulent structures, in particular how particles influence their flow topology and persistence and how this influences the internal dynamics of turbulence production and dissipation and the demixing and segregation of the particles themselves in a turbulent flow. While these features have formed the basis of numerous simulations and experiments, the problem of how these features can be incorporated in a strictly formal way into a PDF formulation has not yet been achieved and remains a significant challenge for the future.

13.5 Applications

Th. Frank, Y. Onishi, and B. van Wachem

13.5.1 Lagrangian Prediction of Performance Parameters in Cyclone Separators

Th. Frank

13.5.1.1 Introduction

Disperse multiphase flows are very common for processes in mechanical and thermal process technology (e.g., gas–particle or gas–droplet flows, coal combustion, pneumatical conveying, and erosion phenomena). Processes for the separation of solid particles from gases or fluids and the classification and particle size analysis are an important field of interest in process technology. Most of the flow regimes in technical processes are real three-dimensional and cannot be restricted to two-dimensional numerical analysis. Therefore, this section deals with a Lagrangian approach for the prediction of three-dimensional, disperse gas–particle flows, and its application for flow simulation in cyclone particle separators.

The investigations of the precipitation of quartz particles were carried out for a series of four geometrically similiar cyclones of different size and for a number of different gas inlet velocities. Numerical results were compared with experiments by König (1990) and showed a very good agreement with experimentally predicted particle precipitation rates.

13.5.1.2 Basic Equations of Fluid Motion

The three-dimensional, two-phase (gas–particle) flow in the cyclone separator is described by assuming that the particulate phase is dilute and the particle loading is rather low. This assumption satisfies the neglect of interparticle effects and contributing source terms in the Navier–Stokes equations due to particle–fluid interaction. Further, the two-phase flow is assumed statistically steady, incompressible, and isothermal. Then, the time-averaged form of the governing gas phase equations can be expressed in the form of the general transport equation :

$$\frac{\delta}{\delta x}(\rho_F u_F \Phi) + \frac{\delta}{\delta y}(\rho_F v_F \Phi) + \frac{\delta}{\delta z}(\rho_F w_F \Phi) \tag{13.261}$$

$$= \frac{\delta}{\delta x}\left(\Gamma_\Phi \frac{\delta \Phi}{\delta x}\right) + \frac{\delta}{\delta y}\left(\Gamma_\Phi \frac{\delta \Phi}{\delta y}\right) + \frac{\delta}{\delta z}\left(\Gamma_\Phi \frac{\delta \Phi}{\delta z}\right) + S_\Phi + S_\Phi^P$$

were Φ is a general variable, Γ_Φ a diffusion coefficient, S_Φ a general source term, and S_Φ^P the source term due to particle–fluid interaction ($S_\Phi^P \equiv 0$ if coupling of the continous and disperse phase can be neglected). The relationship among of S_Φ, Γ_Φ, S_Φ and S_Φ^P and the constants of the standard k–ε turbulence model used for the present numerical simulation are given in Section 13.3.

13.5.1.3 Equations of Motion of the Disperse Phase

The disperse phase is treated by the application of the Lagrangian approach, i.e., discrete particle trajectories are calculated. Each calculated particle represents a large number of physical particles of the same physical properties, which is characterized by the particle flow rate $\dot{N}_P$ along each calculated particle trajectory. The prediction of the particle trajectories is carried out by solving the ordinary differential equations for the particle location and velocities. By assuming that the ratio of fluid to particle density is small ($\rho_F/\rho_P \ll 1$), these equations read as follows:

$$\frac{d}{dt}\begin{bmatrix} x_P \\ y_P \\ z_P \end{bmatrix} = \begin{bmatrix} u_P \\ v_P \\ w_P \end{bmatrix} \tag{13.262}$$

$$\frac{d}{dt}\begin{bmatrix} u_P \\ v_P \\ w_P \end{bmatrix} = \frac{3}{4}\frac{\rho_F}{\left(\rho_P + \frac{1}{2}\rho_F\right)d_P}\left(v_{rel} C_D(Re_p)\begin{bmatrix} u_F - u_P \\ v_F - v_P \\ w_F - w_P \end{bmatrix} \right. \tag{13.263}$$

$$\left. + \frac{2\nu_F^{1/2}}{\pi\left|\boldsymbol{\Omega}\right|^{1/2}} C_A \begin{bmatrix} (v_F - v_P)\Omega_z - (w_F - w_P)\Omega_y \\ (w_F - w_P)\Omega_x - (u_F - u_P)\Omega_z \\ (u_F - u_P)\Omega_y - (v_F - v_P)\Omega_z \end{bmatrix} \right) + \frac{\rho_P - \rho_F}{\rho_P + \frac{1}{2}\rho_F}\begin{bmatrix} g_x \\ g_y \\ g_z \end{bmatrix}$$

with

$$\boldsymbol{\Omega} = rot\mathbf{v}_F \quad Re_p = \frac{d_P v_{rel}}{\nu_F} \quad v_{rel} = \sqrt{(u_F - u_P)^2 + (v_F - v_P)^2 + (w_F - w_P)^2}$$

These equations of motion of the disperse phase include, on the RHS, the drag force, the lift force due to shear in the fluid flow field (Saffman force), the gravitational and added mass force. For the present numerical investigation the Magnus force due to particle rotation is neglected because of there minor importance in the study of the very fine particles in the particle diameter range.

The values for the coefficients C_D and C_A can be found in the literature of Frank et al. (1997), Frank (2002), and Sommerfeld (1996). In addition, for the lift coefficient C_A, the correction obtained by Mei (1992) is taken into account. The effect of fluid turbulence on the motion of the disperse phase, which is regarded to be very important for the particle diameter range under investigation, is modeled by the Lagrangian stochastic–deterministic (LSD) turbulence model proposed by Milojević (1990). The particle–wall collisions are treated according to the irregular bouncing model by Sommerfeld (1992, 1996) in the modified wall roughness formulation given by Tsuji et al. (1991), Frank et al. (1997), and Frank (2002).

13.5.1.4 Solution Algorithm

The time-averaged equations of fluid motion are solved by using the program package MISTRAL-3D, initially developed by Perić (1992) and Schreck and Perić (1992). The program MISTRAL/PartFlow-3D was extensively modified by the authors for gas–particle flow computations. Further modifications involve the implementation of a standard k–ε turbulence model and the parallelization of the solution algorithm by application of a domain decomposition method. The most fundamental features of MISTRAL/PartFlow-3D are :

- Use of nonorthogonal, boundary-fitted, numerical grids with arbitrary hexahedral control volumes
- Use of block-structured numerical grids for geometrical approximation of complex flow domains

- Parallelization using domain decomposition method for both the Eulerian and the Lagrangian part of the computation
- Finite-volume solution approach of SIMPLE kind with colocated variable arrangement; Cartesian vector and tensor components; and full multigrid solution approach

The solution algorithm for the equations of particle motion is based on the program package, PartFlow, developed by the authors. A detailed description of the three-dimensional solution algorithm and the developed parallelization methods for the Lagrangian approach can be found in Frank et al. (1997), Frank and Wassen (1997), and Frank (2002).

13.5.1.5 Gas–Particle Flow in and Performance of a Standard Cyclone

The presented three-dimensional Lagrangian approach was applied to the gas–particle flow in a standard cyclone shown in Figure 13.62. The calculations were based on experimental investigations carried out by König (1990) on a series of geometrically similiar cyclones for a number of different inlet gas velocities.

13.5.1.5.1 Flow Geometry and the Numerical Grid

The cyclones Z10, Z20, Z40 and Z80 investigated in this paper were determined by the following geometrical properties (see also Figure 13.62):

		Z10	Z20	Z40	Z80
Diameter of the cyclon (mm)	D	40	80	160	320
Height of the cyclon (mm)	H	195	390	780	1560
Inlet cross-section (mm^2)	$a \times b$	4.5×18	9×36	18×72	36×144
Diameter of the gas exit (mm)	d_T	10	20	40	80
Height of the gas exit (mm)	H_T	31	62	124	248
Diameter of the particle exit (mm)	d_B	10	20	40	80

Owing to the complex geometry of the cyclone, a numerical grid with 42 different grid blocks and about 250,000 finite-volume elements had to be designed for the numerical calculations of the gas–particle flow. The numerical grid was originally designed for the Z10 cyclone and then proportionally scaled as 1 : 2 : 4 : 8 for the other three cyclones Z20–Z80.

13.5.1.5.2 Prediction of the Gas and Particle Flow, Pressure Loss

In the course of preliminary calculations of the gas flow field in the cyclones, it was found that the numerical mesh needed further improvement and certain grid refinement in regions of large fluid velocity gradients in order to get converged solutions. Grid refinement was applied to the gas inlet and to the region in the vicinity of the lower end of the gas exit tube. But certain restrictions in the mesh generation algorithm prevented an optimum arrangement and design of the finite-volume elements in some regions of the flow geometry. Consequently, strong underrelaxation had to be applied for the solution algorithm in order to obtain convergence, mainly due to the convergence behavior of the k–ε equations.

Calculated flow fields show the typical asymetrical main vortex in the upper cylindrical part of the cyclone. In a more detailed view, a flow recirculation can be found along the lid of this cylindrical part of the cyclone and further downward along the outer wall of the gas exit tube. This type of recirculating flow is well known for cyclone separators from the literature. The flow field in the other parts of the cyclone is also in qualitative agreement with the knowledge available for the flow in cyclone separators. The predicted trajectory of a particle in the Z10 cyclone is shown in Figure 13.63.

The pressure loss over the cyclone was predicted for various gas inlet velocities and compared with the experimental data of König in Figure 13.64. The pressure loss data of König take only into account the difference of the static pressure before and after the cyclone. The figure shows that the numerical calculations underpredict the pressure loss for all gas inlet velocities investigated. The reason for this is most likely due to slight differences between the experimental setup and the flow geometry investigated numerically. The numerical data for the pressure loss show a comparable increase with an increased gas inlet velocity.

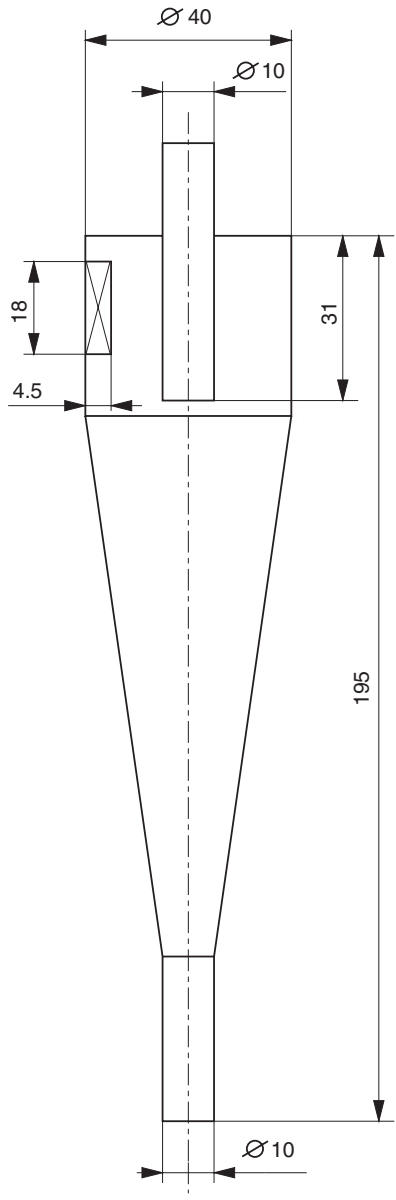

FIGURE 13.62 Scheme of the standard cyclone Z10.

Particle trajectory calculations were carried out using the described Lagrangian approach with the predicted gas flow fields in order to obtain particle collection efficiencies for the four different cyclones (see Figure 13.64). The main difficulties in the calculation of particle motion include :

1 The flow in the cyclone leads to a very large number of particle–wall collisions. The detection of a particle–wall collision results in a decrease in the integration time step of the solution algorithm. Therefore, the large number of particle–wall collisions lead to large computation times for predicting particle motion.
2 The large computation time needed for cyclone flow prediction is also determined by considering the influence of gas flow turbulence on particle motion. In order to ensure accuracy, the integration

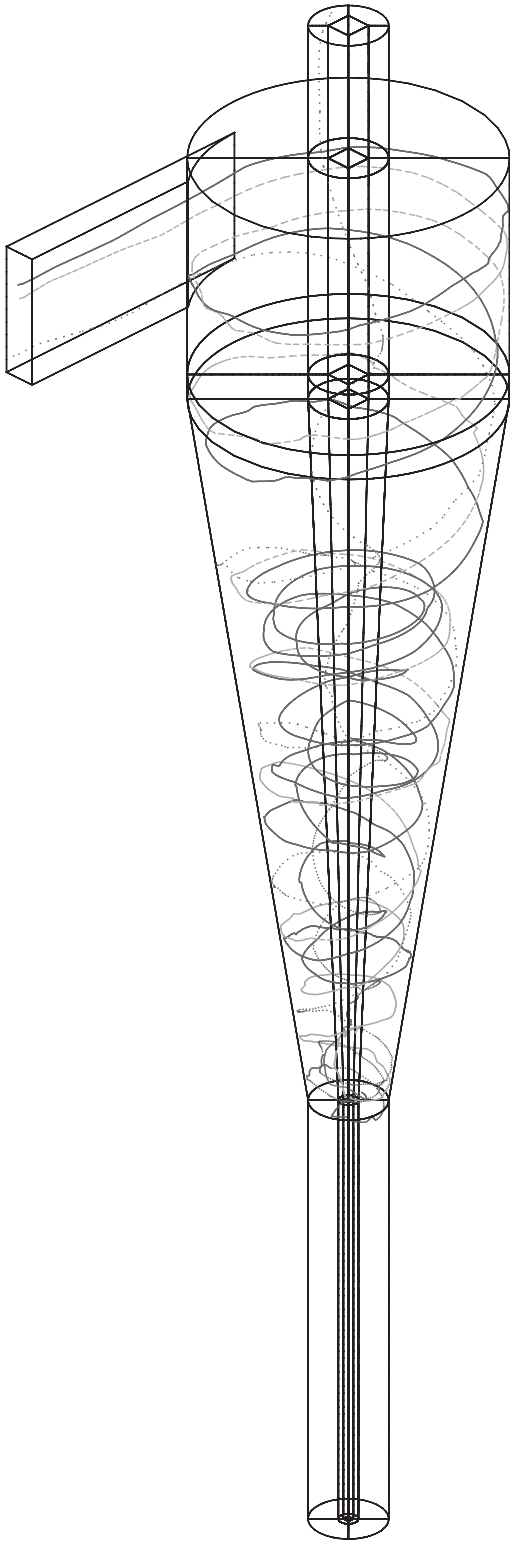

FIGURE 13.63 Particle trajectories in Z10 for gas inlet velocity $v_F = 10$ m/sec, $d_P = 1,...,5$ μm.

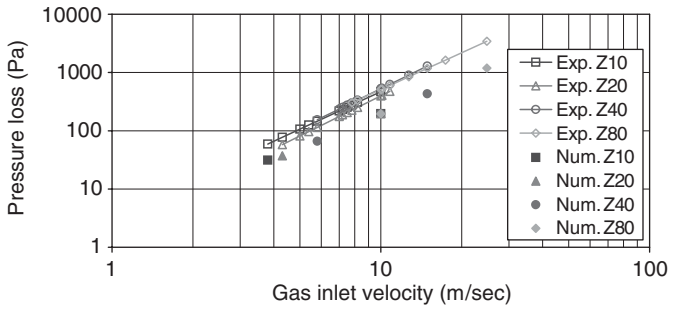

FIGURE 13.64 Comparison of pressure loss vs. gas inlet velocity for Z10,...,Z80 cyclones.

time step is set to be less than one tenth of the turbulent time scale of the LSD turbulence model. The resulting small time steps of the Runge–Kutta solver for the particle equations of motion contribute to the large computational effort needed for the present simulation.

3 The larger geometrical size of the Z40 and Z80 cyclones lead to a substantial increase in particle residence time in the cyclone and thus to larger computation time.

As a result, the calculation of about 10,000 particle trajectories in the cyclone separator takes about 22 hours of CPU-time on a single MIPS R10000 processor of a Silicon Graphics CRAY Origin2000.

13.5.1.5.3 Calculation of the Particle Collection Efficiency

In accordance with the experiments by König (1990), investigations for the prediction of the particle precipitation rate were carried out for the physical properties of quartz particles. The original quartz dust had a particle diameter distribution in the range of $d_p = 0 - 50$ µm with a number mean particle diameter of $\overline{d_p} = 10.9$ µm. The numerical simulations were carried out for 20 particle diameter classes in the range between 0.5 and 15 µm. A total number of 670 particle trajectories with random initial conditions in the inlet cross-section were calculated for each of the 20 particle diameter classes. A particle density of $\rho_p = 2500$ kg/m^3 was assumed for the quartz particles. For the coefficients of restitution and kinetic friction, typical values for quartz particles were used ($k = 0.8, f = 0.35$).

In a first series of calculations, the collection efficiencies for the quartz particles were predicted for all four cyclones Z10, ..., Z80 with an inlet gas velocity of $u_F = 10$ m/sec. The collection efficiency is defined as

$$\eta(d_p) = 1 - \frac{\dot{N}_{out}(d_p)}{\dot{N}_{in}(d_p)}$$

where $\dot{N}_{in}(d_p)$ and $\dot{N}_{out}(d_p)$ are the particle flow rates for a given particle size in the inlet cross-section and gas exit cross-section at the top of the cyclone, respectively. In the numerical prediction, particles are assumed to be collected in the cyclone, if :

1. The particle trajectory reaches the bottom cross-section of the cyclone.
2. The particle sticks to the wall of the cyclone (which means the wall normal velocity of the particle after a particle–wall collision is less than 10^{-5} m/sec).
3. The particle residence time in the cyclone is larger than the maximum allowed computation time, which was set to $T_{max} = 150$ sec for Z10, and Z20 and to $T_{max} = 250$ sec for cyclones Z40 and Z80, due to their larger geometrical size. The value for T_{max} was choosen in a way, that the number of particles with this very large residence time in the cyclone was less than 4–5% of the calculated particle trajectories.

A comparison of the predicted and measured collection efficiencies for the Z20 cyclone operating at two inlet velocities is shown in Figure 13.65. One notes that the shapes of the collection efficiency curves are similiar. The higher inlet velocity leads to the collection of smaller particles. The numerical predictions for

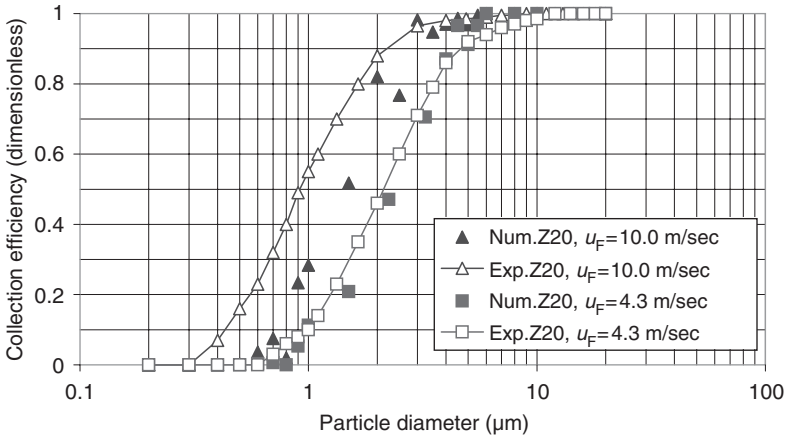

FIGURE 13.65 Comparison of particle collection efficiencies for Z20 and gas inlet velocities $u_F = 4.3$ m/sec and 10 m/sec.

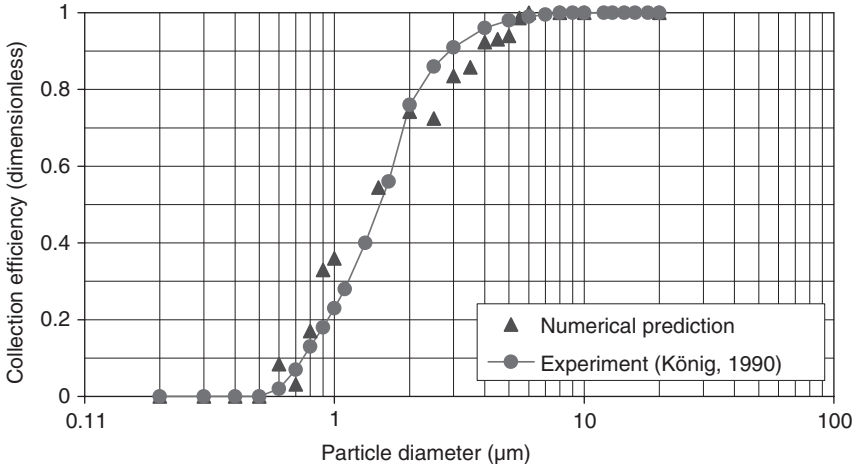

FIGURE 13.66 Comparison of the particle collection efficiencies for the Z80 cyclone, $u_F = 10$ m/sec.

the 4.3 m/sec inlet velocity agree better with experimental results than those for the 10 m/sec inlet velocity. A further comparison of the predicted and measured collection efficiencies for the Z80 cyclone with an inlet velocity of 10 m/sec is shown in Figure 13.66. One notes reasonably good agreement, although the slopes of the efficiency curves differ somewhat near the cut-off diameter (50% efficiency). Numerical predictions for the other cyclone geometries can be found in Frank (2000, 2002).

This section illustrates the capability of the three-dimensional Lagrangian approach to predict multiphase flows in complex geometries. The predictions for pressure loss and collection efficiency agree well with experimental results.

13.5.2 Slurry Flows

Yasuo Onishi

Slurry flows occur in many circumstances, including chemical manufacturing processes, pipeline transfer of coal, sand, and minerals, mud flows, and disposal of dredged materials. In this section, we discuss slurry flow applications related to radioactive waste management.

13.5.2.1 Tank Waste Characteristics and Waste Retrieval Operations

Two-hundred million liters of wastes containing 180 million curies of radioactivity are stored in single- and double-shell underground tanks at the U.S. Department of Energy's Hanford Site in southeastern Washington State (Gephart and Lundgren, 1997). Much of this waste is removed from the tanks and solidified at a waste treatment plant, then buried at disposal sites. These wastes are highly basic (pH 10–14), have high salt content, and are chemically and physically very complex. Sludges, saltcakes, liquids, and vapors often coexist in the same tank. Sludges consist of an interstitial solution and solids that are not dissolvable with water, while saltcakes contain an interstitial solution and water-dissolvable solids.

The solids in the sludges and saltcakes vary widely in chemical and physical characteristics (Onishi et al., 2003; Jewett et al., 2002). The solids contain primary particles to agglomerates, with sizes ranging over five orders of magnitude. The smallest particles comprise many hydrous oxides, including ZrO_2 and FeOOH, whose diameters are 3–6 nm. Other particles such as boehmite (AlOOH) and apatite are 0.1–1 μm in size. These submicron primary particles found in many tanks form agglomerates that are typically 1–10 μm in size, but can reach 100 μm or more. Some of the largest primary particles are gibbsite ($Al(OH)_3$) and uranium phosphate, which can exceed 20 μm in size. Trisodium phosphate hydrates ($Na_3(PO_4)\cdot 12H_2O$) have a needle-like shape and exceed 100 μm in length (Onishi et al., 2002). Hydrated sodium phosphate can interlock to form a gel if sufficient particles exist in the tank. The densities and sizes of primary particles range from 2.26 g/mL for $NaNO_3$ to 11.4 g/mL for pure PuO_2, but agglomerates and flocs tend to be around 1.5 ~ 2.5 g/mL (Onishi et al., 2002). The waste often contains radioactive ^{90}Sr and ^{137}Cs, whose radionuclide decay heats the waste, sometimes to above 100°C.

The sludge and saltcake are mostly non-Newtonian, and the supernatant liquid is Newtonian. The slurry (mixture of sludge or saltcake and supernatant liquid) can be Newtonian or non-Newtonian. Figure 13.67 shows the waste rheology in double-shell tank 241-SY-102, indicating that the sludge can be represented as a Bingham flow, while the sludge diluted by 48 wt% supernatant liquid is Newtonian (Onishi et al., 1996). Figure 13.68 presents the variation in viscosity of boehmite waste with pH, indicating that the viscosity can change with chemical conditions even without dilution.

One to four 300-hp mixer pumps are installed in 28 of the 4000m^3 double-shell tanks at the Hanford Site to stir radioactive sludge or saltcake and supernatant liquid. These mixer pumps withdraw the sludge or saltcake waste from near the tank bottom and inject it back into the tank waste through two 0.3-m-diameter

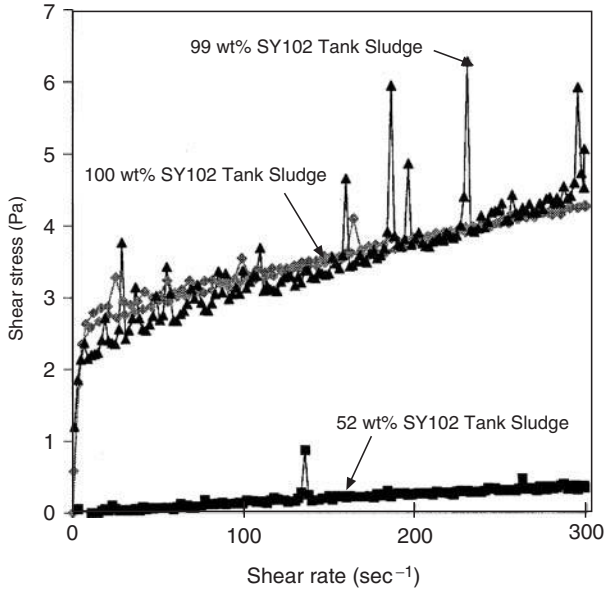

FIGURE 13.67 Rheology of Tank 241-SY-102 Newtonian and non-Newtonian wastes.

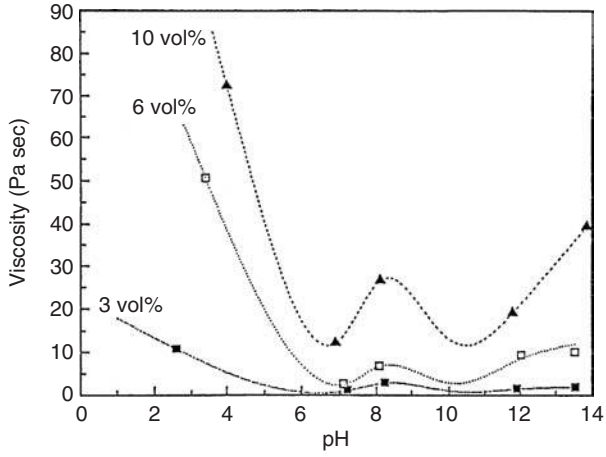

FIGURE 13.68 Viscosity of boehmite in 1*M* $NaNO_3$ as a function of pH and solids loading at a strain rate of 11.5 sec^{-1}.

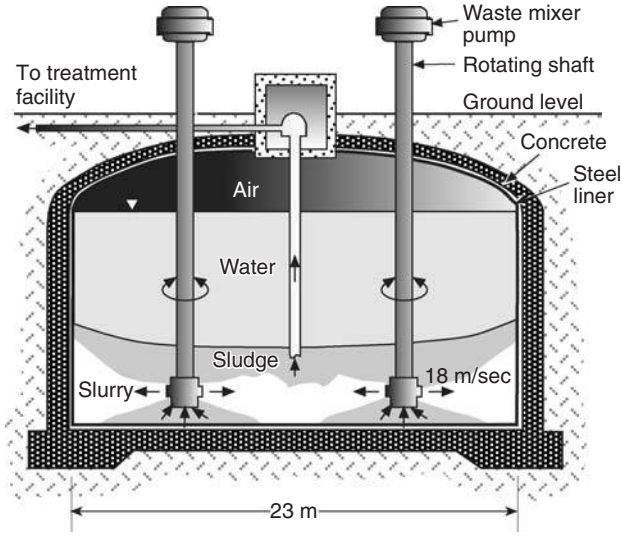

FIGURE 13.69 Mixer pumps in a double-shell tank.

nozzles at 18m/sec exit velocity. The pumps will rotate at 0.5–0.02 r/min to stir up the sludge or saltcake and supernatant liquid in the tank, blending them into a slurry that will be pumped from the tank to a waste treatment facility, as shown in Figure 13.69 (Onishi et al., 2003). In some cases, solvents (e.g., water or sodium hydroxide solution) will be added to dissolve and thus reduce the amount of solids, decrease the density and viscosity of the slurry, and make the waste easier to mix, retrieve, and transfer through pipelines to other tanks or to the treatment facility.

When the sludge is mixed with supernatant liquid or solvent in the tank, physical and chemical changes occur. Dilution alone changes important physical properties. This change can be observed from rheological measurements of double-shell tank 241-SY-102 waste at Hanford (Onishi et al., 1996). As shown in Figure 13.67, the original sludge is non-Newtonian, while the sludge diluted by 48 wt% supernatant liquid is Newtonian. Thus, when the sludge is withdrawn to the mixer pump near the tank bottom and injected back into the sludge layer, the jet is a non-Newtonian flow. The jet entrains the supernatant fluid

as it penetrates and mixes with the waste. The resulting slurry becomes a Newtonian flow with significantly reduced viscosity and shear stress. Furthermore, chemical reactions caused by waste mixing can dissolve or precipitate solids. Thus, changing solid mass as well as the densities and rheologies of sludge, saltcake, and the resulting mixed slurry and supernatant liquid affect waste mixing. For example, if chemical conditions and solids concentrations are such that boehmite and its aggregates form, the waste becomes a gel and the tank waste can neither be removed from the tank nor transferred into treatment facilities through pipelines.

13.5.2.2 Waste Retrieval Assessment Model

Since waste retrieval and treatment cost is very high, the waste retrieval design and operation decision-making must be scientifically defensible. To address the complex interactions among waste mixing, chemical reactions, and rheology during the waste retrieval operation, waste assessment tools that accurately simulate the flow field, turbulence, heat transfer, and chemical reactions are needed.

The ARIEL code (Onishi et al., 1995) is a reactive computational fluid dynamics code that is an example of this type of tool and couples chemistry and fluid dynamics (Yeh and Tripathi, 1989; Steefel and Lasaga, 1994). It is a time-varying, three-dimensional code whose fluid dynamic portion uses integral forms of the following fundamental conservation laws applied in a finite-volume formulation (Trent and Eyler, 1994):

- Conservation of mass (equation of continuity)
- Conservation of momentum (the Navier–Stokes equation)
- Conservation of turbulent kinetic energy and its dissipation (with the k–ε model)
- Conservation of energy (the first law of thermodynamics)
- Conservation of mass for solids, liquids, and gases

These equations are discussed in Sections 13.1 and 13.3. ARIEL has some built-in common Newtonian and non-Newtonian rheology models (e.g., power law and Bingham model), but it can also accept a user-input rheology model. In addition to the free solids settling, it also simulates hindered solids settling.

ARIEL also calculates chemical equilibrium and kinetics. The equilibrium chemistry submodel minimizes the Gibbs free energy to simulate fast aqueous chemical reactions (Felmy, 1995). Since much of the tank waste exists under high ionic-strength conditions, the excess solution free energy is modeled by the Pitzer equations (Pitzer, 1991) in the aqueous-phase modeling. The governing equations to minimize the Gibbs free energy subject to the mass and charge balance are

$$G = \sum_{j=1}^{ns} \mu_j n_j \tag{13.264}$$

subject to

$$\sum_{j=1}^{ns} A_{ij} n_j = b_i \quad i = 1, p \tag{13.265}$$

$$\sum_{j=1}^{nas} z_j n_j = 0 \tag{13.266}$$

$$n_j \geq 0 \quad \text{for all } j \tag{13.267}$$

where G is the Gibbs free energy, μ_j the chemical potential of species j, n_j the number of moles of species j, ns the total number of the chemical species in the system, A_{ij} the number of moles of component i in 1 mol of species j, b_i the number of moles of each component i, p the number of linearly independent mass-balance constraints, z_j the charge of species j, and nas the number of aqueous species.

The kinetic chemistry in ARIEL simulates kinetic reactions of precipitation or dissolution. We used the following rate law for the solid, i, and the associated aqueous species, j:

$$\frac{\mathrm{d}[C_{\mathrm{si}}]}{\mathrm{d}t} = \{k_{\mathrm{i1}} + k_{\mathrm{i2}}[C_{\mathrm{si}}]\}\left\{1 - \frac{Q_{\mathrm{i}}}{K_{\mathrm{i}}}\right\} \tag{13.268}$$

$$\frac{d[C_{wj}]}{dt} = a_{ij}\frac{d[C_{si}]}{dt} \tag{13.269}$$

where $[C_{si}]$ is the molality of solid i; k_{i1} is the reaction rate of solid i's, which is independent of the solid concentration, k_{i2} is solid i's reaction rate, which is dependent on the solid concentration, Q_i the activity product, K_i an equilibrium constant, $[C_{wj}]$ the molality of aqueous species j, and a_{ij} the number of moles of aqueous species j produced from precipitation-dissolution of one mole of solid i.

13.5.2.3 Tank Waste Modeling

We present five simulation cases related to tank waste mixing: (1) generic solid erosion modeling, (2) tank 241-AN-105 sludge waste mixing, (3) tank 241-AZ-102 sludge waste mixing, (4) two-dimensional reactive transport modeling, and (5) three-dimensional reactive transport modeling.

13.5.2.3.1 Generic Solids Erosion Modeling

We examined mobilization and settling of tank wastes having yield strengths of 200, 1000, 2000, or 3000 Pa by simulating pump jet injection into saltcake and sludge and the subsequent mixing. The modeling indicated that the slurry pump jets burrow rapidly into the saltcake and sludge bank, collapsing an overhanging solids layer but eroding only those portions of the solids layer where the normal and shear stresses are greater than or equal to the yield strength of the sludge.

Simulation results (Onishi and Trent, 1999) are shown in Figure 13.70 for saltcake and sludge wastes with yield strengths of 200 Pa (a representative value of saltcake waste) and 1000 Pa (a representative value of sludge waste). As shown on the left panel of the figure, the jet injected by the pump is strong enough to penetrate the entire length of the weaker saltcake (200-Pa yield strength). Its lateral spread is still rather limited because the saltcake resists being mobilized by the weaker jet-induced velocity at the peripheral of the jet. With greater sludge strength of 1000 Pa, the jet did not penetrate the entire length of the sludge (right panel of Figure 13.70). With the 2000 Pa sludge the jet mobilized even less, and the mixer pump mobilized none of the 3000 Pa sludge. These tests showed that solids mobilization and immobilization are strongly controlled by the yield strength of the saltcake and sludge. The solids were eroded little by shear stress but mostly by normal stress; thus, *in situ* or laboratory measurements should obtain the strength of the saltcake and sludge in resisting the combined forces of normal and shear stresses.

13.5.2.3.2 Tank 241-AN-105 Saltcake Waste Mixing

The ARIEL code was applied to Hanford double-shell tank 241-AN-105 to determine whether two 300-hp mixer pumps could mobilize and mix the saltcake, which is 4.5-m thick (1850 m^3) and overlain by

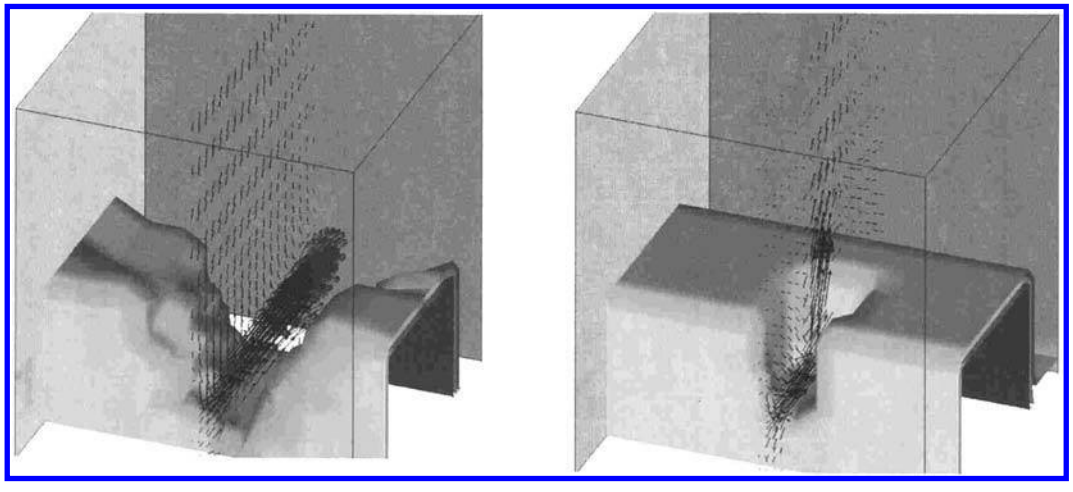

FIGURE 13.70 Three-dimensional distributions of predicted velocity and erosion patterns of the saltcake and sludge with yield strengths of 200 and 1000 Pa, respectively, at one simulation hour.

5.5-m-deep supernatant liquid (2240 m^3) and a 0.4m-thick crust at the top (185 m^3) (Onishi et al., 2003). The viscosity of this tank waste varies seven orders of magnitude from the saltcake to the supernatant liquid, as shown in Figures 13.71 and 13.72. Figure 13.71 presents *in situ* saltcake viscosity measured by a falling ball rheometer at its first and fourth passes, while Figure 13.72 shows both *in situ* and laboratory viscosity measurements (Onishi et al., 2003; Stewart et al., 1996; Herting, 1997). Since commonly used non-Newtonian rheology models do not fit the measured rheology well, we developed and incorporated into the ARIEL code the following tank-specific rheology model (lines in Figure 13.72) as a

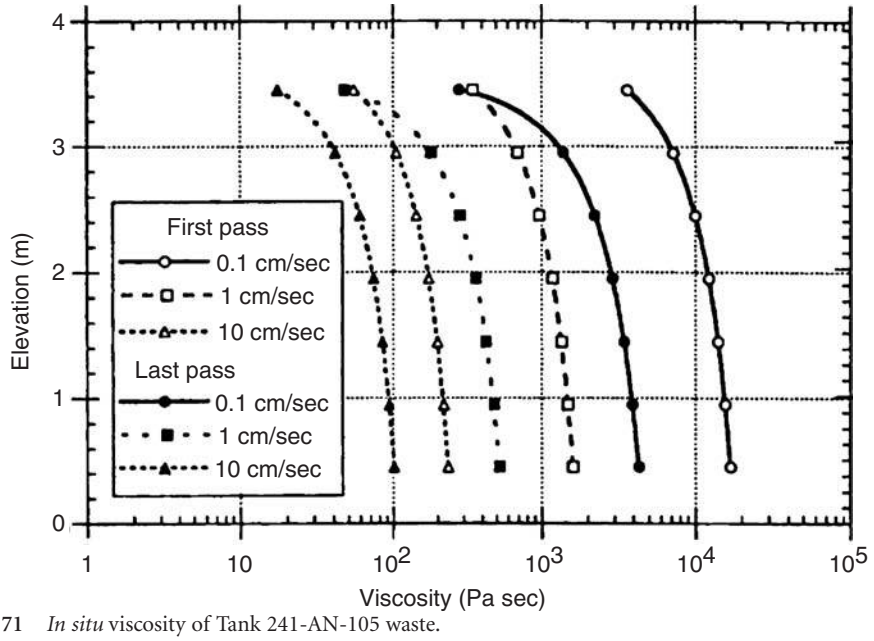

FIGURE 13.71 *In situ* viscosity of Tank 241-AN-105 waste.

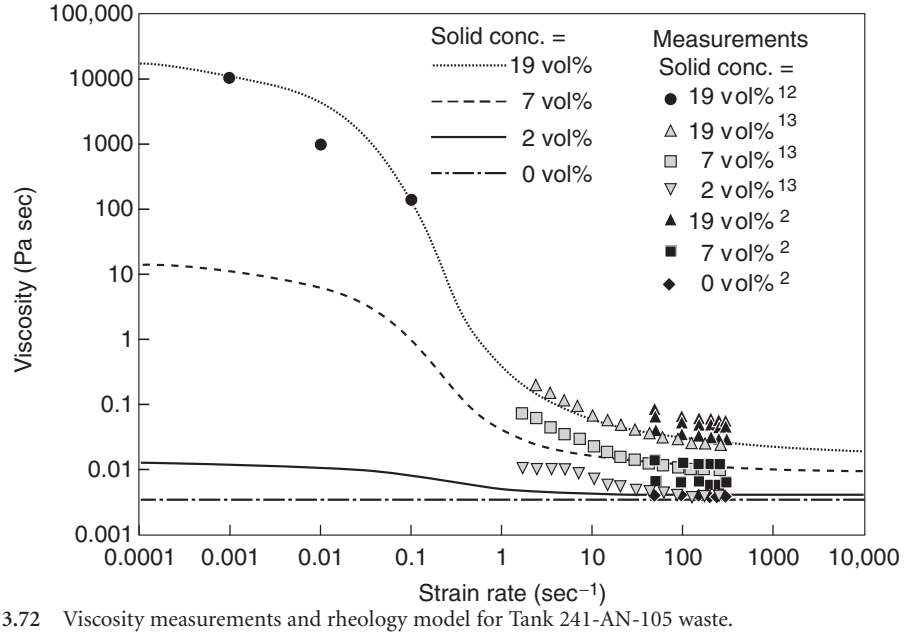

FIGURE 13.72 Viscosity measurements and rheology model for Tank 241-AN-105 waste.

function of solids concentration and strain rate (Onishi et al., 2003).

$$\mu = \mu_L \exp\left(A\left\{1 + a1\left[1 - \frac{2}{\pi}\arctan(a2\ln \lambda\gamma + a3)\right]\right\}\right) \tag{13.270}$$

$$A = \frac{a_4\beta(1 + 4\beta)}{1 - a_5\beta(1 - 2\beta + a_6\beta^2)}, \quad \text{and} \quad \beta = \frac{C_v}{C_{v\ max}}$$

where α_i are constants, C_V a solid volume fraction, C_{Vmax} the maximum solid volume fraction, μ the viscosity (in Pa sec) at solid volume fraction of C_V, μ_L the viscosity, and λ a time constant of the fluid.

The saltcake in all these tanks has a yield strength of about 100 Pa, which was also assigned to this tank model. The simulation results indicate that two mixer pumps would erode all the saltcake and mix the suspended saltcake uniformly with the supernatant liquid. This waste retrieval assessment also provided the resulting waste conditions for the subsequent waste pipeline transfer and waste treatment.

13.5.2.3.3 Tank 241-AN-102 Sludge Waste Pump Jet Mixing

The tank sludge waste contains nonwater-dissolvable solids and is chemically less saturated than saltcake waste. It tends to have greater yield strength but less viscosity. The yield strength of the sludge was measured as about 1540 Pa. The following viscosity model was used to fit measured waste viscosity (Onishi et al., 2000):

$$\mu = \mu_L\left\{\frac{\mu_S}{\mu_L}\right\}^{\beta} \tag{13.271}$$

where μ_S is the viscosity of the sludge layer (0.426 Pa sec at a strain rate of sec^{-1}).

The ARIEL code was applied to this tank to determine the amount of solids two 300-hp mixer pumps would mobilize. This tank also has 22 airlift circulators and heating coils installed to mix and control waste conditions. One of the airlift circulators is shown in Figure 13.73 (the right panal), which shows the model prediction along two vertical planes. This figure indicates that only half of the sludge would be eroded by the two rotating mixer pumps and the suspended solids in that half would be uniformly distributed.

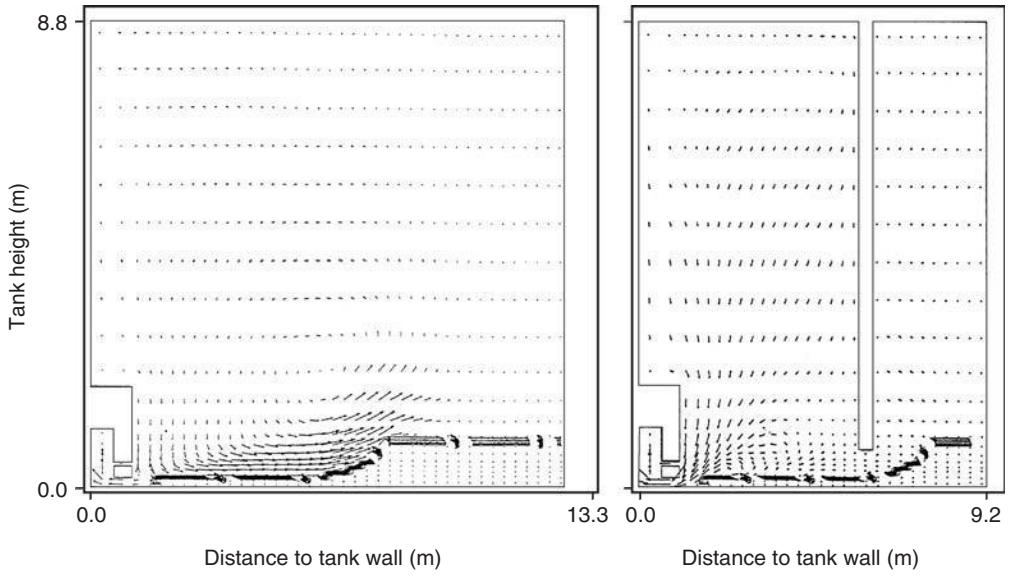

FIGURE 13.73 Predicted distributions of velocity and solid concentrations for Tank 241-AZ-102 at two simulation hours.

ARIEL thus provided useful information on retrieval design and waste feed delivery planning for the treatment plant. The main limitation of ARIEL for these three applications is that waste rheology is not correlated with chemical conditions during the simulation, while actual tank waste rheology is clearly affected by chemical conditions in addition to the physical conditions.

13.5.2.3.4 Two-Dimensional Reactive Transport Modeling:

We tested the interaction between waste chemistry and mixing by simulating an axisymmetric pump jet mixing the saltcake overlain by water (Figure 13.74). Adding water to saltcake waste tanks is the current base retrieval process. Since approximately half of Hanford's double-shell tank waste consists of sodium nitrate and nitrite, we considered their chemical reactions. Six aqueous species (Na^+, NO_2^-, NO_3^-, $NaNO_2$[aq], $NaNO_3$[aq], and H_2O) and three solids [$NaNO_2$[s], $NaNO_3$[s], and nonreactive solids representing nondissolvable solids] were examined. The non-Newtonian viscosity was assigned to be a function of solids volume fraction and strain rate, as expressed by

$$\mu = \mu_L \left\{ \frac{\mu_S}{\mu_L} \right\}^{\beta} \gamma^b \tag{13.272}$$

where $b = 0.75$, representative of some Hanford tank wastes. Other viscosity parameters were the same as those of Eq. (13.173).

The axisymmetric reactive transport model predicted that, as water penetrated into and mixed with the saltcake, $NaNO_2$(s) and $NaNO_3$(s) would be dissolved and only the nonreactive solids remain as solids. As these solids dissolved, the viscosity of the saltcake decreased and the total amount of Na^+, NO_2^-, NO_3^-, $NaNO_2$(aq), $NaNO_3$(aq) in the solution increased. These changes are shown in Figure 13.75 (left panel) for $NaNO_2$(s) concentrations predicted at 45 simulation seconds. As the simulation time progressed, all $NaNO_2$(s) and $NaNO_3$(s) eventually dissolved. Thus, in the actual retrieval operation no slurry pipeline transport would be needed, and much easier liquid pipeline transport would be performed.

Without the chemical reactions (see Figure 13.75, right panel), solids concentration changes are due solely to mixing. Thus, in accounting for the chemical reactions, the mixer pump will encounter a smaller amount of solids and slurry with less viscosity to mobilize. This results in an improved waste mixing and transfer efficiency. This simple numerical test reveals the importance of accounting for the chemical reactions and associated rheology changes to determine the effectiveness of mixer pumps to mobilize the sludge.

13.5.2.3.5 Three-Dimensional Reactive Transport Modeling

The ARIEL code was applied to a more realistic tank waste condition. This case represents non-Newtonian saltcake waste mixed with overlaying water by two 300-hp mixer pumps (see Figure 13.69). Chemical reactions simulated are those in a Na–OH–$Al(OH)_4$–CO_3–SO_4–NO_2–NO_3–$NaNO_2$(aq)–$NaNO_3$(aq)–H_2O system with solids of $Na_2CO_3 \cdot H_2O$, Na_2SO_4, and $Al(OH)_3$. Most of the $Na_2CO_3 \cdot H_2O$ and Na_2SO_4 are expected to be dissolved with water, based on experiments and our chemical modeling. The viscosity of this tank waste varies seven orders of magnitude from saltcake to supernatant liquid, as shown in Figure 13.72.

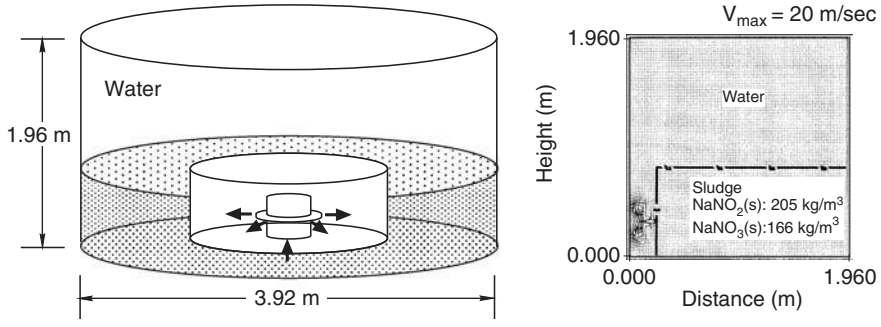

FIGURE 13.74 Axisymmetric reactive transport model setup.

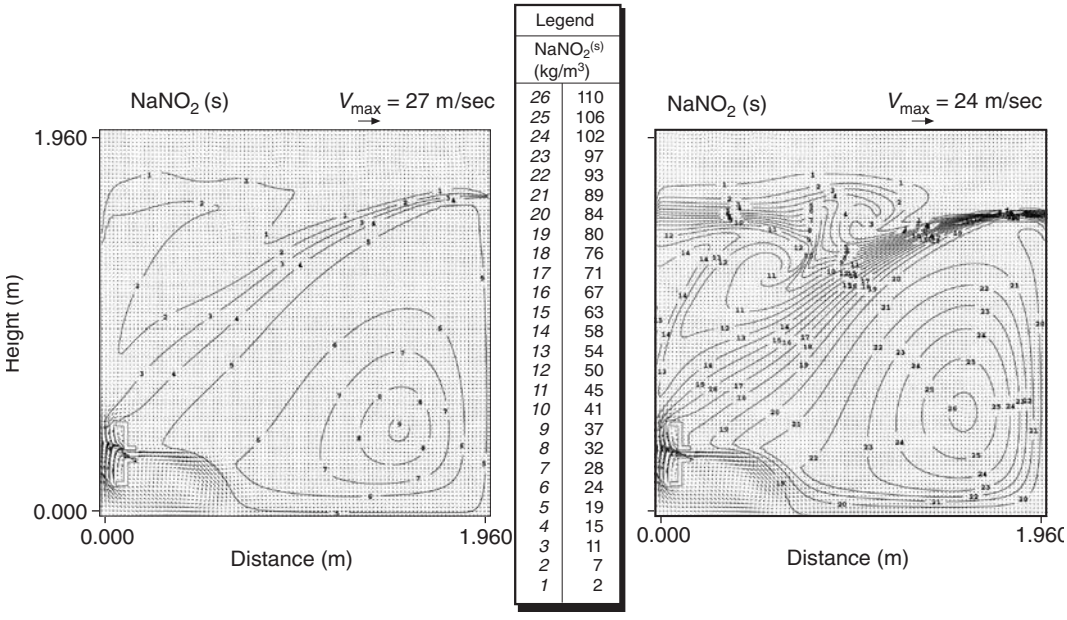

FIGURE 13.75 Predicted $NaNO_2$(s) concentrations at 45 simulation seconds with (left plot) and without (right plot) chemical reactions.

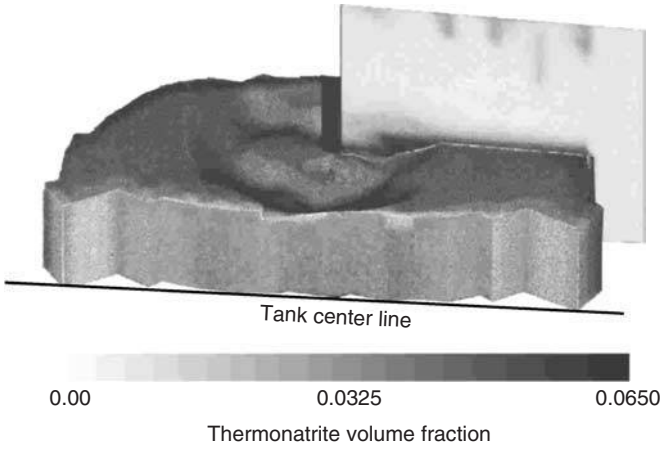

FIGURE 13.76 Predicted thermonatrite ($Na_2CO_3 \cdot H_2O$) volume fractions.

ARIEL began to simulate this case, as shown in the earlier predicted distribution (ten simulation seconds) of thermonatrite ($Na_2CO_3 \cdot H_2O$) in Figure 13.76 (Onishi et al., 1999). Although it simulated more realistic chemical reactions occurring in the tank, it revealed the following limitations:

It takes about ten times the computational time as the same case without chemical reactions.

- It does not account for water mass changes due to dissolution and precipitation of hydrate solids; for example $Na_2CO_3 \cdot H_2O$ dissolves, and the water is released to the solution.
- Some of these hydrates may form agglomerates and gels.

The solution density and slurry rheology are affected by the aqueous chemical species and solids.

13.5.2.4 Summary and Conclusions

Complex interactions occur among waste mixing, chemical reactions, and waste characteristics during radioactive tank waste mixing. We applied the non-Newtonian reactive transport code ARIEL to simulate waste mixing to illustrate these complex interactions. ARIEL couples chemical reactions, multiphase hydrodynamics and transport, and non-Newtonian or Newtonian waste rheology.

The simulation results indicate that (1) the waste has a very complex combination of Newtonian and non-Newtonian rheology, (2) the interaction between waste chemistry and fluid dynamics is important to assess tank waste mixing, and (3) ARIEL is applicable to idealized tank waste conditions — pure crystal solids, no agglomerates, and fast and simple kinetics. The limitations of ARIEL include an extensive computational requirement to simulate waste chemistry and difficulty in handling realistic waste conditions, especially when dealing with hydrates and their associated complexity. Reactive transport modeling of ARIEL represents the first step in developing a scientifically based waste retrieval assessment methodology.

13.5.3 Fluidized Bed

B. van Wachem

This section describes numerical simulations of fluidized systems. The predictions of CFD simulations of bubbling fluidized beds, slugging fluidized beds, and bubble injection into fluidized beds incorporating various models are compared with the "benchmark" experimental data of Hilligardt and Werther (1986), Kehoe and Davidson (1971), Darton et al. (1977), and Kuipers (1990).

13.5.3.1 Frictional Stress

At high solid volume fraction, sustained contacts between particles occur, and the stresses predicted by kinetic theory of granular flow are insufficient. Hence, the additional frictional stresses must be accounted for, in the description of the solid-phase stress. Zhang and Rauenzahn (1997) concluded that particle collisions are no longer instantaneous at high-solid volume fractions, as is assumed in kinetic theory. Several approaches have been presented in the literature to model the frictional stress, mostly originated from geological research groups. Typically, the frictional stress is written in a Newtonian form and has a deviatoric stress-like contribution and a normal stress-like contribution. The frictional stress is added to the stress predicted by kinetic theory for $\alpha_s > \alpha_{s,min}$, where the subscript min stands for threshold value:

$$p_s = p_{kinetic} + p_{frictional} \tag{13.273}$$

$$\mu_s = \mu_{kinetic} + \mu_{frictional} \tag{13.274}$$

Johnson and Jackson (1987) propose a semiempirical equation for the normal frictional stress:

$$p_{frictional} = Fr\frac{(\alpha_s - \alpha_{s,min})^{nn}}{(\alpha_{s,max} - \alpha_s)^{pp}} \tag{13.275}$$

where *Fr*, nn, and pp are empirical material constants, and $\alpha_s > \alpha_{s,min}$, $\alpha_{s,min}$ being the solid volume fraction when frictional stresses become important. The frictional shear viscosity is then related to the frictional normal stress by the linear law proposed by Coulomb (1776) or the approach proposed by Schaeffer (1987):

$$\mu_{frictional} = \frac{p_{frictional}\sin\phi}{\alpha_s\sqrt{\frac{1}{6}\left(\left(\frac{\partial u_s}{\partial x} - \frac{\partial v_s}{\partial y}\right)^2 + \left(\frac{\partial v_s}{\partial y}\right)^2 + \left(\frac{\partial u_s}{\partial x}\right)^2 + \frac{1}{4}\left(\frac{\partial u_s}{\partial y} - \frac{\partial v_s}{\partial x}\right)^2\right)}} \tag{13.276}$$

where ϕ is the angle of internal friction. Values of $\alpha_{s,min}$ are typically in the range 0.55–0.6. Values for the empirical parameters are dependent on the material properties; some examples are given in Table 13.6.

TABLE 13.6 Values for the Empirical Parameters in Eq. (13.174) as Suggested by Various Re-searchers.

Fr (N/m^2)	Nn	*PP*	$\alpha_{s,min}$	ϕ	d_s (μm)	ρ_s (kg/m^3)	Material	Reference
0.05	2	3	0.5	28°	150	2500	Not Specified	Ocone et al. (1993)
3.65×10^{-32}	0	40	–	25.0°	1800	2980	Glass	Johnson and Jackson (1987)
4.0×10^{-32}	0	40	–	25.0°	1000	1095	Polystyrene	Johnson and Jackson (1987)
0.05	2	5	0.5	28.5°	1000	2900	Glass	Johnson et al. (1990)

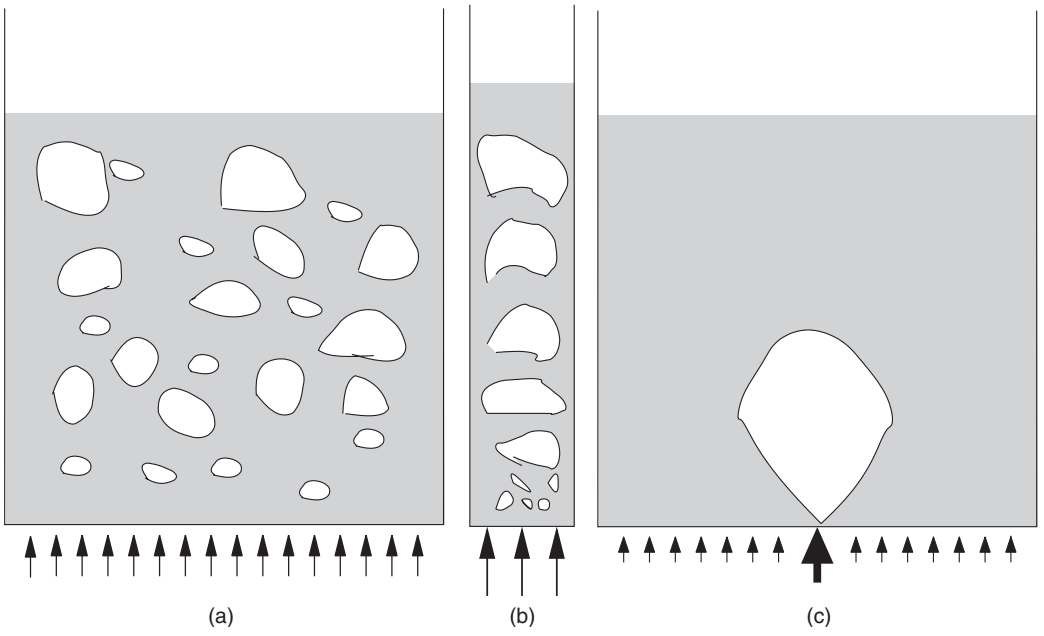

FIGURE 13.77 Flow configurations for the three test cases: (a) fluidized bed; (b) slugging fluidized bed; and (c) bubble injection into a fluidized bed.

13.5.3.2 Simulations

The test cases described in this section are a freely bubbling fluidized bed, a slugging fluidized bed, and a single-bubble injection into a fluidized bed. A sketch of the flow configurations for the three cases is given in Figure 13.77.

The particles in a fluidized bed move due to the action of the fluid through the drag force, thereby resulting in bubbles and complex solids mixing patterns. Typically, the average solid volume fraction in the bed is fairly large, averaging about 40%, whereas in the the free-board of the fluidized bed (the top) there are almost no particles.

The simulations in this work were carried out with the commercial CFD code CFX 4.2. For solving the difference equations, the higher order total variation diminishing (TVD) scheme Superbee is used. This TVD scheme incorporates a modification to the higher-order upwind scheme (second order). The time discretization is done with the second-order back-ward difference scheme. The solution of the pressure from the momentum equations requires a pressure-correction equation, correcting the pressure and the velocities after each iteration; for this, the SIMPLE (Patankar, 1980) algorithm is employed. The calculated pressure is used to determine the density of the fluid phase; the simulations are performed allowing for compressibility of the gas phase. Compressibility is an important effect in fluidized beds, as the gas density varies with 10–30% over a typical fluidized bed. The grid spacing was determined by refining the grid until average properties changed

by less than 4%. Due to the deterministic chaotic nature of the system, the dynamic behavior always changes with the grid. The simulations of the slugging fluidized bed and the freely bubbling fluidized bed were carried out for 25 sec of real time. After about 5 sec of real time, the simulation has reached a state in which averaged properties stay unchanged. Averaged properties, such as bubble size and bed expansion were determined by averaging over the last 15 sec of real time in each simulation. A bubble is defined as a void in the solid phase with a solid volume fraction less than 15%. The bubble diameter is defined as the diameter of a circle having the same surface as the void in the solid phase; this is called the equivalent bubble diameter.

13.5.3.2.1 Boundary Conditions

All the simulations are carried out in a two-dimensional rectangular space in which front and back wall effects are neglected. The left and right walls of the fluidized bed are treated as no-slip velocity boundary conditions for the fluid phase, and free-slip velocity boundary conditions are employed for the particle phase. A possible boundary condition for the granular temperature follows Johnson and Jackson (1987):

$$n\cdot(\kappa\nabla\Theta) = \frac{\pi\rho_s\varepsilon_s\sqrt{3\Theta}}{6\varepsilon_{s,\max}\left[1-\left(\frac{\varepsilon_s}{\varepsilon_{s,\max}}\right)^{1/3}\right]}\left[\varphi'\left|v_{slip}\right|^2 - \frac{3\Theta}{2}(1-e_w^2)\right] \tag{13.277}$$

where the LHS represents the conduction of granular energy to the wall, the first term on the RHS represents the generation of granular energy due to particle slip at the wall, and the second term on the RHS represents dissipation of granular energy due to inelastic collisions. Another possibility for the boundary condition for the granular temperature is proposed by Jenkins (1992):

$$n\cdot(\kappa\nabla\Theta) = -\,v_{slip}\cdot M - D \tag{13.278}$$

where the exact formulations of M and D depend upon the amount of friction and sliding occurring at the wall region. Simulations which are done with an adiabatic boundary condition at the wall ($\nabla\Theta = 0$) show very similar results.

The boundary condition at the top of the free-board (fluid-phase outlet) is the so-called pressure boundary. The pressure at this boundary is fixed to a reference value, 1.013×10^5 Pa. Neumann boundary conditions are applied to the gas flow, requiring a fully developed gas flow. For this, the free board of the fluidized bed needs to be of sufficient height; this is validated through the simulations. In the free board, the solid volume fraction is very close to zero and this can lead to unrealistic values for the particle velocity field and poor convergence. For this reason, a solid volume fraction of 10^{-6} is set at the top of the free board. This way the whole free board is seeded with a very small number of particles, which gives more realistic results for the particle-phase velocity in the free board, but does not influence the behavior of the fluidized bed itself.

The bottom of the fluidized bed is made impenetrable for the solid phase by setting the solid-phase axial velocity to zero. For the freely bubbling fluidized bed and the slugging fluidized bed, Dirichlet boundary conditions are employed at the bottom with a uniform gas inlet velocity. To break the symmetry in the case of the bubbling and slugging beds, initially a small jet of gas is specified at the bottom LHS of the geometry. In the case of the bubble injection, a Dirichlet boundary condition is employed at the bottom of the fluidized bed. The gas inlet velocity is kept at the minimum fluidization velocity, except for a small orifice in the center of the bed, at which a high inlet velocity is specified. Finally, the solids-phase stress, as well as the granular temperature, at the top of the fluidized bed are set to zero.

13.5.3.2.2 Initial Conditions

Initially, the bottom part of the fluidized bed is filled with particles at rest with a uniform solid volume fraction. The gas flow in the bed is set to its minimum fluidization velocity. In the freeboard a solid volume fraction of 10^{-6} is set, as explained above. The granular temperature is initially set to 10^{-10} m^2 sec^{-2}.

13.5.3.3 Test Cases

With an increase in gas velocity above the minimum fluidization velocity, U_{mf}, bubbles are formed as a result of the inherent instability of the gas–solid system. The behavior of the bubbles significantly affects

the flow phenomena in the fluidized bed, for example, solids mixing, entrainment, and heat and mass transfer. The test cases in this comparative study are used to investigate the capabilities of the closure models and governing equations to predict fluidization behaviour, for example, bubble behavior and bed expansion. Simulation results of each test case are compared to generally accepted experimental data and (semi) empirical models. The system properties and computational parameters for each of the test cases are given in Table 13.7.

13.5.3.3.1 Slugging Fluidized Beds

In the case of the slugging fluidized beds, coalescing bubbles eventually reach a diameter of 70% or more of the column diameter, resulting from either a large inlet gas velocity or a narrow bed. The operating conditions employed in the simulations correspond to the conditions reported by Kehoe and Davidson (1971), who present a detailed study of slug flow in fluidized beds. The experiments of Kehoe and Davidson (1971) were performed in slugging fluidized beds of 2.5, 5, and 10 cm diameter columns using Geldart B particles from 50 to 300 μm diameter and with superficial gas inlet velocities up to 0.5 m/sec. X-ray photography was used to determine the rise velocity of slugs and the bed expansion. Kehoe and Davidson (1971) use their data to validate two different equations for the slug rise velocity, both based on two-phase theory:

$$u_{\text{slug}} = U - U_{\text{mf}} + \frac{\varphi}{2}\sqrt{gD_{\text{T}}} \tag{13.279}$$

and

$$u_{\text{slug}} = U - U_{\text{mf}} + \frac{\varphi}{2}\sqrt{2gD_{\text{T}}} \tag{13.280}$$

where φ is the analyitcally determined square root of the Froude number of a single rising bubble. Equation (13.179) is the exact two-phase theory solution; Equation (13.180) is a modification of Eq. (13.179), based on the following observations:

1. For fine particles (<70 μm), the slugs travel symmetrically up in the fluidized bed, thus the slug rise velocity is increased by coalescence.
2. For coarser particles (>70 μm), the slugs tend to move up along the walls, which also increases their velocity.

According to Kehoe and Davidson (1971), Eqs. (13.179) and (13.180) give an upper and lower bound on the slug rise velocity. Furthermore, Kehoe and Davidson (1971) measured the maximum bed expansion

TABLE 13.7 System Properties and Computational Parameters

Parameter	Description	Freely Bubbling Fluidized Bed	Slugging Fluidized Bed	Bubble Injection into Fluidized Bed (Kuipers, 1990)
ρ_s (kg/m^3)	Solid density	2640	2640	2660
ρ_g (kg/m^3)	Gas density	1.28	1.28	1.28
μ_g (Pas)	Gas viscosity	1.7×10^{-5}	1.7×10^{-5}	1.7×10^{-5}
d_s [μm]	Particle diameter	480	480	500
e(-)	Coefficient of restitution	0.9	0.9	0.9
$\varepsilon_{\max}$ (-)	Maximum solid volume fraction	0.65	0.65	0.65
U_{mf} (m/sec)	Minimum fluidization velocity	0.21	0.21	0.25
D (m)	Inner column diameter	0.5	0.1	0.57
H (m)	Column height	1.3	1.3	0.75
H_{mf} (m)	Height at minimum Fluidization	0.97	0.97	0.5
$\varepsilon_{s,\text{mf}}$ (-)	Solids volume fraction At minimum fluidization	0.42	0.42	0.402
Δx (m)	x mesh spacing	7.14×10^{-3}	6.67×10^{-3}	7.50×10^{-3}
Δy (m)	y mesh spacing	7.56×10^{-3}	7.43×10^{-3}	1.25×10^{-2}

(H_{max}) during slug flow. They validated their theoretical analysis which led to the result that

$$\frac{H_{max} - H_{mf}}{H_{mf}} = \frac{U - U_{mf}}{u_{bub}} \tag{13.281}$$

where u_{bub} is the rise velocity of a slug without excess velocity:

$$u_{bub} = \frac{\varphi}{2}\sqrt{gD_T} \tag{13.282}$$

or

$$u_{bub} = \frac{\varphi}{2}\sqrt{2gD_T} \tag{13.283}$$

corresponding to Eqs. (13.179) and (13.182). Hence, they also propose upper and lower bounds on the maximum bed expansion.

13.5.3.3.2 Freely Bubbling Fluidized Beds

In the freely bubbling fluidized-bed case, the gas flow is distributed across the inlet of the bed. Small bubbles form at the bottom of the fluidized bed which rise, coalesce, and erupt as large bubbles at the bed surface. Hilligardt and Werther (1986) have done many measurements of bubble size and bubble velocity under various conditions using the probe developed by Werther and Molerus (1973) and have correlated their data in the form of the Davidson and Harrison (1963) bubble model. Hilligardt and Werther propose a variant of the Davidson and Harrison (1963) model for predicting the bubble rise velocity as a function of the bubble diameter:

$$u_b = \psi(U - U_{mf}) = \varphi\nu\sqrt{gd_b} \tag{13.284}$$

where φ is the analytically determined square root of the Froude number of a single rising bubble in an infinitely large homogeneous area. Pyle and Harrison (1967) have determined that $\varphi = 0.48$ for a two-dimensional geometry, whereas in three dimensions the Davies–Taylor relationship gives $\varphi = 0.71$. ψ and ν, added by Hilligardt and Werther (1986), are empirical coefficients based on their data, that are dependent upon the type of particles and the width and height of the fluidized bed. For the particles and geometry employed in this study, Hilligardt and Werther (1986) proposed $\psi \approx 0.3$ and $\nu \approx 0.8$. Proposals of values for ψ and ν under various fluidization conditions, determined by simulations, are given by van Wachem et al. (1998).

13.5.3.3.3 Bubble Injection in Fluidized Beds

Single jets entering fluidized bed operated at the minimum fluidization velocity through a narrow single orifice provide details of bubble formation and growth. Such experiments were carried out by Kuipers (1990). Kuipers (1990) reported the shape of the injected bubble as well as the quantitative size and growth of the bubble with time by using high-speed photography. The superficial gas inlet velocity from the orifice was $U = 10$ m/sec, and the orifice was $d = 1.5 \times 10^{-2}$ m wide.

13.5.3.4 Results

The governing equations used are those given by Jackson (1997) or by Ishii (1975), and the default closure models are the solid-phase stress of Hrenya and Sinclair (1997), the radial distribution function of Lun and Savage (1986), the frictional model of Johnson and Jackson (1987) with empirical values given by Johnson et al. (1990), and the drag coefficient model by Wen and Yu (1966).

13.5.3.4.1 Slugging Fluidized Beds

Simulations of the slugging bed case were performed with both the Ishii (1975) and the Jackson (1997) governing equations. In some kinetic theory models, a correlation between the gas-phase and particle-phase velocity fluctuations, called J_s, is taken into account. Figure 13.78 shows the predicted maximum

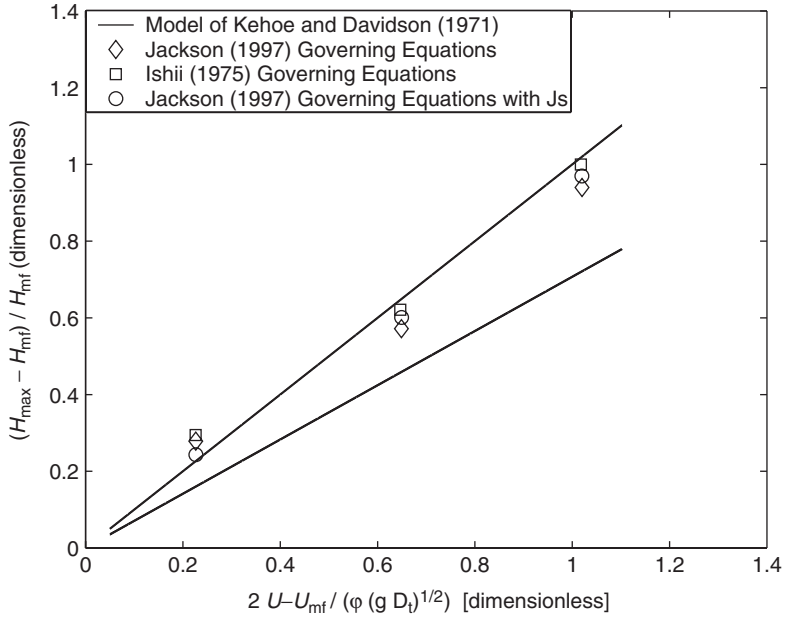

FIGURE 13.78 Predicted maximum expansion of a slugging fluidized bed with an increase in gas velocity the governing equations of Jackson (1997) and Ishii (1975). The predictions are compared with the two-phase theory as proposed and validated by Kehoe and Davidson (1971). (Reprinted from *AIChE J.*, 46, p. 1035, 2001. With kind permission from John Wiley & Sons, Hoboken NJ, USA.)

bed expansion with an increase in gas velocity during the slug flow and the two correlations by Kehoe and Davidson (1971). Figure 13.79 shows the increase in slug rise velocity with an increase in gas velocity. Clearly, the exact formulation of the governing equation or the correlation for J_s do not have any significant influence on the prediction of these macroscopic engineering quantities, and all CFD models do a good job at predicting these quantities.

13.5.3.4.2 Bubbling Fluidized Beds

The exact solid-phase stress description does not influence either the freely bubbling or the slugging fluidized bed predictions. Figure 13.80 shows the predicted bubble rise velocity employing different drag models in a freely bubbling fluidized bed, compared with the empirical correlation of Hilligardt and Werther (1986). All of the investigated drag models are in fairly good agreement with the empirical correlation.

13.5.3.4.3 Bubble Injection

Figure 13.81 shows the quantitative bubble size prediction for a single jet entering a fluidized bed operating at the minimum fluidization velocity on the drag models of Wen and Yu (1966) and Syamlal et al. (1993), which are compared with the experimental data of Kuipers (1990). Frictional stresses can increase the total solid-phase stress by orders of magnitude and is an important contributing force in dense gas–solid modeling, although the size of the bubble is not significantly influenced by the frictional stress, as shown in Figure 13.81. Moreover, Figure 13.82 shows the resulting qualitative predictions of the bubble growth and shape and also compare these with photographs of Kuipers (1990). The Wen and Yu (1966) drag model yields better agreement with findings of Kuipers (1990) for both the bubble shape and size than the Syamlal et al. (1993) drag model. The drag model of The Syamlal et al. (1993), underpredicts the bubble size and produces a bubble that is more circular in shape than in the experiments of Kuipers (1990) and in the simulations with the Wen and Yu (1966) drag model.

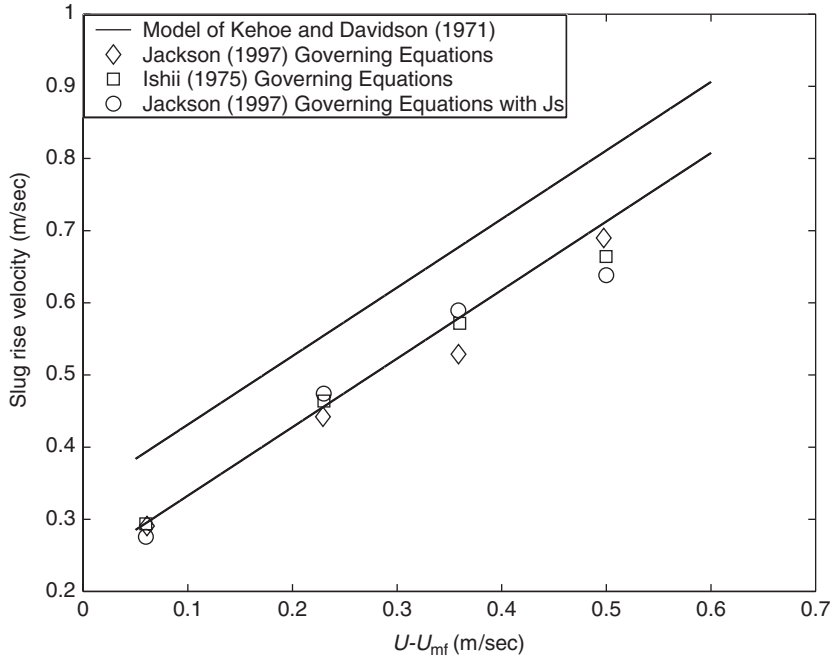

FIGURE 13.79 Predicted slug rise velocity with increasing gas velocity with the govening equations of Jackson (1997) and Ishii (1975). The predictions are compared with the two-phase theory as proposed and validated by Kehoe and Davidson (1971). The constant $\varphi = 0.48$. (Reprinted from AIChE J., 46, 1035, 2001. With kind permission from John Wiley & Sons, Hoboken NJ, USA.)

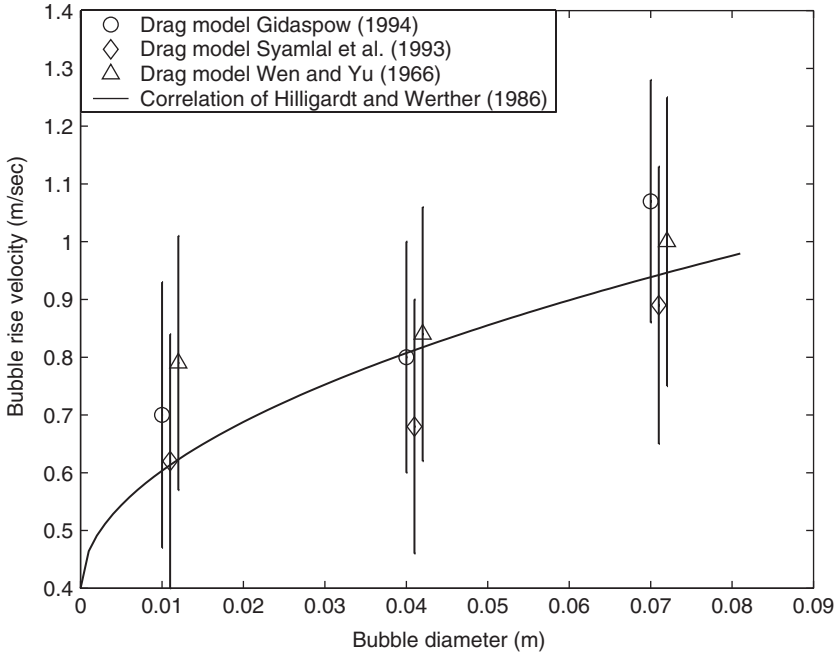

FIGURE 13.80 Predicted bubble rise velocity as a function of the bubble diameter at $U = 0.54$ m/sec based on different drag models and compared to the experimental correlation of Hilligardt and Werther (1986). The vertical lines indicate the spread of the simulated bubble rise velocity. (Reprinted from *AIChE J.*, 46, 1035, 2001. With kind permission from John Wiley & Sons, Hoboken NJ, USA.)

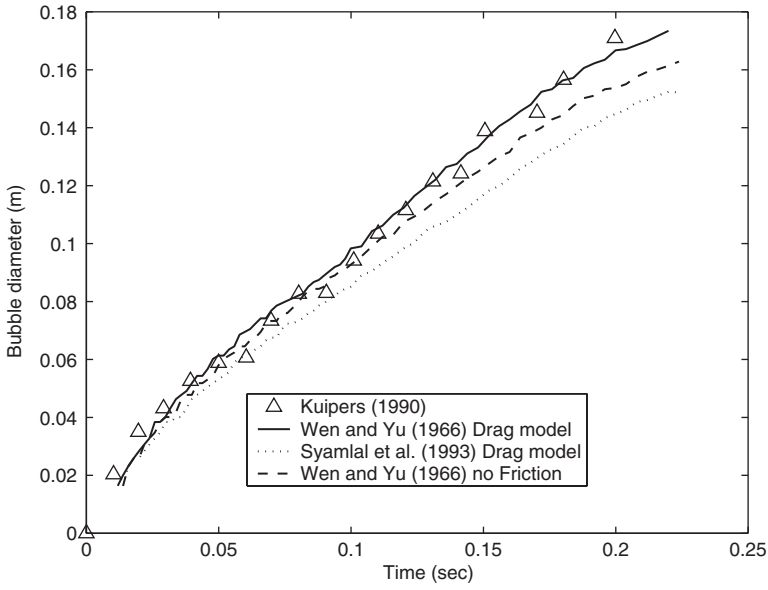

FIGURE 13.81 Bubble diameter as a function of time for a bubble formed at a single jet of $U = 10$ m/sec. A comparison is made between the experiments of Kuipers (1990), simulations using the drag coefficient of Wen and Yu (1966) with and without frictional stress, and simulations using the interphase drag coefficient of Syamlal et al. (1993). (Reprinted from *AIChE J.*, 46, 1035, 2001. With kind permission from John Wiley & Sons, Hoboken NJ, USA.)

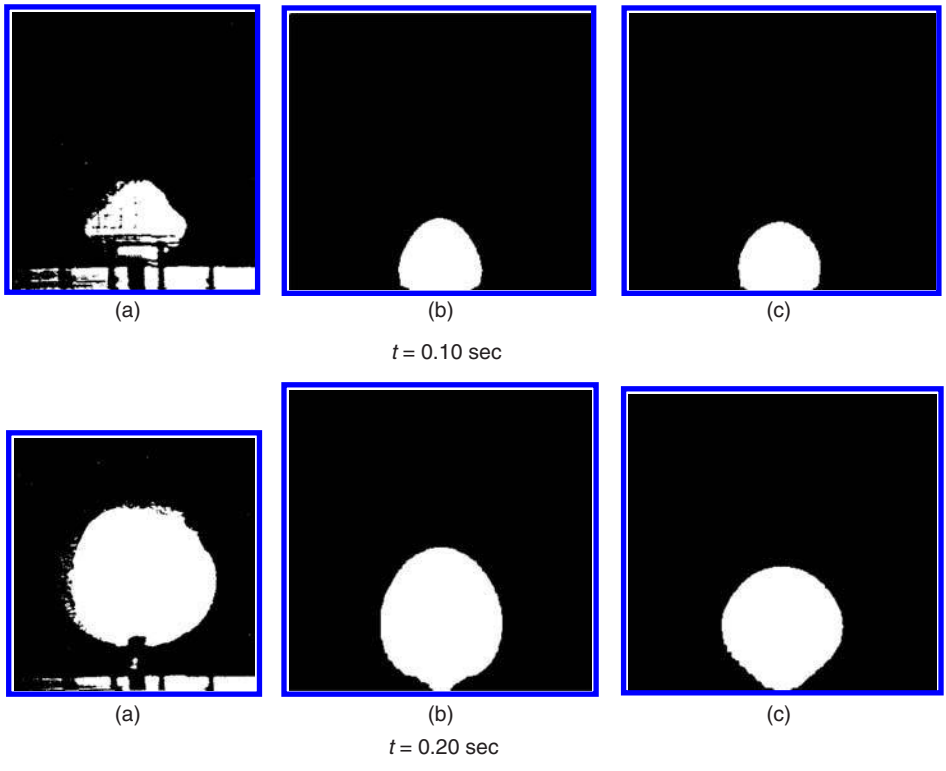

FIGURE 13.82 Experimental and simulated bubble shape associated with a single jet at U 5 10 m/s and at t 5 0.10s and t 5 0.20s. Comparison is made between the (a) experiment of Kuipers (1990), (b) simulation using the interphase drag coefficient of Wen and Yu (1966), and (c) simulation using the interphase drag coefficient of Syamlal et al. (1993). (Reprinted from AIChE J., 46, 1035, 2001. With kind permission from John Wiley & Sons, Hoboken NJ, USA.)

Nomenclature

Latin

A	Area
$\mathbf{A}$	Added mass force
c_d, c_p	Specific heat of dispersed phase
C_L	Lift coefficient
C_D	Drag coefficient
D_g	Molecular diffusion coefficient
$E(\kappa)$	Energy sepctra
f	Ratio of drag to Stokes drag
f_c	Summation of continuous forces
f_p	Summation of fluid forces
$\mathbf{F}$	Force vector
gi, $\mathbf{g}$	Acceleration due to gravity vector
G	Gibbs free energy
$\mathbf{G}_{ij}$	Relative velocity between particles "i" and "j"
h	Enthalpy
h_L	Latent heat
i	Internal energy
k	Thermal conductivity, turbulence energy, reaction rate
l_e	Eddy length scale
L_E	Eulerian length scale
$\mathbf{L}$	Lift force vector
m	Mass
$\dot{m}$	Mass flow rate
$\dot{m}_k$	Mass exchange rate for particle "k"
$\mathbf{M}$	Summation of torques
$\dot{M}$	Total mass flow rate
n	Number density, number of moles
n_i	Unit normal vector
$\dot{n}$	Number flow rate
N	Total number of particles
p	Pressure
p_s	Solids pressure
P_{ij}	Collision frequency
q_i	Heat transfer vector
$\dot{Q}$	Heat transfer rate
Re	Reynolds number
$R(\tau)$	Velocity correlation function
$\mathbf{S}$	Force due to shear gradient
Sh	Sherwood number
Stk	Stokes number
S_mass	Mass source term
S_mom	Momentum source term
t	Time
T	Temperature, inertial time scale
$T(\kappa)$	Spectral energy transfer rate
ui, $\mathbf{u}$, U_i	Velocity vector

v	Particle velocity
V	Volume
V_i	Bubble phase velocity
$\mathbf{w}$	Relative velocity vector
$W(x, t)$	Phase space density
x_i	Coordinate vector
X	Phase space vector

Greek Symbols

α	Volume fraction
α_m	Mass loading ratio
$\underline{\beta}$	Inverse particle response time
β	Ratio of Lagrangian to Eulerian time scales
ε	Void fraction, dissipation rate
$\varepsilon(\kappa)$	Spectral viscous dissipation rate
η	Kolmogorov length scale
Θ	Granular temperature, temperature, wall scattering function
κ	Wave number
λ_k	Ratio of heat transfer to heat transfer at zero Reynolds number
μ	Viscosity
ν	Kinematic viscosity
ξ_s	Solids phase bulk viscosity
ρ	Density
σ	Surface tension
τ_b	Bubble response time
τ_e	Eddy transit time
τ_K	Kolmogorov time scale
τ_L	Lagrangian time scale
τ_p, τ_V	Particle response time
τ_T	Thermal response time
τ_{ij}	Stress tensor
ϕ	Conversion rate of mechanical to thermal energy
$\Psi(\kappa)$	Spectral two-way coupling
ω_A	Mass fraction of species "A"
$\mathbf{\Omega}$	Rotational velocity vector

Subscripts

c	Continuous phase
coll	Collision
d	Discrete phase
D	Drag
eff	Effective
f, F	Fluid
i	Coordinate direction, vector
p, P	Particle
rel	Relative
surf	Surface
0	Initial
@p	At particle position

References

Abrahamson, J., Collision rates of small particles in a vigourously turbulent fluid, *Chem. Eng. Sci.,* 30, 1371–1379, 1975.

Ahmed, A. and Elghobashi, S., On the mechanisms of modifying the structure of turbulent homogeneous shear flows by dispersed particles., *Phys. Fluids*, 12, 2906–2930, 2000.

Ahmed, A. and Elghobashi, S., Direct numerical simulation of particle dispersion in homogeneous turbulent shear flows, *Phys. Fluids*, 13, 3346–3364, 2001.

Al-Rawhai, N. and Tryggvason, G., Numerical simulation of dendritic solidification with convection: Three-dimensional flow, *J. Comput. Phys.*, 194, 677–696, 2004.

Anderson, D.M., McFadden, G.B. and Wheeler, A.A., Diffuse-interface methods in fluid mechanics, *Ann. Rev. Fluid Mech.*, 30; 139–165, 1998.

Anderson, T. B. and Jackson, R., A fluid mechanical description of fluidized beds, *I EC Fundam.* 6, 527, 1967.

Bagchi, P. and Balachandar, S., Effect of turbulence on the drag and lift of a particle, *Phys. Fluids*, 15, 3496–3513., 2003.

Bagnold, R.A., Experiments on a gravity-free dispersion of large solid spheres in a Newtonian-fluid under shear, *Proc. Roy. Soc.London*, A225, 49, 1954.

Baker, G.R., Meiron, D.I., and Orszag, S.A., Vortex simulation of the Rayleigh-Taylor instability, *Phys. Fluids*, **23**; 1485–1490, 1980

Baker, G.R., Meiron, D.I., and Orszag, S.A., Generalized vortex methods for free surface flows problems, *J. Fluid Mech.*, 123; 477, 1982.

Batchelor, G., *An Introduction to Fluid Dynamics*, Cambridge Univ. Press, Cambridge, 1967.

Berlemont, A. and Achim, P., On the fluid/particle and particle/particle correlated motion for colliding particles in Lagrangian approach, *Proceedings of the 3rd ASME/JSME Joint Fluids Engineering Conference, FEDSM99-*7859, 1999.

Berlemont, A., Chang, Z., and Gouesbet, G., Particle Lagrangian Tracking with Hydrodynamic Interactions and Collisions Flow, *Turbulence Combust.* 60, 1–18, 1998.

Berlemont, A., Desjonquères, P., and Gouesbet, G., Particle Lagrangian simulation in turbulent flows, *Int. J. Multiphase Flow*, 16, 19–34, 1990.

Berlemont, A., Achim,P., and Chang, Z., Lagrangian approaches for particle collisions: The colliding particle velocity correlation in the multiple particles tracking method and in the stochastic approach, *Phys. Fluids,* 13, 2946–2956, 2001.

Bird, G.A., *Molecular Gas Dynamics and Direct Simulation of Gas Flow*s, Clarendon Press, Oxford, 1976.

Birkhoff, G., Taylor instability and laminar mixing, Report LA-1862, appendices in Report LA-1927, Los Alamos Scientific Laboratory, 1954 (unpublished).

Blake, J.R. and Gibson, D.C., Growth and collapse of a vapor cavity near a free surface, *J. Fluid Mech.*, 111, 123–140,1981.

Bocksell, T. and Loth, E., Discontinuous and continuous random walk models for particle diffusion in free-shear flows, *AIAA J.*, 39, 1086–1096, 2001.

Boettinger, W.J., Warren, J.A., Beckermann, C., and Karma, A., Phase field simulations of solidification, *Anu. Rev. Mater. Res.*, 32, 163–194, 2002.

Boivin, M., Simonin, O., and Squires, K., Direct numerical simulation of turbulence modulation by particles in isotropic turbulence, *J. Fluid Mech*, 375, 235–263, 1998.

Boivin, M., Simonin,O., and Squires, K., On the prediction of gas-solid flows with two way coupling using large eddy simulation, *Phys. Fluids*, 12, 2080–2090, 2000.

Bolio, E.J. and Sinclair, J.L., Gas turbulence modulation in the pneumatic conveying of massive particles in vertical tubes, *Int. J. Multiphase Flow*, 21, 985, 1995.

Boulton-Stone, J.M. and Blake, J.R., Gas-bubbles bursting at a free-surface, *J. Fluid Mech.*, 254, 437–466, 1993.

Brady, J.F. and Bossis, G., Stokesian dynamics, *Anu. Rev. Fluid Mech.*, 20, 111–157,1988.

Brady, J., Stokesian dynamics simulation of particulate flows, In *Particulate Two-Phase Flow*, Roco, M. (Ed.), Butterworth-Heinemann, Boston, MA, 1993, p. 912.

Bunner, B. and Tryggvason, G., Direct numerical simulations of three-dimensional bubbly flows, *Phys. Fluids*, 11, 1967–1969, 1999.

Bunner, B. and Tryggvason, G., Dynamics of homogeneous bubbly flows, part 1, rise velocity and microstructure of the bubbles, *J. Fluid Mech.*, 466, 17–52, 2002.

Bunner, B. and Tryggvason, G., Dynamics of homogeneous bubbly flows, part 2, fluctuations of the bubbles and the liquid, *J. Fluid Mech.*, 466, 53–84, 2002.

Bunner, B. and Tryggvason, G., Effect of bubble deformation on the stability and properties of bubbly flows, *J. Fluid Mech.*, 495, 77–118, 2003.

Burry, D. and Bergeles G., Dispersion of particles in anisotropic turbulence, Int. *J. Multiphase Flow,* 19, 651–664, 1993.

Buyevich, Y., Statistical hydromechanics of disperse systems. Part 1. Physical background and general equations, *J. Fluid Mech.*, 49, 489–507, 1971.

Buyevich, Y., Statistical hydromechanics of disperse systems. Part 2. Solution of the kinetic equation for suspended particles, *J. Fluid Mech.*, 52, 345–355, 1972a.

Buyevich, Y., Statistical hydromechanics of disperse systems. Part 3. Pseudo-turbulent structure of homogeneous suspensions, *J. Fluid Mech.*, 56, 313–336, 1972b.

Chahine, G.L. and Duraiswami, R., Dynamic interactions in a multibubble cloud, *ASME J. Fluids Eng.*, 114, 680–686, 1992.

Chan, R.K.-C. and Street, R.L., A computer study of finite-amplitude water waves, *J. Comput. Phys.*, 6, 68–94, 1970.

Chandrasekhar, S.K., Stochastic problems in physics and astronomy, *Rev. Modern Phys.* 15, 1–89, 1943.

Chang, Z., Etude de collisions inter-particulaires en écoulement turbulent isotrope ou anisotrope par une approche Lagrangienne à plusieurs trajectoires simultanées. PhD thesis, Université de Rouen, France, March 1998.

Chapman, S. and Cowling, T.G., *The Mathematical Theory of Non-uniform Gases*, Cambridge University Press, Cambridge, 1952.

Chapman, R.B. and Plesset, M.S., Nonlinear effects in the collapse of a nearly spherical cavity in a liquid, *Trans. ASME, J. Basic Eng.*, 94, 142, 1972.

Chen, P.E. and Wood, C.E., A turbulence closure model for dilute gas-particle flows, *Can. J. Chem. Engr.*, 63, 349, 1985.

Choi, H.G. and Joseph, D.D., Fluidization by lift of 300 circular particles in plane poiseuille flow by direct numerical simulation, *J. Fluid Mech.*, 438, 101–128, 2001.

Chung, M.K., Sung, H.J., and Lee, K.B., Computational study of turbulent gas-particle flow in a venturi, *J. Fluids Eng.*, 108, 248, 1986.

Coulomb, C.A., Essai sur une application des règles de maximis et minimis à quelques problèmes de statique, relatifs à l'architecture, *Acad. R. Sci. Mém. Math, Phys. par Divers Savants*, 7, 343–382, 1776.

Crowe, C.T., Sharma, M.P., and Stock, D.E., The Particle-Source-in Cell method for gas droplet flow, *J. Fluid Eng.*, 99, 325, 1977.

Crowe, C.T., Sommerfeld, M., and Tsuji, Y., *Multiphase Flows with Droplets and Particles*, CRC Press, Boca Raton, FL, 1998.

Crowe, C.T., On models for turbulence modulation in fluid-particle flows, *Intl. J. Multiphase Flow*, 26, 719–727, 2000.

Csanady, G.T., Turbulent diffusion of heavy particles with atmosphere, *J. Atmos. Science*, 20, 201–208, 1963.

Daly, B.J., Numerical study of the effect of surface tension on interface instability, *Phys. Fluids*, 12, 1340–1354, 1969.

Daly, B.J., A technique for including surface tension effects in hydrodynamic calculations, *J. Comput. Phys.*, 4, 97–117, 1969.

Daly, B.J. and Pracht, W.E., Numerical study of density-current surges, *Phys. Fluids*, 11, 15–30, 1968.

Dandy, D.S. and Leal, G.L., Buoyancy-driven motion of a deformable drop through a quiescent liquid at intermediate Reynolds numbers, *J. Fluid Mech.*, 208, 161–192, 1989.
Darbyshire, K.F.F. and Swailes, D.C., A PDF model for particle dispersion with stochastic particle-surface interactions, *Gas-Solid Flows,* FED-236, ASME, New York, 1996, pp. 51–56.
Darton, R.C., La Nause, R.D., Davidson, J.F., and Harrison, D., Particle growth due to coalescence in fluidized beds, *Trans. IChem E.*, 55, 274–280, 1977.
Davidson, J.F. and Harrison, D., *Fluidized Particles*, Cambridge University Press, Cambridge, 1963.
DeBar, R., Fundamentals of the KRAKEN Code, Technical report ucir-760, LLNL, 1974.
Derevich, I.V. and Zaichik, L.I., Precipitation of particles from a turbulent flow, *Izvestiyia Akademii Nauk SSR, Mekhanika Zhidkosti Gaza*, 5, 96–104, 1988.
Devenish, B.J., Swailes, D.C., and Sergeev, Y.A., A PDF model for dispersed particles with inelastic particle-wall collisions, *Phys. Fluids,* 11, 1858–1868, 1999.
Ding, J. and Tam, S.W., Asymptotic power spectrum analysis of chaotic behaviour in fluidized beds, *Int. J. Bifurcation Chaos*, 4, 327–341, 1994.
Dorgan, A. and Loth, E., Simulation of particles released near the wall in a turbulent boundary layer, *Int. J. Multiphase Flow*, 2004, to appear.
Drew, D.A., Mathematical modeling of two-phase flows, *Ann. Rev. Fluid Mech.*, 15, 261–291, 1983.
Drew, D.A. and Lahey, R.T. Jr., Analytical modeling of multiphase flow, In *Particulate Two-Phase Flow*, Roco, M.C.(Eds), Butterworth-Heinemann, Boston, 1993, pp. 509–566.
Drew, D.A. and Passman, S.L., Theory of multi-component fluids, *App. Math. Sci.*, Vol. 135, Springer, New York, 1998.
Druzhinin, O. and Elghobashi, S., A lagrangian-eulerian mapping solver for direct numerical simulation of a bubble-laden homogeneous turbulent shear flow using the two-fluid formulation, *J. Comp. Phys.*, 154, 174–196, 1999a.
Druzhinin, O. and Elghobashi, S., On the decay rate of isotropic turbulence laden with microparticles, *Phys. Fluids*, 11, 602–610, 1999b.
Druzhinin, O. and Elghobashi, S., Direct numerical simulation of a spatially-developing three-dimensional bubble-laden mixing layer with two-way coupling, *J. Fluid Mech.*, 429, 23–61, 2001.
Eaton, J. and Fessler, J., Preferential concentration of particles by turbulence, *Int. J. Multiphase Flow*, 20, 169–209, 1994.
Elghobashi, S.E. and Truesdell, G.C., On the two-way interaction between homogeneous turbulence and dispersed solid particles. I: turbulence modification, *Phys. Fluids A*, 5, 1790–1801, 1993.
Elghobashi, S., On predicting particle-laden turbulent flows, *Appl. Sci. Res.*, 52, 309–329, 1994.
Elghobashi, S. and Abou Arab, T., A two-equation turbulence model for two-phase flows, *Phys. Fluids*, 26, 931–938, 1983.
Elghobashi, S. and Truesdell, G., Direct simulation of particle dispersion in decaying isotropic turbulence, *J. Fluid Mech.*, 242, 655–700, 1992.
Elghobashi, S. and Truesdell, G., On the two-way interaction between homogeneous turbulence and dispersed solid particles, Part 1: turbulence modification, *Phys. Fluids* A5, 1790–1801, 1993.
Esmaeeli, A. and Tryggvason, G., An inverse energy cascade in two-dimensional, low Reynolds number bubbly flows, *J. Fluid Mech.*, 314, 315–330, 1996.
Esmaeeli, A. and Tryggvason, G., Direct numerical simulations of bubbly flows, part 1 — low Reynolds number arrays, *J. Fluid Mech.*, 377, 313–345, 1998.
Esmaeeli, A. and Tryggvason, G., Direct numerical simulations of bubbly flows, part 2 — moderate Reynolds number arrays, *J. Fluid Mech.*, 385, 325–358, 1999.
Esmaeeli, A. and Tryggvason, G., Computations of explosive boiling in microgravity, *J. Sci. Computing*, 19, 163–182, 2003.
Ergun, S., Fluid flow through packed columns, *Chem. Engr. Prog.*, 48, 89, 1952.
Faeth, G. M., Mixing, Transport, and combustion in sprays, *Prog. Energ. Combust. Scie.*, 13, 293–345, 1987.
Fedkiw, R., Aslam, T., Merriman, B. and Osher, S., A non-oscilatory eulerian approach to interfaces in multimaterial flows (The ghost fluid method). *J. Comput. Phys.* 152 (1999), 457–492.

Felmy, A.R., GMIN, a Computerized Chemical Equilibrium Program Using a Cconstrained Minimization of the Gibbs Energy: summary report, Chemical Equilibrium and Reaction Models, Soil Science Society of America, Special Publication 42, 1995.

Ferrante, A. and Elghobashi, S., On the physical mechanisms of two-way coupling in particle-laden isotropic turbulence, *Phys. Fluids,* 15, 315–329, 2003.

Ferrante, A. and Elghobashi, S., On the physical mechanisms of drag reduction in a spatially-developing turbulent boundary layer laden with microbubbles, *J. Fluid Mech.* 503, 345–355, 2004.

Feng, J., Hu, H.H., and Joseph, D.D., Direct simulation of initial value problems for the motion of solid bodies in a Newtonian fluid, part 1. sedimation, *J. Fluid Mech.*, 261, 95–134 1994.

Feng, J., Hu, H.H., and Joseph, D.D., Direct simulation of initial value problems for the motion of solid bodies in a Newtonian fluid, part 2. Couette and Poiseuilli flows, *J. Fluid Mech.*, 277, 271–301, 1995.

Fevrier, P. and Simonin, O., Constitutive relations for fluid-particles velocity correlations in gas-slid turbulent flows, *Proceedings of the 3rd International Conference on Multiphase Flows*, ICMF'98, Lyon, France, 8–12, June 1988.

Floryan, J.M. and Rasmussen, H., Numerical analysis of viscous flows with free surfaces, *Appl. Mech. Rev.*, 42, 323–341, 1989.

Foote, G.B., A numerical method for studying liquid drop behavior: Simple oscillations, *J. Comput. Phys.*, 11, 507–530, 1973.

Foote, G.B., The water drop rebound problem: dynamics of collision, *J. Atmos. Sci.*, 32, 390–402, 1975.

Fortes, A., Joseph, D.D., and Lundgren, T., Nonlinear mechanics of fluidization of beds of spherical particles, *J. Fluid Mech.*, 177, 467–483, 1987.

Frank, Th., Wassen, E., and Yu, Q., A 3–Dimensional Lagrangian Solver for Disperse Multiphase Flows on Arbitrary, Geometricaly Complex Flow Domains Using Block–structured Numerical Grids, *Proceedings of the 7th International Symposium on gas–particle flows*, ASME fluids engineering division summer meeting, Vancouver, BC, Canada, June 22–26, 1997, CD–ROM proceedings, FEDSM97–3590.

Frank, Th., and Wassen, E., Parallel Efficiency of PVM– and MPI–Implementations of Two Algorithms for the Lagrangian Prediction of Disperse Multiphase Flows, *JSME Centennial Grand Congress 1997, ISAC' 97 Conference on Advanced Computing on Multiphase Flow*, Tokyo, Japan, July 18–19, 1997.

Frank, Th., Application of Eulerian–Lagrangian Prediction of Gas–Particle Flows to Cyclone Separators, VKI - Von Karman Institute for Fluid Dynamics, Lecture Series Programme 1999–2000, In *Theoretical and Experimental Modeling of Particulate Flow*, Rhode-Saint-Genese (Bruessels), Belgium, April 03–07 2000, pp. 1–52, (Ed.) by Buchlin, J.-M., Von Karman Institute, D/2000/0238/468, 2000.

Frank, Th., 2002, Parallele Algorithmen für die numerische Simulation dreidimensionaler, disperser Mehrphasenströmungen und deren Anwendung in der Verfahrenstechnik, Berichte aus der Strömungstechnik, Shaker Verlag Aachen, p. 328.

Fukai, J., Shiiba, Y., Yamamoto, T., Miyatake, O., Poulikakos, D., Megaridis, C.M., and Zhao, Z., Wetting effects on the spreading of a liquid droplet colliding with a flat surface: experiment and modeling, *Phys. Fluids*, 7, 236–247, 1995.

Gephart, R.E. and Lundgren, R.E., Hanford Tank Cleanup: A Guide to Understanding the Technical Issues, Report PNNL-10773, Pacific Northwest National Laboratory, Richland, Washington.DC, 1997.

Gidaspow, D., *Multiphase Flow and Fluidization*, 1st ed., Academic Press, San Diego, 1994.

Gerz, T., Shumann, U., and Elghobashi, S., Direct numerical simulation of stratified homogeneous turbulent shear flows, *J. Fluid Mech.*, 200, 563–594, 1989.

Glimm, J. and McBryan, O., A computational model for interfaces, *Adv. Appl. Math.*, 6, 422–435, 1985.

Gosman, A.D. and Ioannides, I.E., Aspects of computer simulation of liquid-fuelled combustors. *AIAA J.*, 81, 0323, 1981.

Gourdel, C., Simonin, O., and Brunier, E., Two-Maxwellian equilibrium distribution function for the modeling of a binary mixture of particles, In *Proceedings of the 6th International Conference on Circulating Fluidized Beds,* Werther, J., Ed., DECHEMA, Frankfurt am Main, Germany, 1999, pp. 205–210.

Graham, D.I., Improved eddy interaction models with random length and time scales, *Int. J. Multiphase Flow*, 24, 335–345, 1998.
Harlow, F.H. and Shannon, J.P., The splash of a liquid drop, *J. Appl. Phys.*, 38, 3855–3866, 1967.
Harlow, F.H. and Welch, J.E., Numerical calculation of time-dependent viscous incompressible flow of fluid with a free surface, *Phys. Fluid*, 8, 2182–2189, 1965.
Harlow, F.H. and Welch, J.E., Numerical study of large-amplitude free-surface motions, *Phys. Fluid*, 9, 842–851, 1966.
Harper, J.F., Bubbles rising in line: why is the first approximation so bad? *J. Fluid Mech.*, 351, 289–300, 1997.
Haworth, D.C. and Pope, S.B., A generalized Langevin model for turbulent flow, *Phys. Fluids* 29, 387–405, 1986.
He, J. and Simonin, O., Modelisation Numerique des Ecoulements Turbulents Gaz-Solide en Conduite Verticale, Rapport EDF HE-44/94/021A, 1994.
Herting, D.L., Results of Dilution Studies with Waste from Tank 241-AN-105, Report HNF-SD-WM-DTR-046, Numatec Hanford Corp., Richland, Washington. DC, 1997.
Hilligardt, K. and Werther, J., Local bubble gas hold-up and expansion of gas/solid fluidized beds, *German Chem. Eng.*, 9, 215–221, 1986.
Hinze, J.O., *Turbulence*, 2nd Ed., Mc-Graw-Hill, New York, 1975.
Hirt, C.W., Cook, J.L., and Butler, T.D., A Lagrangian method for calculating the dynamics of an incompressible fluid with a free surface, *J. Comput. Phys.*, 5, 103–124, 1970.
Hirt, C.W. and Nichols, B.D., Volume of fluid (VOF) method for the dynamics of free boundaries, *J. Comput. Phys.*, 39, 201–226, 1981.
Hishida, K. and Maeda, M., Two-phase confined jet: effect of particle density, Fifth Workshop on two-phase flow Predictions, *Proceedings of Erlangen*, March 19–22, 1990.
Hu, H.H., Direct simulation of flows of solid–liquid mixtures, *Int. J. Multiphase Flow*, 22, 335, 1996.
Hou, T.Y., Lowengrub, J.S., and Shelley, M.J., Boundary integral methods for multicomponent fluids and multiphase materials, *J. Comput. Phys.*, 169, 302–362, 2001.
Hrenya, C.M. and Sinclair, J.L., Effects of particle-phase turbulence in gas-solid flows, *AIChE J.*, 43, 853–869, 1997.
Hu, H.H., Direct simulation of flows of solid–liquid mixtures, *Int. J. Multiphase Flow*, 22, 335-352, 1996.
Hyland, K.E., Reeks, M.W., and McKee, S., Derivation of a pdf kinetic equation for the transport of particles in turbulent flow, *J. Phys. A: Math. Gen.,* 32, 6169–6190, 1999a.
Hyland, K.E., Reeks, M.W., and McKee, S., Exact analytic solutions to turbulent particle flow equations, *Phys. Fluids,* 11, 1249, 1999b.
Hyman, J.M., numerical methods for tracking interfaces. *Physica D*, 12 (1984), 396–407.
Illner, R. and Neunzert, H., On simulation methods for the Boltzmann equation, *Transp. Theory Stat. Phys.* 16, 141, 1987.
Ishii, M., *Thermo-Fluid Dynamic Theory of Two-Phase Flow*, Direction des Etudes et Recherches d'Electricité de France, Eyrolles, Paris, France, 1975.
Ishii, M., *Interfacial Area Modeling*, Vol. 3, Chap. 3, McGraw-Hill, New York, 1987, pp. 31–62.
Jackson, R., Locally averaged equations of motion for a mixture of identical spherical particles and a newtonian fluid, *Chem. Eng. Sci.*, 52, 2457–2469, 1997.
Jenkins, J.T., Boundary conditions for rapid granular flow: flat, frictional walls, *J. Appl. Mech.*, 59, 120–127, 1992.
Jenkins, J.T. and Richman M.W., Grads 13-moment system for a dense gas of inelastic spheres, *Arch. Ration. Mech. Anal.*, 87, 355–377, 1985.
Jeong, J.-H., Goldenfield, N., and Dantzig, J.A., Phase field model for three-dimensional dendritic growth with fluid flow, *Phys. Rev E*, 64, 041602, 2001.
Jewett, J.R., et al., 2002, Values of Particle Size, particle Density, and Slurry Viscosity to Use in Waste Feed Delivery Transfer System Analysis, Report RPP-9805, U.S. Department of Energy, Office of River Protection, Richland, Washington. DC, 2002.

Jimenez, J., Computing high-Reynolds-number turbulence: will simulations ever replace experiments?, *J. Turbulence*, 4, 1–14, 2003.

Johnson, P.C. and Jackson, R., Frictional-collisional constitutive relations for granular materials, with application to plane shearing, *J. Fluid Mech.*, 176, 67–93, 1987.

Johnson, P.C., Nott, P., and Jackson, R., Frictional-collisional equations of motion for particulate flows and their application to chutes, *J. Fluid Mech.*, 210, 501–535, 1990.

Johnson, A.A. and Tezduyar, T.E., 3-d simulation of fluid-particle interactions with the number of particles reaching 100, *Comput. Methods Appl. Mech. Eng.*, 145, 301–321, 1997.

Joia, I.A., Ushijima, T., and Perkins, R.J., Numerical study of bubble and particle motion in turbulent boundary layer using proper orthogonal decomposition, *Appl. Sci. Res.,* 57, 263–277, 1997.

Juric, D. and Tryggvason, G., Computations of boiling flows, *Int. J. Multiphase Flow*, 24, 387–410, 1998.

Kajishima, T. and Takiguchi, S., Interaction between particle clusters and particle-induced turbulence, *Int. J. Heat Fluid Flow*, 23, 639, 2002.

Kallio, G.A, and Reeks M.W., A numerical simulation of particle deposition in turbulent boundary layers, *Int. J. Multiphase Flows* 15, 433–446, 1989.

Kawaguchi, T., Sakamoto, M., Tanaka, T., and Tsuji, Y., Quasi-three-dimensional numerical simulation of spouted beds in cylinder, *Powder Technol.*, 109, 3, 2000.

Kanai, A. and Miyata, H., Direct numerical simulation of wall turbulent flows with microbubbles, *Int. J. Num. Meth. Fluids*, 35, 593–615, 2001.

Kang, I.S. and Leal, L.G., Numerical solution of axisymmetric, unsteady free-boundary problems at finite Reynolds number, i. Finite-difference scheme and its applications to the deformation of a bubble in a uniaxial straining flow, *Phys. Fluids*, 30, 1929–1940, 1987.

Kawamura, T. and Kodama, Y., Numerical simulation method to resolve interactions between bubbles and turbulence, *Int. J. Heat Fluid Flow*, 23, 627–638, 2002.

Kehoe, P.W.K. and Davidson, J.F., Continuously slugging fluidised beds, *Inst. Chem. Eng. Symp. Ser.*, 33, 97–116, 1971.

Kim, I., Elghobashi. S., and Sirignana, W.B., On the equation for spherical-particle motion: effect of Reynolds and acceleration numbers, *J. Fluid Mech.*, 367, 221–253, 1998.

Kitron, A., Elperin, T., and Tamir, A., Monte Carlo simulation of gas–solids suspension flows in impinging streams reactors, *Int. J. Multiphase Flow*, 16-1, 1, 1990.

König, C., Untersuchungen zum Abscheideverhalten von geometrisch ähnlichen Zyklonen, Ph.D. thesis, University of Kaiserslautern, Germany, 1990.

Kuipers, J.A., A Two-Fluid Micro Balance Model of Fluidized Beds, Ph.D. thesis, University of Twente, The Netherlands, 1990.

Kuwagi, K. and Horio, M., A numerical study on agglomerate formation in a fluidized bed of fine cohesive particles, *Chem. Eng. Sci.*, 57, 4737, 2002.

Laurent, F. and Massot, M., Multi-fluid modelling of laminar polydisperse spray flames: origin, assumptions and comparison of sectional sampling methods, *Combustion Theory Modelling,* 5, 537–572, 2001.

Laviéville, J., Deutsch, E., and Simonin, O., Large Eddy Simulation of Interactions Between Colliding Particles and a Homogeneous Isotropic Turbulence Field, In *Gas-Solid Flows, ASME FED*, 228, 1995, pp. 347–357.

Lavieville, J., Simonin, O., Berlemont, A., and Chang, Z., Validation of Inter-Particle Collision Models Based on Large-Eddy Simulation in Gas-Solid Turbulent Homogeneous Shear Flow, *Proceedings of the 7th Internationl Symposium on Gas-Particle Flows*, ASME FEDSM97-3623, 1997.

Lee, L. and LeVeque, R.J., An immersed interface method for incompressible Navier–Stokes equations, *SIAM J. Sci. Computing*, 25, 832–856, 2003.

Li, and Pozrikidis, C., Wall-bounded shear flow and channel flow of suspensions of liquid drops, *Int. J. Multiphase Flow*, 26, 1247–1279, 2000.

Liu, Z.H., Kawaguchi, T., Tanaka, T., and Tsuji, Y., The effect of temperature on the minimum fluidization velocity calculated by distinct element method, *JSME Int. J.*, Ser. B, 66, 45–1, 2002.

Liu, B.Y.H. and Agrawal, J.K., Experimental observation of aerosol deposition in turbulent flow, *J. Aerosol. Sci.*, 5, 145–155, 1974.

Loewenberg, M. and Hinch, E.J., Numerical simulation of a concentrated emulsion in shear flow, *J. Fluid Mech.*, 321, 395–419, 1996.

Longuet-Higgins, M.S. and Cokelet, E.D., The deformation of steep surface waves on water, *Proc. R. Soc. London Ser. A*, 358, 1, 1976.

Loth, E., Numerical approaches for motion of dispersed particles, bubbles, and droplets, *Prog. Energ. Combust. Sci.*, 26, 161–223, 2000.

Lun, C.K.K. and Savage, S.B., The effects of an impact velocity dependent coefficient of restitution on stresses developed by sheared granular materials, *Acta Mech.*, 63, 15–44, 1986.

McHyman, J., Numerical methods for tracking interfaces, *Physica D*, 12, 396–407, 1984.

MacInnes, J.M and Bracco, F.V., Stochastic particle dispersion modelling and the tracer particle limit, *Phys Fluids A* 4(12), 2809-2824, 1992.

Maxey, M., The gravitational settling of aerosol particles in homogeneous turbulence and random flow fields, *J. Fluid Mech.*, 174, 441, 1987.

Maxey, M., Chang, E., and Wang, L.-P., Simulation of interactions between microbubbles and turbulent flows, *Appl. Mech. Rev.*, 4, S70, 1994.

Maxey, M.R. and Riley, J.J., Equation of motion for a small rigid sphere in a nonuniform flow, *Phys. Fluids*, 26, 883–889, 1983.

Maxey, M.R., Patel, B.K., Chang, E.J., and Wang, L.-P., Simulations of dispersed turbulent multiphase flow, *Fluid Dyn. Res.*, 20, 143–156, 1997.

Mei, R., Lawrence, C.J., and Adrian, R.J., Unsteady drag on a sphere at finite Reynolds number with small fluctuations in the free-stream velocity, *J. Fluid Mech.*, 233, 613–631, 1991.

Mei, R., An approximate expression for the shear lift force on a spherical particle at finite Reynolds number, *Int. J. Multiphase Flow*, 18, 145–147, 1992.

Mikami, T., Kamiya, H., and Horio, M., Numerical simulation of cohesive powder behaviour in a fluidized bed, *Chem. Eng. Sci.*, 53, 1927, 1998.

Milojević, D., Lagrangian Stochastic-Deterministic (LSD) predictions of particle dispersion in turbulence, *Part. Syst. Charact.*, 7, 181–190, 1990.

Mitchell, T.M. and Hammitt, F.H., Asymmetric cavitation bubble collapse, *Trans ASME, J. Fluids Eng.*, 95, 29, 1973.

Mortazavi, S. and Tryggvason, G., A numerical study of the motion of drops in Poiseuille flow, part 1. lateral migration of one drop, *J. Fluid Mech.*, 411, 325–350, 2000.

Nanbu, K., Direct Simulation Scheme Derived from the Boltzmann Equation. I. Monocomponent Gases, *J. Phy. Soc. of Jpn.*, 49–5, 2042, 1980.

Noh, W.F. and Woodward, P., SLIC (simple line interface calculation), in van de Vooren, A.I. and Zandbergen, P.J., Ed., *Proceedings of the 5th International Conference on Fluid Dynamics*, Vol. 59 of Lecture Notes in Physics, Springer, Berlin, 1976, pp. 330–340.

Ocone, R., Sundaresan, S., and Jackson, R., Gas-particle flow in a duct of arbitrary inclination with particle-particle interactions, *AIChE J.*, 39, 1261–1271, 1993.

Oesterle, B. and Petitjean, A., Simulation of Particle-to-Particle Interactions in Gas–Solid Flows, *Int. J. Multiphase Flow*, 19, 199–211, 1993.

Oguz, H. and Prosperetti, A., Bubble entrainment by the impact of drops on liquid surfaces, *J. Fluid Mech.*, 219, 143–179, 1990.

Oguz, H. and Prosperetti, A., Dynamics of bubble growth and detachment from a needle, *J. Fluid Mech.*, 257, 111–145, 1993.

Onishi, Y., Reid, H.C., and Trent, D.S., Dilution Physics Modeling: Dissolution/Precipitation Chemistry, Report PNL-10815, Pacific Northwest National Laboratory, Richland, Washington, DC, 1995.

Onishi Y., et al., Tank SY-102 Waste Retrieval Assessment: Rheological Measurements and Pump Jet Mixing Simulation, Report PNNL-11352, Pacific Northwest National Laboratory, Richland, Washington, DC, 1996.

Onishi, Y. and Trent, D.S., Mobilization modeling of erosion-resisting radioactive tank waste, *Proceedings of Rheology in the Mineral Industry II*, Oahu, Hawaii, United Engineering Foundation, New York, 1999, pp. 45–56.

Onishi, Y., et al., Simulation of radioactive tank waste mixing with chemical reactions, *Proceedings of 3rd ASME/JSME Joint Fluids Engineering Conference*, San Francisco, 1999.

Onishi, Y., Recknagle, K.P., and Wells, B.E., Pump Jet Mixing and Pipeline Transfer Assessment for High-Activity Radioactive Wastes in Hanford Tank 241-AZ-102, Report PNNL-13275, Pacific Northwest National Laboratory, Richland, Washington, DC, 2000.

Onishi, Y., et al., Pipeline Cross-Site Transfer Assessment for Tank 241-SY-101, Report PNNL-13650, Pacific Northwest National Laboratory, Richland, Washington, DC, 2002.

Onishi, Y., et al., Retrieval and Pipeline Transfer Assessment of Hanford Tank 241-AN-105 Waste, Report, PNNL-14144, Pacific Northwest National Laboratory, Richland, Washington, DC, 2003.

Oran, E.S. and Boris, J. P., *Numerical Simulation of Reactive Flow,* Elsevier, Amsterdam, 1987.

Ormancey, A., Simulation du comportement de particule dans des écoulements turbulents, Thèse de 3ème cycle, Ecole des Mines de Paris, 1984.

Osher, S. and Fedkiw, R.P., Level set methods, *J. Comput. Phys.*, 169, 463–502, 2001.

Pan, T.W., Joseph, D.D., Bai, R., Glowinski, R., and Sarin, V., Fluidization of 1204 spheres: simulation and experiment, *J. Fluid Mech.*, 451, 169, 2002.

Pan, Y. and Banerjee, S., Numerical investigation of the effect of large particle on wake turbulence, *Phys. Fluids*, 9, 3786, 1997.

Pandya, R.V.R. and Mashayek, F., Probability Density Functions Modelling of Evaporating Droplets Dispersed in Isotropic Turbulence, *AIAA J.*, 39, 1909–1915, 2001.

Pandya, R.V.R. and Mashayek, F., Non-isothermal dispersed phase of particles in turbulent flow, *J. Fluid Mech.,* 475, 205–245, 2003.

Papavergos, P.G. and Hedley A.B., Particle deposition behaviour from turbulent flows, *Chem. Eng. Res. Des.,* 62, 275–295, 1984.

Pascal, P. and Oesterlé, B., On the dispersion of discrete particle moving in a turbulent shear flow, *Int. J. Multiphase Flow*, 26, 293–325, 2000.

Patankar, S.V., *Numerical Heat Transfer and Fluid Flow*, Hemisphere, Washington, DC, 1980.

Peric, M., Ein zum Parallelrechnen geeignetes Finite–Volumen–Mehrgitterverfahren zur Berechnung komplexer Strömungen auf blockstrukturierten Gittern mit lokaler Verfeinerung, Abschlußbericht zum DFG–Vorhaben Pe 350/3–1 im DFG–Habilitandenstipendiumprogramm, Stanford University, USA, 1992.

Picard, A., Berlemont, A., and Gouesbet, G., Modeling and predicting turbulence fields and the dispersion of discrete particles transported in turbulent flows, *Int. J. Multiphase Flow*, 12, 237, 1986.

Pigeonneau, F., Modélisation et calcul numérique des collisions de gouttes en écoulement laminaire et turbulent, PhD Thesis, Université de Paris VI, France, October 1998.

Pitzer, K.S., *Activity Coefficients in Electrolyte Solutions*, 2nd ed., CRC Press, Boca Raton, FL, 1991.

Pope, S. G., PDF Methods for turbulent reactive flows, *Prog. Energy Combust. Sci.*, 119–192, 1985.

Pope, S. G., Application of the velocity-dissipation probability density function model to homogeneous turbulent flows, *Phys. Fluids A,* 3, 1947–1957, 1991.

Pozrikidis, C., *Integral and Singularity Methods for Linearized Viscous Flow*, Cambridge Univ. Press, Cambridge, 1992.

Pozrikidis, C., Interfacial dynamics for stokes flow, *J. Comput. Phys.*, 169, 250–301, 2001.

Pozorski, J. and Minier, J.-P., Probability density function modelling of dispersed two-phase turbulent flows, *Phys. Rev. E.*, 59, 855–863, 1998.

Pozorski, J. and Minier, J.-P., On the Lagrangian turbulent dispersionmodels based on the Langevin equation, *Int. J. Multiphase Flow*, 24, 913–945, 1988.

Pyle, D.L. and Harrison, D., The rising velocity of bubbles in two-dimensional fluidized beds, *Chem. Eng. Sci.*, 22, 531, 1967.

Qi, D., Lattice-Boltzmann simulations of fluidization of rectangular particles, *Int. J. Multiphase Flow*, 26, 421, 2000.

Rallison, J.M. and Acrivos, A., A numerical study of the deformation and burst of as viscous drop in an extensional flow, *J. Eng. Mech.*, 89, 191, 1978.

Ramshaw, J. D., Brownian motion in a flowing fluid, *Phys. Fluids,* 22, 1595–1601, 1979.

Reeks, M.W., On the dispersion of small particles suspended in an isotropic turbulent flow, *J. Fluid Mech.*, 83, 529–546, 1977.

Reeks, M.W., Eulerian Direct Interaction applied to the statistical motion of particle in a turbulent fluid, *J. Fluid Mech.,* 97, 569–590, 1980.

Reeks, M.W., The transport of discrete particles in in-homogeneous turbulence, *J. Aerosol Sci.,* 14, 729–739, 1983.

Reeks, M.W., On a kinetic equation for the transport of particles in turbulent flows, *Phys. Fluids A,* 3, 446–456, 1991.

Reeks, M.W., On the continuum equations for dispersed particles in nonuniform flows, *Phys. Fluids A*, 5, 750–761, 1993.

Reeks M.W. and Swailes, D.C., A unifying theory for the deposition of particles in a turbulent boundary layer, *1993b FED* –Vol. 166, *Gas–solid Flows*, *ASME*, New York, 1993, pp. 109–112.

Reeks, M.W. and Swailes, D.C., The near wall behavior of particles in a simple turbulent flow and gravitational settling and partially absorbing wall, *J. Fluid Mech. Res.,* 22, 31–39, 1997.

Rhodes, M. J., Wang, X. S., Nguyen, M., Stewart, P., and Liffman, K., Use of discrete element method simulation in studying fluidization characteristics: influence of interparticle force, *Chem. Engi. Sci.*, 56, 69, 2001.

Rizk, M.A. and Elghobashi, S.E., A two-equation turbulence model for disperse, dilute, confined two-phase flow, *Int. J. Multiphase Flows*, 15, 119, 1989.

Robinson, P.B., Blake, J.R., Kodama, T., Shima, A., and Tomita, Y., Interaction of cavitation bubbles with a free surface, *J. Appl. Phys.*, 89, 8225–8237, 2001.

Rong, D. and Horio, M., Behaviour of particles and bubbles around immersed tubes in a fluidized bed at high temperature and pressure: a DEM simulation, *Int. J. Multiphase Flow*, 27, 89, 2001.

Ruetsch, G. and Meiburg, E., Two-way coupling in shear layers with dilute bubble concentrations, *Phys. Fluids,* 6, 2656, 1994.

Ryskin, G. and Leal, L.G., Numerical solution of free-boundary problems in fluid mechanics. Part 2. buoyancy-driven motion of a gas bubble through a quiescent liquid, *J. Fluid Mech.*, 148, 19–35, 1984.

Saffman, P., On the stability of laminar dusty gas, *J. Fluid Mech.*, 13, 120–128, 1962.

Sangani, A.S. and Didwania, A.K., Dynamic simulations of flows of bubbly liquids at large Reynolds numbers, *J. Fluid Mech.*, 250, 307–337, 1993.

Sankaranarayanan, K., Shan, X., Kevrekidis, I.G., and Sundaresan, S., Analysis of drag and virtual mass forces in bubbly suspensions using an implicit formulation of the Lattice Boltzmann method, *J. Fluid Mech.*, 452, 61–96, 2002.

Savage, S.B., Granular flows at high shear rates, In *Theory of Dispersed Multiphase Flow*, Meyer, R.E. Ed., Academic Press, New York, 1983, p. 339.

Scardovelli, R. and Zaleski, S., Direct numerical simulation of free-surface and interfacial flow, *Annu. Rev. Fluid Mech.*, 31, 567–603, 1999.

Schaeffer, D.G., Instability in the evolution equations describing incompressible granular flow, *J. Differential Equations*, 66, 19–50, 1987.

Schreck, E. and Peric M., Parallelization of Implicit Solution Methods, *ASME Fluids Engineering Conference*, June 22–23, 1992, Los Angeles (CA), USA, 1992.

Schultz, W.W., Huh, J., and Griffin, O.M., Potential-energy in steep and breaking waves, *J. Fluid Mech.*, 278, 201–228, 1994.

Schumann, U., Realizability of Reynolds-stress turbulence models, *Phys. Fluids* 20, 721–725, 1977.

Shrayber, A. A., Euler and Lagrange methods in the theory of two-phase flows with variable particle size of the discrete phase, *Fluid Mech. – Soviet Res.*, 8, 79–87, 1979.

Sethian, J.A., Evolution, implementation, and application of level set and fast marching methods for advancing fronts, *J. Comput. Phys.*, 169, 503–555, 2001.

Shan, X.W. and Chen, H. D., Lattice Boltzmann model for simulating flows with multiple phases and components, *Phys. Rev. E*, 47, 1815–1819, 1993.

Shin, S. and Juric, D., Modeling three-dimensional multiphase flow using a level contour reconstruction method for front tracking without connectivity, *J. Comput. Phys.*, 180, 427–470, 2002.

Shopov, P.J., Minev, P.D., Bazhekov, I.B., and Zapryanov, Z.D., Interaction of a deformable bubble with a rigid wall at moderate Reynolds numbers, *J. Fluid Mech.*, 219, 241–271, 1990.

Shyy, W., Udaykumar, H.S., Rao, M., and Smith, R., *Computational Fluid Dynamics with Moving Boundaries*, Taylor & Francis, Philadelphia, 1996.

Sierou, A. and Brady, J. F., Rheology and microstructure in concentrated noncolloidal suspensions, *J. Rheol.*, 46, 1031–1056, 2002.

Simonin, O., Deutsch, E., and Minier, J.-P., Eulerian Prediction of the Fluid/Particle Correlated Motion in Turbulent Two-Phase Flows, *Appl. Sci. Res.*, 51, 275–283, 1993.

Simonin, O., Eulerian Formulaion for particle Dispersion in Two-phase Flows, In *Proceedings of 5th Workshop on Two-phase Flow Predictions*, Erlangen, 1990, Sommerfeld, M. and Wenneberg, D. (Ed.),Bilateral Seminars of the International Bureau/ Forschugszentrun Julich Gmbh, Vol. 4, 1991, pp. 156–166.

Simonin, O., Statistical and continuum modelling of turbulent reactive particulate flows Part I; theoretical derivation of dispersed Eulerian modelling from probability density function kinetic equations, Part II; Application of a two phase second moment transport model for the prediction of turbulent Gas-particle flows, *Theoretical and Experimental Lecture Series 2000-06*, von Karman Institute for Fluid Dynamics, Rhode Saint Genese, Belgium, 2000.

Simonin, O., Fevrier, P., Lavieville, J., On the Spatial Distribution of Heavy-Particle Velocities in Turbulent Flow : from Continuous Field to Particulate Chaos, *J. Turbulence*, 3, 040, http://stacks.iop.org/1468-5248/37040, 2002.

Sinclair, J.L. and Jackson, R., 1989, Gas-particle flow in a vertical pipe with particle-particle interactions, *AIChE J.*, 35, 1473, 1989.

Sivier, S.A., Loth, E., and Baum, J.D., Dusty shock flow with unstructured adaptive finite elements and parcels, *AIAA J.*, 34, 1078–1080, 1996.

Smereka, P., On the motion of bubbles in a periodic box, *J. Fluid Mech.*, 254, 79–112, 1993.

Sommerfeld, M., The importance of inter-particle collisions in horizontal gas-solid channel flows, *Gas-Particle Flows, ASME Fluids Engineering Conference*, Hiltons Head, USA, FED-Vol. 228, pp. 335–345, 1995.

Sommerfeld, M., Validation of a stochastic Lagrangian modeling approach for inter-particle collisions in homogeneous isotropic turbulence, *Int. J. Multiphase Flow*, 27, 1829–1858, 2001.

Sommerfeld, M., Modelling of particle–wall collisions in confined gas–particle flows, *Int. J. of Multiphase Flows*, 18, 905–926, 1992.

Sommerfeld, M., Modellierung und numerische Berechnung von partikelbeladenen turbulenten Strömungen mit Hilfe des Euler/Lagrange–Verfahrens, *Berichte aus der Strömungstechnik*, Shaker Verlag, Aachen, Germany, 1996.

Son, G. and Dhir, V.K., Numerical simulation of film boiling near critical pressures with a level set method, *J. Heat Trans.*, 120, 183–192, 1998.

Spalart, P.R., Strategies for Turbulence Modeling and Simulations, *4th International Symposium On Engineering Turbulence Modeling and Measurements*, Corsica, France, May 24–26, 1999.

Spalart, P.R., Strategies for Turbulence Modeling and Simulations, *Int. J. of Heat and Fluid Flow*, 21, 252–263, 2000.

Speziale, C.G., Sarkar, S., and Gatski, T.B., Modeling the pressure–strain correlation of turbulence: an invariant dynamical systems approach, *J. Fluid Mech.*, 227, 245–272, 1991.

Squires K. and Eaton, J., Particle response and turbulence modification in isotropic turbulence, *Phys. Fluids A* 2, 1191–1203, 1990.

Squires K. and Eaton, J.K., Preferential concentration of particles by turbulence, *Phys. Fluids* A, 3, 130, 1991.

Steefel, C.L. and Lasaga, A.C., A coupled model for transport of multiple chemical species and kinetic precipitation/dissolution reactions with application to reactive flow in single phase hydrothermal systems, *Am. J. Sci.*, 294, 529, 1994.

Stewart, C.W., et al., *In Situ* Rheology and Gas Volume in Hanford Double-Shell Waste Tanks, Report PNNL-11296, Pacific Northwest National Laboratory, Richland, Washington, 1996.

Sundaram, S. and Collins, L., A numerical study of the modulation of isotropic turbulence by suspended particles, *J. Fluid Mech.*, 379, 105–143, 1999.

Swailes, D.C. and Reeks, M.W., Particle deposition from a turbulent flow: a steady state model for high inertial particles, *Phys. Fluids A,* 6, 3392–3403, 1994.

Swailes, D.C., Darbyshire. K.F.F., Reeks, M.W., Analysis of particle dispersion using a PDF equation; results for simple shear and rotating flows, *ASME FED*-Vol. 228, *Gas-Particle Flows ASME Summer Meeting*, Hilton Head Island, SC, August, 1995, pp. 257–263.

Swailes D.C. and Darbyshire, K.F. F., A generalised Fokker-Planck equation for particle transport in random media, *Physica A*, 242, 38–48, 1997.

Swailes, D.C. and Sergeev, Y.A., Chapman-Enskog closure approximation in the kinetic theory of dilute turbulent gas-particulate suspensions, *Physica A,* 254, 517–547, 1998.

Syamlal, M., Rogers, W., and O'Brien, T.J., Mfix documentation theory guide, U.S. Department of Energy, Office of Fossil Energy, DOE/METC-94/1004(DE94000087), Technical Note, 1993.

Takada, N., Misawa, M., Tomiyama, A., and Fujiwara, S., Numerical simulation of two- and three-dimensional two-phase fluid motion by Lattice Boltzmann method, *Comput. Phys. Commun.,* 129, 233–246, 2000.

Takada, N., Misawa, M., Tomiyama, A., and Hosokawa, S., Simulation of bubble motion under gravity by Lattice Boltzmann method, *J. Nucl. Sci. and Technol.*, 38, 330–341, 2001.

Tanaka, T., and Tsuji, Y., Numerical Simulation of Gas-Solid Two-Phase Flow in a Vertical Pipe: on the Effect of Inter-Particle Collision, In *Gas-Solid Flows, ASME FED*, Vol. 121, 1991, 123–128.

Tanaka, T., Yonemura, S., Kiribayashi K., and Tsuji, Y., Cluster formationand particle-induced instability in gas–solid flows predicted by the DSMC method, *JSME Int. J.*, Ser. B, 39–2, 239, 1996.

Tanaka, T., Noma, K., Ide, Y., and Tsuji, Y., Particle clusters formed in dispersed gas–solid flows: simulation and experiment, *Proceedings of World Congress on Particle Technology* 4 (CD-ROM), July 21–25, Sydney, Australia, (2002), Paper No. 658.

Tchen, C.M., Mean values and correlation problems connected with the motion of small particles suspended in a turbulent fluid, Doctoral dissertation, Delft, Holland, 1949.

Tennekes, H. and Lumley, J.L., *A First Course in Turbulence*, MIT Press, Cambridge, MA, 1972.

Tomiyama, A., Zun, I., Sou, A., and Sakaguchi, T., Numerical analysis of bubble motion with the VOF method, *Nucl. Engr. Des.*, 141, 69–82, 1993.

Tonhardt, R. and Amberg, G., Phase-field simulations of dendritic growth in a shear flow, *J. Crystal Growth*, 194, 406–425, 1998.

Trent, D.S. and Eyler, L.L., TEMPEST: A Computer Program for Three-dimensional Time-Dependent Computational Fluid Dynamics, Report PNL-8857 Vol. 1, Pacific Northwest National Laboratory, Richland, Washington DC, 1994.

Tryggvason, G., Bunner, B., Esmaeeli, A., Juric, D., Al-Rawahi, N.,Tauber, W., Han, J., Nas, S., and Jan, Y.-J., A front tracking method for the computations of multiphase flow, *J. Comput. Phys.*, 169, 708–759, 2001.

Tsuji, Y., Shen, N.Y., and Morikawa, Y., Lagrangian simulation of dilute gas–solid flows in a horizontal pipe, *Adv. Powder Technol.*, 2, 2, 63–81, 1991.

Tsuji, Y., Tanaka, T. and Ishida, T., Lagrangian Numerical Simulation of Plug Flow of Cohesionless Particles in a horizontal Pipe, *Powder Technology*, 71, 239, 1992.

Tsuji, Y., Kawaguchi, T., and Tanaka, T., Discrete particle simulation of two-dimensional fluidized bed, *Powder Technol.*, 77, 79, 1993.

Unverdi, S.O. and Tryggvason, G., Computations of multi-fluid flows, *Physica D*, 60, 70–83, 1992.

Unverdi, S.O. and Tryggvason, G., A front-tracking method for viscous, incompressible, multi-fluid flows, *J. Comput Phys.*, 100, 25–37, 1992.

van Wachem, B.G.M., Schouten, J.C., Krishna, R., and den Bleek, C.M., Eulerian simulations of bubbling behaviour in gas–solid fluidised beds, *Comput. Chem. Eng.*, 22, S299–S306, 1998.

Vandromme, D., Introduction to the Modeling of Turbulence: Turbulence Modeling for Compressible Flows and Acoustics, von Karman Institute for Fluid Dynamics, Lecture Series 1997-03, March 1977.

Vermorel, O., Bedat, B., Simonin, O., Poinsot, T., Numerical Study and Modelling of Turbulence Modulation in a Particle Laden Slab Flow, *J. Turbulence*, 4, 025, 2003, http ://stacks.iop.org/ 1468-5248/4/025.

Vinje, T. and Brevig, P., Numerical simulations of breaking waves, *Adv. Water Resour.*, 4, 77–82, 1981.

Von Karman, T. and Howarth, L., On the statistical theory of isotropic turbulence, *Proc. Roy. Soc., London* A, 164, 192–215, 1938.

Wang, L.-P. and Maxey, M., The motion of microbubbles in a forced isotropic and homogeneous turbulence, *Appl. Sci. Res.*, 51, 291, 1993a.

Wang, L.P. and Maxey, M.R., Settling velocity and concentration distribution of heavy particles in homogeneous isotropic turbulence, *J. Fluid Mech.*, 256, 27–68, 1993.

Wang, L.P. and Stock, D.E., Numerical simulation of heavy particle dispersion: time-step and nonlinear drag consideration, *J. Fluids Eng.*, 114, 100–106, 1992

Wang, Q. and Squires, K.D., Large Eddy Simulation of particle laden turbulent channel flow, *Phys. Fluids*, 8, 1207–1223, 1996.

Welch, S.W.J. and Wilson, J., A volume of fluid based method for fluid flows with phase change, *J. Comp. Phys.*, 160, 662–682, 2000.

Wells, M.R. and Stock, D.E., The effects of crossing trajectories on the dispersion of particles in a turbulent flow, *J. Fluid Mech.*, 136, 31–36, 1983.

Wen, C.Y. and Yu, Y.H., Mechanics of fluidization, *Chem. Eng. Progr. Symp.* Ser., 62, 100, 1996.

Werther, J. and Molerus, O., The local structure of gas fluidized beds. I. A Statistically based measuring system, *Int. J. Multiphase Flow*, 1, 103–122, 1973.

White, F.M., *Viscous Fluid Flow*, McGraw-Hill, New York, 1991.

Xu, J., Maxey, M., and Karniadakis, G.E., Numerical simulations of turbulent drag reduction using microbubbles, *J. Fluid Mech.*, 468, 271–281, 2002.

Xue, M., Xu, H.B., Liu, Y.M. and Yue, D.K.P., Computations of fully nonlinear three-dimensional wave–wave and wave–body interactions, part 1. dynamics of steep three-dimensional waves, *J. Fluid Mech.*, 438, 11–39, 2001.

Yabe, T., Xiao, F., and Utsumi, T., The constrained interpolation profile (cip) method for multi-phase analysis, *J. Comput. Phys.*, 169, 556–593, 2001.

Yu, D. and Tryggvason, G., The free surface signature of unsteady, two-dimensional vortex flows, *J. Fluid Mech.*, 218, 547–572, 1990.

Ye, T., Mittal, R., Udaykumar, H.S., and Shyy, W., An accurate cartesian grid method for viscous incompressible flows with complex immersed boundaries, *J. Comput. Phys.*, 156, 209–240, 1999.

Yeh, G.T. and Tripathi, V.S., A critical evaluation of recent developments in hydrogeochemical transport models of reactive multichemical components, *Water Resour. Res.*, 25, 93, 1989.

Yeung P.K. and Pope S.B., Lagrangian statistics from direct numerical simulations of isotropic turbulence, *J. Fluid Mech.*, 207, 1989.

Yonemura, S., Tanaka, T., and Tsuji, Y., Cluster formation in gas–solid flow predicted by DSMC method, *ASME/FED Gas–Solid Flows*, 166, 303, 1993.

Yoon, H.Y., Koshizuka, S., and Oka, Y., Direct calculation of bubble growth, departure, and rise in nucleate pool boiling, *Inte. J. Multiphase Flow*, 27, 277–298, 2001.

Youngren, G.K. and Acrivos, A., On the shape of a gas bubble in a viscous extensional flow, *J. Fluid Mech.*, 76, 433, 1976.

Yu, D. and Tryggvason, G., The free surface signature of unsteady, two-dimensional vortex flows, *J. Fluid Mech.*, 218, 547–572, 1990.

Yudine, M.I., Physical considerations on heavy-particle dispersion, *Advances in Geophysics*, Vol. 6, Academic Press, New York, 1959, pp. 185–191.

Zaichik, L.I., Modelling of particle dynamics and heat transfer using equations for first and second moments of velocity and temperature fluctuations, *Proceedings of the 8th International Symposium on Turbulent Shear Flows*, Technical University of Munich, 1991, pp. 10-2-1 to 10-2-6.

Zhang, D.Z. and Prosperetti, A., Ensemble phase-averaged equations for bubbly flows, *Phys. Fluids*, 6, 2956–2970, 1994.

Zhang, D. and Prosperetti, A., Momentum and energy equations for disperse two-phase flows and their closure for dilute suspensions, *Int. J. Multiphase Flow*, 23, 245–453, 1997.

Zhang, D.Z. and Rauenzahn, R.M., A viscoelastic model for dense granular flows, *J. Rheol.*, 41, 1275–1298, 1997.

Zhou, L.X. and Li, Y., A κ –ε for simulating gas-particle flows, *Proceedings of the 6th Erlangen-Merseburg Workshop on Two-Phase Flow Predictions*, Sommerfeld, M. Ed., Merseburg, May 1996.

Zhou, Y., Wexler, A.S., and Wang, L.P. On the collision rate of small particles in isotropic turbulence. II. Finite inertia case, *Phys. Fluids*, 10, 1206–1216, 1998.

Zhou, H. and Pozrikidis, C., The flow of ordered and random suspensions of two-dimensional drops in a channel, *J. Fluid Mech.*, 255, 103–127, 1993.

Zinchenko, A.Z. and Davis, R.H., An efficient algorithm for hydrodynamical interaction of many deformable drops, *J. Comput. Phys.*, 157, 539–587, 2000.